Quasi-Periodicity in the Parsec-Scale Jet of the Quasar 3C 345

A High Resolution Study using VSOP and VLBA

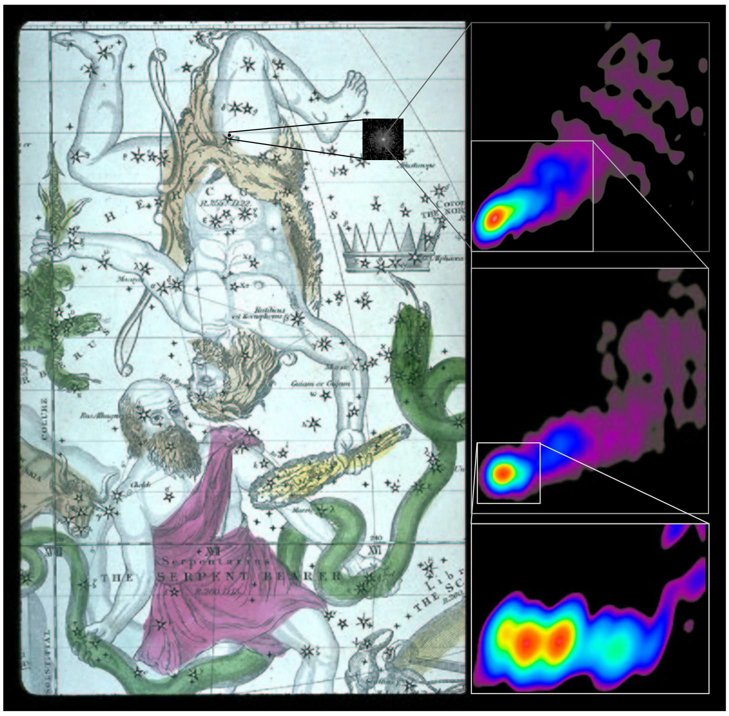

Dissertation

zur
Erlangung des Doktorgrades (Dr. rer. nat)
der
Mathematisch-Naturwissenschaftlichen Fakultät
der
Rheinischen Friedrich-Wilhelms-Universität Bonn

vorgelegt von

Jens Klare
aus
Langenhagen

Bonn (Februar) 2003

Chapter 1

Introduction

1.1 Radio Astronomy

The birth of radio astronomy happened by chance in 1932 when the engineer Karl Jansky, from the Bell Telephone Laboratories in New Jersey, USA, investigated disturbances of overseas phone calls. He found a noise signal from a static source which appeared every day four minutes earlier. What he found was the radio emission from the center of our galaxy. The first radio survey of the sky was done by Grote Reber with a 9.5 m parabolic antenna at $\lambda = 1.8\,\mathrm{m}$ in his backyard in 1939. The construction of many single radio telescopes around the world, the design of radio interferometers (e.g. the VLA[1]), aperture synthesis (Ryle 1957, Scott *et al.* 1961, Ryle & Neville 1962), VLBI[2] (Clark *et al.* 1968a,b) down to mm-wavelengths (e.g. Krichbaum 1999, Doeleman & Krichbaum 1999, Lobanov 2000), the dedicated instrument VLBA[3] and finally SVLBI[4] (see chapter 2.5), led to a unique, overwhelming expansion of our knowledge of the universe.

1.2 Active Galactic Nuclei

After three of the strongest radio sources were identified with nearby galaxies (Virgo A - M87, Centaurus A - NGC 5182, Cygnus A) it was obvious that the origin of many radio sources has to be extragalactic (Bolton *et al.* 1949, Smith 1951, Baade & Minkowski 1954). A few percent of the galaxies contain extremely compact centers which are much brighter than the radiation of all the stars in the galaxy together and which can exceed the radiation of our own galaxy by a factor larger than 1000. These AGN[5] are the most powerful energy phenomena known in the universe. The class of AGN contains several types of objects (OVV[6], BL Lac, Quasar[7], Seyfert 1/2, Radio Galaxies FR[8]I/FRII) which show different properties but are assumed

---

[1] Very Large Array

[2] Very Long Baseline Interferometry

[3] Very Long Baseline Array

[4] Space VLBI

[5] Active Galactic Nuclei

[6] Optically Violent Variables

[7] Quasi Stellar Radio Source

[8] Fanaroff and Riley (Types I and II)

to have the same astrophysical origin, seen at different geometric orientations and can be sketched in the unified model of AGN (Figure 1.1, Ferrari 1998). The first member of this class, the quasar 3C 273, was discovered in 1963 (Schmidt 1963). It is generally assumed that AGN produce their energy by accreting matter onto

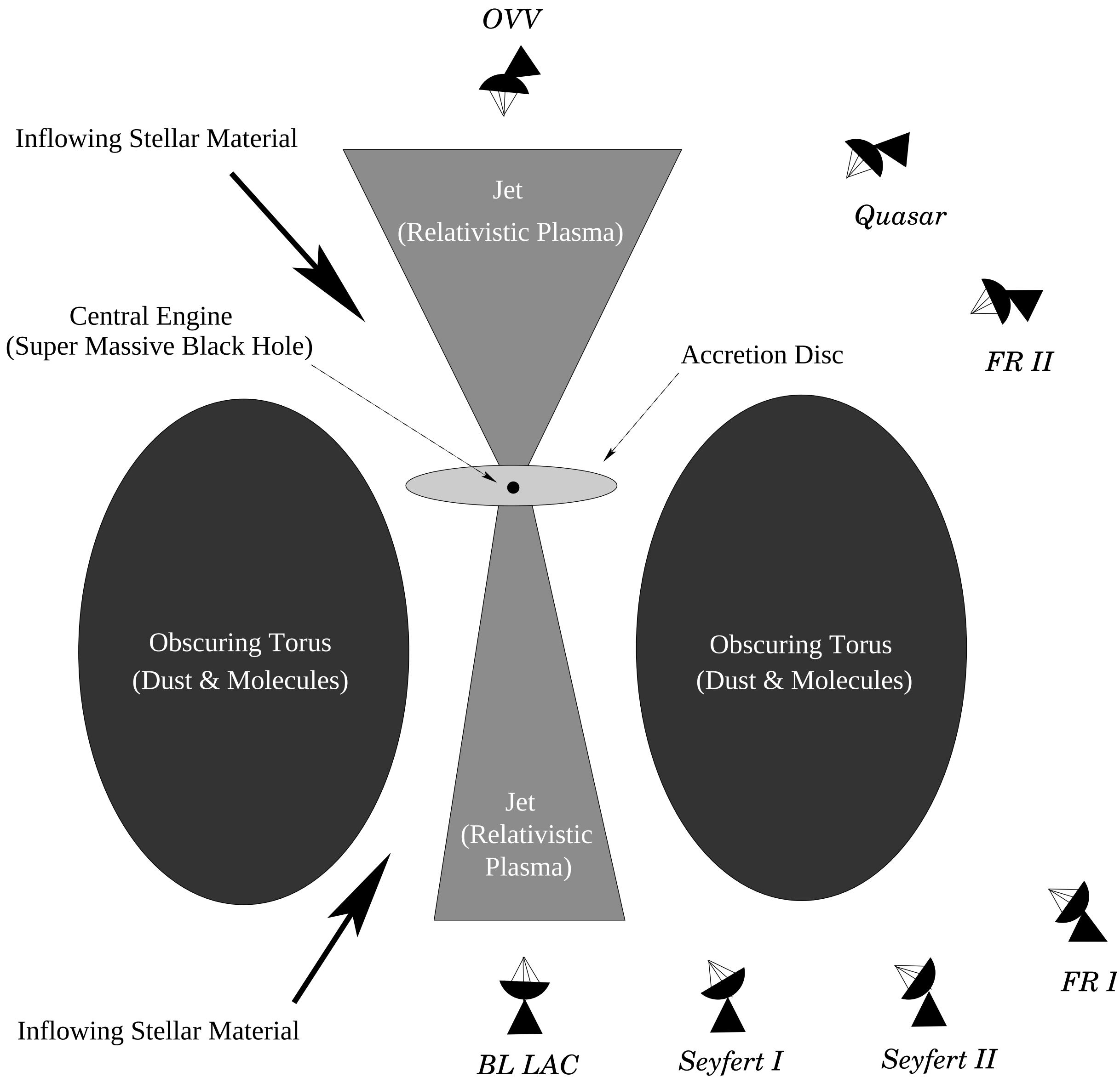

Figure 1.1: Unified scheme of AGN: Matter is accreting from a disc onto a supermassive black hole. A fraction of this matter is ejected from the system in collimated relativistic jets which continue until they dissipates their energy due to friction with the surrounding medium. The different astrophysical observables (e.g. luminosity, variability, spectral lines) are strongly dependent on the angle from which the jet is seen. This leads to the present classification of AGN.

the central engine which is supposed to be a *supermassive black hole* (Rees 1984). Many of these objects have highly collimated relativistic outflows, the *jets*, which get their energy from accretion (Blandford & Rees 1974). These plasma jets are formed perpendicular to the accretion disc, become accelerated to highly relativistic speeds and can be observed in the radio regime, due to their synchrotron radiation. Because of the relativistic beaming effect, the radiation of the approaching jet becomes amplified while the receding jet is attenuated. This effect causes many AGN jets to appear one-sided, depending on their spatial orientation with respect to the Earth, and the sensitivity of the radio telescopes. VLBI observations of jets in AGN (e.g. 3C 273, in the early '70s) led to the discovery of enhanced emission regions (*components*), which show apparent superluminal motions. This is an illusion caused by their relativistic velocity combined with a small angle to the line of sight (Moffet *et al.* 1971, Cohen *et al.* 1971, Whitney *et al.* 1971). The improvement of the VLBI technique since the '70s provided an enormous amount of information on jet kinematics, morphology, physical conditions and evolution of the innermost part of AGN (Zensus & Pearson 1987). Observations with VLBI, together with radio observations with connected interferometers and single antennas, in combination with complementary observations across the electromagnetic spectrum, evolved into a detailed picture of AGN which allowed different physical models to be elaborated. Many theoretical models are based on three fundamental assumptions: relativistic beaming, relativistic injection (Rees 1966) and accretion of matter onto a supermassive black hole (Begelman *et al.* 1984). Common models of AGN are the relativistic shock model (Blandford & Königl 1979, Königl 1981), the more evolved *shock-in-jet* model (Marscher & Gear 1985), and the two-fluid model (Sol *et al.* 1989).

Although many aspects of the unified AGN model are widely accepted, many details are poorly understood (e.g. the composition of the jet, the process of acceleration and collimation, the origin of variability, the physical cause of the jet components and the strong curvature of parsec-scale structures). VLBI observations at the shortest wavelengths in combination with SVLBI with its longest baselines are unique tools to investigate AGN at the highest spatial resolution, in the immediate vicinity of the central engine. This helps to develop, to improve and to verify physical AGN models.

1.3 The Quasar 3C 345

The 16th magnitude quasar 3C 345 ($z = 0.595$) can be regarded as one of the archetypical sources for studies of superluminal motion of components on strongly curved trajectories in its one-sided jet. Several components with an apparent velocity of $2-20c$ have been observed in the jet (e.g. Zensus, Cohen, & Unwin 1995, hereafter ZCU95). The curvature of these trajectories may result from a periodic process driven at the jet base, by Kelvin-Helmholtz instabilities (Hardee 1987; Steffen *et al.* 1995; Qian *et al.* 1996) or a binary black hole system (Roos *et al.* 1993, Lobanov 1996). A relativistic shock model for helical jets has been modeled by Gómez *et al.* (1994) and applied to 3C 345 by Steffen *et al.* (1995) to explain the observed component trajectories and flux variations. Physical conditions in the jet have been derived from ZCU95, using the inhomogeneous jet model of Königl (1981) for the core in combination with homogeneous spheres for the superluminal features.

The morphology on pc-scales has been monitored with VLBI (Biretta, Moore, & Cohen 1986, hereafter BMC86, ZCU95, Lobanov 1996) and the total radio emission by single dish observations (Hughes *et al.* 1991, Teräsranta *et al.* 1992). Flux measurements has been done by the UMRAO[9] at 5, 8 and 15 GHz and the Metsähovi Radio Research Station in Finland at 22 and 37 GHz (e.g. Stevens *et al.* 1994). The VLBI monitoring has been done mainly at 5, 10.7 and 22.3 GHz and sporadically at 1.4, 2.3, 8.4, 43 and 86 GHz.

Images of the linear polarized emission at 1.3 and 2 cm reveal an alignment of the electric vector with the extremely curved inner section of the jet. Strong fractional polarization ($m \sim 15\%$) is seen at 6 cm with the electric vector being oriented perpendicular to the jet. This is consistent with a transition between two emission regimes in the jet: the inner shock-dominated region, and the outer, dominated by plasma interaction (Ros *et al.* 2000).

Lobanov & Zensus (1999) have presented a model which describes the evolution of the core spectrum with a sequence of five "flare like" events and is able to predict changes in the flux density observed in the core for the periods 1981 to 1996. The flares occur approximately every 3.5–4 years and correlate with the appearance of new jet components.

The likely domination of an electron-positron plasma in the jet rather than a normal plasma, evaluated for the components C2–C5 and C7, was suggested by Hirotani *et al.* (2000).

3C 345 shows strong activity from radio to UV but is only a weak X-ray emitter. The long term optical variability shows quasi-periodicity with a period of about 1560 days (Babadzhanyants & Belokon 1984a,b, Kidger 1990, Babadzhanyants *et al.* 1995).

CCD photometry of Zhang *et al.* (2000) showed a significant correlation between brightness and colors. Their results showed good agreement with their prediction of the variability period for the optical outbursts of about 10 years.

C7, the youngest component of 3C 345 in 1992–1993, was the dominant X-ray source during this time period rather than the core (Unwin *et al.* 1997).

1.4 Aim of this Ph.D.

3C 345 is a unique research object which provides a much deeper understanding of the AGN physics. As mentioned in section 1.3, the one-sided jet of 3C 345 shows jet components which move in strongly curved trajectories. The ejection angles of these components vary, and the component trajectories differ significantly from each other. The curvature of the component trajectories increases towards the optically thick region of the jet (the *core*), while the trajectories straighten at larger core separations. This makes the innermost region most interesting for studying the kinematics of the jet components, the jet itself and the energy production mechanism of AGN. Thus, it is important to investigate the behaviour of the jet features at a very early evolutionary stage. This makes 3C 345 a prime candidate for high-resolution imaging with VLBI at the shortest wavelengths and longest baselines. VLBA observations at 22 and 43 GHz and SVLBI observations at 1.6 and 5 GHz were used for this Ph.D. to study in detail the innermost jet region in the immediate vicinity

---

[9] University of Michigan Radio Astronomy Observatory, http://www.astro.lsa.umich.edu/obs/radiotel/umrao.html

of the central engine. The observations were made between 1997.40 and 1999.69 and allowed an intensive study of 5 jet components in the inner 3 mas to be made. Three of them were ejected during this time period and have been followed at the beginning of their evolution much more precisely than it done for older components. The observations at four different frequencies have allowed spectral studies of the jet to be made. This Ph.D. work leads to an expansion of the knowledge of the archetypical quasar 3C 345.

Chapter 2

Interferometry and Imaging

A summary of the fundamentals of interferometry and imaging and a detailed description of SVLBI are given in this chapter. Section 2.1 introduces the mathematical formulae which describe the electromagnetic field of an astronomical object measured by an interferometer. Section 2.2 shows the principle of an interferometer and 2.3 presents the techniques for calibrating the received and recorded radio waves. The methods which are necessary to obtain a radio-image of the observed astronomical objects are described in section 2.4. For a more detailed description of the sections mentioned above, see e.g. Rohlfs & Wilson (1996), Thompson, Moran & Swenson (1998), and Taylor, Carilli & Perley (1999). A detailed presentation of SVLBI in general and VSOP in particular is given in section 2.5.

2.1 The Observed Electric Field

The electric field $\mathbf{E}(\mathbf{R}, t)$ from a radio source can be represented as a series of quasi-monochromatic Fourier coefficients $\mathbf{E}_\nu(\mathbf{R})$.

$$\mathbf{E}_\nu(\mathbf{r}) = \int \mathbf{E}_\nu(\mathbf{R}) P_\nu(\mathbf{R}, \mathbf{r}) \, dS \tag{2.1}$$

The function $P_\nu(\mathbf{R}, \mathbf{r})$ is the propagator which describes how the electric field, emitted at $\mathbf{R}$, is influenced until it reaches the spatial point $\mathbf{r}$ of the measurement (Figure 2.1). One simplification is made by the assumption that the astronomical objects are far away from the observer. Thus, a description of the object structure in the third spatial dimension (the depth) is impossible and all one can measure is the *surface brightness* of the astronomical source. With the simplification that the space between the source and the observer is empty and following Huygens' Principle, the propagator has the following form:

$$P_\nu(\mathbf{R}, \mathbf{r}) = \frac{e^{2\pi i \nu |\mathbf{R} - \mathbf{r}|/c}}{|\mathbf{R} - \mathbf{r}|} \tag{2.2}$$

Now, one can describe the electric field as follows:

$$\mathbf{E}_\nu(\mathbf{r}) = \int \mathbf{E}_\nu(\mathbf{R}) \frac{e^{2\pi i \nu |\mathbf{R} - \mathbf{r}|/c}}{|\mathbf{R} - \mathbf{r}|} \, dS \tag{2.3}$$

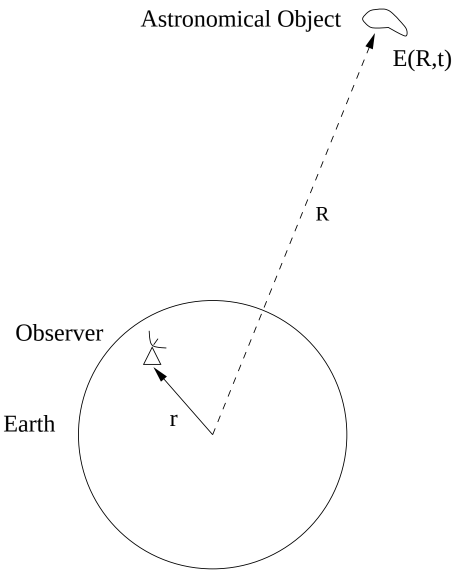

Figure 2.1: Principle geometry of the astronomical object and the observer.

The correlation of an electric field at two different locations $\mathbf{r_1}$ and $\mathbf{r_2}$ is defined as the expected value of the following product:

$$V_\nu(\mathbf{r_1}, \mathbf{r_2}) = \langle \mathbf{E}_\nu(\mathbf{r_1}) \mathbf{E}^*_\nu(\mathbf{r_2}) \rangle \tag{2.4}$$

This product is called *visibility*. The star denotes the complex conjugate. Now, one can substitute $\mathbf{E}_\nu(\mathbf{r})$ in (2.4) with equation (2.3):

$$V_\nu(\mathbf{r_1}, \mathbf{r_2}) = \left\langle \int\int \mathbf{E}_\nu(\mathbf{R_1}) \mathbf{E}^*_\nu(\mathbf{R_2}) \frac{e^{2\pi i\nu|\mathbf{R_1}-\mathbf{r_1}|/c}}{|\mathbf{R_1}-\mathbf{r_1}|} \frac{e^{-2\pi i\nu|\mathbf{R_2}-\mathbf{r_2}|/c}}{|\mathbf{R_2}-\mathbf{r_2}|} \, dS_1 \, dS_2 \right\rangle \tag{2.5}$$

Assuming that the radiation from astronomical objects is spatially incoherent, i.e. $\langle \mathbf{E}_\nu(\mathbf{R_1}) \mathbf{E}^*_\nu(\mathbf{R_2}) \rangle$ is zero for $\mathbf{R_1} \neq \mathbf{R_2}$, the equation (2.5) changes to:

$$V_\nu(\mathbf{r_1}, \mathbf{r_2}) = \int \langle |\mathbf{E}_\nu(\mathbf{R})|^2 \rangle |\mathbf{R}|^{-2} \frac{e^{2\pi i\nu|\mathbf{R}-\mathbf{r_1}|/c}}{|\mathbf{R}-\mathbf{r_1}|} \frac{e^{-2\pi i\nu|\mathbf{R}-\mathbf{r_2}|/c}}{|\mathbf{R}-\mathbf{r_2}|} \, dS \tag{2.6}$$

With $\mathbf{s} = \mathbf{R}/|\mathbf{R}|$ for the unit vector, $I_\nu(\mathbf{s}) = \langle |\mathbf{E}_\nu(\mathbf{s})|^2 \rangle |\mathbf{R}|^{-2}$ for the observed intensity, neglecting $|\mathbf{r}/\mathbf{R}|$ because $|\mathbf{r}| \ll |\mathbf{R}|$ and substituting the surface element dS on the celestial sphere by $|\mathbf{R}|^2 d\Omega$, the equation (2.6) becomes:

$$V_\nu(\mathbf{r_1}, \mathbf{r_2}) \approx \int I_\nu(\mathbf{s}) e^{-2\pi i\nu \mathbf{s}(\mathbf{r_1}-\mathbf{r_2})/c} d\Omega \tag{2.7}$$

This is the so-called *spatial coherence function* of the electric field $\mathbf{E}_\nu(\mathbf{r})$. One should note that equation (2.7) depends only on the separation of the vectors $\mathbf{r_1}$ and $\mathbf{r_2}$ and not on their absolute positions. To measure the correlation properties of the radiation field, one keeps one point fixed and moves the other point around. An interferometer is a device to measure this spatial coherence function.

2.1.1 Measurement in the uv-Plane

The measurements are made in a plane and the vector spacing in the coherence function is measured conveniently in units of wavelengths with $|\mathbf{r_1} - \mathbf{r_2}| = \lambda(u, v, 0) = c\nu^{-1}(u, v, 0)$. In this coordinate system the components of the unit vector $\mathbf{s}$ are $(l, m, \sqrt{1 - l^2 - m^2})$. Substituting in (2.7) gives:

$$V_\nu(u, v, w = 0) = \int\int I_\nu(l, m) \frac{e^{-2\pi i(ul+vm)}}{\sqrt{1 - l^2 - m^2}}\, dl\, dm \tag{2.8}$$

Hence one has a Fourier transform relation between the spatial coherence function $V_\nu(u, v, w = 0)$ and the modified intensity $I_\nu(l, m)/\sqrt{1 - l^2 - m^2}$, where the conjugate coordinates of the spatial coherence function are expressed in units of wavelengths and the intensity is expressed in direction cosines.

With the assumption that the radiation comes only from a small fraction of the celestial sphere and the image center is chosen at the position of zero phase, one can introduce a unit vector $\mathbf{s} = \mathbf{s_0} + \sigma$ pointing to this origin. $\mathbf{s_0}$ is a position which is close to the region of interest. All components in the second power of σ can be neglected. With another coordinate system with $\mathbf{s_0} = (0, 0, 1)$ one gets:

$$V'_\nu(u, v, w) = e^{-2\pi i w} \int\int I_\nu(l, m) e^{-2\pi i(ul+vm)}\, dl\, dm \tag{2.9}$$

Usually one omits the factor in front of the integrals:

$$V_\nu(u, v) = \int\int I_\nu(l, m) e^{-2\pi i(ul+vm)}\, dl\, dm \tag{2.10}$$

With the inversion of this Fourier function one gets the coherence function in the direction $\mathbf{s_0}$, the phase tracking center:

$$I_\nu(l, m) = \int\int V_\nu(u, v) e^{2\pi i(ul+vm)}\, du\, dv \tag{2.11}$$

In practice, the spatial coherence function is known only for a limited number of measured points in the uv-plane. Thus, one can describe the region measured with a *sampling function* $S(u, v)$, which is zero where no data were taken.

$$I^D_\nu(l, m) = \int\int V_\nu(u, v) S(u, v) e^{2\pi i(ul+vm)}\, du\, dv \tag{2.12}$$

$I^D_\nu(l, m)$ is called the *dirty image* and

$$B(l, m) = \int\int S(u, v) e^{2\pi i(ul+vm)}\, du\, dv \tag{2.13}$$

is called the *dirty beam* or *point spread function* corresponding to the sampling function $S(u, v)$. The dirty beam is characterized by a central maximum of roughly Gaussian shape, the FWHM[1] and sidelobes around the origin.

With a *weighting function* $W(u, v) = \mathcal{T}(u, v)\mathcal{D}(u, v)\mathcal{R}(u, v)$ one can influence the weighting of the data, which changes the effective beam shape and the sidelobe level caused by the antenna array used. The *weighting function* is split up into three parts:

---

[1] Full Width at Half Maximum

1. $\mathcal{T}(u,v)$ is called `tapering` function and is used to down or up-weight a selected part of the uv-coverage (e.g with a Gaussian function). This is helpful for instance when one wants to focus on the extended structure of an astronomical object by down weighting the longer baselines.

2. $\mathcal{D}(u,v)$ is the density weighting function which reduces the side lobe level by weighting an inhomogeneous uv-coverage which can be caused by gaps between short and long baselines. The $\mathcal{D}(u,v)$ functions most often used are the *uniform* and the *natural* ones. In the natural weighting case $\mathcal{D}(u,v) = 1$, while the uniform uses $\mathcal{D}(u,v) = 1/N_s(k)$ where $N_s(k)$ is the number of data points inside a region of the uv-plane (e.g. a square) of characteristic width s centred on the kth data point. The natural weighting case results in a lower angular resolution but provides a better SNR than uniform weighting.

3. $\mathcal{R}(u,v)$ is a weighting which takes into account the reliability of each single measurement in the uv-plane. It may depend on the system temperature, antenna gains, the integration time, and the bandwidth used for each data point.

The *point spread function* together with $W(u,v)$ results in:

$$B(l,m) = \int\int S(u,v)W(u,v)e^{2\pi i(ul+vm)}\,du\,dv \tag{2.14}$$

With the convolution theorem applied to a Fourier transform one gets finally:

$$I_\nu^D(l,m) = I_\nu * B \tag{2.15}$$

I_ν^D is given by the true intensity distribution I_ν convolved with the synthesized beam B.

2.2 Principle of an Interferometer

A simple diagram of an interferometer is given in Figure 2.2. The antennas convert the incoming electric field into voltage waveforms which are amplified and mixed down to a manageable frequency by using the heterodyne principle (e.g. video converters and local oscillators for VLBI). The geometric delay τ_g of the wave front has to be compensated. Since the visibility function is Hermitian $V_\nu(-u,-v) = V_\nu^*(u,v)$, each measurement between two telescopes results in two points of the visibility in the uv-plane. With n antennas the interferometer has $b = n(n-1)/2$ baselines. The rotation of the Earth allows one to sample a large range of uv-coordinates by rotating the baselines of the antennas with respect to the observed source (see Figure 2.7 as an example for a uv-coverage). The voltages $U_1(t)$ and $U_2(t)$ obtained from the two antennas are cross-correlated in the correlator by using a voltage multiplier followed by a time averaging. The correlator output is:

$$r(\tau) = \lim_{T\to\infty} \frac{1}{2T}\int U_1(t)U_2^*(t-\tau)\,dt \tag{2.16}$$

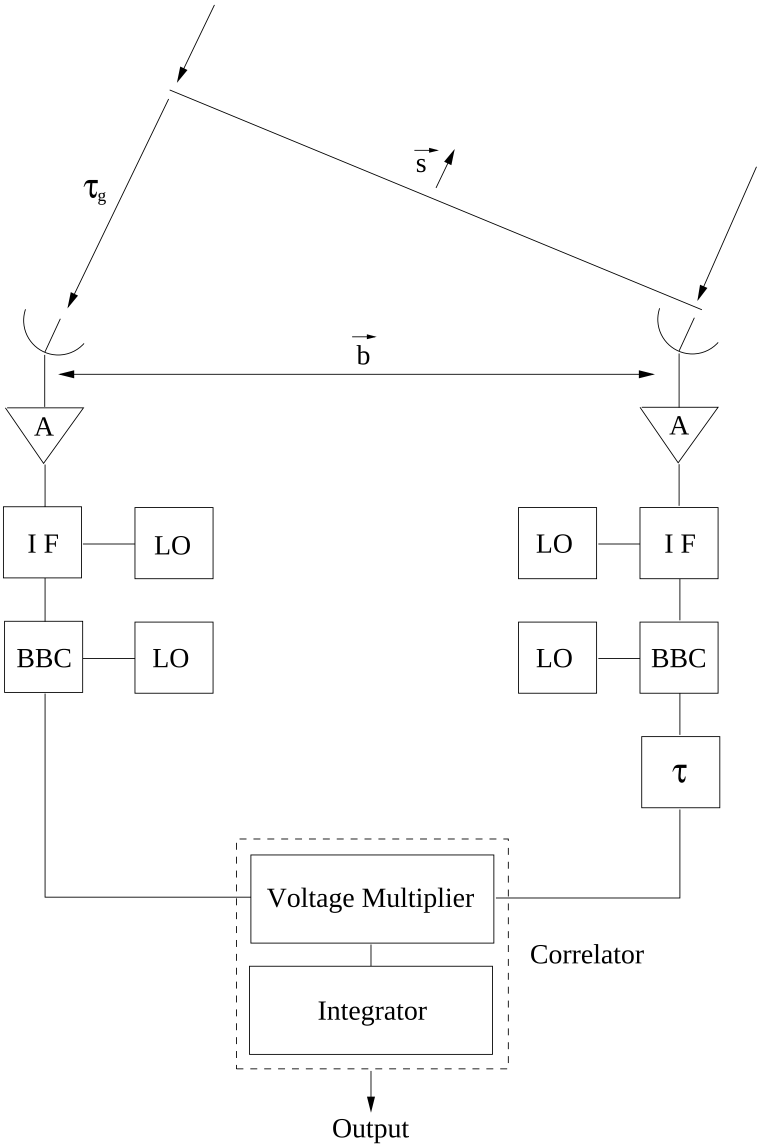

Figure 2.2: Simple diagram of an interferometer. The received electromagnetic waves are amplified (A), mixed down to a manageable intermediate frequency (IF) and converted to a baseband by using baseband converters (BBC) and local oscillators (LO). A delay (τ) is introduced to align the wavefronts of the telescopes with each other. The signals obtained are processed in the correlator which consist of a voltage multiplier and an integration unit.

τ is the delay between the times of reception of the electromagnetic wave at the two telescopes and T indicates the truncation applied to the time variability of the functions $U_1(t)$ and $U_2(t)$. The condition $T \to \infty$ is used for mathematical convenience and indicates that a very large number of variations of the signal amplitude occur during the time $2T$.

2.3 Calibration

2.3.1 Fringe Fitting

Let's imagine a large flat area normal to the zenith on which the antennas are located. With a source not at the zenith, the wavefront of the source does not reach the antennas simultaneously. The difference in time of arrival between 2 antennas is the *geometrical delay* $\tau_g = \mathbf{b} \cdot \mathbf{s}/c$ (Figure 2.2). Additionally one has to take account of Earth rotation which causes different Doppler shifts (the *fringe rate*). Furthermore the atmosphere, the antenna clock epoch and rate, antenna position errors, errors in the Earth model and the electronics cause additional delays in the phase. An estimate of the delay and the rate is calculated by the geometrical model in the correlator which produces an "imperfect" delay model. Therefore the exact values for delay and rate have to be determined empirically. An overview of the terms in the geometrical model is given in Walker (1999). The phase errors caused by the delays are:

$$\Delta\phi_{t,\nu} = 2\pi\nu d\tau_t \tag{2.17}$$

To first order, an error in the interferometer phase is given by:

$$\Delta\phi_{t,\nu} = \phi_0 + \left(\frac{\partial\phi}{\partial\nu}\Delta\nu + \frac{\partial\phi}{\partial t}\Delta t\right) \tag{2.18}$$

ϕ_0 is the phase error at the reference frequency and time. The *residual delay* offset $\partial\phi/\partial\nu$ shows up as a phase slope as a function of frequency. If the delay error changes with time $\partial\phi/\partial t$ there will be a slope of phase with time, the *delay rate*. The delay error between two antennas i and j is calculated by:

$$\Delta\phi_{i,j} = \phi_{i,0} - \phi_{j,0} + \left(\left[\frac{\partial\phi_i}{\partial\nu} - \frac{\partial\phi_j}{\partial\nu}\right]\Delta\nu + \left[\frac{\partial\phi_i}{\partial t} - \frac{\partial\phi_j}{\partial t}\right]\Delta t\right) \tag{2.19}$$

The technique to find and correct the delay rates and delay residuals is called *fringe fitting*. Various methods are used for it (e.g. Cotton 1995, Schwab & Cotton 1983, Walker 1989a,b).

2.3.2 Amplitude Calibration

The relation between the observed visibility $V_{ij}(\nu, t)$ and the true visibility $V'_{ij}(\nu, t)$ for the antennas i and j is given by:

$$V_{ij}(\nu, t) = \mathcal{G}_{ij}(\nu, t)V'_{ij}(\nu, t) + \epsilon_{ij}(\nu, t) + \eta_{ij}(\nu, t) \tag{2.20}$$

$\epsilon_{ij}(\nu, t)$ is a complex offset and $\eta_{ij}(\nu, t)$ is the thermal noise on the baseline from i to j. The complex antenna gain for the two antennas is described by:

$$\mathcal{G}_{ij}(\nu, t) = g_i(\nu, t)g_j^*(\nu, t) = a_i(\nu, t)a_j(\nu, t)e^{i(\Phi_i(\nu,t) - \Phi_j(\nu,t))} \tag{2.21}$$

For the amplitude calibration one can ignore the phase terms, the complex offset and the noise term. If one equates the amplitude of the true visibility $V'_{ij}(\nu, t)$ with the calibrated, correlated flux density $S_{ij}(\nu, t)$, one gets with (2.20):

$$S_{ij}(\nu, t) = \frac{A_{ij}(\nu, t)}{a_i(\nu, t)a_j(\nu, t)} \tag{2.22}$$

$A_{ij}(\nu, t)$ represents the measured visibility amplitude which comes from the correlator. One can rewrite equation (2.22) in a more practical form:

$$S_{ij} = bA_{ij}\sqrt{\frac{T_{s_i}T_{s_j}}{K_iK_j}} \tag{2.23}$$

The factor b is a constant value related to the correlator used which includes specific scaling factors and corrections for digitization losses. T_{s_i} and T_{s_j} are the system temperatures of the antennas i and j measured in Kelvin. These values are measured in between the observing scans. K_i and K_j are the sensitivities of the antennas (the gain) measured in KJy^{-1}. Gain curves are measured in single dish observations. If the source is strong enough one can measure the antenna temperatures T_{a_i} and T_{a_j} instead of K_i and K_j. With the total flux density S_{tot} one gets:

$$S_{ij} = bA_{ij}S_{tot}\sqrt{\frac{T_{s_i}T_{s_j}}{T_{a_i}T_{a_j}}} \tag{2.24}$$

For a more detailed description in amplitude calibration, see e.g. Moran & Dhawan (1995).

2.4 Imaging

2.4.1 Deconvolution

After calibration of the data (chapter 2.3) one can use equation (2.15) to calculate the true intensity distribution. Because there is only a finite number of samples of the measured visibility function, one can not recover I_ν directly. Non-linear, iterative deconvolution techniques are required. The most common methods are the MEM[2] and the CLEAN algorithm. A description of MEM can be found in Cornwell & Braun (1989) and Narayan & Nityananda (1986). The CLEAN algorithm was introduced by Högbom (1974) and modified by Clark (1980) and Schwab & Cotton (1983). The CLEAN algorithm implemented in the astronomical software package DIFMAP[3] (Pearson *et al.* 1994) was used for this thesis. The scheme of the of CLEAN algorithm is as follows:

1. The area outside the field of interest is assumed to be empty. Within the defined *mapsize* the algorithm finds the position of the peak with the highest intensity in the *dirty map*. If the source structure is known, one can use CLEAN *windows* within the *mapsize* to confine the search to this area only.

2. Subtract from the *dirty map*, at the position of the peak, the *dirty beam* multiplied by the peak flux and a damping factor $\gamma \leq 1$ (the loop gain).

3. The position and flux of the subtracted point source is recorded in a model as a CLEAN component.

---

[2] Maximum Entropy Method

[3] Difference Mapping Program developed at the California Institute of Technology

4. Go back to (1) unless the brightest point is below a user-specified limit. The remains of the *dirty map* are called *residuals.*

5. Convolve the CLEAN component model with an idealized beam which is usually an elliptical Gaussian, fitted to the central lobe of the dirty beam.

6. Add the residuals of the *dirty map* to the CLEAN image.

In summary, the true intensity distribution of the astronomical source is represented by a two dimensional grid of δ-functions. A detailed description of the CLEAN algorithm can be found e.g. in Cornwell (1995) and Wilkinson (1989).

2.4.2 Closure Quantities

Antenna-dependent phase and amplitude errors can be removed using *closure quantities* (e.g. Jennison 1958, Readhead *et al.* 1980). With the equations (2.20) and (2.21) one gets the relation between the phase of the observed visibility and the phase of the true visibility as:

$$\tilde{\psi}_{ij}(t) = \psi_{ij}(t) + \phi_i(t) - \phi_j(t) + \text{noise} \tag{2.25}$$

If one now takes a closed loop of three baselines, formed by the antennas i, j and k, one can define the closure phase which is independent of local phase errors:

$$\begin{aligned} \tilde{\mathcal{C}}_{ijk}(t) &= \tilde{\psi}_{ij}(t) + \tilde{\psi}_{jk}(t) + \tilde{\psi}_{ki}(t) \\ &= \psi_{ij}(t) + \psi_{jk}(t) + \psi_{ki}(t) + \text{noise} \\ &= \mathcal{C}_{ijk}(t) + \text{noise} \end{aligned} \tag{2.26}$$

With an interferometer of n antennas one gets $(n-1)(n-2)/2$ closure phase triangles. The ratio of independent closure phases to single baseline phases approaches unity as n increases. For 4 antennas the ratio is 0.5 and for 10 antennas it is 0.8. Thus, most of the baseline phase information is recoverable for large values of n. Similarly a closed loop of four antennas i, j, k and l cancels out the local amplitude errors:

$$\Gamma_{ijkl}(t) = \frac{\left|\tilde{V}_{ij}(t)\right| \left|\tilde{V}_{kl}(t)\right|}{\left|\tilde{V}_{ik}(t)\right| \left|\tilde{V}_{jl}(t)\right|} \tag{2.27}$$

There are $\frac{1}{2}n(n-1) - n$ closure amplitudes. Closure quantities cannot be used directly to form an image. An iterative algorithm has been developed to produce CLEAN images which are consistent with the closure quantities (e.g. Readhead & Wilkinson 1978, Cotton 1979). Both closure quantities give useful constraints on the true intensity distribution and are used during self-calibration.

2.4.3 Self-Calibration

Self-calibration is a technique to refine the quality of the imaging from the self-consistence of the data, based on some assumptions (e.g. the positivity of brightness and constraints of the structure). The aim is to determine the sky intensity distribution $\hat{I}$. One method is to adjust the complex gain elements g_i and g_j and the Fourier transform $\widehat{V}_{ij}$ of the model intensity distribution $\hat{I}$ (Schwab 1980):

$$S = \sum_{k} \sum_{\substack{i,j \\ i \neq j}} w_{ij}(t_k) \left| \tilde{V}_{ij}(t_k) - g_i(t_k) g_j^*(t_k) \widehat{V}_{ij}(t_k) \right|^2 \tag{2.28}$$

w_{ij} is a factor to weight the SNR of the corresponding visibility V_{ij}. By minimizing S one improves the antenna gains which are then used to correct the phase and amplitude errors of the observed visibility. The corrected visibility is:

$$V_{ij,corr}(t) = \frac{\tilde{V}_{ij}(t)}{g_i(t) g_j^*(t)} \tag{2.29}$$

With the corrected data, a new model is formed, using again constraints of the source structure. It is helpful to first perform several loops of phase self-calibration before applying amplitude calibration. The amplitude calibration should start with a big time interval for the gain solutions (e.g. with the whole observing time) and scale down stepwise. A detailed description of self-calibration is given by Cornwell & Fomalont (1999).

2.4.4 Model Fitting

Model fitting is a technique to recover the true brightness distribution from the measured one. In our case one uses a parametric model of the sky brightness distribution to calculate the expected measurements. To get the best fit, the parameters of the model must be adjusted. The statistical technique to estimate the parameters of the model is the *maximum likelihood* method (e.g. Press 1992, Bevington & Robinson 1992). For Gaussian errors it is the same as the *least squares* method. Consider a model $F(u, v)$ of the N observed visibilities $V_i(u, v)$. The model depends on M parameters a_j which are in our case typically six per *model component*: component flux density, two sky coordinates, angular size, axial ratio, and orientation:

$$V(u, v) = F(u, v; a_1, ..., a_M) + \text{noise} \tag{2.30}$$

One has to minimize χ^2 which is the weighted sum of the squared deviations between the data and the model. σ_i is the standard deviation of each visibility measurement V_i when the noise in the observations is Gaussian.

$$\chi^2 = \sum_{i=1}^{N} \left(\frac{V_i - F(u_i, v_i; a_1, ..., a_M)}{\sigma_i} \right)^2 \tag{2.31}$$

The *reduced chi-squared* $\chi^2/(N - M)$ represents the goodness of the optimized fit. It should be close to 1 for a good fit. A large value indicates a bad fit while a value lower than one indicates a fit which is “too good” and can be caused by an overestimation of the errors σ_i. For a more detailed discussion of model fitting see e.g. Pearson (1999).

2.5 Space Very Long Baseline Interferometry

The increase of resolution achieved by enlarging the distance between the ground VLBI radio telescopes is limited by the physical dimensions of the Earth. To overcome this limit, and thus obtain a more detailed view of the astronomical objects, one has to use a radio telescope in orbit (e.g. Priorities in Space Research, 1971). The ground telescopes, together with the space antenna(s), synthesize an aperture much larger than the Earth diameter (see Figure 2.3). In the first section, a short review of the first steps in SVLBI is given. In section 2.5.2 SVLBI missions are described in general. A detailed description of the VSOP[4] mission, using the space radio antenna mounted on the satellite HALCA[5], is given in section 2.5.4. Future SVLBI missions are presented in section 2.5.5.

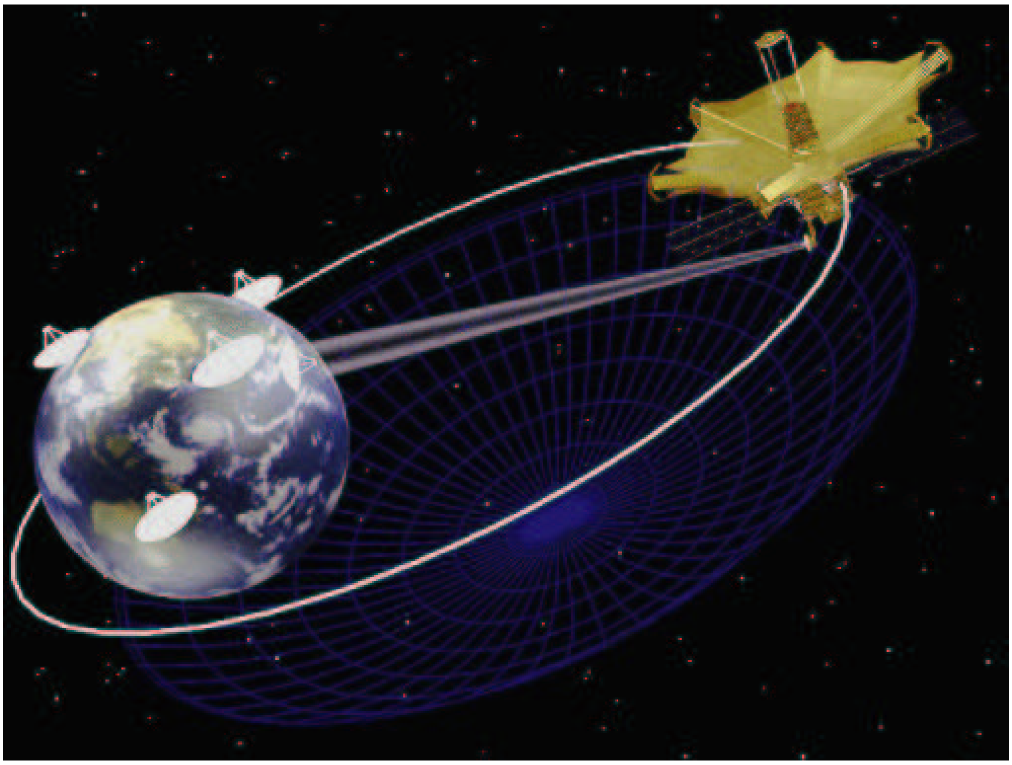

Figure 2.3: An artist's impression of the space radio telescope mounted on the satellite HALCA (not to scale) together with ground telescopes, synthesizing a radio telescope (sketched as the large dish) with size much larger than the Earth. (Courtesy of the Japanese Institute of Space and Astronautical Science)

2.5.1 First Steps in SVLBI

Several aspects have to be taken into account in order to get the best compromise for different astronomical questions when projecting a SVLBI mission. The main

---

[4] VLBI Space Observatory Programme

[5] Highly Advanced Laboratory for Communication and Astronomy

constraint, apart from the available financial budget, is given by the size of the launch vehicle which limits the size of the satellite and its components.

One of the first studies for SVLBI was QUASAT[6]. The concept was originated at JPL and proposed to ESA as a joint ESA-NASA SVLBI mission in December 1982 (Schilizzi 1988). The proposal considered a 15 m antenna in an elliptical orbit observing at 22, 5, 1.6 and 0.3 GHz with both hands of circular polarization. It was intended to change the orbit during the first 1–2 years of operation from the initial orbit with a perigee of 5000 km, an apogee of 36000 km and a period of 12.2 hrs down to the final orbit at an apogee height of 22000 km and a period of 7.75 hrs. This would have had two advantages. On the one hand, the higher initial orbit would have provided a higher angular resolution and the final orbit would have been used for high quality imaging. On the other hand, one could have shared the launch to a geostationary transfer orbit, and thus share the costs. The QUASAT proposal reached Phase-A stage before it was stopped because of other budget priorities. Nevertheless, the QUASAT study led to an important international discussion about SVLBI and provided a lot of new advances in this field.

The first successful demonstration of SVLBI was made with an existing spacecraft, the TDRSS[7] (Sade & Deerkoski 1981) which was used as an orbiting antenna because it appeared to have all the requirements for a SVLBI experiment (Levy *et al.* 1986). TDRSS was designed to relay data between ground stations and low orbit satellites via geosynchronous satellites. Both 4.9 m antennas on the spacecraft and two 64 m ground antennas in Australia and Japan were used as a first test array. With a maximum projected baseline of 1.4 Earth diameters at an observing frequency of 2.3 GHz the quasars NRAO 150, 1510–089 and 1741–038 were observed during July and August 1986 and fringes were found on all sources. 15 GHz observations with a baseline of 2.15 Earth diameters but with a drop in sensitivity of a factor of 6 were performed successfully together with two ground antennas in spring 1988 (Linfield 1990). That showed the feasibility and the potential of an orbiting radio-antenna and led finally to the development of the Japanese SVLBI satellite project VSOP.

2.5.2 Fundamentals of SVLBI

Parameterization of the orbit:

The orbit of a spacecraft is described with six parameters (Bate, Mueller & White 1971):

a = semi-major axis of the orbit, which results in the orbital period $T=2.76(a/10^4\,\mathrm{km})^{3/2}$ hours

e = orbital eccentricity

i = inclination with respect to Earth equator

---

[6] Quasar Satellite Project

[7] Tracking and Data Relay Satellite System

Ω = right ascension (or longitude) of the ascending node (intersection of the equatorial plane with the satellite orbital plane, when the satellite is moving northwards of the equator.)

ω = argument of perigee (angle between the ascending node and the perigee along the orbital plane); for a perigee in the northern hemisphere ω is between 0° and 180°.

M = mean anomaly (measured in degrees, $M/360°$ gives the time ratio elapsed since the last perigee)

Considerations on the orbit height:

An increased orbit height leads to higher angular resolutions. However, several disadvantages and constraints occur with higher orbits:

1. The resolution (and therefore the size) of the orbit should be matched with the physical phenomena which one wants to observe, in order to avoid over-resolving or under-resolving of the astronomical images.
2. Ground-space baselines, which are much longer than the ground-ground baselines, lead to holes in the uv-plane which limit the dynamic range of the images.
3. Some sources might vary during the orbital period and therefore falsify the images obtained. In this case one can observe only for a fraction of the orbital period.
4. The correlated flux of resolved objects drops on longer baselines. Thus, there is a limit in the brightness temperature sensitivity.
5. The costs of the mission increase with the height of the orbit. About 10%-30% of the overall mission budget is assigned only for the launch vehicle.

An elliptical orbit yields an acceptable compromise. A high apogee supports the images with high angular resolution and a low perigee fills the uv-plane without appreciable gaps between ground-ground and ground-space baselines.

Observing constraints:

1. At perigee, the speed of the spacecraft becomes relatively high (about $10\,\mathrm{km\,s^{-1}}$ for HALCA) and the projected space-ground baselines shorten to about 1000 km. One usually needs hundreds of seconds of integration time to detect fringes to the space antenna. Thus, u and v can double during a fringe-fit interval near perigee. Therefore, the structure phase in the visibility function may change, and lead to a loss of coherence and SNR in the fringe fit, in time intervals longer than tens of seconds (Ulvestad 1999). This effect is negligible at apogee because of the larger u and v values and the lower satellite speeds of about 1–$3\,\mathrm{km\ s^{-1}}$.

2. The quality of the uv-coverage depends on the location of the source with respect to the orbital plane. The best uv-coverage with the highest two-dimensional resolution is achieved when the source lies in the direction normal to the orbital plane. If the source lies near the orbital plane, the uv-coverage is extremely elongated and almost one-dimensional. An example of the uv-coverage for HALCA-VLBA baselines is given in Figure 2.4, for various right ascensions and declinations.

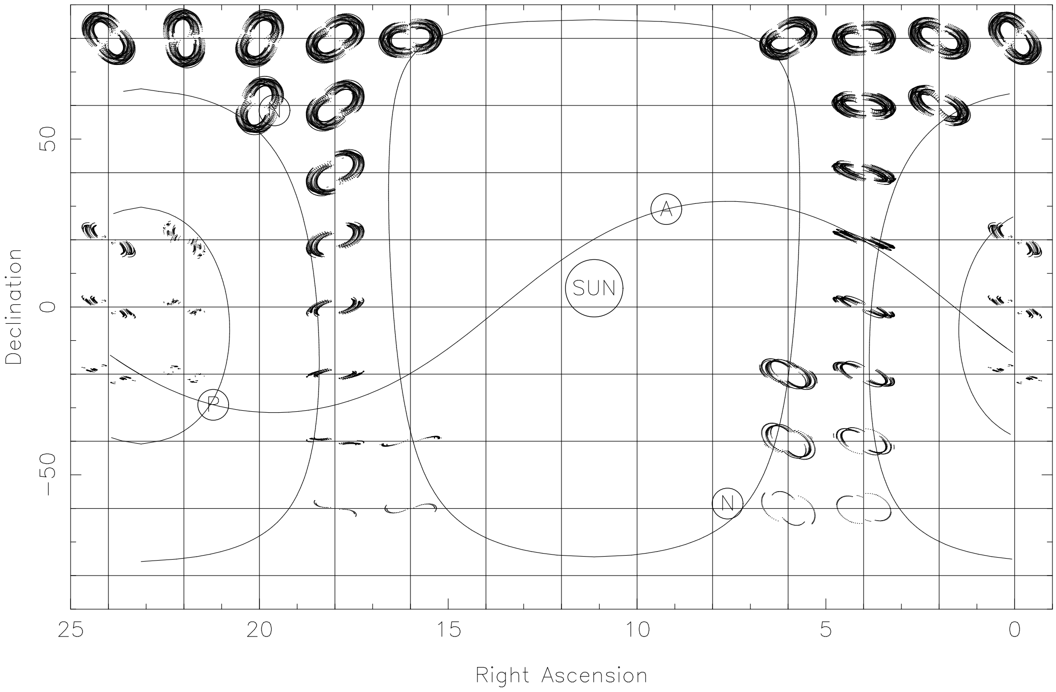

Figure 2.4: HALCA-VLBA (5 GHz) uv-coverage as a function of α and δ after considering all the observing constraints (e.g. Sun, tracking station availability) for September 10th, 1999. In circles, P = Perigee, A = Apogee, and N = normals to the orbital plane. The big holes without any uv-coverage are due to the observing constraints.

3. The geometry of the uv-plane changes with time due to precession of the orbital parameters ω and Ω, caused by the oblateness of the Earth. This means that the orientation of the orbital plane and the location of the perigee change with time, which leads to a change in the uv-coverage. Therefore, the "best" uv-coverage is realized for a given source at a certain epoch (see Figure 2.5). The comparison and interpretation of images at different epochs can become difficult because of this effect. The rates of precession due to the J_2 term in Earth's gravitational potential are given by (e.g. Boden 1992):

$$\dot{\Omega}(J_2) = -752 \frac{\cos i}{(1-e^2)^2} \left(\frac{\alpha}{10^4 \text{ km}}\right)^{-\frac{7}{2}} \text{deg year}^{-1} \tag{2.32}$$

$$\dot{\omega}(J_2) = -\frac{1}{2} \left(\frac{5\cos^2 i - 1}{\cos i}\right) \dot{\Omega} \tag{2.33}$$

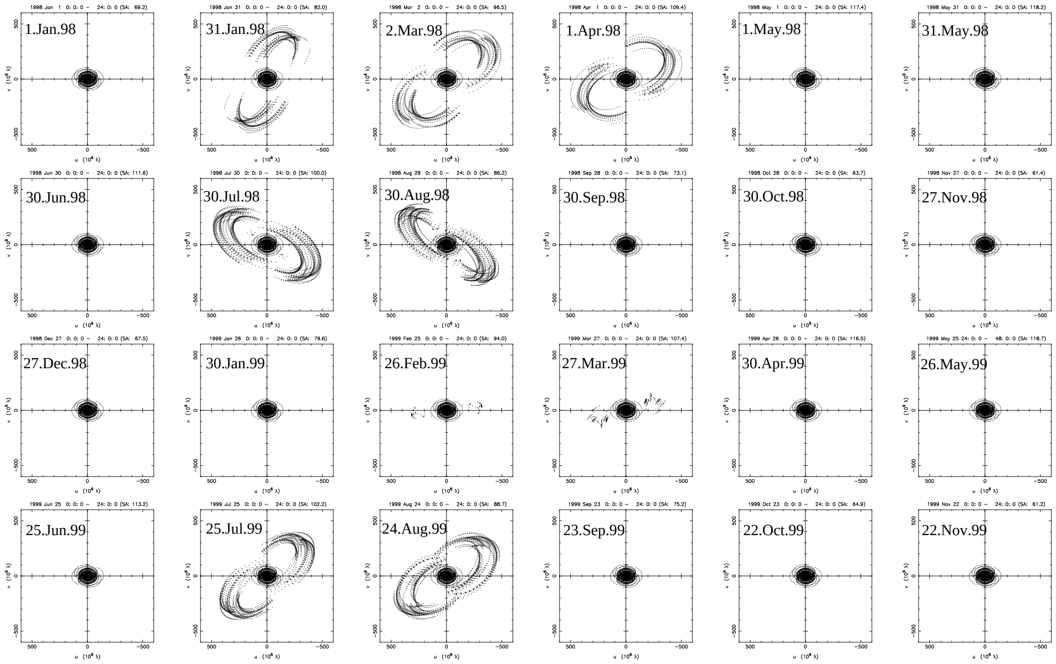

Figure 2.5: *uv*-coverage of 3C 345 between January 1998 and November 1999, including all observing constraints during a 24 h observation. 3C 345 is observable with HALCA with good *uv*-coverage during the months January, March, April, July and August in 1998 and during July and August in 1999.

4. The spacecraft link-antenna needs a clear line of sight to one of the tracking stations, otherwise no observation is possible. Data are down-linked in real-time and stored at the tracking station. This requirement can be violated because of blockage of the link-antenna by the spacecraft itself.

5. The slow slew rate of the space antenna limits some particular observing programs (e.g. switching between different astronomical objects). Phase referencing SVLBI is very difficult and is only possible for pairs of sources lying within the primary beam of the space antenna (e.g. sources which are separated by $\sim$ 14 arcmin for HALCA, Porcas *et al.* 2000).

6. On the one hand, the solar panels have to be illuminated by the Sun which can be hindered by solar and lunar eclipse and parts of the satellite itself (the large antenna in particular can shadow the panels). On the other hand, some parts of the satellite have to be shielded from direct sunlight.

7. Miscellaneous constraints like command-storage capabilities have to be taken into account.

All constraints mentioned above are included in the sequence of *uv*-coverages for HALCA in Figure (2.5). The constraints cause the incomplete and absent elongated ellipses which represent the ground-space baselines.

2.5.3 The Tracking Stations

The tracking stations provide a stable frequency reference for the VLBI sub system in space (called *time transfer* or *phase transfer*) and derive the correct time at which data were received (e.g. Levy et al. 1989) (Figure 2.6). Received data are recorded on tapes which are shipped later to the correlator. The spacecraft orbit and position are predicted with a permanently updated orbit model. The orbital parameters of the satellite are additionally improved with Doppler measurements of the frequency reference signal. Errors in knowledge of the orbit cause a coherence loss approximately proportional to the square of the observing frequency. Several tracking stations in the northern and in the southern Hemisphere are necessary, to provide a good *uv*- and time coverage for baselines to the space antenna.

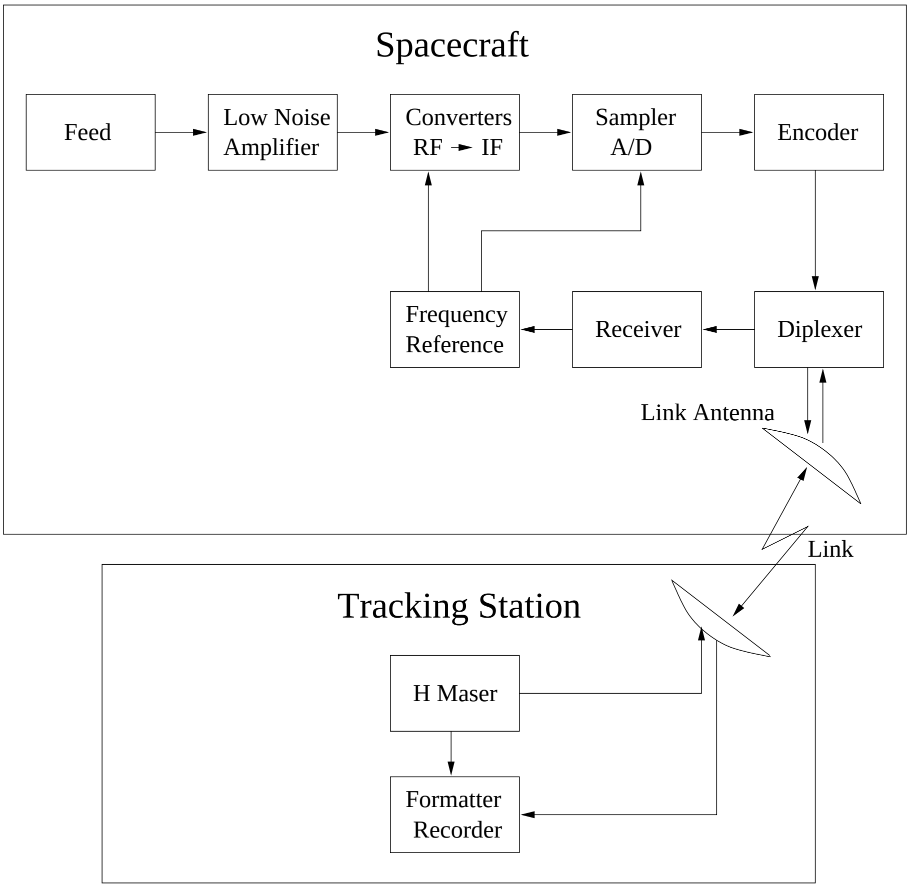

Figure 2.6: Schematic diagram of a space radio telescope, consisting of the space antenna and a tracking station.

2.5.4 The VSOP Mission

The VSOP mission is formed by the satellite HALCA and a global international network of more than 30 ground radio telescopes (VLBA, VLA, EVN[8], APT[9],

---

[8] European VLBI Network

[9] Asia Pacific Telescope

100 m Effelsberg and other antennas) all around the world. VSOP is operated from Sagamihara at ISAS[10] in Japan in collaboration with the Japanese NAO[11]. The VSOP project started formally in April 1989 (Hirabayashi 1989) and the spacecraft HALCA was launched successfully (under the former name MUSE-B[12]) by the first Japanese M-V rocket from the Kagoshima Space Center on 12 February 1997 (VSOP newsletter 55). The first signal from a celestial radio source was detected on 24 March 1997 and first fringes between HALCA and ground telescopes were found of the source PKS 1519-273 at 1.6 GHz in May 1997 (VSOP newsletter 63). The first SVLBI image was generated for PKS 1519-273 in mid June 1997 (VSOP newsletter 67).

Main Parameters of HALCA:

The radio telescope on the 800 kg satellite HALCA has Cassegrain optics. It collects the radio waves in the main reflector (area of $50.1\,\mathrm{m}^2$), equivalent to an 8 m dish. The 1.1 m hexagonal sub-reflector, the 2.5 m feed horn and a three-waveband coaxial feed complete the optical system. The main reflector is made of a thin mesh ("wire-tension-truss" concept, Mirua 1986) which is fixed by cables mounted on the satellite structure. Both reflectors were unfolded in space.

A quarter-wave plate combines the two orthogonal linear polarizations into LCP[13] which is send to a LNA[14] (Figure 2.6). The losses from the feeds through the coaxial cable and the LNAs contribute 40–55 K to the overall system temperature (VSOG 2000). The signals from each RF[15] band are converted to IF[16] and split up into two channels. Depending on the observing mode, the channel signals pass through either 16 MHz or 32 MHz low pass filters. Both signals are one- or two-bit digitized, encoded, amplified and sent to the steerable link antenna of 45.5 cm diameter. The data rate of the down-link signal is $128\,\mathrm{Mbit\,sec}^{-1}$ and is received at 14.2 GHz at one of the ground tracking stations. Frequency-reference and operation commands sent by the tracking stations and the control station are received via this link antenna at 15.3 GHz.

The planned observing bands were 1.60–1.73 GHz, 4.7–5.0 GHz and 22.0–22.3 GHz. The 22 GHz system showed unexpected high system temperatures, which might be caused by an impaired waveguide connecting the front-end and the feed horn, produced by heavy vibrations during the launch. Anyhow, fringes were detected successfully at 22 GHz during the strong outburst of the Orion-KL water vapor maser in March 1998 which demonstrated the principle of working at this frequency. Three epoch maps of this source were made with peak fluxes of 3.5×10^5, 9.2×10^5 and 4.7×10^5 Jy/beam (Kobayashi 2000). Because of the sensitivity problem, imaging at 22 GHz was not possible for any other source (Hirabayashi 2000a).

---

[10] Institute of Space and Astronautical Science

[11] National Astronomy Observatory

[12] Second Mu Space Engineering Satellite

[13] Left Circular Polarization

[14] Low Noise Amplifier

[15] Radio Frequency

[16] Intermediate Frequency

Observations at 1.6 and 5 GHz worked perfectly and led to many hundred VSOP observations of various astronomical objects.

The orbit elements of HALCA are (VSOG 2000):

$a = 17{,}342.353\,\mathrm{km}$

$e = 0.60300$

$i = 31.4500°$

$\Omega = 185.1264°$

$\omega = 238.6360°$

$M = 75.7474°$

Which results in:

apogee* $= 21{,}400\,\mathrm{km}$ ($v = 9.6\,\mathrm{km\ s^{-1}}$)

perigee* $= 560\,\mathrm{km}$ ($v = 2.4\ \mathrm{km\ s^{-1}}$)

orbital period $= 6.32\,\mathrm{h}$

When the source lies in the direction normal to the orbit, the projected baseline length can extend up to 33,000 km, depending on the location of the ground telescopes. While ground-based VLBI reaches only a maximum projected baseline length of about 10,000 km, the gain in resolution with HALCA is larger than 3 (Figure 2.7). In addition to this high orbit, the low satellite position at perigee provides a filled aperture without an annular gap between ground-ground and ground-space baselines.

From equations (2.32) and (2.33) and the parameters for HALCA's orbit, it follows that $\dot{\Omega}(J_2) = -231°\mathrm{yr}^{-1}$ and $\dot{\omega}(J_2) = +356°\mathrm{yr}^{-1}$, which leads to a precession period for Ω and ω between 1 and 1.7 years (VSOG 2000). The major consequence of the Ω precession is the change of the orbit normal with time (and thus the optical transfer function (the beam)), which makes more sources visible with a good *uv*-coverage in the satellite's lifetime, but makes it difficult to compare different epochs of the same source (see section 2.5.2 (3)). The major impact of the ω precession is on the amount of tracking station time which is available, and thus the amount of SVLBI data which can be obtained. Four of the five tracking stations (Goldstone/CA USA, Robledo/Spain, Tidbinbilla/Australia, Usuda/Japan and Green Bank/WV USA) are located in the Northern hemisphere ($180° < \omega < 360°$). Thus, more SVLBI data will be obtained when the apogee is in the Northern hemisphere than in the Southern one ($0° < \omega < 180°$). Because of the precession of Ω and ω, a good *uv*-coverage for all parts of the sky is given at least during a few epochs during the lifetime of HALCA.

---

*above the Earth surface

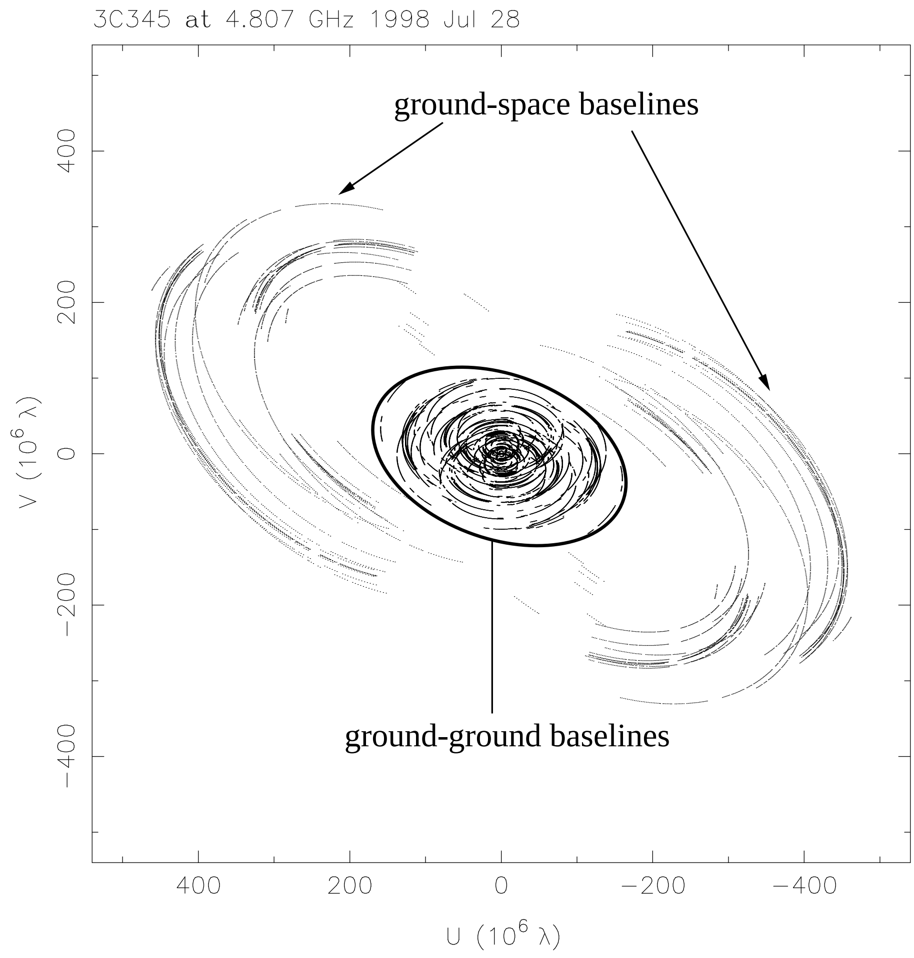

Figure 2.7: VSOP uv-coverage for 3C 345 at 5 GHz on July 28, 1998 with a radio telescope array consisting of the VLBA, the phased-VLA, Effelsberg and HALCA. The comparison of the large ground-space ellipses with the smaller ground-ground ellipses demonstrates the gain in resolution with HALCA.

The FWHM beam size (using HALCA and the VLBA) for a source which lies along the direction of the orbit normal (or anti-normal) is related to the observing frequency as follows:

$$\theta_{minor} \approx 1.2 \left(\frac{\nu}{\mathrm{GHz}}\right)^{-1} \mathrm{mas}$$

$$\theta_{major} \approx 2.3 \left(\frac{\nu}{\mathrm{GHz}}\right)^{-1} \mathrm{mas}$$

For sources that do not lie along orbit normals, the FWHM beam sizes are larger than these values. For HALCA observations at 5 GHz, the smallest obtainable beam size is $\theta_{minor} = 0.24$ mas and $\theta_{major} = 0.46$ mas.

Parameters and Constraints for the Observations:

HALCA's observing time is divided into the 'General Observing Time' and the 'VSOP Survey Program'. The total data transfer rate of 128 Mbit $\sec^{-1}$ constrains the combination of bandwidth, sampling and channelisation. The standard observing mode supports two channels of 16 MHz bandwidth and 2-bit sampling. A single command station with a 20 m antenna in Kagoshima (Japan) sends the control and observing commands once a day (except for Sunday) to the spacecraft. The five tracking stations (10 m dishes) supply the satellite with a frequency reference, receive the observed space data and record them on VLBI tapes. A normal observation lasts between 7–14 hours. One has to take the following observing constraints into account:

HALCA observations are limited by the solar panels which have to be illuminated at 100 %. This is not possible for sources within about 70° of the Sun, because the main antenna shadows the solar panels. In-orbit experience showed that for certain angles beyond 70° the torques imposed by solar radiation pressure are larger then expected, which makes HALCA unable to observe within Sun angle ranges up to 84°-100°.

HALCA cannot observe within 5.0° and 1.8° from the Moon's center at 1.6 GHz and 5 GHz. Sources which are occulted by the Earth cannot be observed by HALCA. However this constraint is less strict than for ground telescopes. The Earth obscures 30% of the sky at perigee and 1.3% at apogee.

Another constraint is the occultation of the Sun by Earth or Moon eclipses. Batteries power the satellite during this time, while observations are not possible because of the high energy requirements. Re-charging of the batteries takes about one orbit, during which no observations can be done. The eclipses can last at most about 90 minutes and produce gaps in the uv-coverages which stay fixed from orbit to orbit on timescales of an observation duration of 7–14 h.

A tracking station has to be above the minimum elevation limit of 5°, in order to receive the observed data in real time and to send the oscillator phase reference to the spacecraft. Furthermore, the link antenna, which is mounted on a boom opposite the main antenna, has a limited field of view. No observation is possible when the tracking station lies within about 70° of the source direction. The constrains on the field of views together with ωs limit the number of tracking stations available for certain sources under certain conditions. For example, when the apogee lies in the Northern hemisphere and one wants to observe far Southern sources at or near apogee, then the link-antenna might point away from the Earth and no communication with a tracking station is possible. The amount of orbit time when HALCA sees a tracking station varies from 55% (for the worst case when $\omega = 90°$) to 85% (for the best case when $\omega = 270°$).

For changing between sources, the slewing rate of HALCA is $2.25° \mathrm{min}^{-1}$. The slewing process is performed in two stages. First, the satellite slews around the spacecraft-Sun axis, followed by a slew about the solar-panel axis, which means that the total slewing angle is larger than the angle between the two sources. A 180° slew takes at least 80 minutes. After each slew, about 3 minutes are needed until the antenna settles. Moreover, source changes are impossible during eclipse and sufficient star tracker data must be obtained to determine the attitude with a precision which is good enough for scientific observations. In summary, the slewing process between sources is a complex procedure which lasts typically between 4 and 10 hours.

Correlation and Correlator Model:

Three data-correlating facilities are available. Socorro (NRAO, USA) with a 20-station VLBA/MkIV correlator, Mitaka (NAO, Japan) with a 10-station VSOP-T correlator and Penticton (DRAO[17], Canada) with a 6-station S2 correlator. All tracking stations are equipped with VLBA and S2 recorders, while the Usuda tracking station is also equipped with a VSOP-T recorder.

To correlate the data, the orbit of HALCA has to be reconstructed precisely and the time corrections for each tracking station have to be calculated. The spacecraft orbit is derived from the same data which are used for the time correction.

A detailed model of the Earth's gravitational field is applied, being very important at perigee. An additional refinement in the orbit determination is provided by application of a solar wind pressure model, which takes into account the position of the satellite and the direction of the 8 m antenna. Because of HALCA's large size, the high area/mass ratio becomes more important than for other spacecraft. With a two way Doppler-shift measurement, the orbit can be determined with a r.m.s. of 15 m in position and 6 mm/s in velocity which is good enough for VLBI correlation. Phase referencing experiments even showed that the uncertainty of the spacecraft orbit reconstruction is likely to be between 2 and 5 m (Porcas *et al.* 2000, Guiardo *et al.* 2001).

The "delay model" represents the delay in the wavefront which reaches the telescopes, referred to the arrival time of the wavefront at the center of the Earth. The observed data are referenced to the delay model so that the interference fringes are almost stopped. This results in small residuals in the delays and delay rates, which allows for longer coherent integration in fringe-fitting, so that fringes can be detected on weaker sources.

SVLBI requires some special features in for the delay model. In ground VLBI τ_g (the geometric part of the delay) is always ahead of the center of the Earth which results in a negative value of the delay, with a maximum magnitude of about 21 msec. The maximum rate of change of τ_g is ≤ 3 μsec sec^{-1}. For SVLBI the maximum delay and fringe rate are much larger. For example, for an apogee height of 90,000 km the delay is approximately 0.3 sec. The geometric delay has about the same magnitude. Fortunately, most correlators can handle an unlimited offset of total delay and geometric delay.

A bigger problem is caused by the delay rate. One can estimate the maximum delay rate by dividing the maximum speed of the satellite ($\sim$ 10 km sec^{-1}) by the speed of light, which yields a delay rate of $\sim$ 33 μsec sec^{-1}. This means that more accurate delay models with a more frequent update are required to have a reasonable polynomial model for the delay.

---

[17] Dominion Radio Astrophysical Observatory

For ground VLBI observations, the standard window size for the correlation is about 4 μsec for the delay, and 0.25 Hz for the fringe rate. The r.m.s. position error for HALCA corresponds to a delay of less than 100 ns. Therefore, an increase in the residual delay window for space-ground baselines is not necessary, being a constant offset for the tracking stations determined.

A fringe rate error of 0.17 Hz at a frequency of 5 GHz is caused by a velocity error of 1 cm $\sec^{-1}$. This is also in the same range as for ground-ground baselines. Thus the correlator output for a ground-space baseline of a 5 GHz experiment is 1.04 sec integration time, which corresponds to a residual rate window of 0–48 Hz.

Amplitude Calibration:

The antenna gain of HALCA was measured on the calibration source Cygnus A and is 4.3 mK Jy^{-1} at 1.6 GHz (24% efficiency) and 6.2 mK Jy^{-1} at 5 GHz (34% efficiency). The lower gain at 1.6 GHz is caused by the limited size of the sub-reflector which was constrained by the dimensions of the rocket nose. Neither receiver is cryogenically cooled, due to mass and power limitations. The system temperatures are $T_{\mathrm{sys}} \approx 75$ K at 1.6 GHz and $T_{\mathrm{sys}} \approx 95$ K at 5 GHz. T_{sys} is rather constant from orbit to orbit at about 2% and changes within one orbit due to thermal variations by only about 5% (Ulvestad 1999). Compared with some ground-VLBI stations which are involved in VSOP, this is an excellent stability. Measurements of the system temperature are made before and after each observing run. The SEFD[18] (noise/gain temperature) is 17,400 Jy at 1.6 GHz and 15,300 Jy at 5 GHz, with an uncertainty of 10%.

Amplitude calibration of SVLBI data has some differences with respect to ground VLBI. The constraints in the observing directions, the slow slew rate of the satellite and the low sensitivity (small antenna, uncooled receivers) make it difficult for pointing during observations. This means that the target source itself has to be strong enough for pointing. A big advantage for the calibration is the lack of atmosphere above the spacecraft. Calibration of polarized data is rather difficult because of the low SNR. The absence of rotation of the parallactic angle makes calibration of the polarization leakage terms difficult.

Fringe Fitting:

Fringe fitting for VSOP data also has some differences compared with ground-based VLBI. The sensitivity of the 8 m antenna is much lower than for the 25 and 100 m ones (VLBA and Effelsberg respectively). Furthermore, success in the fringe search is dependent on the accuracy of the orbit knowledge which means that one has to use wider windows for an initial search.

For fringe-fitting, it is useful to first have a good amplitude calibration, in order to get a proper weight for the baselines with the strongest signals. In AIPS one should force the fringe search task FRING or KRING to do the search with reference to

---

[18] System Equivalent Flux Density

the antenna giving the highest SNR. Setting a low SNR cutoff (e.g. SNR=3) for ground-space baselines increases the number of good detections during fringe-fitting.

2.5.5 Next Steps in SVLBI

Driven by the success of the VSOP mission, further SVLBI missions are planned. The successor of VSOP is the proposed VSOP-2 mission. With a 10-15 m antenna, cooled receivers, observing frequencies up to 43 GHz, a data rate of 1 Gbit $\sec^{-1}$ and an increase in sensitivity of about 10, this orbiting VLBI project will extend the horizon of our astronomical knowledge (Hirabayashi 2000b).

The RadioAstron project (Kardashev 1997) is the first SVLBI mission developed under the leadership of the Astro Space Center in Moscow, Russia. The progress of this mission is delayed because of financial problems. The launch might take place sometime during the next few years. The project plans to deploy a 10 m radio-antenna with receivers up to 22 GHz. A high orbit with an apogee nearly 80,000 km and an initial perigee height of 4000 km will lead to a 28-hr orbit. Even a 4 to 8 day orbit is discussed.

A NASA study discusses the ARISE[19] mission (e.g. Ulvestad & Linfield 1998), without a time plan for the near future. The idea is to put a VLBA-equivalent dish (a 25 m inflatable antenna), in space. The orbit would have an apogee of 40,000 km and a perigee of 5,000 km with a 13 h period. A data rate of 1–8 Gbit $\sec^{-1}$ would be achieved. The observing frequencies are supposed to be up to 86 GHz which results in a spatial resolution of $10 - 20\mu$arcsec. The sensitivity would be 50 times better than with VSOP.

---

[19] Advanced Radio Interferometry between Space and Earth, http://arise.jpl.nasa.gov

Chapter 3

Observations of 3C 345

3.1 Overview

Observations specially made and used for this thesis were done between 1997.40 and 1999.69. Four VSOP observations were performed at 1.6 GHz and four at 5 GHz in 1998 – 1999. Our ongoing VLBA monitoring program contributed with 7 epochs at 22 GHz and 9 epochs at 43 GHz. Two 22 GHz observations at epoch 1996.41 and 1996.82 from Ros *et al.* (2000) were modeled again, to obtain consistency in the sequence of models. A time gap in our monitoring program in 1998 at 43 GHz forced us to ask A. Marscher to make his 3C 345 epochs in 1998 available to us so that modelfits to these epochs could be made consistent with our own. Altogether the data base contains 9 epochs at 22 GHz and 14 epochs at 43 GHz. A list of all observations made and used for this thesis is given in Figure 3.1. Previous observations from the literature were used to complete the study.

3.2 Calibration and Imaging of the VSOP Data

All VSOP observations at 1.6 and 5 GHz were made in the standard VSOP mode with two 16 MHz IFs (2-bit sampling). Each IF was split up into 128 channels. Because of a drop in the bandpass, several channels in both IFs had to be flagged for all stations (see Table 3.1).

The amplitude and phase (fringe fitting) calibration was done in AIPS[1] in a standard manner (see cookbook[2]). To obtain a high detection rate for fringe fitting, the SNR limit for space baselines had to be set to 3 or 5 (depending on the data set). Los Alamos was used as a reference antenna for fringe fitting for all epochs. All the channels in each IF were frequency-averaged into one and the data were exported into DIFMAP for editing and imaging. Obviously-bad data points (e.g. with too high or too low amplitude) were flagged with the tasks `radplot` and `vplot`. The maps including HALCA baselines were particularly sensitive to bad points. A careful inspection with moderate data flagging led to a significant improvement in the map. After this editing, the data were time-averaged in 42 s bins which is a multiple of the 4.2 s integration time for the ground telescopes and the 2.1 s integration time for HALCA.

---

[1] Astronomical Image Processing System from NRAO

[2] http://www.aoc.nrao.edu/aips/cook.html

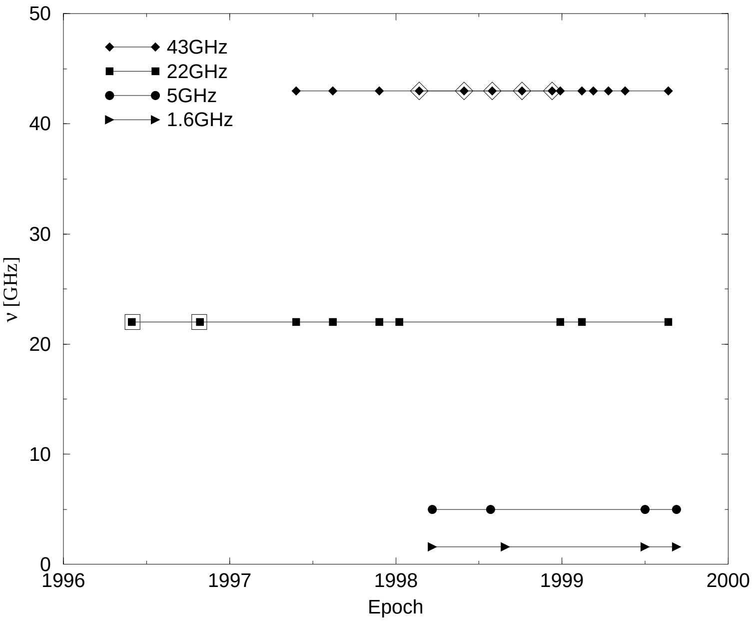

Figure 3.1: Time plot of observations made and used for this thesis: 4 VSOP epochs at 1.6 GHz, 4 VSOP epochs at 5 GHz, 9 VLBA epochs at 22 GHz and 14 VLBA epochs at 43 GHz were analyzed. 5 epochs (1998.15–1998.94) of Marscher were made available for our own model fitting to fill out our observation gap at 43 GHz in 1998 (marked with $\diamond$). Two epochs (1996.41 and 1996.82, marked with a white square) presented in Ros *et al.* (2000) were re-modeled for consistency.

This was necessary to reduce the file to a manageable size for imaging. The data were again edited for bad points after averaging. A minimum of three telescopes for phase- and 4 telescopes for amplitude self-calibration were required to exist in a closed loop for a given solution interval, otherwise the data were flagged. One can avoid this by setting `SELFFLAG false`. Uniform weighting was used with a grid weighting scaled by the errors to the power -1. `CLEAN/phase-SELF-CALibration` loops were used for imaging. First, only ground telescopes were used and all ground-space baselines were flagged. To get a ground map with high dynamic range, long baseline data were down-weighted with a Gaussian function of FWHM equal to a given UV-radius during the `CLEAN/phase-SELF-CALibration` process. This tapering was lifted successively in 25 Mλ steps from about a tenth to the full uv-range. With this process one can concentrate successively on different parts of the radio-emission, from the extended jet to the compact core. After a good map was obtained, self-calibration of the amplitude was performed with a time interval of half the total observing time. After this, imaging including tapering was continued. The process `(CLEAN, phase SELF-CALibration, UVTAPER, amplitude SELF-CALibration)` was repeated using half the value of the previous amplitude calibration interval, ending finally at 1 minute.

The procedure to obtain the map including space baselines was as follows. First, the original data set which was obtained after flagging and averaging was loaded into DIFMAP and all space baselines were flagged. Then, the model obtained from the ground baseline map was loaded. Amplitude calibration was performed

epoch	Frequency [GHz]	flagged Channels	kept Bandwidth
1998.22	5	1, 108-128	83%
1998.22	1.6	1, 108-128	83%
1998.57	5	1, 111-128	85%
1998.66	1.6	1, 108-128	83%
1999.50	1.6	1, 108-128	83%
1999.50	5	1, 108-128	83%
1999.69	1.6	1, 105-128	81%
1999.69	5	1, 108-128	83%

Table 3.1: Summary of the VSOP observations. Because of a drop in bandpass several channels had to be flagged, eliminating 15–19 % of the bandwidth. Additionally the channels 1–5 and 90–128 for Goldstone had to be flagged at 1.6 GHz in 1999.50.

using the DIFMAP task `GSCALE`. After this, auto-flagging of the HALCA baselines (obtained from the phase-self-calibration included in `GSCALE`) was undone, with the task `UNCALIB false, false, true`. Now, the `CLEAN/SELFCAL` algorithm including tapering (50 Mλ steps) and amplitude calibration as described for the ground map, was used for all baselines.

Model fitting with Gaussian components was performed in DIFMAP. For this, several initial start models were used with the following variations:

- different number of initial components
- variation of the initial position of the components
- variation of the initial flux density of the components
- variation of the component shape (circular/elliptical, fixed/variable)

After the components became stable (no big changes in their parameters anymore), small parameter variations were introduced to check if they change back to their initial values. The most stable model with $\chi^2 \leq 5$ was favored. If an additional component led to a decrease of χ^2 of only a few tenths and the stability of the model remained the same as before then the previous, simpler model was used. Another criterion was the sum of the component flux densities, which should be similar to the total flux in the `clean`-map. Naturally, the modelled map should show the same features in the jet as seen in the `clean`-map. Furthermore, the models of the different epochs had to be consistent with each other, to be able to describe the jet changes in time. A circular Gaussian component instead of an elliptical one was introduced when the component became a line (axis ratio equals zero) or the component became so elongated that it overlapped with another component. The errors for the components were calculated using the variance of different stable models obtained with the same number of Gaussians and with the same quality (smallest χ^2, consistency between epochs, reproducibility of the `clean` map).

The nomenclature of the jet components was taken the literature (e.g. ZCU 1995, Lobanov 1996, and Ros *et al.* 2000) and continued. The synchrotron self-absorbed core is called 'D' and the jet components are named 'C' followed by a number corresponding to the sequence of their appearance.

3.3 VSOP Imaging at 1.6 GHz

The mapping results from 4 VSOP epochs of 3C 345 at 1.6 GHz (close in time to the 5 GHz VSOP observations described in section 3.4) are presented here. The time range from the first to the last epoch covers about 18 months. The observations were made on March 22, 1998 (1998.22); August 28, 1998 (1998.66); July 1, 1999 (1999.50) and September 9, 1999 (1999.69). The symbols used in the model fit Tables 3.2, 3.3, 3.4 and 3.5 are as follows: S - component flux density; r - component distance relative to the core; Θ - component position angle; a - component major axis; b/a - component axial ratio; Φ - component major axis position angle. The mapping parameters for these observations can be found in Tables 3.6 and 3.7.

3.3.1 March 22, 1998 (1998.22)

The three tracking stations used (Robledo, Goldstone and Green Bank) provided good data for this observation. In the ground baseline map (Figure 3.2), the jet extends out to $r \approx 60$ mas at a level of 400 mJy/beam and to $r \approx 100$ mas at a level of 80 mJy/beam. There is a bend to the north in the radio emission at about 12 mas from the compact core. At a core-distance beyond 35 mas the jet becomes fainter. In the VSOP map (Figure 3.3) the inner jet is visible. It appears elongated in the direction to the west up to $r \approx 3$ mas (P.A. $\approx -90°$). Then the jet makes a strong bend to the north (P.A. $\approx -62°$) and shows a big feature in the east-west direction. At further distance ($r > 10$ mas) the jet becomes broad and resolved.

Four elongated Gaussians model the outer part (beyond 4 mas) of the jet. The components at 20.8 and 44.7 mas core distance can be assigned to the jet features C1 and C0. The jet feature C3 rather than C2 is represented by the Gaussian at 11.5 mas. The Gaussian at $r = 5.7$ mas is the sum of C4 and C5. The separation of this complex into two components leads to only a small improvement of χ^2. However, the separation of this complex allows an assignment of C5 and C4 consistent with the literature (Ros *et al.* 2000) for all 1.6 GHz epochs presented in this chapter. The jet features C2 and C6 cannot be identified.

For the inner jet at a core distance smaller than 4 mas there exist two possibilities:

- Scenario 1: This first scenario consists of a model with two Gaussians (Figure 3.5) which leads to a map with $\chi^2 = 0.57^*$ and represents C7 and the core. However, when one compares this model with the ones at later epochs, it is obvious that both Gaussians would cover the core and two jet features (C8 and C7). The eastern Gaussian lies somewhere between the core and C8 and the western Gaussian lies between C8 and C7. This model is inconsistent with later epochs, it hides the component C8 and falsifies the parameters of C7 and the core.

- Scenario 2: The second scenario consists of a model with three Gaussians, representing C7, C8 and the core. Figure 3.6 shows three different jet models with differently shaped Gaussians for this scenario. In the first model C7, C8 and the core are fixed to be circular. In the second model only C7 and C8 are

---

$^*\chi^2 < 1$ because of an overestimation of the errors

> fixed to be circular and in the third model all axis ratios are variable. The agreement factors of the fits ($\chi^2 = 0.57$, 0.57 and 0.55) have the same quality as for the first scenario with two Gaussians. These different models show strong disagreements in position and flux density for the three Gaussians. They yield different distances for C8, from 0.60 ± 0.16 to 0.85 ± 0.16 mas and a difference in flux density from 1.18 ± 0.3 to 2.72 ± 0.3 Jy. The flux density of C8 is completely anti-correlated with the flux density of the core which ranges from 2.47 ± 0.5 to 0.36 ± 0.5 Jy. Also C7 varies for the different models, in distance and flux density from 1.70 ± 0.14 to 2.06 ± 0.14 mas and from 1.00 ± 0.05 to 1.56 ± 0.05 Jy respectively. The models are also influenced by the unresolved component C9, which was already detected at 5 GHz in 1998.22 (see section 3.4.1) and at 15 GHz in 1996.81 (Ros *et al.* 2000).

Different possible solutions with good and similar statistical agreement factors demonstrate the difficulty in determining the parameters of very close components which are additionally influenced by an unresolved component. Scenario 2 with all degrees of freedom is favored, because it shows the best agreement for C7 and C8 with the next epochs. The "disadvantage" of this model is that the core also includes the flux of C9, yielding $S = 2.47$ Jy. The parameters of the model fits are presented in Table 3.2.

Name	S [Jy]	r [mas]	Θ [°]	a [mas]	b/a	Φ [°]
D+C9	2.47 ±0.50	0	0	1.0 ±0.2	0.9 ±0.1	89 ±10
C8	1.18 ±0.30	0.85 ±0.16	-96.1 ±5.0	1.5 ±0.2	0.5 ±0.2	-34 ±10
C7	1.00 ±0.05	1.70 ±0.14	-102.1 ±0.5	0.9 ±0.1	0.6 ±0.2	-43 ±5
C5	0.84 ±0.05	4.34 ±0.40	-68.9 ±1.0	2.5 ±0.4	1	0
C4	0.90 ±0.05	6.98 ±0.40	-65.9 ±2.0	2.6 ±0.8	1	0
C3	0.44 ±0.20	11.50 ±1.00	-71.7 ±2.0	6.4 ±0.8	0.6 ±0.2	-68 ±5
C1	0.53 ±0.20	20.80 ±2.00	-54.3 ±3.0	11.0 ±1.0	0.7 ±0.2	-82 ±5
C0	0.32 ±0.15	44.70 ±5.00	-50.6 ±3.0	45.3 ±3.0	0.4 ±0.2	-37 ±5

Table 3.2: Model fit components for epoch 1998.22 (March 22, 1998). See also Figure 3.6 bottom. The C5/C4 complex is modeled with two Gaussians.

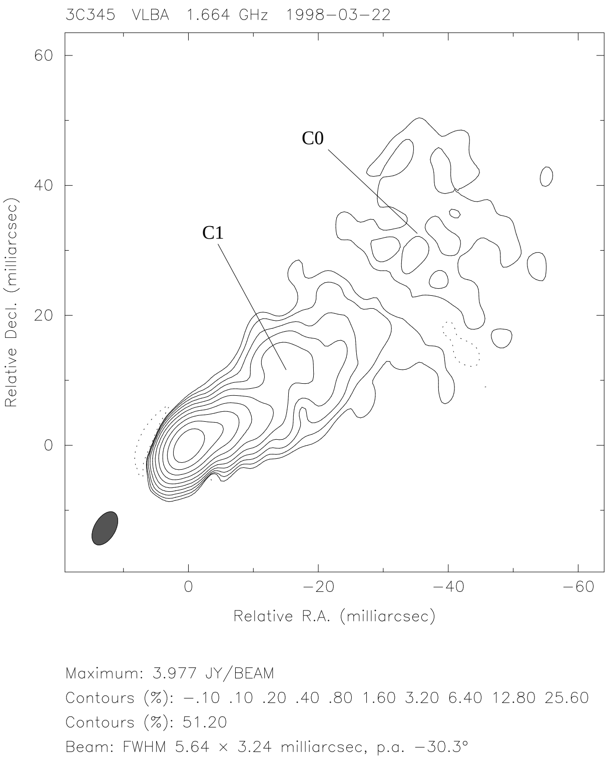

Figure 3.2: 1.6 GHz ground VLBI image of 3C 345 on March 22, 1998 (1998.22). The core is centered at zero and the jet extends to the north-west. At about $r \approx 12$ mas a bend to the north is seen in the jet. The jet becomes fainter at $r > 35$ mas.

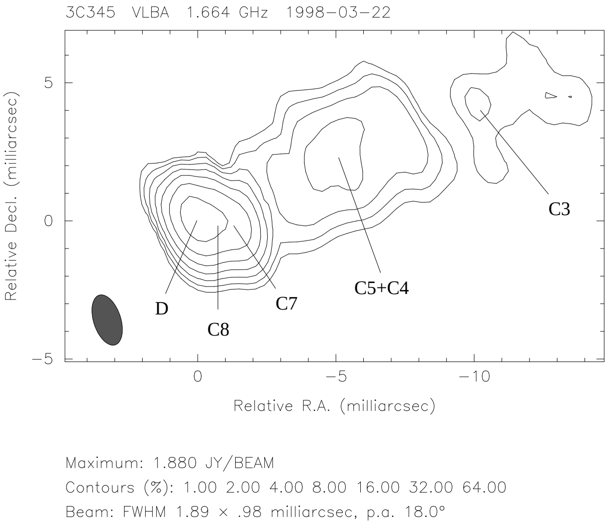

Figure 3.3: 1.6 GHz VSOP image of 3C 345 on March 22, 1998 (1998.22). The core is centered at zero and the inner part of the jet extends to the west out to $r \approx 3$ mas. After a bend to the north a feature is seen in the east-west direction.

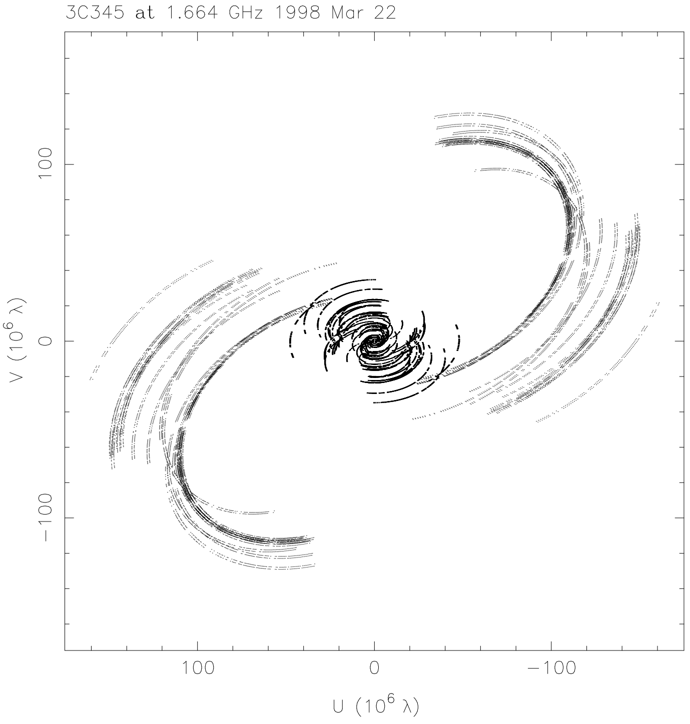

Figure 3.4: *uv*-coverage of the 1.6 GHz VSOP observation of 3C 345 on March 22, 1998 (1998.22). The long elongated arcs are the projected ground-space baselines.

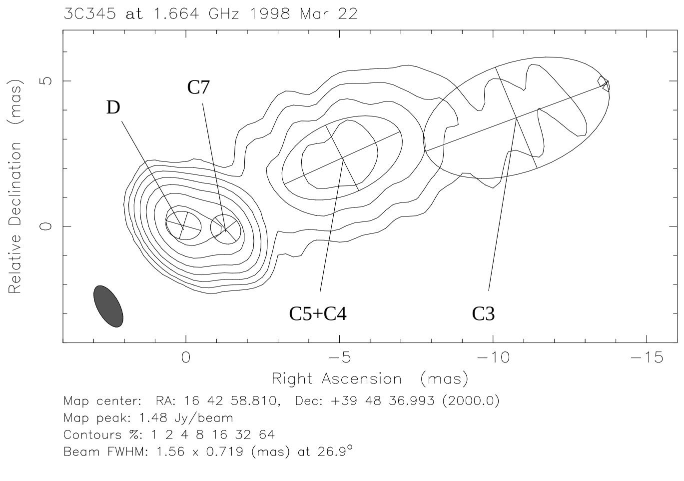

Figure 3.5: Scenario 1: 1.6 GHz model fit of the inner part of the pc-scale jet of 3C 345 on March 22, 1998 (1998.22), including the HALCA baselines. This uses two elliptical components in the core region (D and C7) in contrast with the three components presented in Figure 3.6. Two big features (C4+C5 and C3) are seen at $r \approx 5$ mas and $r \approx 11$ mas to the north-west. The two outer components C1 and C0 lie outside of this image.

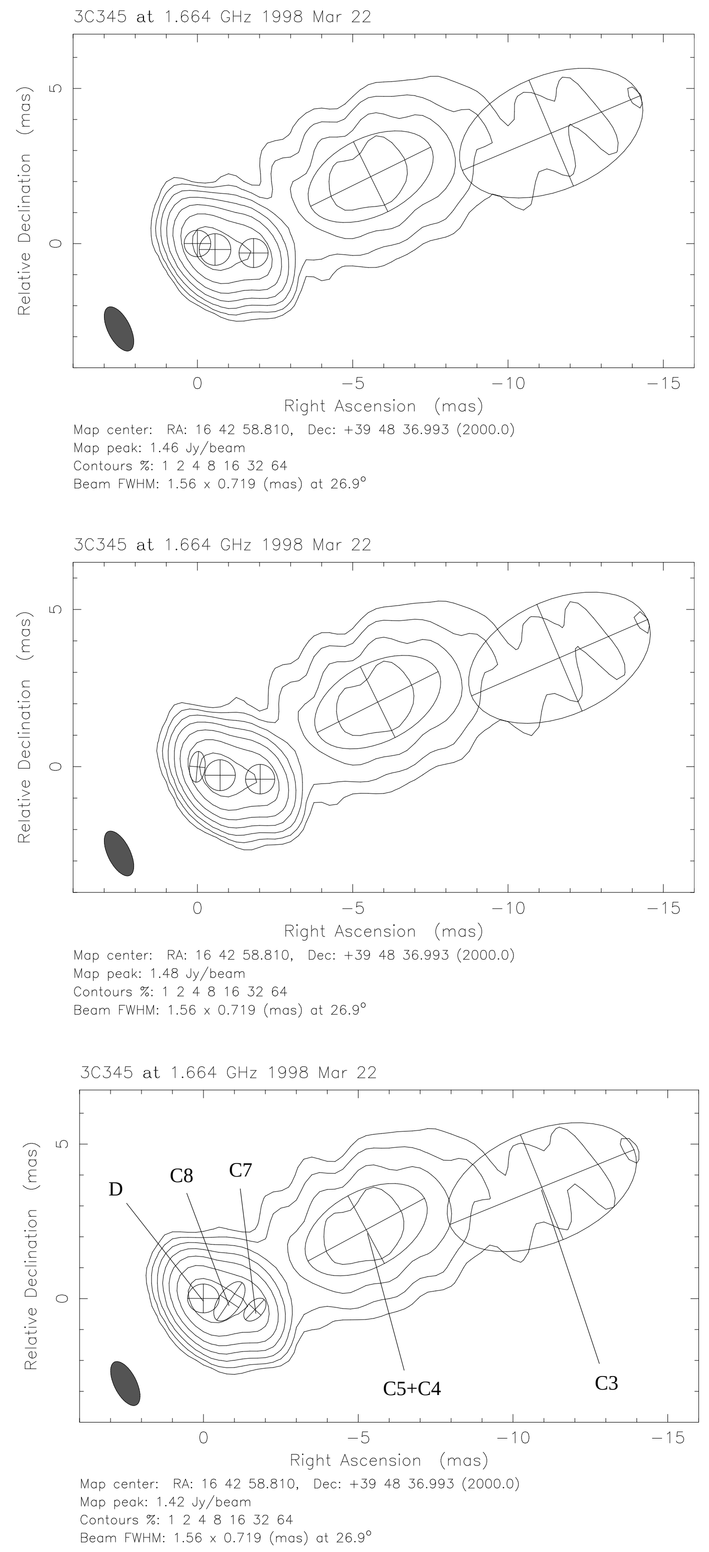

Figure 3.6: Scenario 2: Different model fit results using three Gaussians (D, C8 and C7) in the inner 4 mas of the 3C 345 jet at 1.6 GHz on March 22, 1998 (1998.22). The different shapes of the Gaussians lead to different flux densities and core-distances for the jet components (see text for details). The bottom picture shows the most satisfactory model (parameters are given in Table 3.2).

3.3.2 August 28, 1998 (1998.66)

The tracking station in Robledo produced good data for two tracking paths at the beginning and at the end of the 11 hr observation. Tape problems at the Green Bank tracking station and big scatter in phase and amplitude in the data from the Tidbinbilla tracking station reduced the good observing time with HALCA from the total of 5 h 45 min to 4 h 10 min.

The ground image (Figure 3.7) shows a collimated jet extending $r \approx$12 mas to the west (P.A. $\approx -73°$). At this position the jet becomes broader and turns northwards. At a distance $r >$30 mas the jet becomes resolved. The VSOP image (Figure 3.8) shows in the inner jet an east-west elongation similar to the previous epoch (Figure 3.3). The feature between 4 mas and 10 mas from the core (P.A. $\approx -70°$) looks like one big blob. At this epoch the P.A. of the space VLBI beam is almost perpendicular to these of other epochs, which results from the different uv-coverage of the ground-space baselines (compare Figure 3.9 with 3.4, 3.13, and 3.17) and leads to a slightly different map.

The inner jet was modeled with two components C8 and C7. Since the unresolved jet component C9 influences C8 and the core, there exist two possible cases:

- Case A: With a variable shape for C8 and the core, C8 becomes more elongated in the jet direction and the core becomes a small ellipse in the north-south direction (Figure 3.10 top). In this case, C8 includes more of the flux density of the unresolved jet feature C9 than the core.
- Case B: C8 is fixed to be circular in shape. The core is variable in shape and becomes more extended in the jet direction than for case A (Figure 3.10 middle and bottom). It includes more of the flux density of the unresolved jet feature C9 than C8. Thus the flux density of C8 is lower and the flux density of the core is higher, in contrast to case A.

Both models give $\chi^2 = 0.55$. Case B is favored, to trace the evolution of C8 with preferably less influence of the unresolved component C9. The core-distances and flux densities of the outer components are almost unaffected by the shape of C8 and the core. The outer jet consists of the model components C0, C1, C3 and C5+C4. The separation of the C5+C4 complex does not improve the χ^2 very much. However, the separation of this complex allows an assignment of C5 and C4 consistent with the literature (Ros *et al.* 2000) for all 1.6 GHz epochs presented in this chapter. The jet features C2 and C6 can not be identified. The parameters of the model fits (including both cases) are presented in Table 3.3.

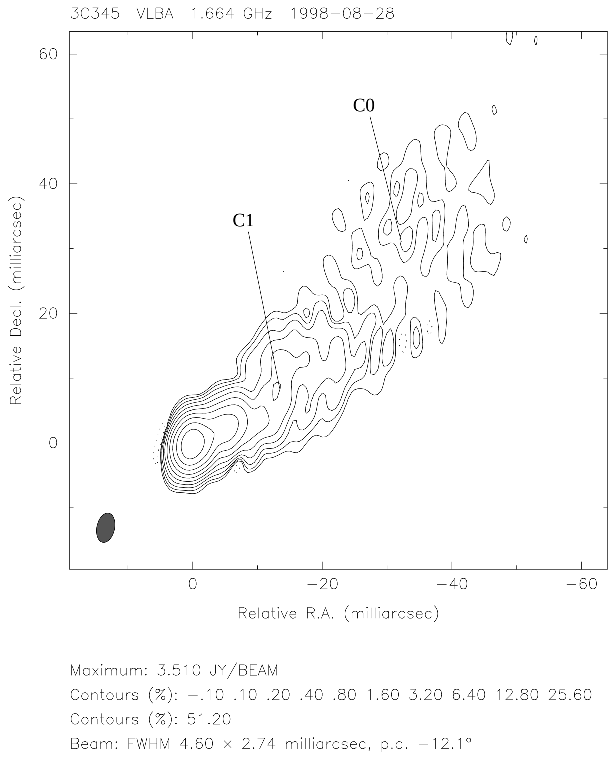

Figure 3.7: 1.6 GHz ground map of 3C 345 on August 28, 1998 (1998.66). The jet turns at a core distance of $r \approx 12$ mas to the north and becomes broad. At a distance of $r > 35$ mas the jet become resolved.

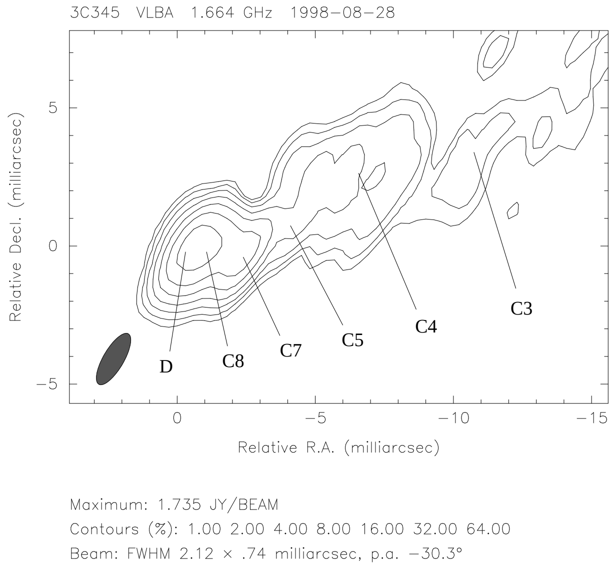

Figure 3.8: 1.6 GHz VSOP map of 3C 345 on August 28, 1998 (1998.66). The core is centered at position (0,0). At $r \approx 4$ mas to the west, the jet turns to the north.

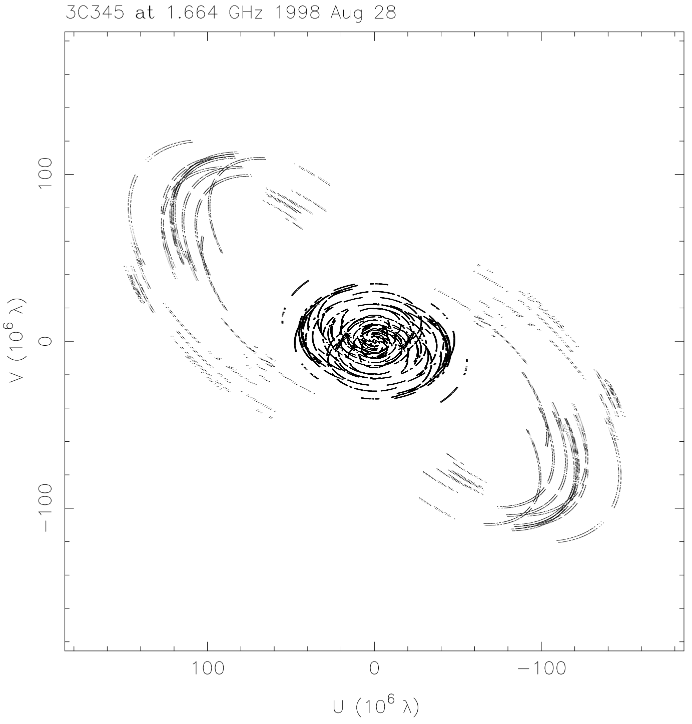

Figure 3.9: uv-coverage of the 1.6 GHz observation of 3C 345 on August 28, 1998 (1998.66). The long elongated arcs are the projected baselines between HALCA and the ground telescopes.

	Name	S [Jy]	r [mas]	Θ [°]	a [mas]	b/a	Φ [°]
A	D	0.87±0.50	0	0	1.1±0.2	0.4 ±0.2	-31±9
	C8+C9	2.60±0.50	0.66±0.16	-101.3 ±5.0	1.1±0.2	0.6 ±0.2	-89±9
B	D+C9	1.58±0.50	0	0	0.9±0.1	0.6 ±0.2	-26±9
	C8	1.81±0.30	0.74±0.16	-95.9 ±5.0	0.7±0.2	1	0
B	C7	1.29±0.05	1.95±0.15	-97.8 ±0.5	0.7±0.1	0.7 ±0.1	66±5
	C5	0.76±0.05	4.61±0.40	-69.3 ±1.0	2.3±0.4	1	0
	C4	0.74±0.05	7.22±0.40	-66.5 ±1.0	2.4±0.4	1	0
	C3	0.50±0.20	11.31±1.00	-72.5 ±2.0	7.1±0.8	0.5 ±0.2	-67±5
	C1	0.52±0.20	20.76±2.00	-54.8 ±3.0	11.2±1.0	0.6 ±0.2	-80±5
	C0	0.30±0.15	45.21±5.00	-49.8 ±3.0	43.5±3.0	0.4 ±0.2	-34±5

Table 3.3: Model fit components for epoch 1998.66 (August 28, 1998). C9 is still unresolved at this frequency and influences dramatically the flux density of the core and C8. Case A: The shape of C8 is variable which extends this component in the jet direction. This leads to a higher flux density of C8, including most of the flux density of the unresolved C9. Case B: C8 is fixed to be circular. This results in a more extended core in the jet direction with a higher flux density, including most of the flux density of the unresolved C9. Result: Case B was chosen for further analysis, in order to trace a consistent flux density evolution of C8 in further epochs. Thus, the parameters of the outer components from case B are used.

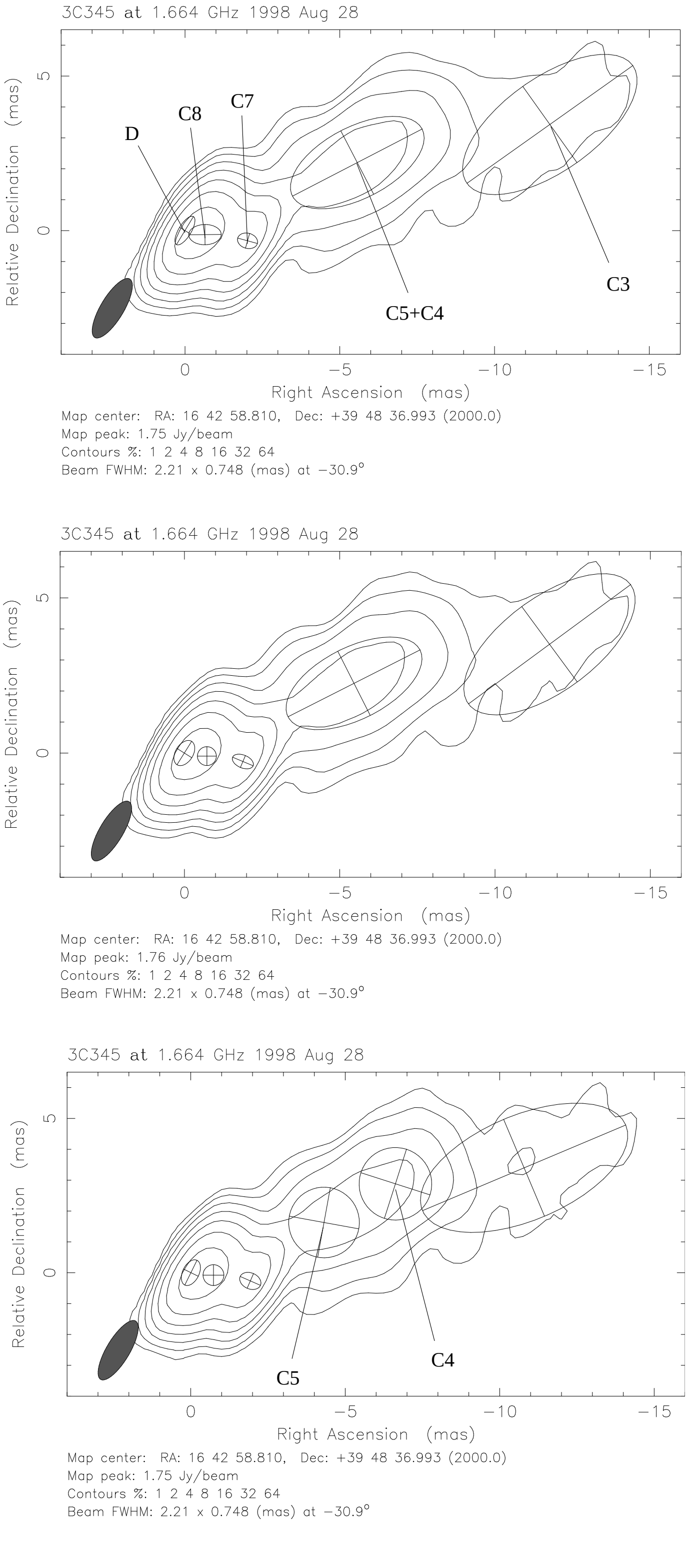

Figure 3.10: 1.6 GHz VSOP Model fit of 3C 345 on August 28, 1998 (1998.66). Top (Case A): C8 is variable in shape and becomes elongated east-west. C8 includes most of the flux density of the unresolved component C9. Middle (Case B): The shape of C8 is fixed to be circular. The core is more extended in the direction of the jet than for case A and includes most of the flux of the unresolved component C9. Bottom: Same as case B but with a separation of the C5/C4 complex in 2 features. See also text and Table 3.3.

3.3.3 July 1, 1999 (1999.50)

The tracking stations Goldstone, Usuda and Tidbinbilla recorded data at this epoch. Usuda showed a big scattering in phase and amplitude forcing the flagging of 50% of the data. The resolution is slightly worse than the other epochs and made it more difficult to model the innermost region of the jet. Anyhow, the data allow an investigation of the innermost jet in a manner which is impossible with ground VLBI only at this frequency.

The ground image (Figure 3.11) shows a collimated jet to the north-west (P.A. $\approx -70°$) and a kink to the north at $r \approx$20 mas core distance (P.A. $\approx -55°$). At a larger distance ($r > 40$ mas) the jet becomes broad and resolved. The VSOP image (Figure 3.12) has an inferior resolution to that at other epochs. The jet lies apparently straight in the north-west direction. The strong kink at $r \approx 4$ mas (P.A. $\approx -90°$) seen in previous epochs looks more like a soft bend.

With the knowledge of the next epoch results at this frequency (1999.69) and the results at 5 GHz for this epoch (section 3.4.3), it was known that the recently ejected component C9 is in the range of the resolution limit and should be detectable. Allowing a variation of the parameters for all components, C9 could not be modeled with the available data. The limited resolution perpendicular to the jet leads to models for C9, C8 and C7 which are inconsistent with the previous epochs and the next epoch. To constrain the model, the circular sizes and the positions of D, C9, C8 and C7 were taken from the next epoch (1999.69) and used as a starting model for this epoch. Nevertheless, the flux-densities and the core-distances of these components is still strongly depend on their size. A model with variable major-axes for all Gaussians still results in an unstable model. Also a variable size of C7 alone is strongly correlated with the positions and flux densities of C8 and C9. Therefore, it was necessary to keep the core and the innermost three jet components circular and similar in size to these of the next epoch (1999.69). With these constraints a stable and consistent model with $\chi^2 = 0.81$ containing the inner jet features C9, C8 and C7 was achieved (see Figure 3.14 and Table 3.4).

Five elongated Gaussians (C0, C1, C3, C4 and C5) model the outer part (beyond 4 mas) of the jet. The assignment of these Gaussians to components identified in the literature is the same as for the previous epochs. The jet features C2 and C6 can not be identified. The parameters of the model fits are presented in Table 3.4.

Name	S [Jy]	r [mas]	Θ [°]	a [mas]	b/a	Φ [°]
D	0.40 ±0.30	0	0	0.4 ±0.1	1	0
C9	1.86 ±0.30	0.70 ±0.16	-90.7 ±6.0	0.4 ±0.1	1	0
C8	1.33 ±0.30	1.44 ±0.16	-90.6 ±5.0	0.4 ±0.1	1	0
C7	1.26 ±0.05	2.61 ±0.16	-95.1 ±1.0	0.8 ±0.1	1	0
C5	0.71 ±0.10	5.45 ±0.40	-70.4 ±2.0	2.3 ±0.4	1	0
C4	0.64 ±0.10	8.02 ±0.40	-66.9 ±2.0	2.7 ±0.4	1	0
C3	0.43 ±0.20	12.82 ±1.00	-73.4 ±3.0	6.8 ±0.8	0.5 ±0.2	-63 ±5
C1	0.48 ±0.20	21.38 ±2.00	-55.6 ±3.0	12.0 ±1.0	0.6 ±0.2	-77 ±5
C0	0.25 ±0.10	44.07 ±5.00	-52.3 ±3.0	44.5 ±3.0	0.5 ±0.2	-31 ±5

Table 3.4: Model fit components for epoch 1999.50 (July 1, 1999).

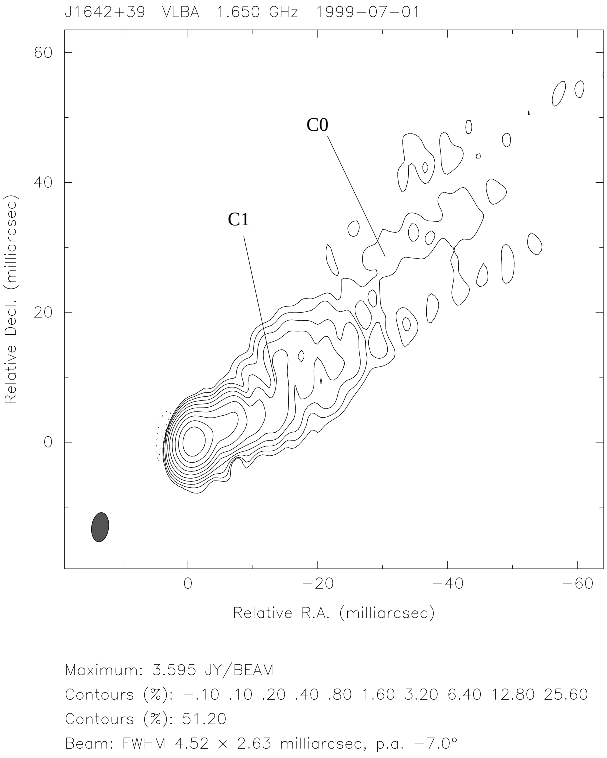

Figure 3.11: 1.6 GHz ground VLBI map of 3C 345 on July 1, 1999 (1999.50). The core is centered at position zero and the jet lies to the north-west. A bend to the north is seen at $r \approx 12$ mas core distance. The jet becomes resolved beyond $r \approx 40$ mas.

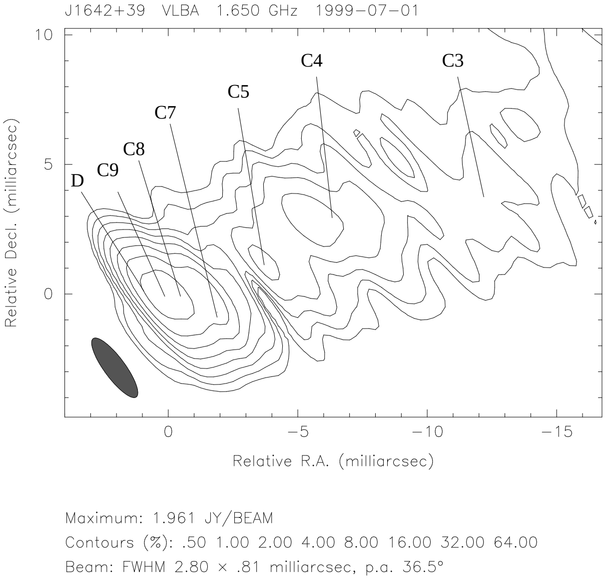

Figure 3.12: 1.6 GHz VSOP map of the inner pc-scale structure of 3C 345 on July 1, 1999 (1999.50). The core is centered at position (0,0). The jet shows a slight bend to the north at a core distance of $r \approx 4$ mas.

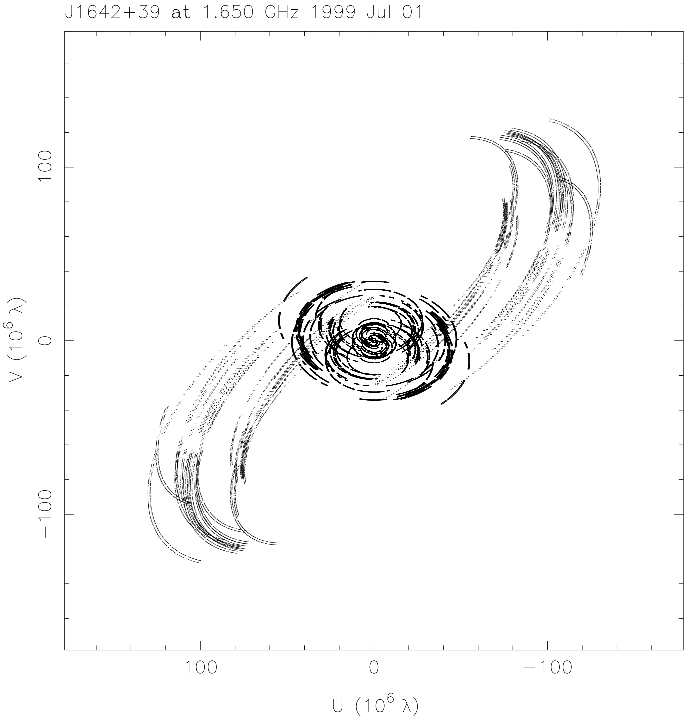

Figure 3.13: *uv*-coverage of the 1.6 GHz observation of 3C 345 on July 1, 1999 (1999.50). The long elongated tracks are the projected baselines between the space telescope and the ground antennas.

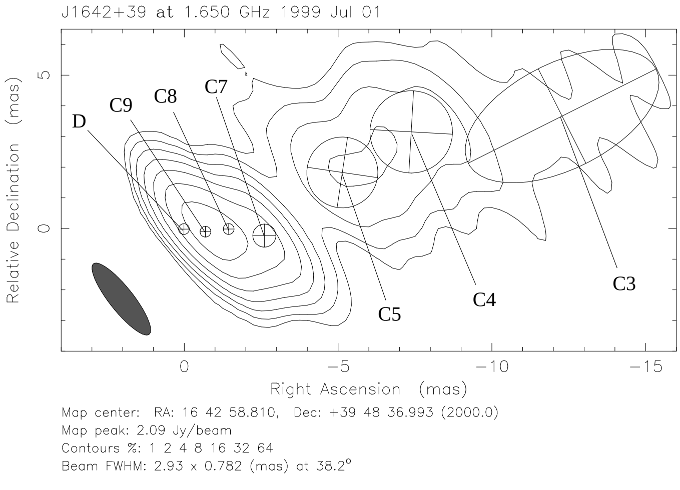

Figure 3.14: The inner 7 of the 9 Gaussian components used in the model fit for 3C 345 observed on July 1, 1999 (1999.50) at 1.6 GHz. C9 was detectable for the first time at this frequency. The core, C9, C8, C7, C5 and C4 have a fixed circular shape.

3.3.4 September 1, 1999 (1999.69)

The tracking stations Green Bank, Tidbinbilla and Robledo recorded data from HALCA. The big scatter in amplitude and phase at the Robledo tracking station forced the flagging of about 1 hr 30 min of the data. Nevertheless, 8 h of usable space-data were obtained, leading to the highest space-VLBI time coverage of the four 1.6 GHz observations presented (see also *uv*-coverage in Figure 3.17).

In the ground image (Figure 3.15) a collimated jet to the west extending out to $r \approx 12$ mas (P.A.$\approx -75°$) is seen. At larger distances the jet becomes broad and bends to the north. The jet fans out at $r > 40$ mas to the north-west. The VSOP image (Figure 3.16) shows a straight inner jet to the west out to $r \approx 4$ mas (P.A.$\approx -90°$). Afterwards the jet makes a strong bend to the north with a big feature elongated in the east-west direction. The jet is resolved beyond 10 mas from the core.

The inner 4 mas of the jet are modeled with four Gaussians (Figure 3.18 and Table 3.5). The component C9 is clearly detectable in the model fit. Anyhow, a stable model varying all the parameters of the inner components was impossible and led to some degenerate components. The core, C9 and C8 were fixed to a circular shape but the major axis of the core and C9 were allowed to vary. The major axis of C8 was fixed to a size similar to C9 and the core. With these constraints the most stable model was achieved and, additionally, this model could be used as an input model for the previous epoch (see section 3.3.3). The consistency obtained between 1999.50, 1999.69 and 5 GHz VSOP observations makes this model convincing. Nevertheless, one should note that only two months elapsed between the previous epoch and this one. It is impossible to make any statement about component motion between these epochs. The conclusion is that both epochs show a clear identification of the new component C9.

Five elongated Gaussians (C0, C1, C3, C4 and C5) model the outer part (beyond 4 mas) of the jet. The assignment of these Gaussians to components identified in the literature is the same as for the previous epochs. The jet features C2 and C6 can not be identified. The parameters of the model fits are presented in Table 3.5.

Name	S [Jy]	r [mas]	Θ [°]	a [mas]	b/a	Φ [°]
D	0.90 ±0.30	0	0	0.4 ±0.2	1	0
C9	1.80 ±0.30	0.66 ±0.16	-92.6 ±5.0	0.3 ±0.2	1	0
C8	1.05 ±0.30	1.30 ±0.16	-85.7 ±5.0	0.4 ±0.2	1	0
C7	1.26 ±0.05	2.36 ±0.15	-95.3 ±1.0	1.0 ±0.1	0.8 ±0.1	-70 ±5
C5	0.71 ±0.10	5.28 ±0.40	-69.9 ±2.0	2.3 ±0.4	1	0
C4	0.64 ±0.10	7.86 ±0.40	-65.7 ±2.0	2.6 ±0.4	1	0
C3	0.47 ±0.20	12.51 ±1.00	-72.4 ±2.0	7.1 ±0.8	0.5 ±0.2	-60 ±5
C1	0.48 ±0.20	21.19 ±2.00	-54.6 ±3.0	11.6 ±1.0	0.6 ±0.2	-82 ±5
C0	0.31 ±0.10	45.85 ±5.00	-50.5 ±3.0	43.3 ±3.0	0.4 ±0.2	-35 ±5

Table 3.5: Model fit components for epoch 1999.69 (September 9, 1999).

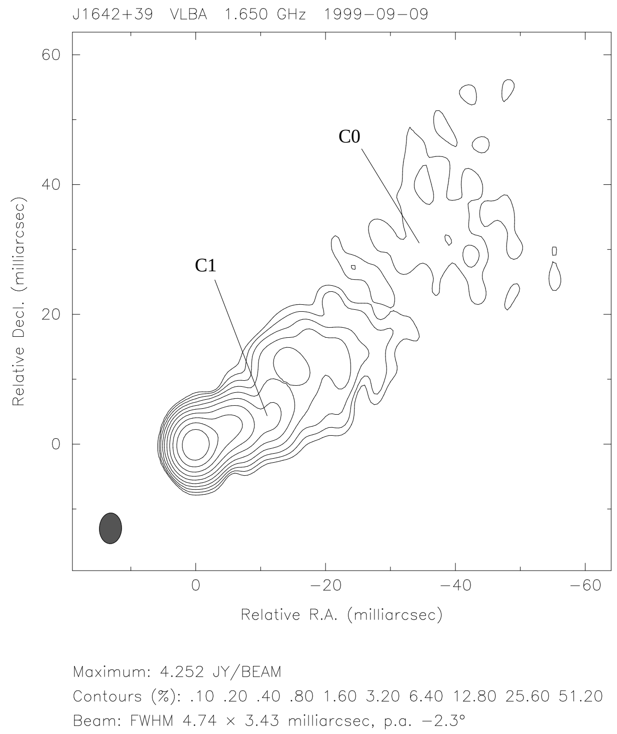

Figure 3.15: 1.6 GHz ground VLBI image of 3C 345 on September 9, 1999 (1999.69). The core is centered at position zero and the jet lies in the north-west direction. The jet bends to the north at $r \approx 12$ mas core distance.

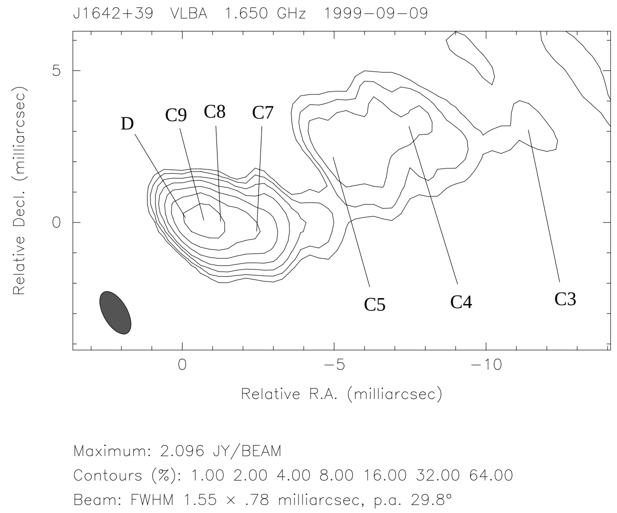

Figure 3.16: 1.6 GHz VSOP image of 3C 345 on September 9, 1999 (1999.69). The core is centered at position (0,0). The inner jet lies straight to the west until $r \approx 4$ mas core-distance. Then the jet bends to the north with a big feature in the east-west direction.

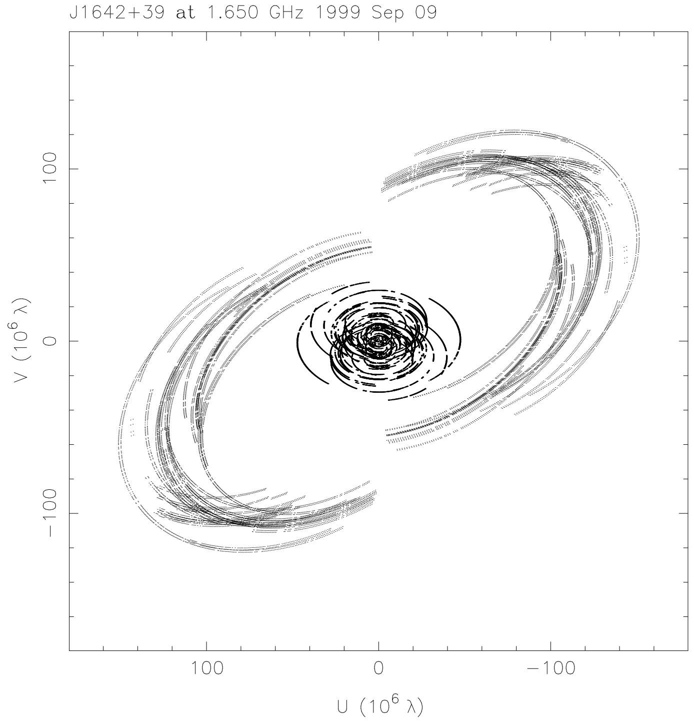

Figure 3.17: *uv*-coverage of the 1.6 GHz observation of 3C 345 on September 9, 1999 (1999.69). The long elongated tracks are the projected baselines between the space antenna and the ground telescopes.

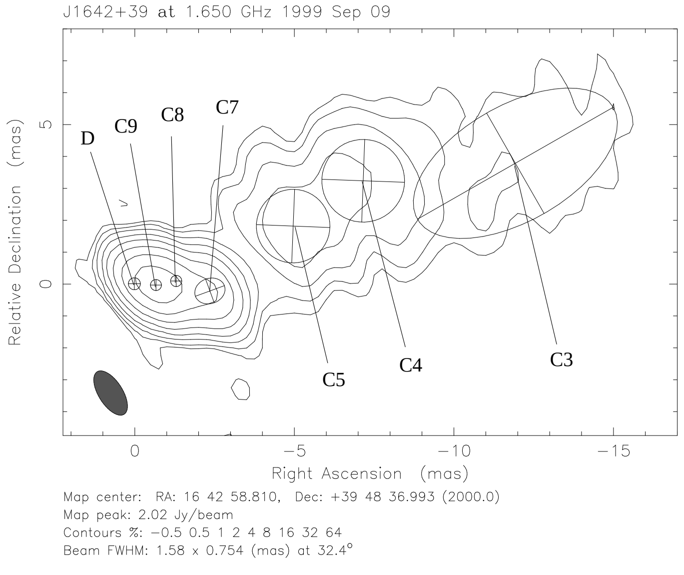

Figure 3.18: 1.6 GHz model fit of 3C 345 on September 9, 1999 (1999.69). The inner jet is modeled with the components C9, C8 and C7. Two big jet features at $r \approx 21$ mas and $r \approx 47$ mas core-distance lie outside this map.

3.3.5 Summary

Four VSOP observations made at 1.6 GHz in a time period of about 18 months between March 21, 1998 and September 10, 1999 were presented in this chapter. These first space VLBI observations at 1.6 GHz reveal the inner 15 mas of the jet, which cannot be seen by ground-only VLBI at this frequency. The jet components C8 and C9 were detected at 1.6 GHz for the first time. This provides an opportunity to compare them with observations at higher frequencies at the beginning of their evolution and to trace them in the immediate vicinity of the core. In addition, the components C7, C5, C4, C3, C1 and C0 were modeled, which gives a unique opportunity to investigate the jet from the innermost jet feature at $r \approx 0.7$ mas to the outermost one at $r \approx 44$ mas, at the same epoch and the same frequency. The jet features C2 and C6 have disappeared and cannot be identified anymore. The resolution is comparable with 5 GHz ground-only VLBI observations. This made it possible to produce high resolution spectral index maps between 1.6 GHz and 5 GHz (see section 6.2).

Ground Array Observing and Map Parameters of 3C 345 at 1.6 GHz

Epoch	Ground Telescopes	t_{tot} [h]	bas_g [Mλ]	$\Delta\nu$ [MHz]	bg_{maj} [mas]	bg_{min} [mas]	Φg [°]	S_{tot} [Jy]	S_{peak} [Jy]	C_{low} [mJy]	rms [mJy]	dr
1998.22	VLBA, phVLA, GO	9	48	26.50	5.64	3.24	-30.3	7.4	3.98	4.0	3	1:1327
1998.66	VLBA, phVLA, EB	11	57	26.50	4.60	2.74	-12.1	7.0	3.51	3.5	3	1:1170
1999.50	VLBA (without HN), EB, RO, GO	10	57	26.50	4.52	2.63	-7.0	7.1	3.60	3.6	3	1:1200
1999.69	VLBA, GO	13	48	25.75	4.74	3.43	-2.3	7.7	4.25	4.2	3	1:1417

Table 3.6: t_{tot} - total observing time; bas_g - longest projected ground-ground baseline; $\Delta\nu$ - remaining bandwidth after flagging channels; bg_{maj} - beam major axis; bg_{min} - beam minor axis; Φv - angle of the beam major axis; S_{tot} - total flux density; S_{peak} - peak flux density; C_{low} - lowest map contour; rms - root-mean-square of the map noise; dr - dynamic range; EB - Effelsberg; GO - Goldstone; RO - Robledo; phVLA - phased VLA; VLBA stations: MK - Mauna Kea; OV - Owens Valley; KP - Kitt Peak; BR - Brewster; PT - Pie Town; FD - Fort Davis; LA - Los Alamos; NL - North Liberty; HN - Hancock; SC - St. Croix

VSOP Observing and Map Parameters of 3C 345 at 1.6 GHz

Epoch	t_{VSOP} [h]	bas_{vs} [Mλ]	bas_{vl} [Mλ]	bv_{maj} [mas]	bv_{min} [mas]	Φv [°]	S_{peak} [Jy]	C_{low} [mJy]	rms [mJy]	dr
1998.22	6.00	33	165	1.89	0.983	18.0	1.88	18.8	10	1:188
1998.66	4.17	47	175	2.12	0.743	-30.3	1.74	17.4	14	1:124
1999.50	4.33	17	168	2.80	0.806	36.5	1.96	9.8	7	1:280
1999.69	8.00	38	160	1.55	0.780	29.8	2.11	21.1	15	1:141

Table 3.7: t_{VSOP} - VSOP observing time; bas_{vs} - shortest projected ground-space baseline; bas_{vl} - longest projected ground-space baseline; bv_{maj} - beam major axis; bv_{min} - beam minor axis; Φv - angle of the beam major axis; S_{peak} - peak flux density; C_{low} - lowest map contour; rms - root-mean-square of the map noise; dr - dynamic range

3.4 VSOP Imaging at 5 GHz

The mapping results from 4 VSOP observations of 3C 345 at 5 GHz made during a time period of 18 months (close in time to the 1.6 GHz VSOP observations presented in section 3.3) are presented here. The observations were made on March 21, 1998 (1998.22); July 28, 1998 (1998.57); July 02, 1999 (1999.50) and September 10, 1999 (1999.69). The legends of the model fit Tables 3.8, 3.9, 3.10 and 3.11 are as follows: S - component flux density; r - component distance relative to the core; Θ - component position angle; a - component major axis; b/a - component axial ratio; Φ - component major axis position angle. The mapping parameters of these observations can be found in Tables 3.12 and 3.13.

3.4.1 March 21, 1998 (1998.22)

HALCA tracking stations Goldstone, Robledo, Tidbinbilla and Green Bank were used for this epoch. While the first three stations provided good data with reasonable error bars in amplitude and phase, the data from the Green Bank tracking station had to be flagged due to a huge scatter in phase. This reduced the total HALCA observing time from 9.5 h to 8.5 h. Nevertheless, this was still about 59% of the total observing time (see the *uv*-coverage in Figure 3.21).

The ground map (Figure 3.19) shows the typical core-jet structure of this quasar, with the core centred at position (0,0). The inner 2 mas structure of the source extends to the west (P.A. $\approx -90°$). Further out a strong kink to the north is present at about 4 mas with a long elongated feature. At a distance between 8 and 16 mas, the jet direction makes a small bend to the west. Beyond 16 mas, the jet shows again a strong kink to the north and becomes resolved. The interferometric beam of the VSOP image is ~ 0.22 mas in the east-west direction, while the ground array has only ~ 1 mas resolution. The VSOP map (Figure 3.20) and the VSOP model fit (Figure 3.22) show clearly this gain in resolution. With this high image resolution, the synchrotron self-absorbed core and three inner jet components (C9, C8 and C7) are identified. The core and these components appear blended in the ground array image.

With the model fit technique the best fit (χ^2 =1.4) is obtained with 4 Gaussians within the inner 3 mas of the jet and 4 Gaussians for the outer part. The parameters of these Gaussians can be found in Table 3.8. The two eastern-most Gaussians show the core and a newly ejected component C9 (first seen at epoch 1986.81 at 15 GHz by Ros *et al.* 2000) at a core distance of $r = 0.38$ mas and P.A. $\approx -109°$. The core is weak ($S = 0.64$ Jy) compared with the new component C9 ($S = 2.64$ Jy) presumably due to synchrotron self absorption. A fit with only one component for the core and C9 gives $\chi^2 = 3.3$ and does not reproduce the corresponding image well.

Jet component C8 looks like a blob with a small dent to the east. A fit with an additional long elongated component to the left of C8 leads to no improvement of the model. Thus, this component can be best fitted with one Gaussian component. C8 is the brightest feature in the jet with $S = 3.02$ Jy.

The component C7 at 2.15 mas core distance is extended in the jet direction and, at $S = 1.34$ Jy, weaker than C8 and C9. To model the outer part of the jet in a stable way, two circular components at 5.07 mas and 7.63 mas core distance had to be introduced, which refer to the components C5 and C4 (e.g. Ros et al. 2000). Beyond these components, the rest of the observable jet can still be fitted with two Gaussians which refer to the jet features C3 and C1. The components C6 and C2 cannot be identified.

Name	S [Jy]	r [mas]	Θ [°]	a [mas]	b/a	Φ [°]
D	0.64±0.02	0	0	0.40±0.01	0.31±0.01	11±1
C9	2.64±0.02	0.38±0.02	-108.8±0.5	0.46±0.01	0.46±0.01	43±1
C8	3.02±0.02	1.09±0.02	-98.0±0.5	0.48±0.01	0.73±0.01	-9±1
C7	1.34±0.05	2.15±0.02	-96.3±0.5	0.98±0.05	0.59±0.03	79±1
C5	0.42±0.05	5.10±0.50	-74.5±0.5	2.30±0.10	1	0
C4	0.57±0.05	7.60±0.50	-68.5±0.5	2.70±0.20	1	0
C3	0.19±0.05	11.00±1.00	-73.2±1.5	7.43±0.20	0.35±0.05	-68±2
C1	0.26±0.05	20.61±1.50	-54.7±2.0	11.93±0.20	0.66±0.05	-72±2

Table 3.8: Model fit components for epoch 1998.22

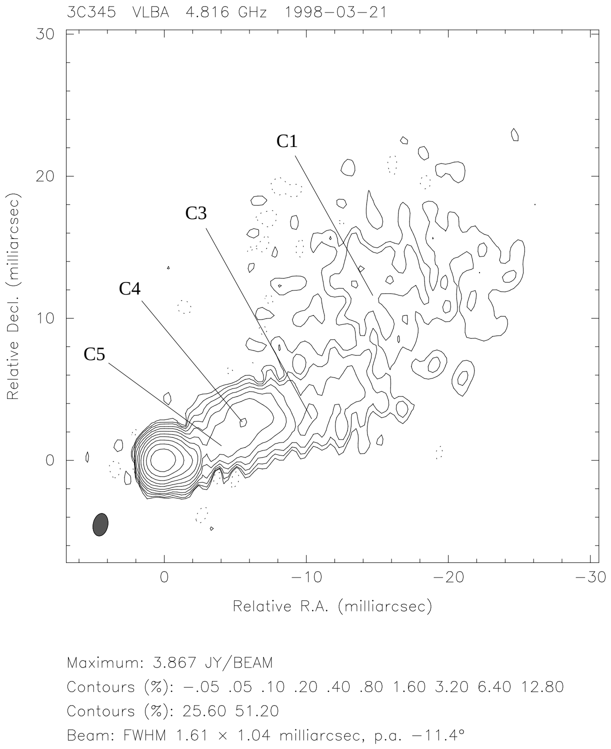

Figure 3.19: 5 GHz ground VLBI image of 3C 345 on March 21, 1998 (1998.22). The quasar shows its typical core-jet structure. The core is centred at position zero. The jet extends to the west and further out to the north, fading out at a distance $r > 20$ mas.

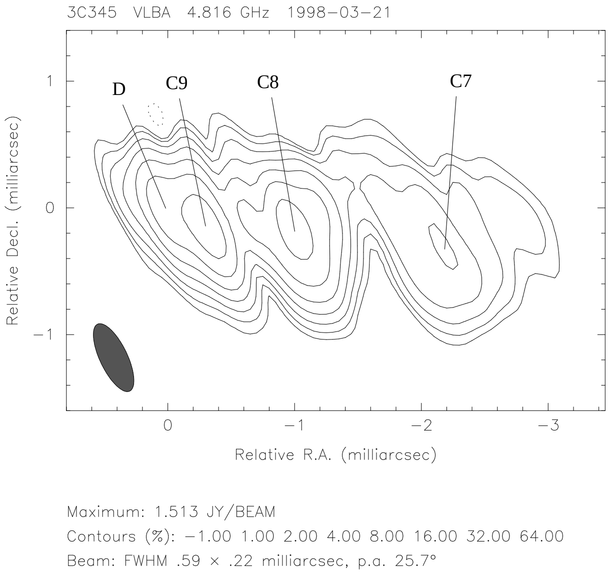

Figure 3.20: 5 GHz VSOP map of 3C 345 on March 21, 1998 (1998.22). The faint synchrotron self absorbed core lies at position (0,0) and the inner jet components C9, C8 and C7 lie to the west of the core. These components appear blended in the ground image.

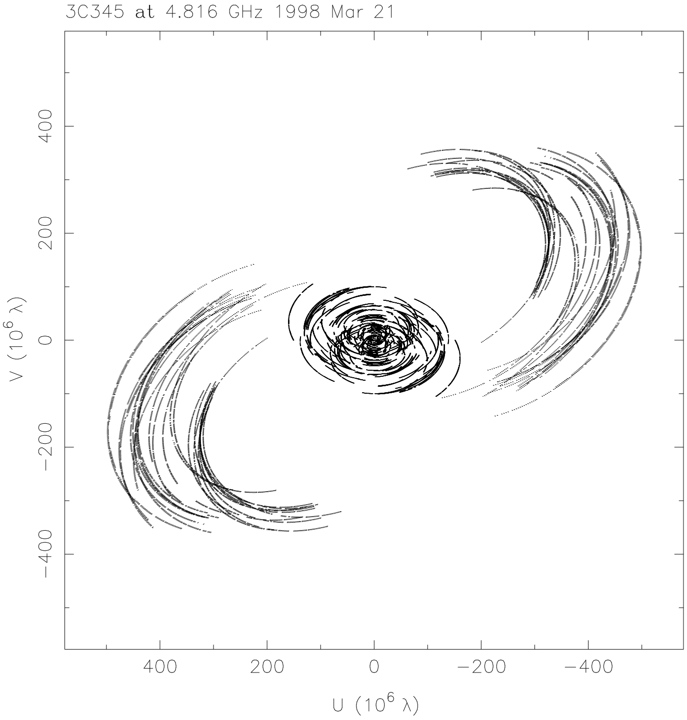

Figure 3.21: *uv*-coverage from 3C 345 on March 21, 1998 (1998.22). The long elongated tracks are the projected baselines between HALCA and the ground telescopes.

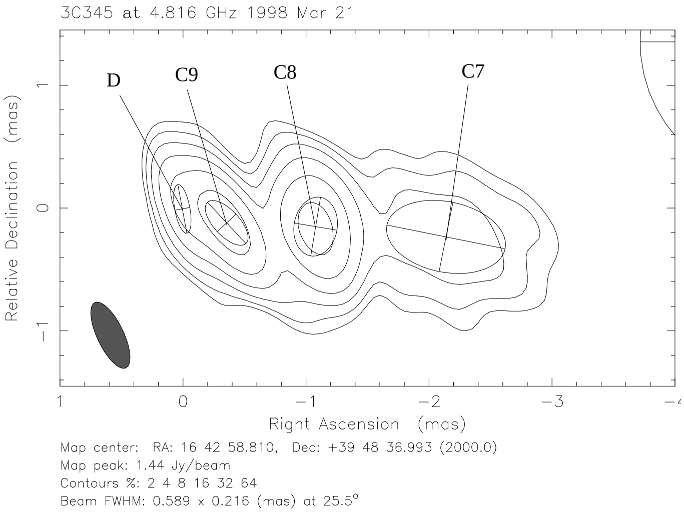

Figure 3.22: Model fit of 3C 345 on March 21, 1998 (1998.22) with $\chi^2 = 1.4$ The components C9, C8 and C7 form the inner jet. The four outer jet components lie outside this picture.

3.4.2 July 28, 1998 (1998.57)

HALCA data from the tracking stations Tidbinbilla, Robledo and Green Bank were obtained for this epoch. Data from Tidbinbilla had to be flagged for several baselines because of a big scatter in phase and amplitude. However this does not influence the data set significantly because Tidbinbilla participated for only ~10 min which was very short compared with the whole HALCA time of 10.0 h. With 71% VSOP time during this observation, the *uv*-coverage for the space-baselines was even better than for the previous epoch (see Figure 3.25).

The ground map (Figure 3.23) shows the core at position (0,0). The compact inner jet region is elongated out to $r \approx 3$ mas at P.A.$\approx -90°$. At this point the jet bends to the north and a big elongated feature appears at $r \approx 5$ mas (P.A.$\approx -75°$). At $r \approx 10$ mas the jet bends back to the west (P.A.$\approx -80°$) and a strong kink follows at $r \approx 16$ mas (P.A.$\approx -60°$) again to the north. After this distance the jet becomes resolved. The VSOP map (Figure 3.24) decomposes the inner jet region into the synchrotron self absorbed core and the components C9, C8 and C7. Compared with the previous epoch (Figure 3.20), the core is now clearly separated from the component C9. It is obvious that the core, C9 and C8 do not lie in a straight line which results from the wiggled structure of this jet. The beam is almost perpendicular to those at other epochs which results in a slightly different shape for the jet.

A model fit with Gaussian components ($\chi^2 = 3.4$) provides the following results. All three inner jet components (C9 – C7) and the core can be modeled in a stable way with elliptical Gaussian components, allowing all component parameters to vary. In this model, a flux density for the core of 0.79 Jy, weaker than C9 and C8 with 2.56 Jy and 2.47 Jy respectively, was obtained. C7 is elongated in the east-west direction and with 1.07 Jy is also brighter than the core. The outer components beyond 3 mas have a shape which is difficult to model with Gaussian components. C5 and C4 for example, can't be described in a reasonable way with two elongated Gaussians. Only one fit, with a big overlap of two remarkably elongated components, is possible. With a fixed circular shape, both components appear in a stable, clearly separated way. With this picture, this model is consistent with the other epochs. The outer part of the jet is modeled with two Gaussians corresponding to C3 and C1.

Name	S [Jy]	r [mas]	Θ [°]	a [mas]	b/a	Φ [°]
D	0.79±0.03	0	0	0.18±0.01	0.82±0.02	-82±2
C9	2.56±0.01	0.54±0.02	-112.5±0.5	0.42±0.01	0.73±0.05	32±4
C8	2.37±0.01	1.20±0.02	-97.6±0.5	0.53±0.01	0.55±0.05	-25±4
C7	1.07±0.05	2.32±0.02	-97.6±0.5	0.97±0.04	0.52±0.07	89±4
C5	0.33±0.10	5.30±0.20	-75.0±2.0	2.10±0.50	1	0
C4	0.48±0.05	7.60±0.50	-68.0±5.0	2.60±0.20	1	0
C3	0.19±0.05	11.34±1.00	-73.1±5.0	7.74±0.20	0.31±0.10	-66±10
C1	0.29±0.15	21.30±2.00	-54.7±7.0	12.60±1.50	0.72±0.10	-83±10

Table 3.9: Model fit components for epoch 1998.57 (July 28, 1998)

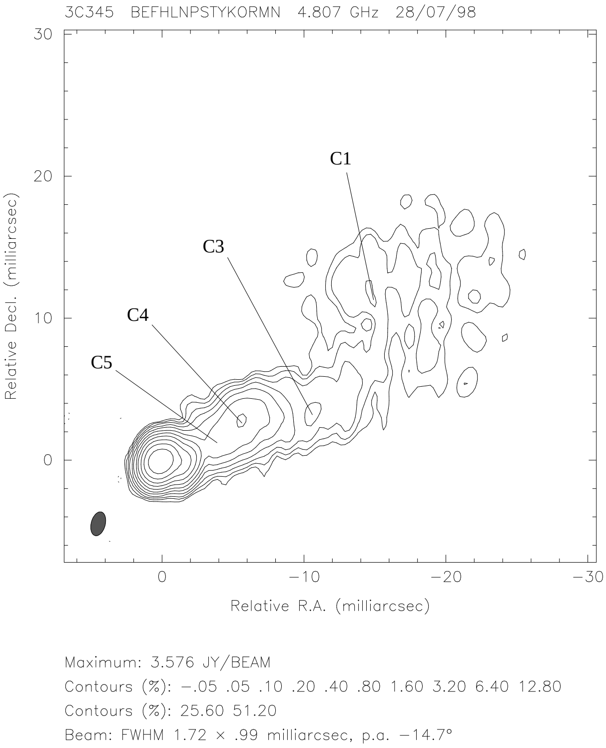

Figure 3.23: 5 GHz ground map of 3C 345 on July 28, 1998 (1998.57). The compact part to the left is the core and the inner unresolved jet region. The jet to the north-west shows a curved structure until it becomes resolved beyond $r \approx 16$ mas core-distance.

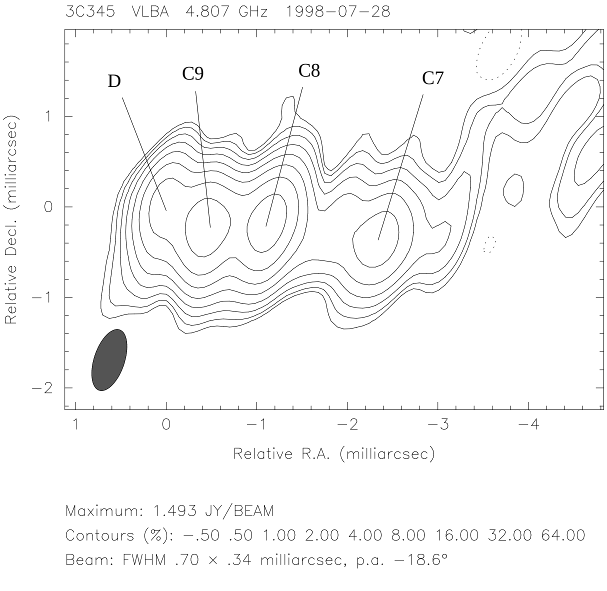

Figure 3.24: 5 GHz VSOP map of 3C 345 on July 28, 1998 (1998.57). The core is centred at position (0,0) and the inner jet components C9, C8 and C7 trace the curved jet structure in the east-west direction. Synchrotron self absorption obscures the core at this (relatively) low frequency.

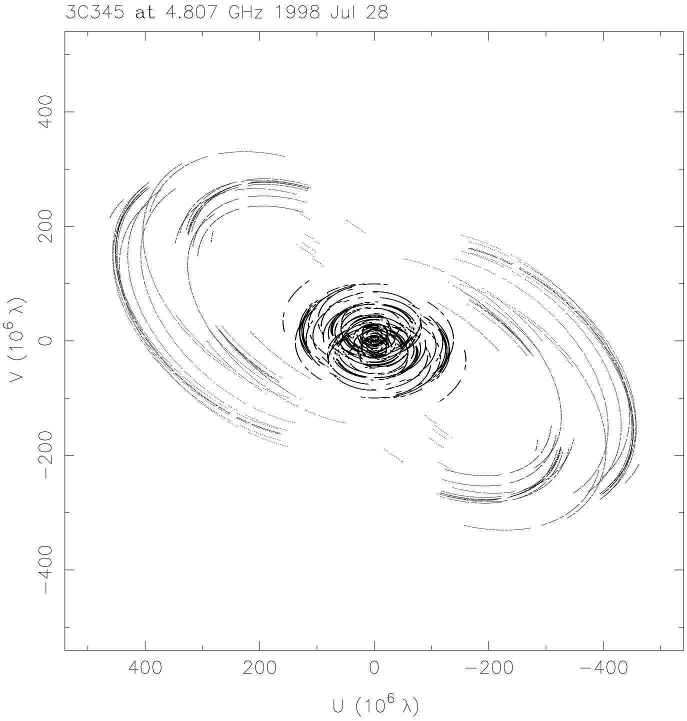

Figure 3.25: *uv*-coverage of the 5 GHz observation of 3C 345 on July 28, 1998 (1998.57). The long elongated tracks are the projected ground-space baselines.

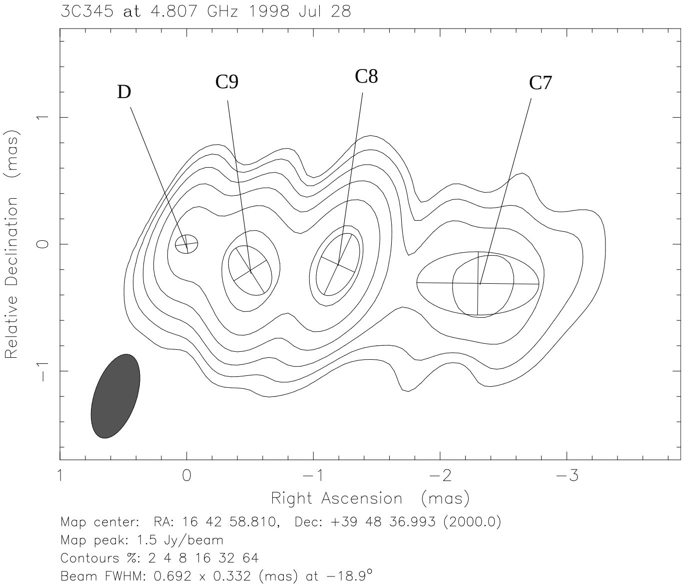

Figure 3.26: Model fit of the inner part of the pc-scale jet in 3C 345 at 5 GHz on July 28, 1998 (1998.57) with $\chi^2 = 3.4$ The components C9, C8 and C7 form the inner jet. The four outer components lie outside of this image.

3.4.3 July 2, 1999 (1999.50)

The Goldstone tracking station supplied good data for 1 h 40 min. The error bars for the visibility amplitudes for the Usuda tracking station were rather large and additionally data for more than 1 h could not be used because of a failure on the tape. Only ~40 min of useful data were obtained from Usuda. Thus HALCA participated for only 2 h 20 min with good data, from a total of 10 h for the ground array. This is the shortest VSOP time of all four epochs (see Table 3.13) and results in only 23% space data.

With also the shortest ground observing time of all four epochs (see Table 3.12), the quality of the ground map (Figure 3.27) does not reach that of the other epochs. Nevertheless, the core and the curved jet-structure is well seen. The jet is resolved at about 12 mas core distance. Because of the lower orbit of HALCA, the beam is bigger than in earlier epochs which leads to a lower resolution of 0.363 mas in the jet direction and 0.985 mas perpendicular to the jet (see Table 3.13). The quality of the map suffers also from the short space observation time (see the *uv*-coverage in Figure 3.29). Anyhow, the structure of the inner jet is clearly observable (Figure 3.28). The components C9 and C8 seem to be merged into one.

The visibilities were modeled with elliptical Gaussians. The model shows clearly the core and the three inner jet features C9, C8 and C7 (Figure 3.30). C9 is the brightest with a flux density of 3.04 Jy. Component C8 is close to C9 and weaker with 1.21 Jy. The short distance and the large difference in flux-density result in a single, large component in the map. The outer jet is modeled with 4 components for C5, C4, C3 and C2 as in the previous epochs. For a better comparison between the different epochs, circular Gaussians are used for C4 and C5. The model for the core and the 7 jet components yields $\chi^2 = 1.2$.

Name	S [Jy]	r [mas]	Θ [°]	a [mas]	b/a	Φ [°]
D	1.80±0.03	0	0	0.42±0.01	0.54±0.02	82.6±0.5
C9	3.04±0.03	0.82±0.02	-105.3±0.5	0.55±0.01	0.81±0.05	51±4
C8	1.21±0.03	1.38±0.02	-89.4±0.5	0.59±0.01	0.65±0.05	-85±2
C7	0.86±0.05	2.60±0.02	-95.7±0.5	1.06±0.04	0.61±0.07	-63±4
C5	0.16±0.05	5.20±0.10	-78.0±2.0	1.30±0.10	1	0
C4	0.45±0.05	7.30±0.20	-67.1±2.0	2.70±0.20	1	0
C3	0.19±0.05	11.19±1.00	-75.1±2.0	5.03±0.20	0.80±0.10	-88±7
C1	0.15±0.05	19.06±1.50	-53.8±5.0	6.21±0.50	0.72±0.10	-81±5

Table 3.10: Model fit components for epoch 1999.50 (July 2, 1999)

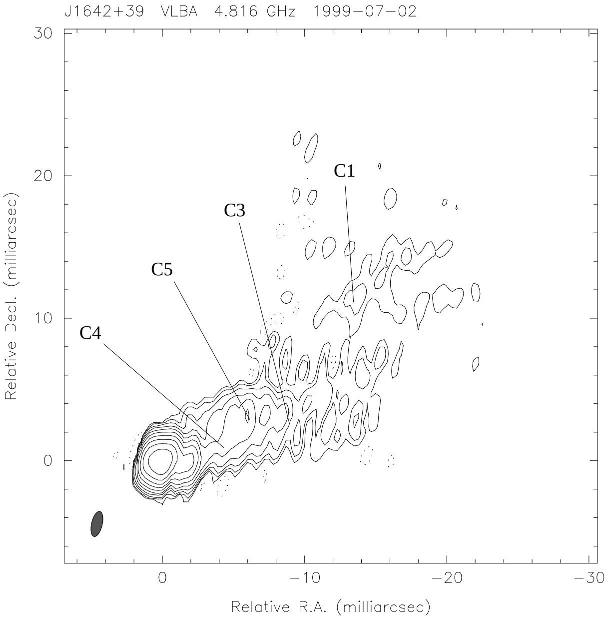

Maximum: 3.208 JY/BEAM
Contours (%): −.10 .10 .20 .40 .80 1.60 3.20 6.40 12.80 25.60
Contours (%): 51.20
Beam: FWHM 1.80 × .76 milliarcsec, p.a. −13.2°

Figure 3.27: 5 GHz ground image of 3C 345 on July 2, 1999 (1999.50). The core is centred at position zero. The jet shows a curved structure and become resolved at $r \approx 12$ mas core distance.

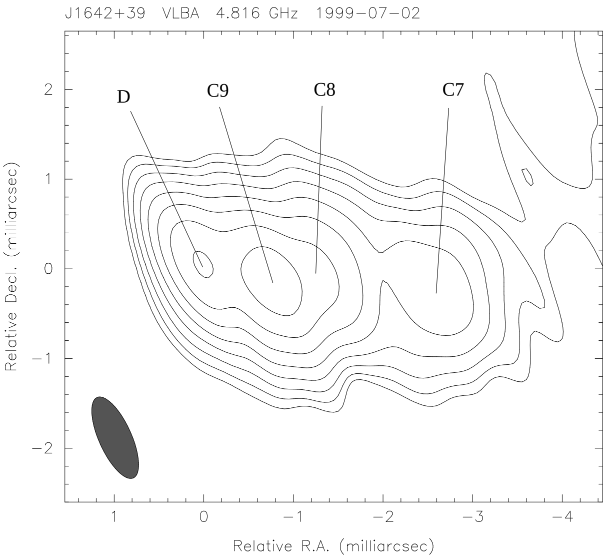

Maximum: 1.811 JY/BEAM
Contours (%): .50 1.00 2.00 4.00 8.00 16.00 32.00 64.00
Beam: FWHM .98 × .36 milliarcsec, p.a. 24.3°

Figure 3.28: 5 GHz VSOP image from 3C 345 on July 2, 1999 (1999.50). The core lies at position zero and the jet component C8 is weaker than C9.

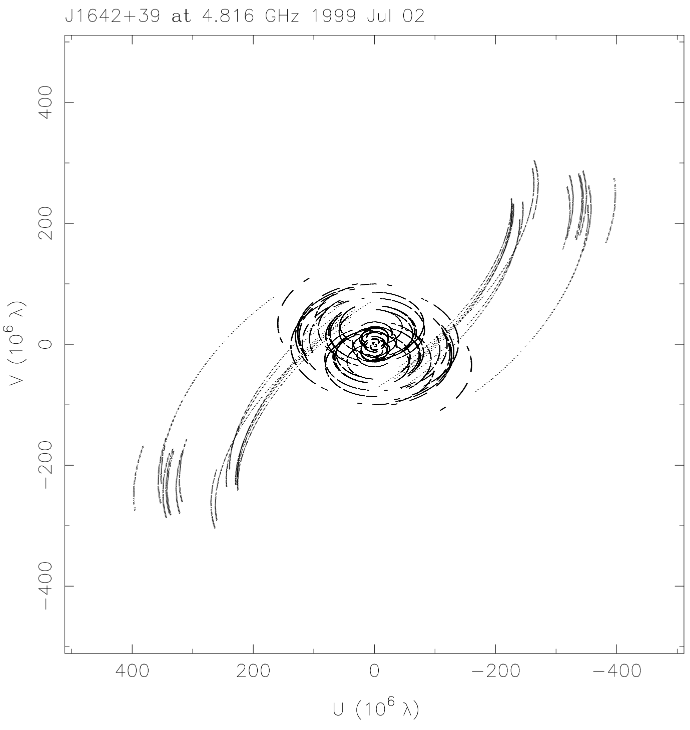

Figure 3.29: *uv*-coverage of the 5 GHz observation of 3C 345 on July 2, 1999 (1999.50). The long curves are the projected ground-space baselines.

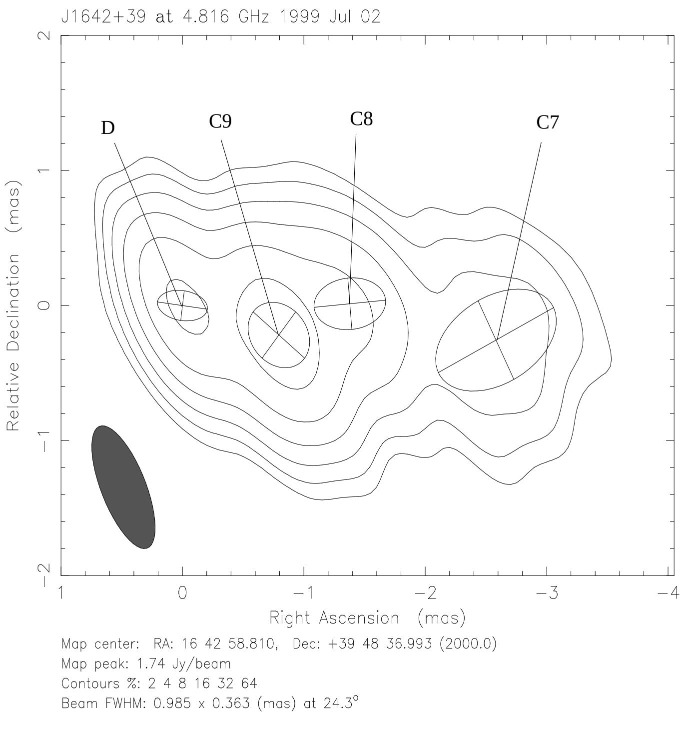

Figure 3.30: Model fit of the inner part of the pc-scale jet in 3C 345 on July 2, 1999 (1999.50) with $\chi^2 = 1.2$. The components C9, C8 and C7 can be clearly identified.

3.4.4 September 10, 1999 (1999.69)

The three tracking stations Goldstone, Tidbinbilla and Robledo provided good data, yielding space observing time of 72% of the ground array observing time.

The ground image (Figure 3.31) shows a curved jet similar to the previous epochs. The VSOP image (Figure 3.32) shows clearly the core, C9 and a weak C8 at P.A.≈ 15° with respect to C9. C7 is more extended and lies at $r = 2.69$ mas, P.A.≈ −96°.

The model fit (Figure 3.34) shows an expanded component C8 to the north-west of C9. The size of C8 is limited to prevent overlap with C9. The best fit for C8 is obtained with a major axis of 0.6 mas and an axial ratio of 0.7, P.A.≈ −55°. The component C9 is the brightest feature with $S = 2.7$ Jy. Between the core and C9 a new component C10 is discovered at a core distance of 0.48 mas. A circular shape for C10 is needed to get a stable model. The flux density of C10 (1.13 Jy) is about half the flux density of the core. The outer flux was modelled again with two circular Gaussians (C5 and C4) and two elongated Gaussians, representing C3 and C1. This model gives to $\chi^2 = 1.7$.

Name	S [Jy]	r [mas]	Θ [°]	a [mas]	b/a	Φ [°]
D	2.17±0.04	0	0	0.19±0.01	0.60±0.02	-76.9±0.5
C10	1.13±0.04	0.48±0.02	-102.2±0.5	0.32±0.01	1	0
C9	2.75±0.03	0.98±0.02	-103.3±0.5	0.43±0.01	0.71±0.05	6±4
C8	1.24±0.03	1.49±0.02	-88.4±0.5	0.6	0.7	-55±2
C7	0.87±0.05	2.69±0.05	-95.9±0.5	1.02±0.04	0.57±0.07	-53±4
C5	0.30±0.05	5.30±0.50	-74.0±2.0	2.20±0.10	1	0
C4	0.40±0.05	7.80±1.00	-68.5±2.0	2.60±0.20	1	0
C3	0.19±0.05	11.34±1.20	-74.5±2.0	8.19±0.20	0.28±0.10	-66±8
C1	0.28±0.05	21.23±2.00	-56.3±3.0	13.25±0.50	0.71±0.10	-60±10

Table 3.11: Model fit components for epoch 1999.69 (September 10, 1999).

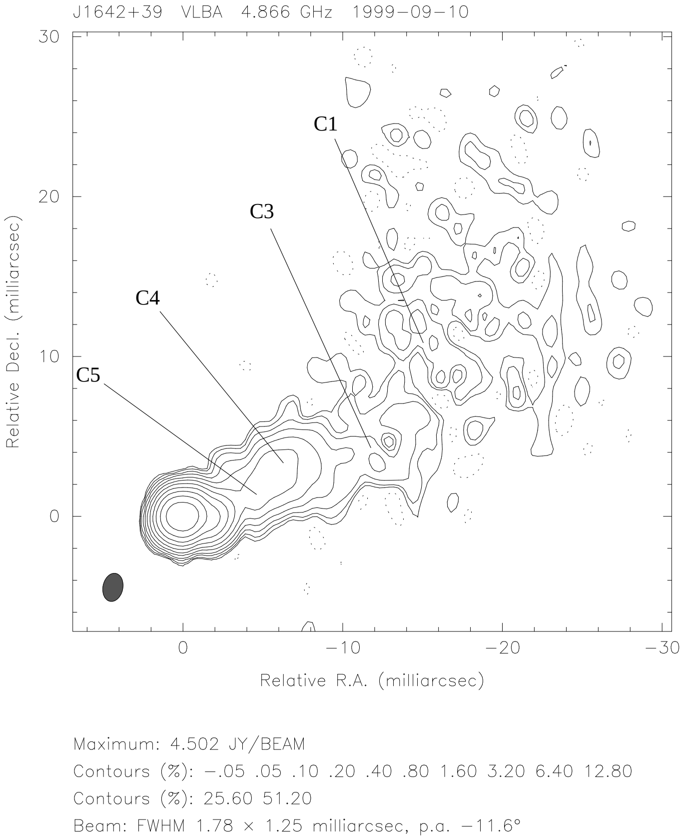

Figure 3.31: 5 GHz ground map of 3C 345 on September 10, 1999 (1999.69). The core is centred at position zero and the jet extends to the north-west.

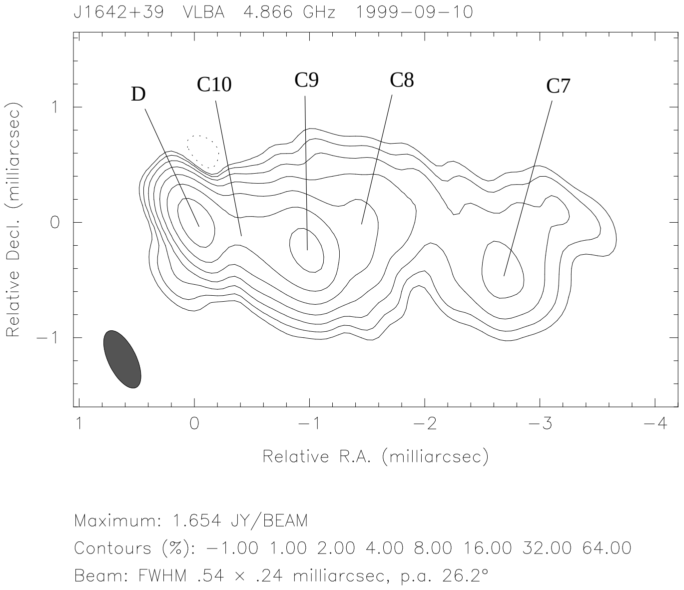

Figure 3.32: 5 GHz VSOP map of 3C 345 on September 10, 1999 (1999.69). Between the core and C9 the ejection of a new component C10 is seen as a bright bridge. C8 became more expanded and moved slightly to the north-west.

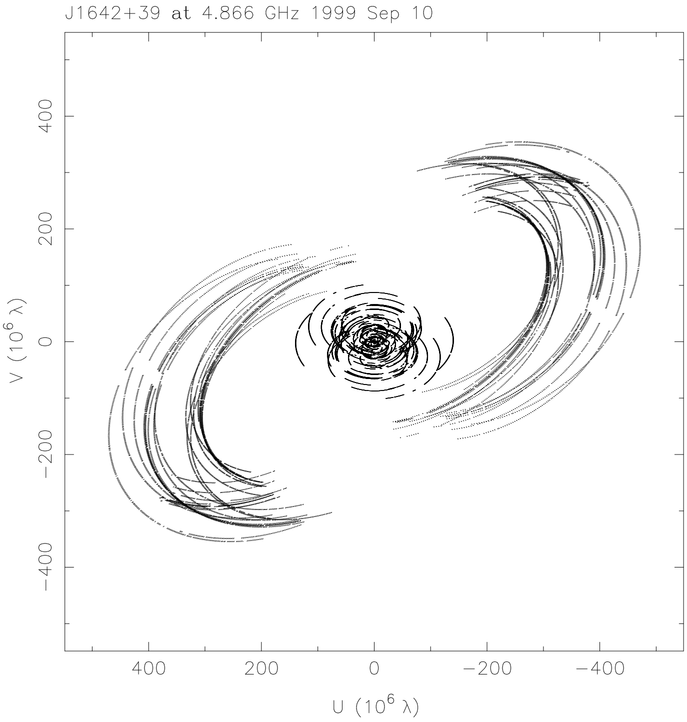

Figure 3.33: *uv*-coverage of the 5 GHz VSOP observation of 3C 345 on September 10, 1999 (1999.69). The elongated tracks are the projected ground-space baselines.

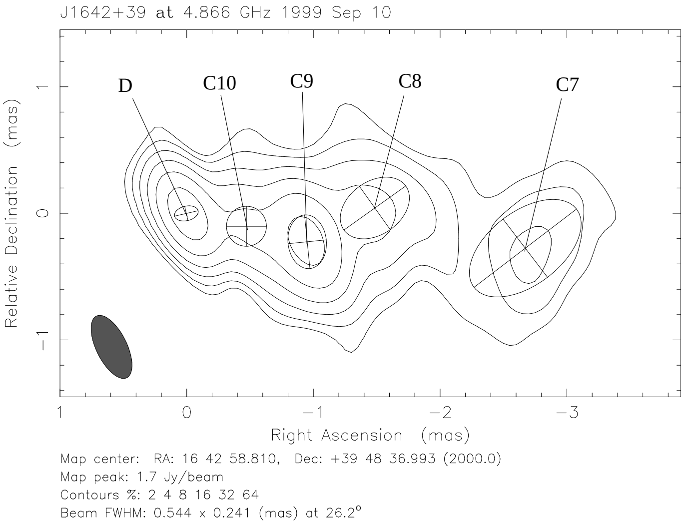

Figure 3.34: Model fit of 3C 345 on September 10, 1999 (1999.69) with $\chi^2 = 1.7$. A new jet component C10 is visible between the core and C9.

3.4.5 Summary

Four VSOP observations of 3C 345 at 5 GHz, made within a time period of about 18 months between March 21, 1998 and September 10, 1999 were presented in this chapter. The ground-space baselines which were more than three times larger than the ground-ground baselines, lead to a threefold improvement in resolution, which allowed the innermost jet region to be resolved into several components. These components appear blended in the ground VLBI images. Within the time span of these observations, two new jet components (C9 and C10) were detected for the first time at 5 GHz. This allowed the jet features in the immediate vicinity of the core to be studied, which is not possible at 5 GHz with ground VLBI observations. The resolution of these VSOP observations is comparable with the 22 GHz VLBA observations presented in section 3.5. This made it possible to produce high resolution spectral index maps between 5 and 22 GHz (section 6.3). A stacked arrangement of the VSOP images shows the evolution of the inner jet region during about 18 months (Figure 3.35).

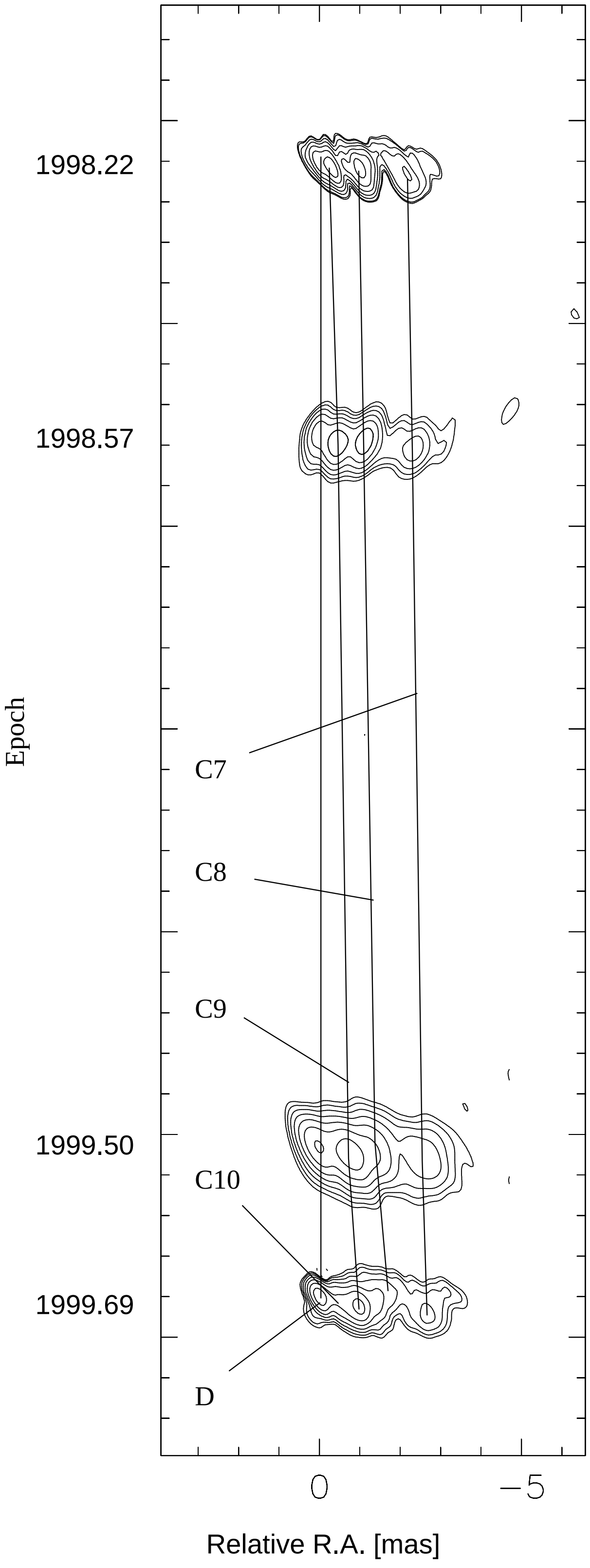

Figure 3.35: Stacked 5 GHz VSOP CLEAN maps. The straight lines connect the detected jet components at different epochs.

Ground Array Observing and Map Parameters of 3C 345 at 5 GHz

Epoch	Ground Telescopes	t_{tot} [h]	bas_g [Mλ]	$\Delta\nu$ [MHz]	bg_{maj} [mas]	bg_{min} [mas]	Φg [°]	S_{tot} [Jy]	S_{peak} [Jy]	C_{low} [mJy]	rms [mJy]	dr
1998.22	VLBA, EB	16	166	26.50	1.61	1.04	-11.4	8.4	3.87	3.8	3	1:1290
1998.57	VLBA, EB, phVLA	14	166	27.25	1.72	0.994	-14.7	8.5	3.58	3.6	1.5	1:2387
1999.50	VLBA, EB	10	130	26.50	1.80	0.756	-13.2	8.9	3.21	3.2	2	1:1605
1999.69	VLBA, phVLA	13	140	26.50	1.78	1.25	-11.6	9.3	4.5	4.5	3	1:1500

Table 3.12: t_{tot} - total observing time; bas_g - longest projected ground-ground baseline; $\Delta\nu$ - remaining bandwidth after flagging of channels; bg_{maj} - beam major axis; bg_{min} - beam minor axis; Φg - angle of the beam major axis; S_{tot} - total flux density; S_{peak} - peak flux density; C_{low} - lowest map contour; rms - root-mean-square of the map noise; dr - dynamic range; EB - Effelsberg; phVLA - phased VLA

VSOP Observing and Map Parameters of 3C 345 at 5 GHz

Epoch	t_{VSOP} [h]	bas_{vs} [Mλ]	bas_{vl} [Mλ]	bv_{maj} [mas]	bv_{min} [mas]	Φv [°]	S_{peak} [Jy]	C_{low} [mJy]	rms [mJy]	dr
1998.22	9.5	166	545	0.574	0.217	25.8	1.51	15.1	9	1:168
1998.57	10.0	130	510	0.692	0.332	-18.9	1.48	14.8	7	1:211
1999.50	2.3	60	480	0.985	0.363	24.3	1.82	18.2	11	1:165
1999.69	9.3	123	517	0.543	0.242	26.2	1.65	16.5	8	1:206

Table 3.13: t_{VSOP} - VSOP observing time; bas_{vs} - shortest projected ground-space baseline; bas_{vl} - longest projected ground-space baseline; bv_{maj} - beam major axis; bv_{min} - beam minor axis; Φv - angle of the beam major axis; S_{peak} - peak flux density; C_{low} - lowest map contour; rms - root-mean-square of the map noise; dr - dynamic range

3.5 VLBA Imaging at 22 GHz

Seven VLBA observations of 3C 345 at 22 GHz made during a time range of 27 months between May 26, 1997 and August 23, 1999 are presented in this section. These images show the inner 3 mas of the jet. At larger distances (3 – 10 mas), the radio emission is already resolved. For four epochs it was possible to image this region with a tapered map, which is shown in a separate image. The tapered maps are down-weighted for the longer baselines with a Gaussian function. Observing and map parameters can be found in Table 3.23. All inner jet components were preferentially modeled with circular Gaussians, in order to achieve consistency of the models. The legends of the model fit Tables (shown in each sub-section) are as follows: S - component flux density; r - component distance relative to the core; Θ - component position angle; a - component major axis; b/a - component axial ratio; Φ - component major axis position angle

3.5.1 May 26, 1997 (1997.40)

The VLBA image (Figure 3.36 right) shows a very well collimated jet within the inner 3 mas. While C7 has already become elongated, C8 is still unresolved. The clear identification of the components C9 and C10 is only possible with the model fit technique. In the CLEAN map both appear as one elongated feature to the south-west of the core. This is the first detection of C10 at 22 GHz. C4 is already completely resolved, but it is well recognizable in the tapered map (Figure 3.36 left). For this, the long baselines are down-weighted with a Gaussian taper function of 0.5 at 100 Mλ. The core dominates the VLBI scale emission with 1.75 Jy. The C10–C8 complex shows a rise from 0.77 to 1.21 Jy. All three components are located in the south-west direction at position angles between $-100°$ and $-119°$. C7 has the lowest flux density of the innermost jet components with 0.64 Jy. All parameters of the model fits are given in Table 3.14.

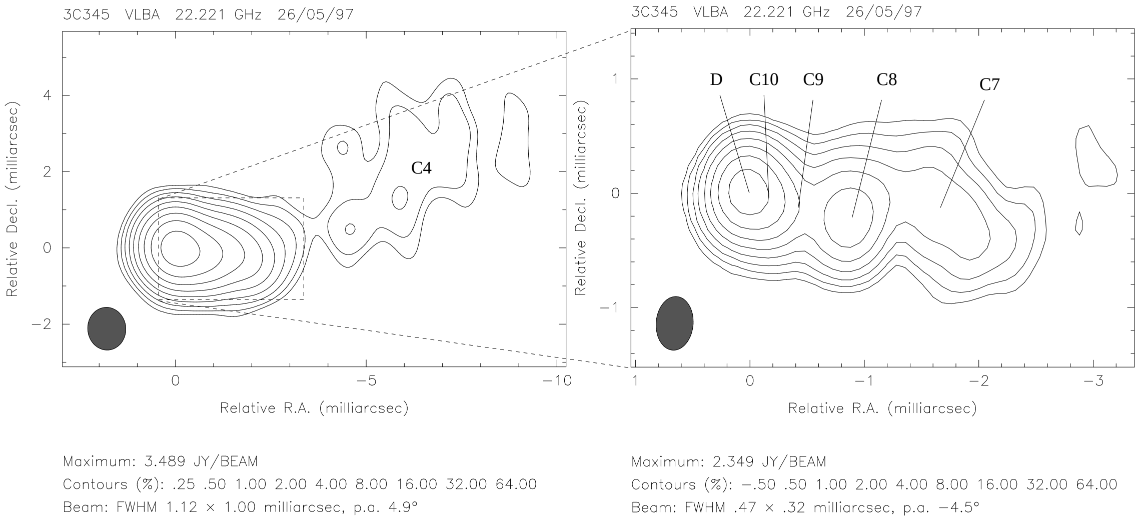

Figure 3.36: 22 GHz image of 3C 345 on May 26, 1997 (1997.40). Left: The jet feature C4 is identified in the tapered map. Right: The inner jet is formed by the components C10, C9, C8 and C7. This is the first detection of C10 at 22 GHz.

Name	S [Jy]	r [mas]	Θ [°]	a [mas]	b/a	Φ [°]
D	1.75 ±0.30	0	0	0.10 ± 0.02	1	0
C10	0.77 ±0.30	0.14 ±0.02	-100.2 ±7.0	0.05 ± 0.02	1	0
C9	0.92 ±0.05	0.32 ±0.02	-118.6 ±3.0	0.21 ± 0.10	1	0
C8	1.21 ±0.10	0.98 ±0.03	-104.6 ±3.0	0.34 ± 0.10	1	0
C7	0.64 ±0.10	1.88 ±0.10	-96.7 ±4.0	0.73 ± 0.20	1	0
C4	0.31 ±0.10	6.54 ±0.70	-70.7 ±10.0	3.51 ± 0.70	1	0

Table 3.14: Model fit components for epoch 1997.40 (May 26, 1997).

3.5.2 August 15, 1997 (1997.62)

This map (Figure 3.37 right) looks very similar to the previous one. The inner jet components C10, C9, C8 and C7 are well localized by model fitting. C4 is clearly visible in the tapered image (Figure 3.37 left) and is modeled with a circular Gaussian. For the tapered map, the long baselines are down-weighted with a Gaussian taper function of 0.5 at 100 Mλ. The flux density of C10 has increased compared to the epoch 1997.40 while the core has dimmed. Both have almost the same flux density of ≈ 1.2 Jy. The flux densities of C9, C8, C7 and C4 have changed slightly. The P.A. of C10 shows an 18° "jump" to the north. The other components show only slight changes in position angle. A detailed overview of the model parameters is given in Table 3.15.

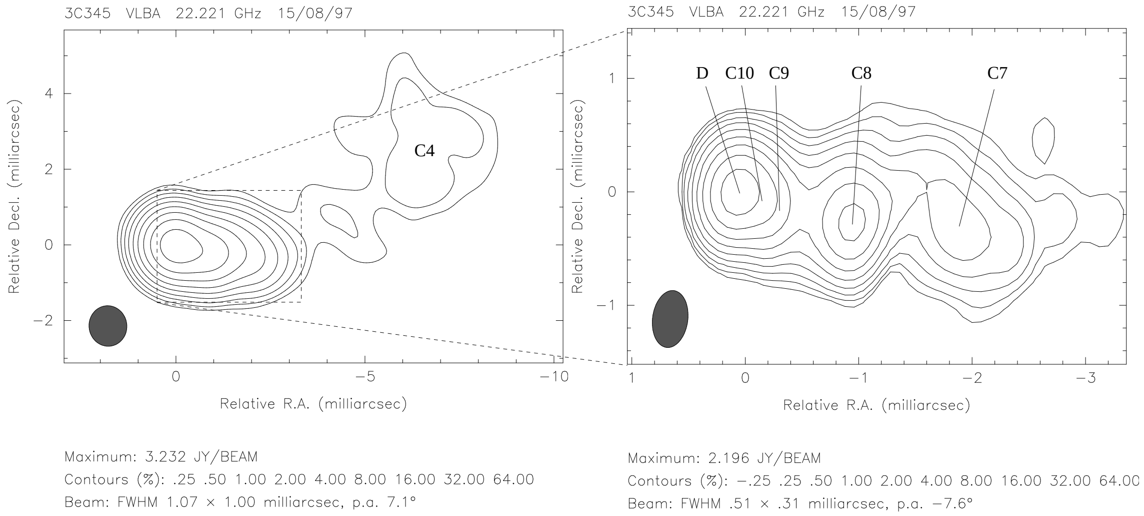

Figure 3.37: 22 GHz image of 3C 345 on August 15, 1997 (1997.62). Left: The jet feature C4 is seen in the tapered map at a core distance of 6.74 mas (P.A.$\approx -68°$). Right: The inner well collimated jet consists of the components C10–C7.

Name	S [Jy]	r [mas]	Θ [°]	a [mas]	b/a	Φ [°]
D	1.20 ±0.30	0	0	0.05 ± 0.02	1	0
C10	1.18 ±0.20	0.14 ±0.02	-82.3 ± 7.0	0.05 ± 0.02	1	0
C9	0.97 ±0.05	0.38 ±0.02	-110.0 ± 2.0	0.25 ± 0.10	1	0
C8	1.37 ±0.10	1.11 ±0.03	-103.7 ± 2.0	0.28 ± 0.10	1	0
C7	0.59 ±0.07	2.03 ±0.10	-96.8 ± 3.0	0.79 ± 0.20	1	0
C4	0.27 ±0.10	6.74 ±0.70	-67.8 ± 11.6	2.92 ± 0.90	1	0

Table 3.15: Model fit components for epoch 1997.62 (August 15, 1997).

3.5.3 November 11, 1997 (1997.90)

Although the observation at epoch 1997.90 lasted only ~ 0.2 hours (see Table 3.23), all inner jet features are clearly seen (Figure 3.38 right). C9 is now clearly separated from C10. The accuracy of the P.A. of C10 is still influenced by its closeness to the core. The extended jet feature C4 is almost completely resolved but still detectable in the tapered map (Figure 3.38 left) and could be modeled with a circular Gaussian. The long baselines are down-weighted in this map by a Gaussian taper function of 0.5 at 50 Mλ. The flux density changes of the core and C10–C8 are below 8% in contrast to the previous epoch. The model for this epoch is presented in Table 3.16.

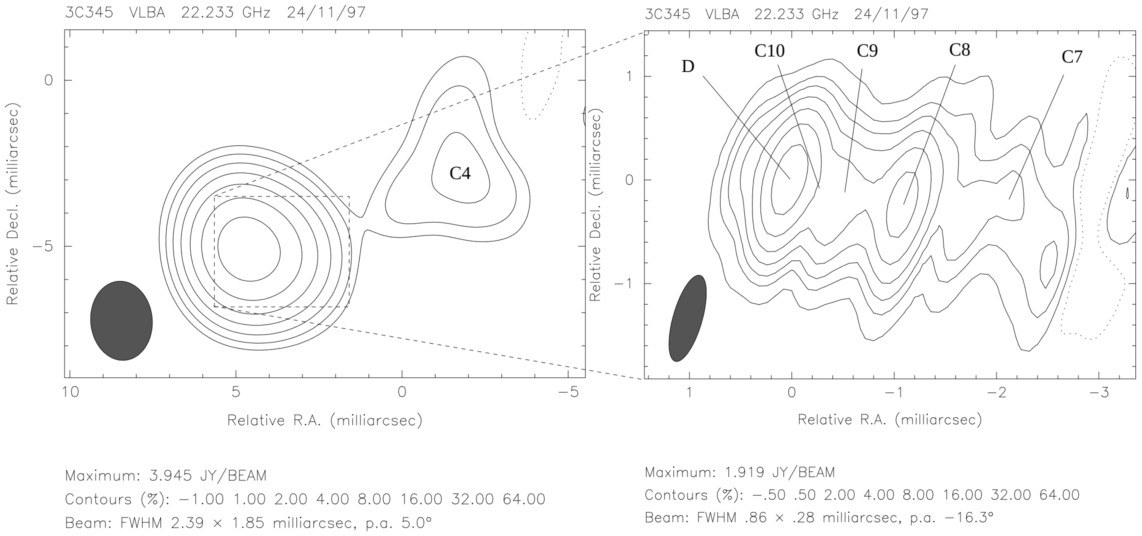

Figure 3.38: 22 GHz image of 3C 345 on November 11, 1997 (1997.90). Due to short observing time, the image quality is somewhat worse than that of the previous epochs. Nevertheless, the inner jet features C10–C7 (right image) and the extended component C4 (tapered left image) are clearly detectable.

Name	S [Jy]	r [mas]	Θ [°]	a [mas]	b/a	Φ [°]
D	1.11 ±0.30	0	0	0.05 ± 0.02	1	0
C10	1.13 ±0.30	0.14 ±0.02	-95.3 ±7.0	0.05 ± 0.02	1	0
C9	1.03 ±0.05	0.47 ±0.02	-110.8 ±2.0	0.37 ± 0.10	1	0
C8	1.31 ±0.10	1.21 ±0.03	-103.0 ±2.0	0.27 ± 0.10	1	0
C7	0.47 ±0.07	2.12 ±0.10	-98.0 ±3.0	0.78 ± 0.20	1	0
C4	0.34 ±0.10	5.97 ±0.90	-68.8 ±15.0	3.39 ± 1.30	1	0

Table 3.16: Model fit components for epoch 1997.90 (November 11, 1997).

3.5.4 January 08, 1998 (1998.02)

The image of epoch 1998.02 (Figure 3.39 right) shows the strongly collimated inner jet with the features C10–C7. The outer component C4 is resolved but still seen in the tapered image (Figure 3.39 left) and can be modeled by an elliptical Gaussian component. The long baselines are down-weighted in this map by a Gaussian taper function of 0.5 at 45 Mλ. The core flux density is about halved (0.53 Jy), compared with the previous epoch, while the flux density of C10 reaches 1.60 Jy. C9 follows its trend with a slight increase of its flux density, resulting at this epoch in 1.14 Jy. C8 has passed its maximum and it is now weaker by 0.18 Jy than in November 1997. Model fit parameters are given in Table 3.17.

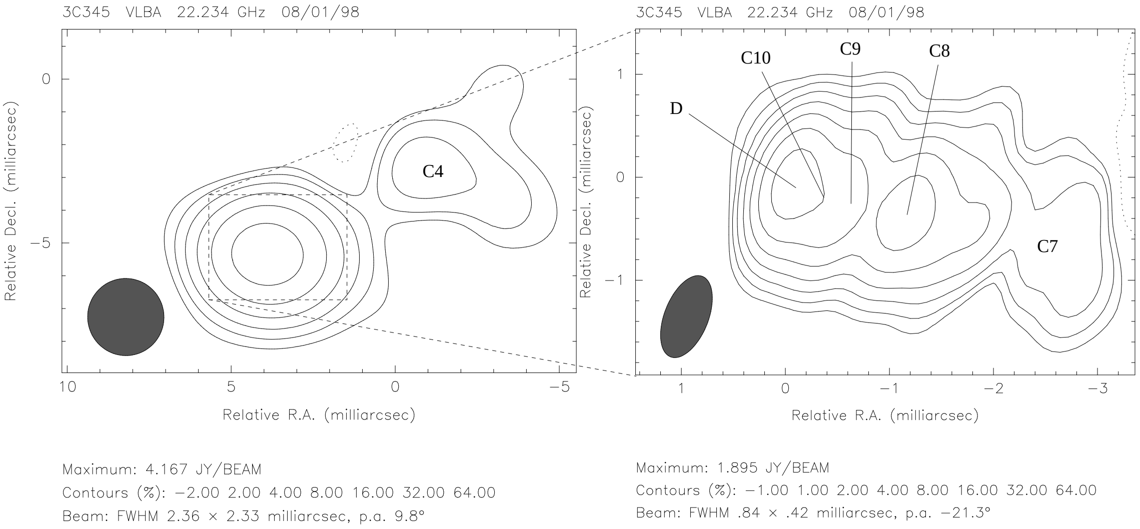

Figure 3.39: 22 GHz image of 3C 345 on January 08, 1998 (1998.02). Left: The extended jet feature C4 can be identified in the tapered image. Right: The inner jet is well defined by the jet features C10–C7.

Name	S [Jy]	r [mas]	Θ [°]	a [mas]	b/a	Φ [°]
D	0.53 ±0.30	0	0	0.05±0.02	1	0
C10	1.60 ±0.30	0.15 ±0.02	-109.3 ±8.0	0.05±0.02	1	0
C9	1.14 ±0.05	0.55 ±0.02	-111.7 ±2.0	0.39±0.10	1	0
C8	1.13 ±0.10	1.30 ±0.04	-103.8 ±2.0	0.26±0.10	1	0
C7	0.47 ±0.08	2.04 ±0.25	-96.9 ±4.0	0.76±0.20	1	0
C4	0.43 ±0.10	7.77 ±0.70	-76.5 ±12.0	3.61±1.30	0.7±0.3	55±20

Table 3.17: Model fit components for epoch 1998.02 (January 08, 1998).

3.5.5 December 28, 1998 (1998.99)

The beam shape is affected, at this epoch, by the absence of the VLBA antenna St. Croix, which leads to a reduction of the longest baselines (Figure 3.40). The most spectacular change from the previous epoch is the enormous increase of the flux density of the core which has risen from 0.53 Jy in January 08, 1998 to 4.63 Jy. As known from the 43 GHz observations (see section 3.6.5 and 3.6.10), a new component C11 was ejected at this time but was not yet detectable at 22 GHz. The flux density of C10 has decreased from 1.60 to 0.80 Jy. C9 has kept its flux density, while C8 dropped. The extended jet emission is completely resolved and can no longer be identified as C4 in the CLEAN map. The parameters of the modeled jet features are listed in Table 3.18.

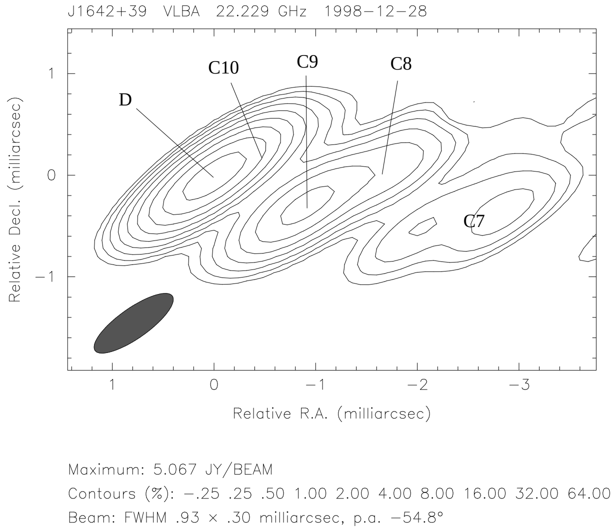

Figure 3.40: 22 GHz image of 3C 345 on December 28, 1998 (1998.99). The absence of the VLBA antenna St. Croix results in a different beam shape, in comparison with the other 22 GHz observations. The flux density is strongly dominated by the core. The jet component C8 has moved northward.

Name	S [Jy]	r [mas]	Θ [°]	a [mas]	b/a	Φ [°]
D	4.63 ±0.30	0	0	0.05±0.02	1	0
C10	0.80 ±0.10	0.29 ±0.02	-80.7 ±5.0	0.07±0.02	1	0
C9	1.03 ±0.05	0.87 ±0.02	-113.4 ±2.0	0.18±0.05	1	0
C8	0.60 ±0.10	1.47 ±0.05	-94.9 ±2.0	0.28±0.10	1	0
C7	0.50 ±0.10	2.63 ±0.20	-93.2 ±3.0	0.81±0.10	1	0

Table 3.18: Model fit components for epoch 1998.99 (December 28, 1998).

3.5.6 February 11, 1999 (1999.12)

The image of epoch 1999.12 (Figure 3.41) shows the strongly collimated inner jet with the components C10–C7. The core still dominates the flux density with $S \approx 4$ Jy, and the new jet feature C11 (seen at 43 GHz) is still undetectable. C10 is well separated from the core. Its flux density has further decreased to 0.47 Jy. Both C9 and C8 have increased slightly in flux density, while the flux density of C7 has dropped. The extended jet emission is completely resolved. The model fit parameters are listed in Table 3.19.

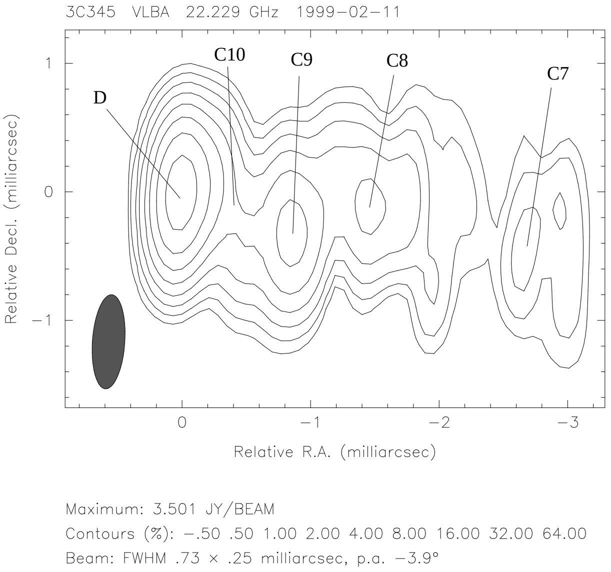

Figure 3.41: 22 GHz image of 3C 345 on February 11, 1999 (1999.12). The collimated inner jet region is well defined by the components C10–C7.

Name	S [Jy]	r [mas]	Θ [°]	a [mas]	b/a	Φ [°]
D	4.01 ±0.30	0	0	0.16±0.02	1	0
C10	0.47 ±0.30	0.27 ±0.03	-89.4 ±6.0	0.05±0.02	1	0
C9	1.33 ±0.05	0.90 ±0.02	-108.6 ±1.0	0.36±0.10	1	0
C8	0.71 ±0.10	1.53 ±0.08	-94.0 ±2.0	0.49±0.10	1	0
C7	0.28 ±0.10	2.71 ±0.20	-97.6 ±3.0	0.53±0.10	1	0

Table 3.19: Model fit components for epoch 1999.12 (February 11, 1999).

3.5.7 August 23, 1999 (1999.64)

The image of epoch 1999.64 (Figure 3.42) shows the strongly collimated inner jet with the features C10–C7. The jet emission is still dominated by the strong core flux density which has decreased slightly to $S = 3.60$ Jy. The new jet feature C11 is still undetectable at 22 GHz. The component C10 is clearly separated from the core. Its flux density is about the same as at the previous epoch. The flux densities of C9, C8 and C7 have decreased. The modelfit parameters are given in Table 3.20.

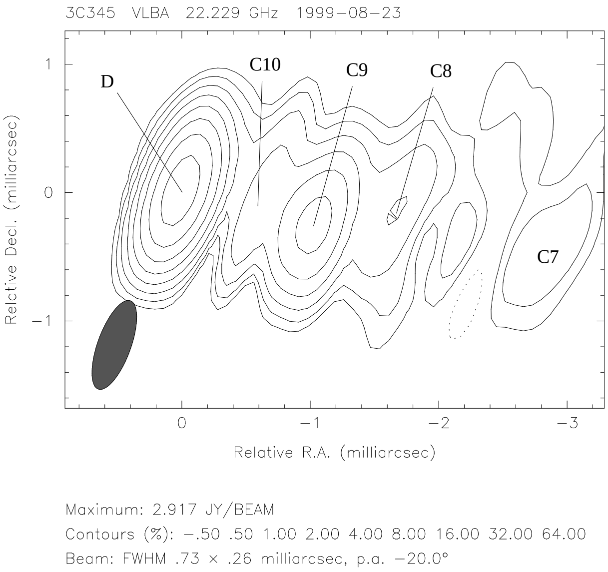

Figure 3.42: 22 GHz image of 3C 345 on August 23, 1999 (1999.64). The inner 3 mas of the jet are dominated by the components C10–C7. The innermost jet component C10 is clearly separated from the core.

Name	S [Jy]	r [mas]	Θ [°]	a [mas]	b/a	Φ [°]
D	3.60 ±0.30	0	0	0.20±0.05	1	0
C10	0.42 ±0.20	0.44 ±0.02	-92.9 ±2.0	0.47±0.10	1	0
C9	0.82 ±0.20	1.06 ±0.02	-105.2 ±2.0	0.25±0.05	1	0
C8	0.52 ±0.20	1.54 ±0.20	-91.9 ±2.0	0.69±0.10	1	0
C7	0.17 ±0.20	2.89 ±0.20	-96.8 ±3.0	0.56±0.20	1	0

Table 3.20: Model fit components for epoch 1999.64 (August 23, 1999).

3.5.8 Re-Modeled Data of Epochs 1996.41 and 1996.82

The epochs 1996.41 and 1996.82 from Ros *et al.* (2000), had to be re-modeled by Gaussian components, in order to achieve consistency with the other models of this section. They are presented in Table 3.21 and 3.22. Both observations were made before the other observations of this section.

Name	S [Jy]	r [mas]	Θ [°]	a [mas]	b/a	Φ [°]
D	0.88 ±0.30	0	0	0.09±0.02	1	0
C9	1.20 ±0.05	0.14 ±0.02	-99.5 ±3.0	0.05±0.02	1	0
C8	1.26 ±0.15	0.58 ±0.03	-115.2 ±3.0	0.25±0.05	1	0
C7	0.90 ±0.10	1.45 ±0.20	-93.6 ±2.0	0.47±0.10	1	0
C5	0.07 ±0.03	4.37 ±0.50	-82.5 ±5.0	1.93±1.00	1	0
C4	0.18 ±0.04	6.58 ±0.50	-70.0 ±3.0	2.50±1.50	1	0

Table 3.21: Model fit components for epoch 1996.41 (May 31, 1996) from the data published in Ros *et al.* (2000).

Name	S [Jy]	r [mas]	Θ [°]	a [mas]	b/a	Φ [°]
D	1.42 ±0.30	0	0	0.11±0.02	1	0
C9	1.19 ±0.05	0.17 ±0.02	-107.1 ±3.0	0.05±0.02	1	0
C8	1.12 ±0.10	0.71 ±0.03	-109.3 ±2.0	0.39±0.10	0.7± 0.1	-63±5
C7	0.71 ±0.10	1.56 ±0.20	-94.4 ±2.0	0.70±0.10	0.5± 0.2	58±8
C4	0.23 ±0.04	6.47 ±0.50	-68.6 ±5.0	3.34±1.40	1	0

Table 3.22: Model fit components for epoch 1996.82 (October 25, 1996) from the data published in Ros *et al.* (2000).

3.5.9 Summary

Seven images and model fits from our ongoing monitoring program at 22 GHz were presented in this section. A new jet component C10 was identified and the inner parsec-scale jet was modeled with 4 jet components C7, C8, C9 and C10. The emission at larger scales can be represented at four epochs by one Gaussian and identified with the jet feature C4. These observations sample an evolution of the jet components in kinematics and flux density at sub-mas scales. The change of the jet morphology can be seen in the stacked image of all CLEAN maps obtained (Figure 3.43). The straight lines connect the jet components identified at different epochs. The motion of the features is obvious.

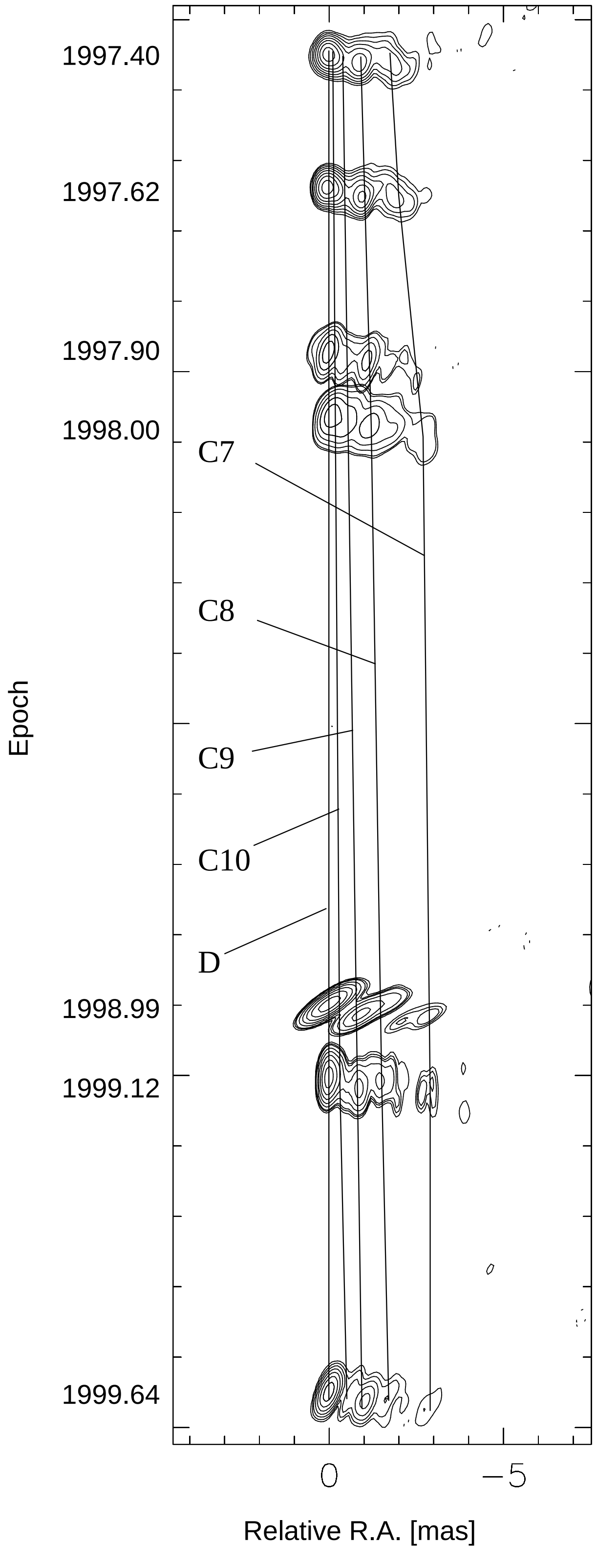

Figure 3.43: Stacked image of the 22 GHz CLEAN maps. The straight lines connect the detected jet components at different epochs.

Observing and Map Parameters of 3C 345 at 22 GHz												
Epoch	Telescopes	t_{tot} [h]	bas [Mλ]	$\Delta\nu$ [MHz]	b_{maj} [mas]	b_{min} [mas]	Φ [°]	S_{tot} [Jy]	S_{peak} [Jy]	C_{low} [mJy]	rms [mJy]	dr
1997.40	VLBA	1.10	636	32	0.470	0.323	-4.5	5.6	2.35	11.7	5	1:470
1997.62	VLBA (without FD)	0.90	638	32	0.505	0.311	-7.6	5.5	2.20	5.5	6	1:367
1997.90	VLBA (without HN)	0.17	635	8	0.864	0.284	-16.3	5.1	1.92	9.6	4	1:480
1998.00	VLBA	0.33	516	3.6	0.840	0.423	-21.3	5.5	1.90	19.0	10	1:190
1998.99	VLBA (without OV and SC)	0.47	499	14	0.931	0.298	-54.8	7.4	5.07	12.7	4	1:1268
1999.12	VLBA	3.00	638	16	0.734	0.252	-3.9	6.6	3.50	17.5	9	1:389
1999.64	VLBA	2.75	637	14	0.732	0.256	-20.0	5.3	2.92	14.6	10	1:292

Table 3.3: t_{tot} - total observing time; bas - longest projected baseline; $\Delta\nu$ - remaining bandwidth after flagging channels; b_{maj} - beam major axis; b_{min} - beam minor axis; Φ - angle of the beam major axis; S_{tot} - total flux density; S_{peak} - peak flux density; C_{low} - lowest map contour; rms - root-mean-square of the map noise; dr - dynamic range; VLBA stations: MK - Mauna Kea; OV - Owens Valley; KP - Kitt Peak; BR - Brewster; PT - Pie Town; FD - Fort Davis; LA - Los Alamos; NL - North Liberty; HN - Hancock; SC - St. Croix

3.6 VLBA Imaging at 43 GHz

Nine VLBA observations at 43 GHz made during a 27 month period between May 26, 1997 and August 23, 1999 are presented in this section. The images show the inner 3 mas of the jet. Observing and map parameters can be found in Table 3.38. The legends of the model fit parameters (presented in each sub-section) are as follows: S - component flux density; r - component distance relative to the core; Θ - component position angle; a - component major axis; b/a - component axial ratio; Φ - component major axis position angle

3.6.1 May 26, 1997 (1997.40)

The VLBA image (Figure 3.44) shows a detailed view of the inner 3 mas of the jet. The core and the innermost jet component C10 are clearly distinguishable by model fitting. The core has the highest flux density ($S = 1.03$ Jy) followed by C10 with $S = 0.85$ Jy. The jet feature C9 is still unresolved and lies at P.A.$\approx -114°$ with about half of the flux density of C10. C8 appears as a big blob at a core distance of 1.04 mas, slightly brighter than C9. The faintest component C7 is already elongated, and has a flux density of 0.29 Jy. A summary of the model fit parameters is given in Table 3.24.

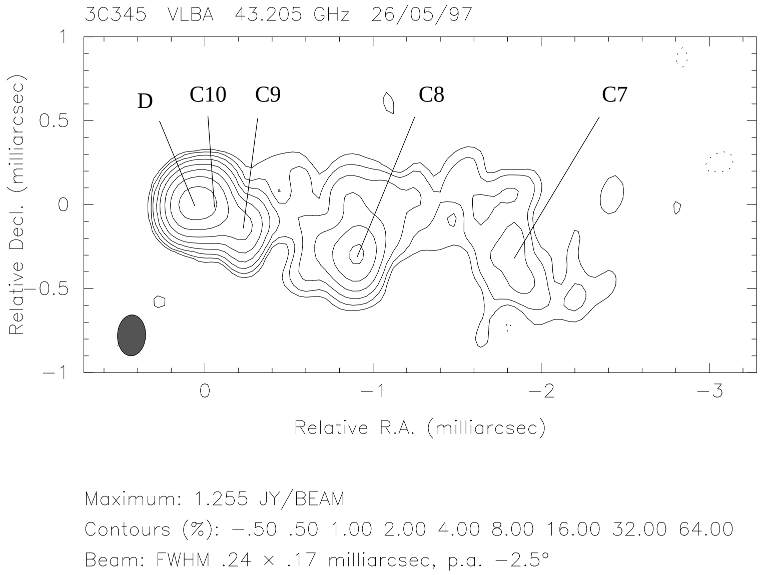

Figure 3.44: 43 GHz image of 3C 345 on May 26, 1997 (1997.40). The innermost jet region contains the components C10, C9, C8 and C7.

Name	S [Jy]	r [mas]	Θ [°]	a [mas]	b/a	Φ [°]
D	1.03 ±0.20	0	0	0.07±0.01	1	0
C10	0.85 ±0.05	0.13 ±0.02	-84.6 ±1.5	0.05±0.01	1	0
C9	0.43 ±0.02	0.34 ±0.02	-113.7 ±1.5	0.16±0.01	1	0
C8	0.51 ±0.10	1.04 ±0.03	-105.6 ±3.0	0.23±0.02	1	0
C7	0.29 ±0.10	1.81 ±0.10	-94.9 ±4.0	0.62±0.36	1	0

Table 3.24: Model fit components for epoch 1997.40 (May 26, 1997).

3.6.2 August 15, 1997 (1997.62)

The CLEAN map (Figure 3.45) of the innermost jet region shows a curved jet structure in direction to the west. The flux density of the core increased in comparison with the previous epoch. C10 and C9 kept its level while C8 shows almost a twofold increase in flux density. C7 has an elongated shape, and the lowest flux density of 0.24 Jy. The model parameters of the jet components are listed in Table 3.25.

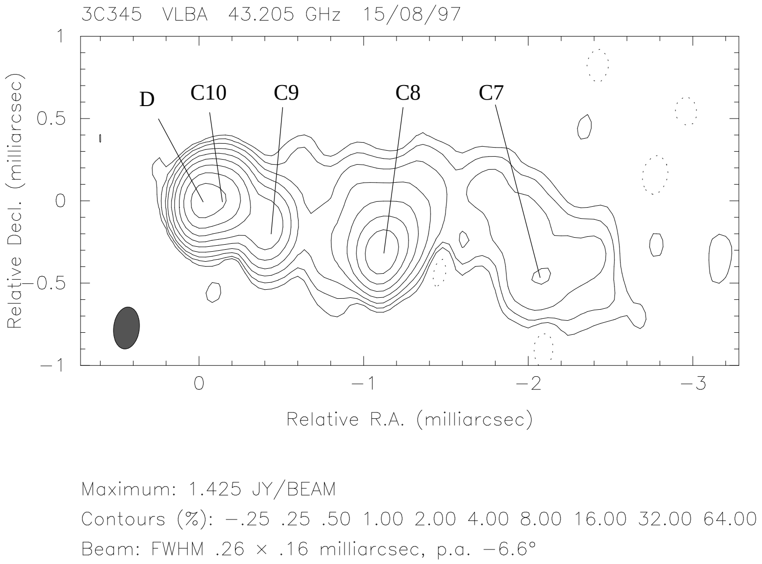

Figure 3.45: 43 GHz image of 3C 345 on August 15, 1997 (1997.62). The curved jet structure is well seen.

Name	S [Jy]	r [mas]	Θ [°]	a [mas]	b/a	Φ [°]
D	1.32 ±0.20	0	0	0.05±0.01	1	0
C10	0.95 ±0.05	0.15 ±0.02	-86.9 ±1.5	0.10±0.01	1	0
C9	0.37 ±0.02	0.41 ±0.02	-110.5 ±1.5	0.16±0.01	1	0
C8	0.93 ±0.10	1.13 ±0.03	-102.0 ±5.0	0.50±0.03	1	0
C7	0.24 ±0.10	2.08 ±0.10	-98.4 ±3.0	0.56±0.26	1	0

Table 3.25: Model fit components for epoch 1997.62 (August 15, 1997).

3.6.3 November 24, 1997 (1997.90)

At this epoch, a smaller bandwidth and shorter observing time (see Table 3.38) lead to reduced image quality (Figure 3.46), compared to the previous epochs. Nevertheless, the inner jet components are seen in the CLEAN image and could be modeled with circular Gaussians. The flux density of C10 dropped while it remained almost constant for the core within the errors. All jet component parameters are listed in Table 3.26.

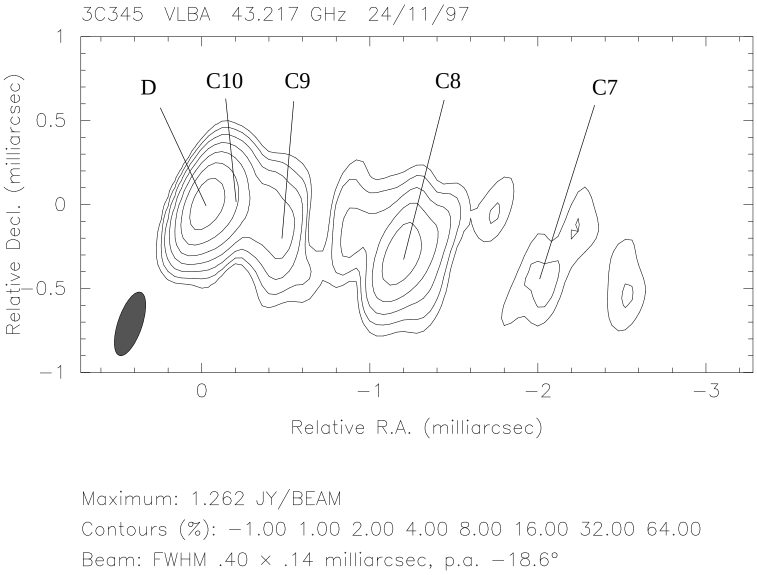

Figure 3.46: 43 GHz image of 3C 345 on November 24, 1997 (1997.90).

Name	S [Jy]	r [mas]	Θ [°]	a [mas]	b/a	Φ [°]
D	1.22 ±0.20	0	0	0.07±0.01	1	0
C10	0.62 ±0.05	0.15 ±0.02	-86.8 ±1.5	0.11±0.01	1	0
C9	0.28 ±0.02	0.50 ±0.02	-109.1 ±1.5	0.23±0.05	1	0
C8	0.56 ±0.10	1.21 ±0.03	-104.2 ±2.0	0.18±0.01	1	0
C7	0.30 ±0.10	1.85 ±0.10	-92.5 ±3.0	1.27±0.31	1	0

Table 3.26: Model fit components for epoch 1997.90 (November 24, 1997).

3.6.4 December 28, 1998 (1998.99)

This 43 GHz observation has the shortest observing time of only 10 min. Nevertheless, the core and the jet features C8 and C9 can be clearly identified in the CLEAN image (Figure 3.47), and all four components can be modeled with Gaussians. The biggest change compared with the last epoch is the rise in flux density of the core up to 3.05 Jy. This is also seen at the same epoch at 22 GHz which is a strong indication of the ejection of a new jet component. With a longer observation at epoch 1998.94 (Table 3.37) this new component C11 is already detectable. This implies that the identified core region at epoch 1998.99 is actually the blend of the true core and C11. The component C10 increased in flux density. The other components show slight variations. The parameters of the model fits are given in Table 3.27.

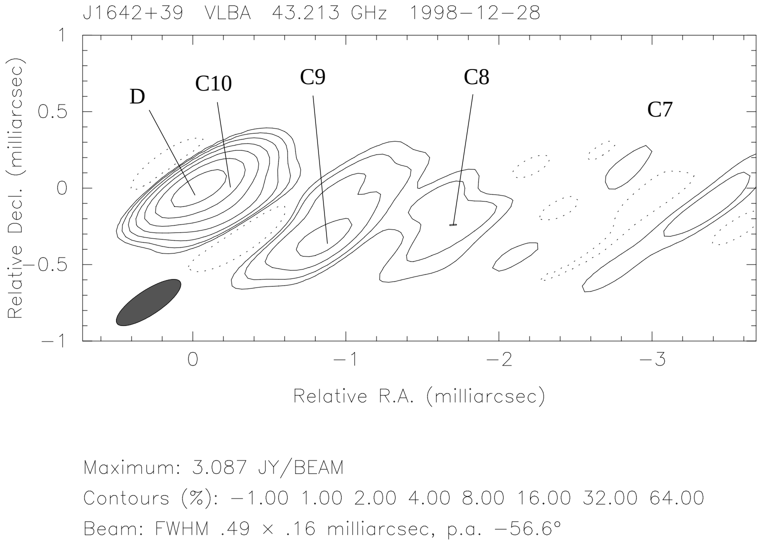

Figure 3.47: 43 GHz image of 3C 345 on December 28, 1998 (1998.99). The short observing time of only 10 min strongly influences the quality of the map. The core/C10-ellipse, C9 and C8 are clearly seen.

Name	S [Jy]	r [mas]	Θ [°]	a [mas]	b/a	Φ [°]
D+C11	3.05 ±0.20	0	0	0.05±0.01	1	0
C10	0.96 ±0.05	0.18 ±0.02	-87.3 ±1.5	0.08±0.01	1	0
C9	0.54 ±0.02	0.90 ±0.02	-111.8 ±1.5	0.33±0.03	0.6±0.1	73±2
C8	0.36 ±0.04	1.51 ±0.03	-93.3 ±2.0	0.44±0.11	1	0
C7	0.14 ±0.04	2.57 ±0.10	-96.2 ±2.0	0.45±0.18	1	0

Table 3.27: Model fit components for epoch 1998.99 (December 28, 1998).

3.6.5 February 11, 1999 (1999.12)

The much better data quality of this epoch (Figure 3.48) compared with the previous one made it possible to separate the core from a recently ejected jet component C11. The core distance of this jet feature is less than 0.1 mas which corresponds to about 0.38 pc ($q_0 = 0.5$, $H_0 = 100\mathrm{kms}^{-1}\mathrm{Mpc}^{-1}$). C10 drops in flux density to less than half compared with epoch 1998.99. The core has decreased in flux density from 3.05 Jy to 2.03 Jy (probably because of deblending of C11). C9, C8 and C7 are well modeled by Gaussian components. Their changes are small in flux density with regard to epoch 1998.99. A summary of the model parameters is given in Table 3.28.

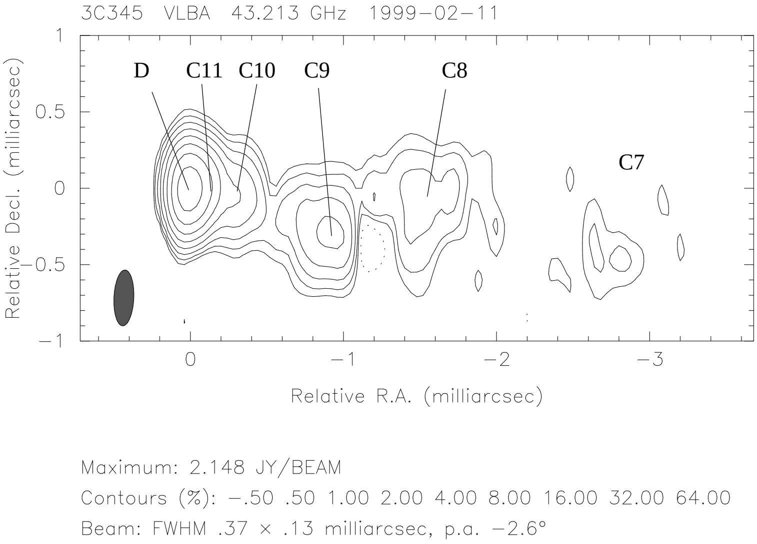

Figure 3.48: 43 GHz image of 3C 345 on February 11, 1999 (1999.12). The different jet features of the collimated jet are well seen. A new jet component C11 emerged at a core distance less than 0.1 mas.

Name	S [Jy]	r [mas]	Θ [°]	a [mas]	b/a	Φ [°]
D	2.03 ±0.30	0	0	0.08±0.01	1	0
C11	1.16 ±0.20	0.097 ±0.005	-87.3 ±1.0	0.10±0.01	1	0
C10	0.41 ±0.02	0.24 ±0.01	-84.7 ±1.0	0.19±0.01	1	0
C9	0.63 ±0.02	1.00 ±0.02	-108.5 ±1.3	0.33±0.04	0.8±0.1	-77±2
C8	0.32 ±0.04	1.63 ±0.05	-93.6 ±1.8	0.45±0.10	0.6±0.1	-61±3
C7	0.15 ±0.04	2.85 ±0.16	-99.5 ±3.3	0.63±0.33	1	0

Table 3.28: Model fit components for epoch 1999.12 (February 11, 1999).

3.6.6 March 11, 1999 (1999.19)

This VLBA observation shows a clear identification of the inner jet components C11–C7 (Figure 3.49). The core and C11 have increased in flux density by about 0.4 Jy. C10 is seen in the CLEAN map as an unresolved feature. The jet components C9 and C8 show slight variations in flux density while C7 is the weakest component with $S = 0.15$ Jy. All parameters of the modeled jet components can be found in Table 3.29.

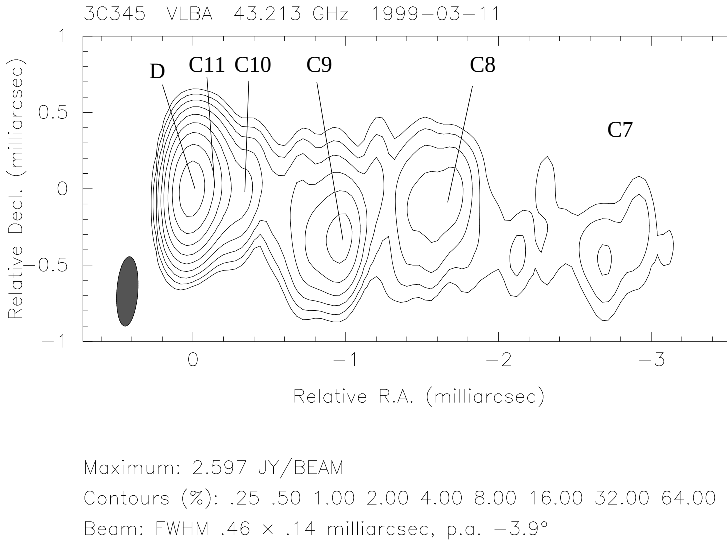

Figure 3.49: 43 GHz image of 3C 345 on March 11, 1999 (1999.19). The inner jet components C10–C7 are clearly seen. The innermost jet component C11 lies close to the core.

Name	S [Jy]	r [mas]	Θ [°]	a [mas]	b/a	Φ [°]
D	2.40 ±0.30	0	0	0.09±0.01	1	0
C11	1.51 ±0.20	0.091 ±0.005	-85.6 ±1.0	0.10±0.01	1	0
C10	0.39 ±0.05	0.26 ±0.01	-83.8 ±0.9	0.22±0.01	1	0
C9	0.72 ±0.02	1.05 ±0.03	-107.9 ±0.6	0.28±0.02	0.9±0.1	-7±2
C8	0.35 ±0.04	1.65 ±0.10	-93.0 ±1.2	0.47±0.07	0.7±0.1	-47±2
C7	0.15 ±0.04	2.88 ±0.20	-98.9 ±2.9	0.55±0.29	1	0

Table 3.29: Model fit components for epoch 1999.19 (March 11, 1999).

3.6.7 April 12, 1999 (1999.28)

The CLEAN map (Figure 3.50) shows a clear separation of the meanwhile expanded jet feature C10 which has decreased slightly in flux density. The innermost feature (C11) has increased in flux density to a value of 1.81 Jy while the core decreased. The outer, resolved components show small variations while C7 stayed at its previous flux density level. The model fit parameters are listed in Table 3.30.

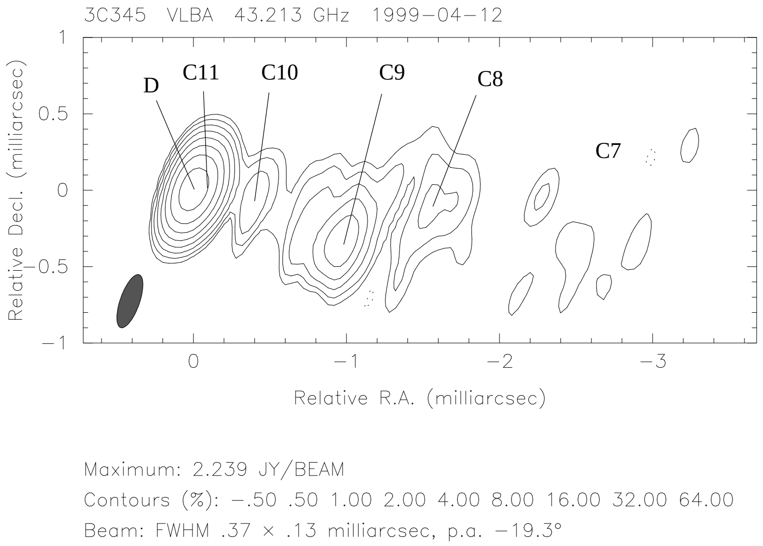

Figure 3.50: 43 GHz image of 3C 345 on April 12, 1999 (1999.28). The innermost jet feature C11 lies close to the core. C10 has enlarged already and C7 is resolved.

Name	S [Jy]	r [mas]	Θ [°]	a [mas]	b/a	Φ [°]
D	1.88 ±0.30	0	0	0.07±0.01	1	0
C11	1.81 ±0.20	0.105 ±0.005	-88.0 ±1.0	0.08±0.01	1	0
C10	0.31 ±0.05	0.30 ±0.02	-87.6 ±1.0	0.23±0.02	1	0
C9	0.60 ±0.02	1.06 ±0.03	-108.8 ±1.0	0.19±0.03	1	0
C8	0.48 ±0.04	1.44 ±0.20	-93.3 ±2.0	0.69±0.30	1	0
C7	0.15 ±0.04	2.87 ±0.20	-97.0 ±2.0	0.49±0.35	1	0

Table 3.30: Model fit components for epoch 1999.28 (April 12, 1999).

3.6.8 May 18, 1999 (1999.38)

This observation in May 1999 (Figure 3.51) is dominated by the highest flux density of C11 with 2.60 Jy. The core flux density is only 1.48 Jy, while the other jet features are below 1 Jy. The closest feature to the dominant C11 is C10 with only $S = 0.22$ Jy. This is almost at the level of the resolved component C7 with $S = 0.17$ Jy. C9 and C8 show substantial flux density changes, probably due to the variable sizes of the model components. The parameters of the model fits can be found in Table 3.31.

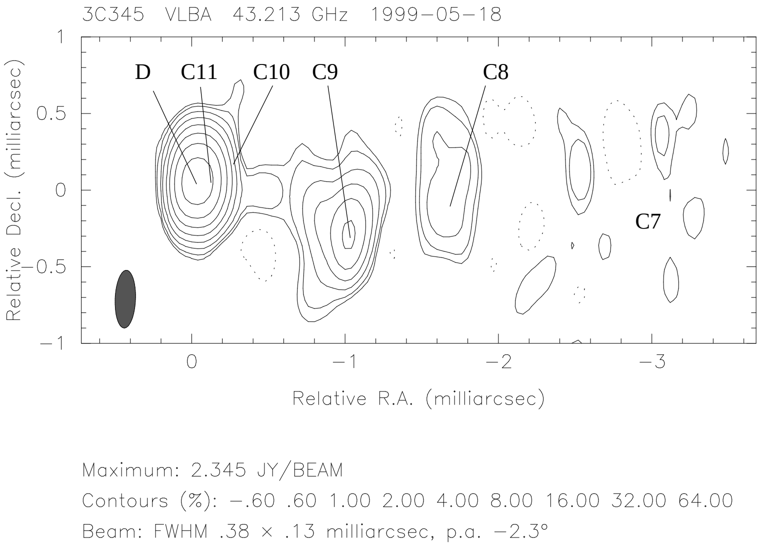

Figure 3.51: 43 GHz image of 3C 345 on May 18, 1999 (1999.38). The jet is resolved at distances $r \geq 2$ mas.

Name	S [Jy]	r [mas]	Θ [°]	a [mas]	b/a	Φ [°]
D	1.48 ±0.30	0	0	0.06±0.01	1	0
C11	2.60 ±0.20	0.116 ±0.005	-90.3 ±1.0	0.12±0.01	1	0
C10	0.22 ±0.02	0.28 ±0.02	-71.1 ±1.0	0.07±0.01	1	0
C9	0.89 ±0.02	1.13 ±0.03	-107.0 ±1.0	0.30±0.02	0.6±0.1	-13±2
C8	0.24 ±0.04	1.71 ±0.20	-95.0 ±2.0	0.47±0.12	0.6±0.1	-2±2
C7	0.17 ±0.04	3.04 ±0.20	-102.2 ±9.0	0.88±0.50	1	0

Table 3.31: Model fit components for epoch 1999.38 (May 18, 1999).

3.6.9 August 23, 1999 (1999.64)

The last 43 GHz observation shows a curved jet on scales $r \leq 3$ mas (Figure 3.52). The flux density of the innermost jet feature (C11) has decreased from 2.60 to 1.70 Jy while the flux density of the core has increased from 1.48 to 2.47 Jy. C11 is extremely close to the core, and both components are strongly correlated in their flux density. The features C10 and C7 have stayed at their low flux density level, while C9 and C8 have varied. The most expanded feature C7 is at the detection limit. The parameters of the model fits can be found in Table 3.32.

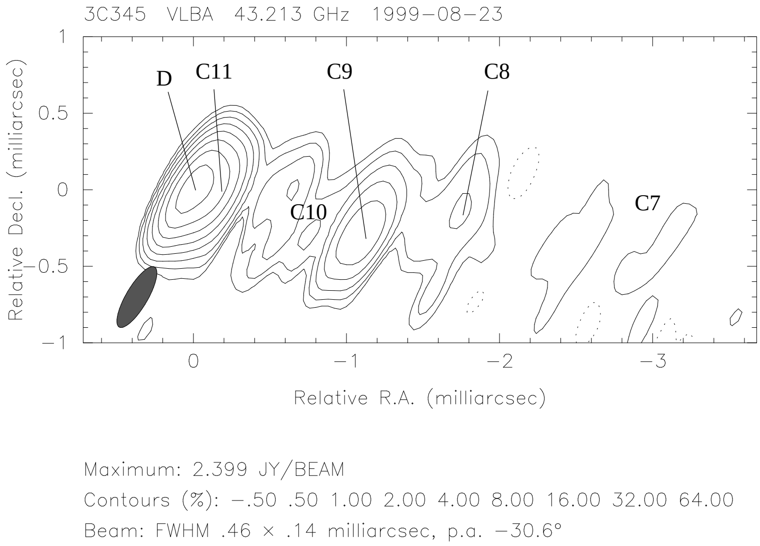

Figure 3.52: 43 GHz image of 3C 345 on August 23, 1999 (1999.64). The wiggled jet structure with its features C11–C7 is well seen.

Name	S [Jy]	r [mas]	Θ [°]	a [mas]	b/a	Φ [°]
D	2.47 ±0.30	0	0	0.07±0.01	1	0
C11	1.70 ±0.20	0.149 ±0.005	-90.5 ±1.0	0.14±0.01	1	0
C10	0.28 ±0.05	0.60 ±0.02	-101.6 ±6.0	0.46±0.14	1	0
C9	0.62 ±0.02	1.14 ±0.03	-105.2 ±1.0	0.22±0.01	0.8±0.1	-44±2
C8	0.42 ±0.04	1.55 ±0.20	-91.0 ±1.5	0.86±0.08	0.8±0.1	80±2
C7	0.14 ±0.04	3.00 ±0.20	-97.2 ±3.6	0.63±0.38	1	0

Table 3.32: Model fit components for epoch 1999.64 (August 23, 1999).

3.6.10 Modeled Data from A.Marscher

Since we had a gap in our observations in 1998, we asked A. Marscher to let us use his data to perform own model fits for consistency reasons. His data were only used for model fitting. The parameters of the model fits obtained for the epochs 1998.15, 1998.41, 1998.58, 1998.76 and 1998.94 are presented in the following Tables.

Name	S [Jy]	r [mas]	Θ [°]	a [mas]	b/a	Φ [°]
D	1.56 ±0.30	0	0	0.04±0.01	1	0
C11	1.24 ±0.10	0.075 ±0.005	-84.8 ±1.0	0.05±0.01	1	0
C10	0.28 ±0.02	0.22 ±0.02	-82.3 ±1.5	0.10±0.01	1	0
C9	0.48 ±0.02	0.60 ±0.02	-110.1 ±1.5	0.26±0.03	1	0
C8	0.75 ±0.10	1.32 ±0.04	-101.2 ±1.0	0.30±0.04	1	0
C7	0.22 ±0.10	2.28 ±0.10	-97.0 ±3.9	0.70±0.31	1	0

Table 3.33: Model fit components for epoch 1998.15 (March 25, 1998).

Name	S [Jy]	r [mas]	Θ [°]	a [mas]	b/a	Φ [°]
D	1.95 ±0.30	0	0	0.04±0.01	1	0
C11	1.92 ±0.10	0.090 ±0.005	-87.3 ±1.0	0.05±0.01	1	0
C10	0.31 ±0.02	0.23 ±0.02	-81.3 ±1.5	0.11±0.01	1	0
C9	0.57 ±0.02	0.69 ±0.02	-111.3 ±1.8	0.32±0.04	1	0
C8	0.72 ±0.10	1.38 ±0.04	-99.1 ±1.7	0.36±0.08	1	0
C7	0.18 ±0.05	2.44 ±0.13	-97.4 ±3.0	0.58±0.26	1	0

Table 3.34: Model fit components for epoch 1998.41 (May 31, 1998).

Name	S [Jy]	r [mas]	Θ [°]	a [mas]	b/a	Φ [°]
D	2.13 ±0.30	0	0	0.03±0.01	1	0
C11	2.81 ±0.10	0.096 ±0.005	-91.8 ±1.0	0.06±0.01	1	0
C10	0.30 ±0.02	0.26 ±0.02	-84.7 ±1.5	0.09±0.01	1	0
C9	0.61 ±0.02	0.78 ±0.02	-114.0 ±1.6	0.29±0.04	1	0
C8	0.65 ±0.10	1.43 ±0.03	-97.7 ±2.1	0.40±0.10	1	0
C7	0.16 ±0.10	2.55 ±0.11	-98.6 ±2.5	0.53±0.23	1	0

Table 3.35: Model fit components for epoch 1998.58 (July 31, 1998).

Name	S [Jy]	r [mas]	Θ [°]	a [mas]	b/a	Φ [°]
D	2.21 ±0.30	0	0	0.04±0.01	1	0
C11	2.29 ±0.10	0.094 ±0.005	-90.3 ±1.0	0.06±0.01	1	0
C10	0.78 ±0.02	0.21 ±0.02	-89.9 ±1.5	0.10±0.01	1	0
C9	0.68 ±0.02	0.85 ±0.02	-113.8 ±1.5	0.26±0.01	1	0
C8	0.63 ±0.10	1.48 ±0.03	-95.9 ±1.3	0.45±0.07	1	0
C7	0.15 ±0.10	2.65 ±0.08	-97.9 ±1.8	0.53±0.17	1	0

Table 3.36: Model fit components for epoch 1998.76 (October 5, 1998).

Name	S [Jy]	r [mas]	Θ [°]	a [mas]	b/a	Φ [°]
D	1.48 ±0.30	0	0	0.03±0.01	1	0
C11	2.11 ±0.10	0.080 ±0.005	-84.3 ±1.0	0.06±0.01	1	0
C10	0.59 ±0.02	0.23 ±0.02	-88.0 ±1.5	0.13±0.01	1	0
C9	0.53 ±0.02	0.90 ±0.02	-111.4 ±1.1	0.29±0.03	1	0
C8	0.42 ±0.10	1.54 ±0.05	-94.2 ±1.8	0.46±0.09	1	0
C7	0.12 ±0.10	2.72 ±0.14	-97.9 ±3.0	0.51±0.28	1	0

Table 3.37: Model fit components for epoch 1998.94 (December 10, 1998).

3.6.11 Summary

9 VLBA observations from our ongoing monitoring campaign of 3C 345 at 43 GHz were presented in this section. Additionally, 5 epochs of data from A. Marscher were modeled. A new jet feature C11 was identified which could be traced from the shortest core distance of 0.075 mas up to 0.149 mas. This is the most precise measurement of a jet component at this small core distance ever made for 3C 345. The inner jet was modeled consistently with the components C10, C9, C8 and C7 at each epoch. The images and model fit results show a clear evolution of these features within the jet. A scaled arrangement of all 9 CLEAN images illustrates the jet evolution over a 27 month period (Figure 3.53).

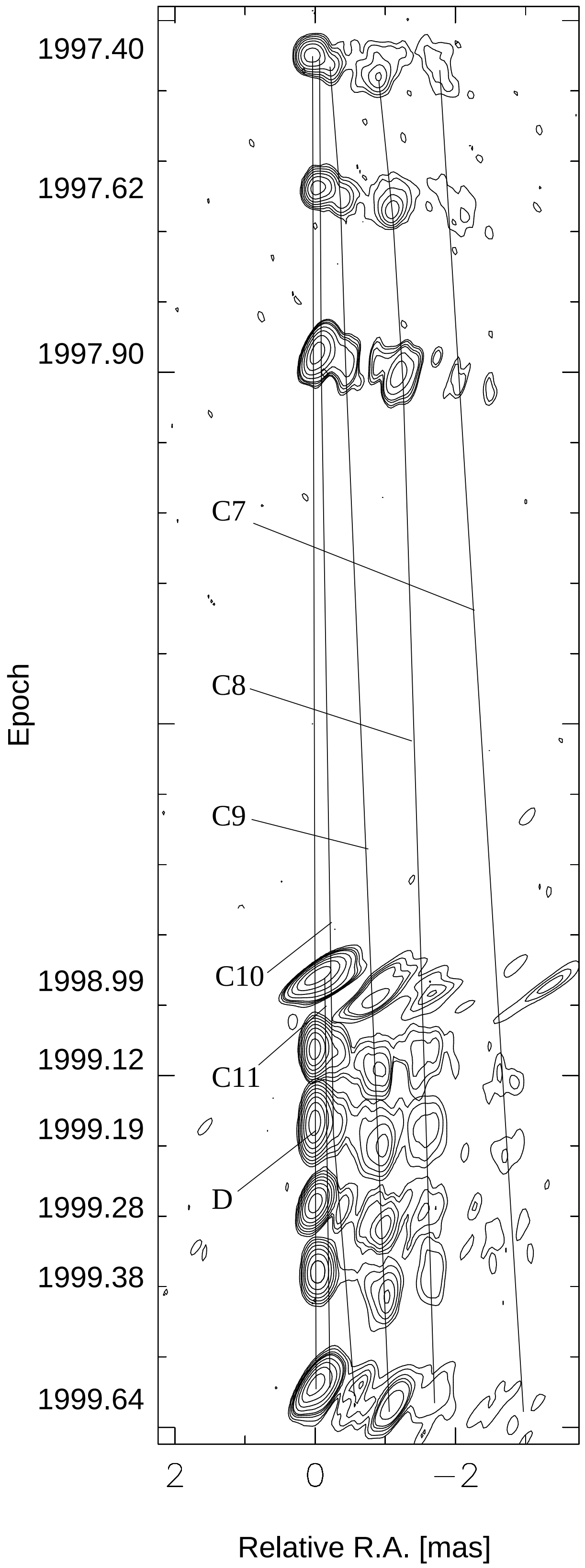

Figure 3.53: Stacked image of the 43 GHz CLEAN maps. The straight lines connect the detected jet components at different epochs.

Observing and Map Parameters of 3C 345 at 43 GHz

Epoch	Telescopes	t_{tot} [min]	bas [Mλ]	$\Delta\nu$ [MHz]	b_{maj} [mas]	b_{min} [mas]	Φ [°]	S_{tot} [Jy]	$S_p{}^{eak}$ [Jy]	C_{low} [mJy]	rms [mJy]	dr
1997.40	VLBA	63	1236	32	0.244	0.167	-2.49	3.1	1.26	6.3	6	1:210
1997.62	VLBA (without FD)	56	1241	32	0.256	0.157	-6.64	3.9	1.43	3.6	3	1:477
1997.90	VLBA (without HN)	22	1247	8	0.397	0.144	-18.6	3.1	1.26	12.6	9	1:140
1998.99	VLBA (without SC)	10	965	14	0.494	0.162	-56.6	4.0	3.09	30.9	16	1:193
1999.12	VLBA	165	1240	16	0.365	0.130	-2.57	4.6	2.15	10.7	9	1:239
1999.19	VLBA	165	1241	16	0.456	0.138	-3.87	5.3	2.60	6.5	6	1:433
1999.28	VLBA	165	1241	16	0.366	0.127	-19.3	5.1	2.22	11.2	9	1:247
1999.38	VLBA	165	1241	14	0.377	0.135	-2.32	5.5	2.35	14.1	9	1:261
1999.64	VLBA (without SC)	165	1081	14	0.455	0.141	-30.6	5.6	2.40	12.0	10	1:240

Table 3.38: t_{tot} - total observing time; bas - longest projected baseline; $\Delta\nu$ - remaining bandwidth after flagging channels; b_{maj} - beam major axis; b_{min} - beam minor axis; Φ - angle of the beam major axis; S_{tot} - total flux density; $S_p{}^{eak}$ - peak flux density; C_{low} - lowest map contour; rms - root-mean-square of the map noise; dr - dynamic range. VLBA stations: MK - Mauna Kea; OV - Owens Valley; KP - Kitt Peak; BR - Brewster; PT - Pie Town; FD - Fort Davis; LA - Los Alamos; NL - North Liberty; HN - Hancock; SC - St. Croix

Chapter 4

Kinematic Properties of the Jet

The kinematic properties of the parsec scale jet are discussed in this chapter. The focus will be mainly on the inner part ($r \leq 4\,\mathrm{mas}$; components C7 – C11), reflecting its much more complex evolution compared with the outer part of the jet (components C0 – C5). The jet feature C6 was last seen at epoch 1993.89 and disappeared afterwards.

4.1 How to Measure Kinematics of the Jet

The model fit results presented in chapter 3 are used to study the kinematic properties of the jet. One of the peculiarities of the jet in 3C 345 is the occurrence of enhanced emission features (the components) which move along the jet. This enables the study of the evolution of these particular jet features. The identification of the same component at different epochs is, in general, difficult. However, with the dense time sampling of the observations presented in chapter 3, a clear identification of the components at different epochs is possible. An accurate description of the component kinematics requires choosing a good reference point in the VLBI images. In this study, the core of the jet is used as the reference point. Bartel *et al.* (1986) used the phase reference technique to determine a possible core motion with respect to the nearby quasar NRAO 512. They found that the core of 3C 345 is stationary in right ascension within 20 μarcsec yr^{-1}. Thus, the narrow end of the jet (the core) can be used as a reference point, and one can measure the offset of the jet components with respect to the core. The proper motion of a component in right ascension and declination with respect to the core can be fit by polynomials:

$$x(t), y(t) = \sum_{n=0}^{N} a_n (t - T_{ref})^n \tag{4.1}$$

They represent not the physical path of a component but its projection on the sky plane. The reference epoch T_{ref} (close in time to the extrapolated ejection epoch T_0) is only introduced to improve the fit algorithm. The quality of the fit is strongly dependent on the time intervals between the observations. Combining observations at different frequencies, one can increase the density of data sampling, thus improving the quality of the fit. Since the core is optically thick, it appears closer to the central engine at higher frequencies. This means for 3C 345 that the reference point is shifted to the east at higher frequencies (Figure 4.1). According to Königl 1981, the observed jet origin is shifted with respect to the "true" jet origin by:

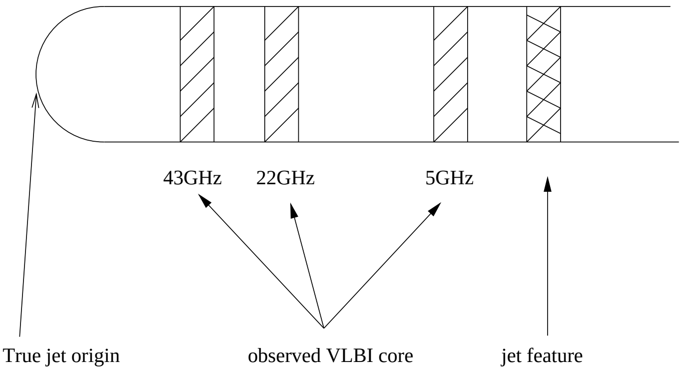

Figure 4.1: The observed jet origin (the core) is frequency dependent and shifted with regard to the true jet origin.

$$r \propto \nu^{-1/k_r} \tag{4.2}$$

The observed jet origin (the core) is seen where the opacity (τ) caused by synchrotron self-absorption equals 1. With model fits at different frequencies and close epochs one can determine the core shift with respect to a compact, optically-thin jet feature. The calculated core shift allows one to combine $x(t)$ and $y(t)$ positions of a jet feature at different frequencies. This substantially improves the accuracy of the component trajectories obtained. This enhancement of the trajectories leads to a better determination of physical parameters of the jet, because even small variations of component trajectories have a large influence on the derived physical properties of the jet (see section 4.13.1). For the outer part of the jet (C4, C5), the errors of the component positions exceed the frequency-dependent core shift. Thus, the core shift can be neglected at the outer part of the jet.

The calculated core shift is also used for aligning maps at different frequencies and similar epochs to produce spectral index maps (chapter 6).

In the next sections, each jet component trajectory will be described separately, and the core shift (if determinable) will be calculated. Then the trajectories of all components will be compared with each other, and physical jet parameters of the inner jet will be calculated.

In all following plots, open symbols are used for data points taken from the literature (mainly Lobanov 1996 and Ros *et al.* 2000). Filled symbols mark data points resulting from this thesis work (see chapter 3 for details).

A summary of the $x(t)$ and $y(t)$ polynomials of the jet components is given in Table 4.1. The most simple polynomial which fitted the data reliably was taken. An error weighting of $1/\Delta y^2$ was used for the calculation of the polynomials. The observed time range T_{obs} is the actual time range when observations where done. The extrapolated ejection epochs T_0 are obtained from back extrapolation of the observed component trajectories.

Comp.	a_0	a_1	a_2	a_3	a_4	a_5	T_{ref}	T_0	T_{obs}
C4							1979.00	1979.00	1980.52 - 1999.69
$x(t)$	0.00561828	0.0603281	0.0146249	0.000537818	-2.57647e-05				
$y(t)$	0.00755288	-0.143283	0.0402291	-0.00290576	8.31964e-05				
C5							1980.00	1980.00	1983.09 - 1999.69
$x(t)$	-0.00636276	-0.00574258	0.0204835	-0.000495609	7.92735e-06				
$y(t)$	-0.0646932	0.194583	-0.063861	0.00520136	-0.000113543				
C7							1988.00	1988.00	1989.20 - 1999.69
$x(t)$	-0.0753316	0.407393	-0.256248	0.0598064	-0.00514885	0.000155589			
$y(t)$	-0.185233	0.264812	-0.0993381	0.0156243	-0.00114581	3.06743e-05			
C8							1991.00	1991.43	1992.39 - 1999.69
$x(t)$	-0.198392	0.566926	-0.276689	0.0526871	-0.00294252				
$y(t)$	-0.0860553	0.228496	-0.0829694	0.00638642	4.36969e-05				
C9							1994.00	1994.75	1996.41 - 1999.69
$x(t)$	-0.181543	0.375411	-0.209824	0.0566158	-0.00423774				
$y(t)$	0.16639	-0.364364	0.246524	-0.0686842	0.00599379				
C10							1995.00	1995.50	1997.40 - 1996.69
$x(t)$	-0.128362	0.426119	-0.453564	0.251782	-0.0627885	0.00573671			
$y(t)$	0.0758382	-0.292194	0.376383	-0.210157	0.0520707	-0.00466224			
C11							1996.00	1996.62	1998.51 - 1999.64
$x(t)$	0.0603201	-0.240284	0.297386	-0.116115	0.0149406				
$y(t)$	-0.0186131	0.0517505	-0.0446759	0.0157134	-0.00191548				

Table 4.1: Polynomial fits of the component trajectories. T_{ref} is the reference epoch which was used to calculate the polynomials. T_0 marks the extrapolated ejection epoch. T_{obs} shows the time range in which the data were obtained.

4.2 Jet Component C4

The component C4 is one of the best studied features in the jet. A detailed study of its early part of evolution is given in ZCU95 and Lobanov (1996). Qian *at al.* (1992) suggested a motion which followed a spiral-shaped magnetic line and Steffen *et al.* (1995) applied a helical model to it. Spectral evolution of C4 is studied in Lobanov & Zensus (1999). This component belongs meanwhile to the outer part of the jet and no longer shows the characteristical strong curvature seen for components in the inner part. In the data for this thesis, C4 is detected in 8 VSOP observations at 1.6 and 5 GHz and in 8 VLBA observations at 22 GHz. To obtain the best possible fit over the full time range, some outliers were excluded at the epochs 1990.49, 1991.68, 1997.90, 1998.02 and 1998.99, but plotted for completeness.

It was impossible to fit all data in a reasonable way for the full time range with one polynomial. Since the inner part of the C4 trajectory has already been extensively discussed in the literature mentioned above, two 4th degree polynomials (representing $x(t)$ and $y(t)$) were chosen to fit the data as well as possible in the outer region (Figure 4.2). The reconstructed component trajectory is presented in Figure 4.3. As one sees in this Figure, C4 has turned northwards. It reached a core distance of $r \approx 8\,\mathrm{mas}$ at a position angle of about -67° in 1999.69. Circles at the trajectory mark time steps of 6 months. They illustrate a continuous acceleration of C4.

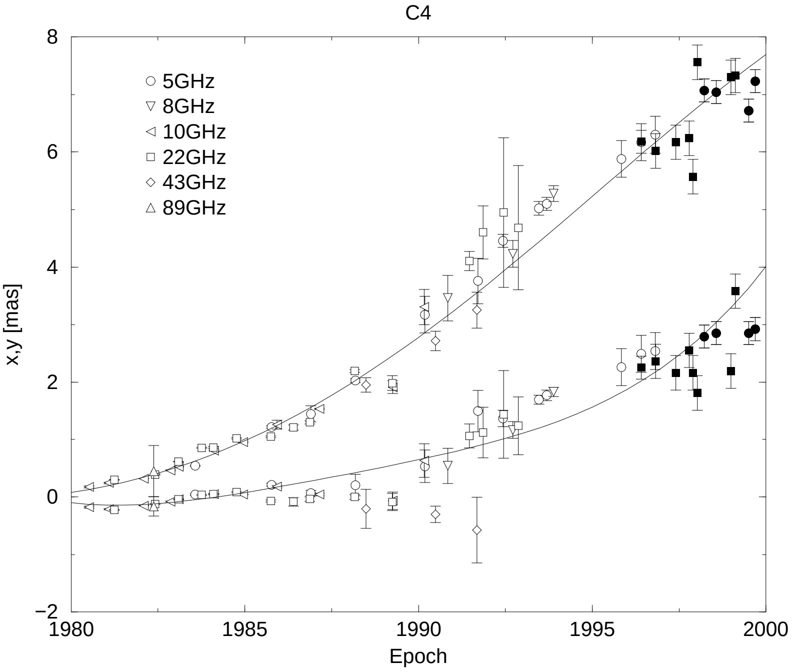

Figure 4.2: Polynomial fits of the $x(t)$ and $y(t)$ position of C4. Filled symbols denote data from this thesis.

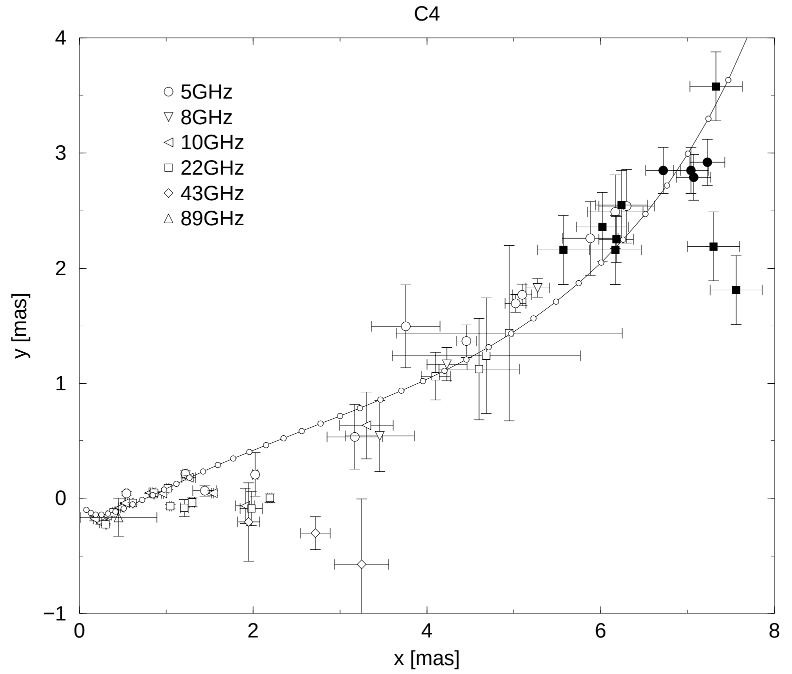

Figure 4.3: Reconstructed trajectory made of the $x(t)$ and $y(t)$ fits for C4. The circles at the trajectory mark time steps of 6 months and illustrate a continuous acceleration of C4.

4.3 Jet Component C5

The jet feature C5 is one of the most closely studied components in the jet (e.g. ZCU95, Lobanov 1996, Qian *at al.* 1992, Steffen *et al.* 1995, Lobanov & Zensus 1999). The peculiarity of this component is a long trend of its trajectory to the south-west before it turns to the north at a core distance $r \approx 1.5$ mas. This feature could be identified in all VSOP observations at 1.6 and 5 GHz and in one 22 GHz observation.

It was impossible to fit all data in a reasonable way for the full time range with one polynomial. Since the inner part of the C5 trajectory is extensively discussed in the literature mentioned above, the 4th degree polynomials obtained represent the best fit for the outer part of the data (Figure 4.4). The reconstructed trajectory is presented in Figure 4.5. Circles along the trajectory mark time steps of 6 months. They illustrate an acceleration at $x(t) \approx 1 - 3$ mas.

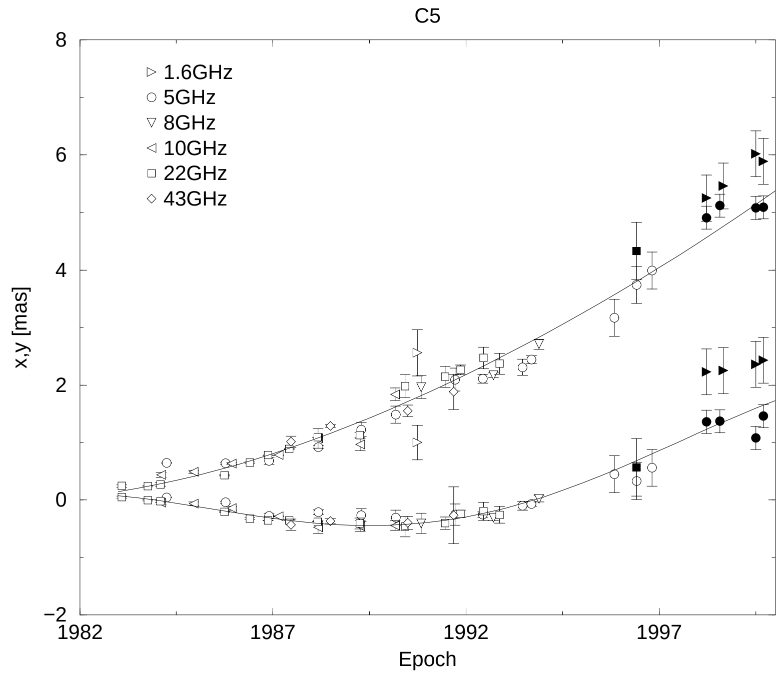

Figure 4.4: Polynomial fits of the $x(t)$ and $y(t)$ position of C5. Filled symbols denote data from this thesis.

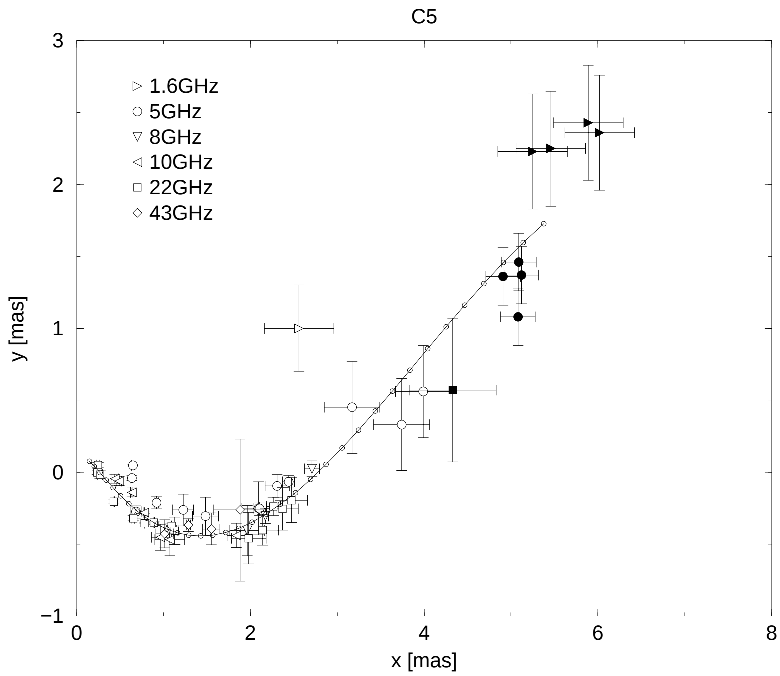

Figure 4.5: Reconstructed trajectory made of the $x(t)$ and $y(t)$ fits of C5. The circles along the trajectory mark time steps of 6 months. They illustrate an acceleration at $x(t) \approx 1 - 3\,\mathrm{mas}$.

4.4 Jet Component C7

4.4.1 Core Shift

The densely-sampled data from epochs between 1997.40 and 1999.69 at four different frequencies allow the determination of the core shift of component C7, using a linear regression (see Figure 4.6). The linear regression was applied for data points at core distances larger than 1 mas. Epoch 1999.50 at 1.6 GHz was excluded, because the position of C7 was affected at this epoch by blending with the strong feature C9. 43 GHz is used as the reference frequency and we obtain a shift of 0.10 mas at 22 GHz, 0.27 mas at 5 GHz and 0.66 mas at 1.6 GHz. This results in a frequency dependent shift of the core: $r_{core} \propto \nu^{(-0.76 \pm 0.02)}$ (Figure 4.7).

4.4.2 Trajectory

The core shift found is applied for all positions of C7 at distances larger than 1 mas. This allows using all 4 frequencies to determine the $x(t)$ and $y(t)$ of C7 (Figure 4.8). Because of the long time covered by the observations, it was necessary to select a time range to give an optimal fit. The inner part of C7 is discussed in Lobanov (1996), thus the focus of this work is the outer part of the trajectory. A 5th degree polynomial represents this part well. This leads to a slightly decreased quality of the fit for data points at distances $r \leq 0.5$ mas. The slight scatter of the data points at larger distances (especially for $y(t)$) is due to a substantial increase of the size of C7. In Figure 4.9, the reconstructed trajectory made from the $x(t)$ and $y(t)$ polynomials is presented. The white circles mark time intervals of 3 months. The trajectory fitted shows that C7 moved almost straight to the south-west and strongly accelerated at distances $x(t) \geq 0.5$ mas. At the end point of this trajectory, C7 reached the point where it is expected to turn to the north (due to the geometry of the outer jet), so that one can expect trajectory changes in the near future.

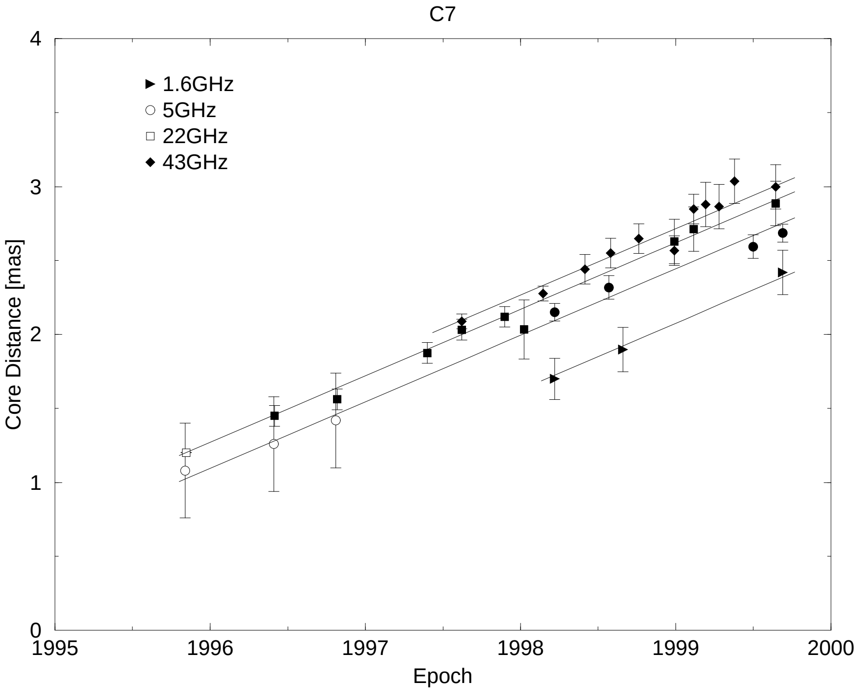

Figure 4.6: Core shift of C7 at 1.6, 5, 22 and 43 GHz at distances larger than 1 mas. With 43 GHz as the reference frequency, the core shift amounts to 0.10 mas at 22 GHz, 0.27 mas at 5 GHz and 0.66 mas at 1.6 GHz. Filled symbols denote data from this thesis.

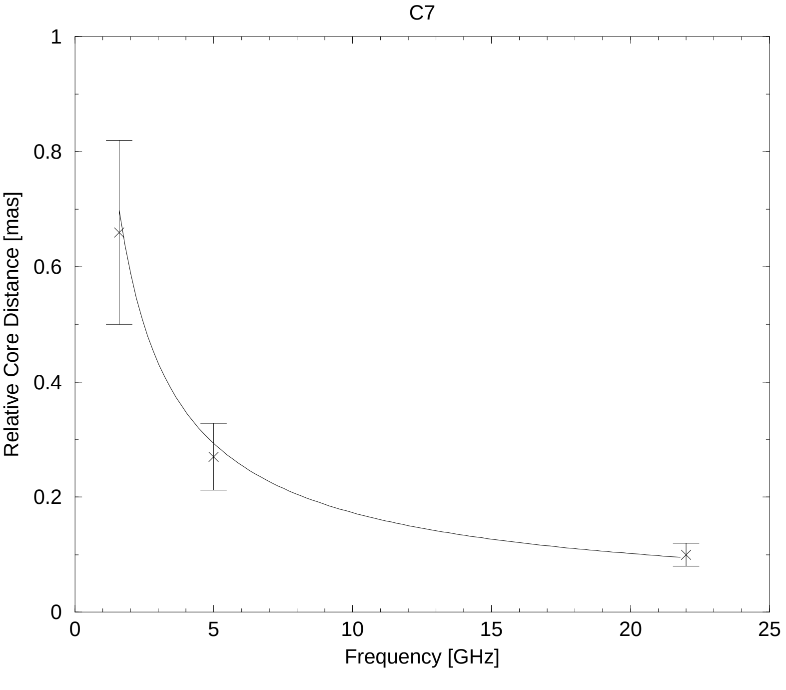

Figure 4.7: Frequency dependent shift of C7 at a core distance larger than 1 mas, with the reference frequency of 43 GHz. The fit corresponds to $r_{core} \propto \nu^{(-0.76\pm0.02)}$.

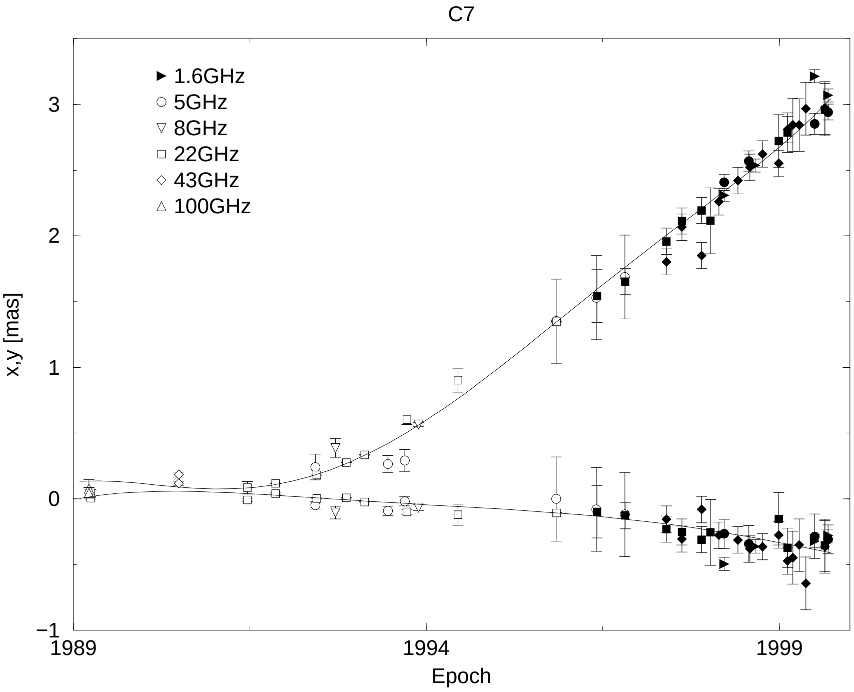

Figure 4.8: Polynomial fits for the $x(t)$ and $y(t)$ position of C7. The determined core shift is applied to the data in the the range 1995–2000. Filled symbols denote data from this thesis.

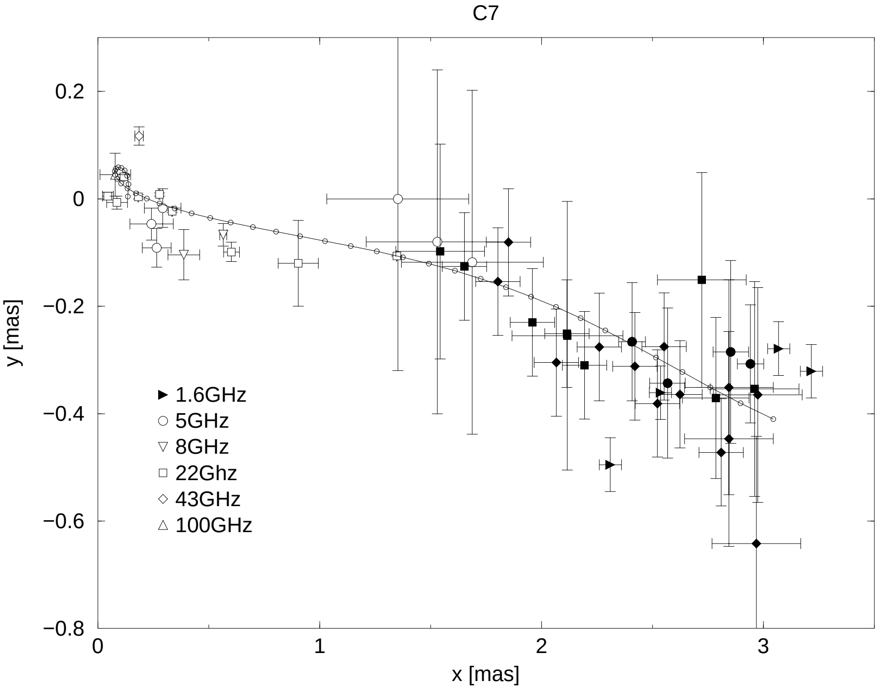

Figure 4.9: Reconstructed trajectory made of the $x(t)$ and $y(t)$ polynomials. The white circles mark time steps of 3 months. At distances larger than 1 mas C7 moved nearly straight to the south-west and accelerated strongly.

4.5 Jet Component C8

4.5.1 Core Shift

Four different frequencies have been combined to determine the core shift with regard to C8 between 1996.41 and 1999.69. At the beginning of 1999, C8 started to expand and decreased in flux density, which resulted in increasing errors for the component position at higher frequencies. The core shift could be determined for each frequency with respect to the reference frequency of 43 GHz. While there was a dense monitoring at 43 GHz in 1998, an observation gap at 22 GHz had to bridged over during this year. On average, a core shift of 0.028 mas was measured between both frequencies, from 1997.40 until 1999.20 (Figure 4.10). To measure the core shift at 5 GHz, the 22 GHz observations have been used for comparison, because of a lack of 43 GHz measurements between 1996.41 and 1997.40. In order to consider the curved jet geometry during these three years of evolution, a quadratic fit was applied (Figure 4.11). The average core shift between both frequencies is 0.182 mas. Thus, the core shift between 5 and 43 GHz is 0.210 mas. C8 could be modeled at 1.6 GHz at all four VSOP epochs. In the second epoch (1998.66), C9 emerged and influenced the position of C8 strongly. As a result, C8 is closer to the core compared with the previous epoch (1998.22). Using only the first epoch and the last two epochs (1999.50 and 1999.69), a parallel linear fit with respect to the 43 GHz fit could be applied and allowed the determination of the core shift at 1.6 GHz. The difference between both frequencies results in 0.409 mas (Figure 4.12). With the determined core shift for 1.6, 5 and 22 GHz with respect to 43 GHz, the frequency depending shift of the core could be calculated (Figure 4.13): $r_{core} \propto \nu^{(-1.10\pm0.14)}$

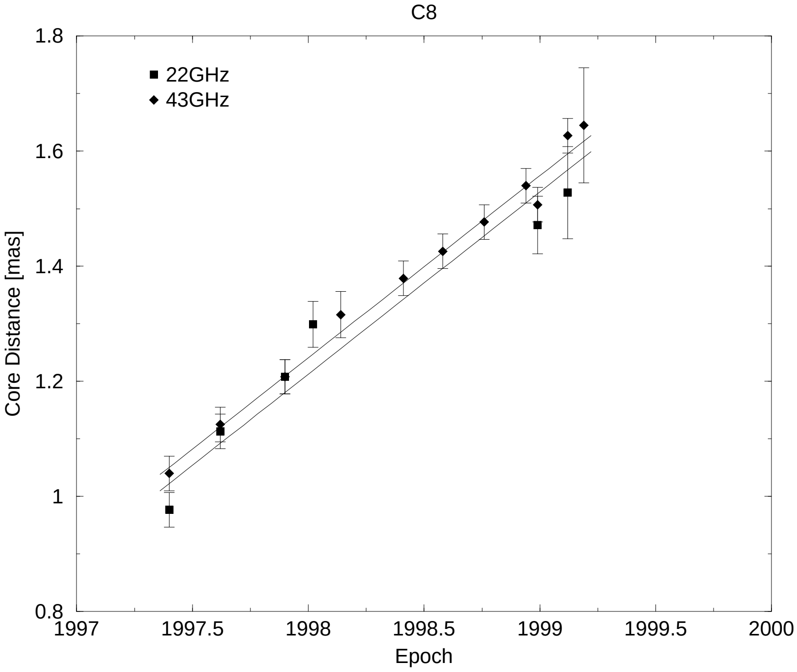

Figure 4.10: Core shift of C8 between 22 and 43 GHz. The averaged distance between both frequencies is 0.028 mas.

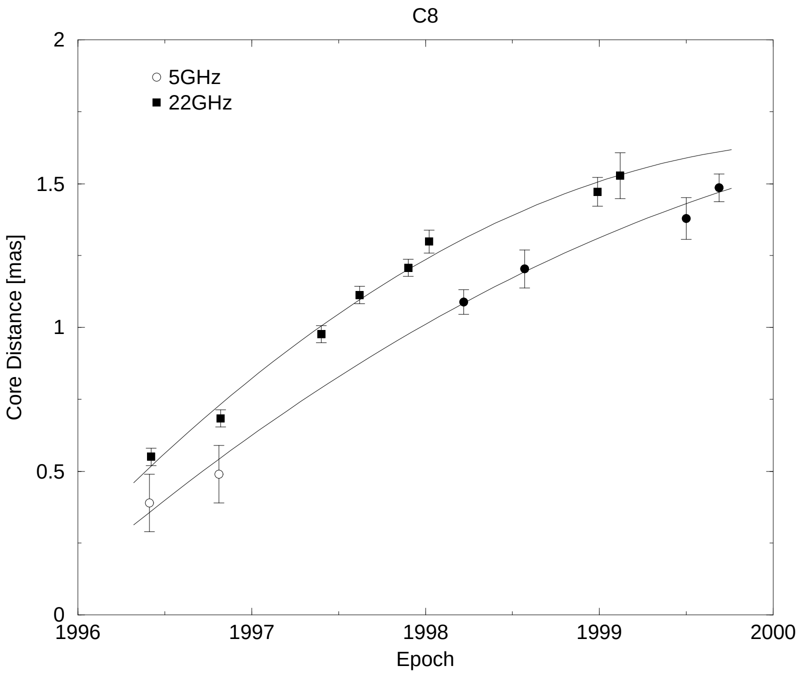

Figure 4.11: Core shift of C8 between 5 and 22 GHz. The averaged distance between both frequencies is 0.182 mas. Filled symbols denote data from this thesis.

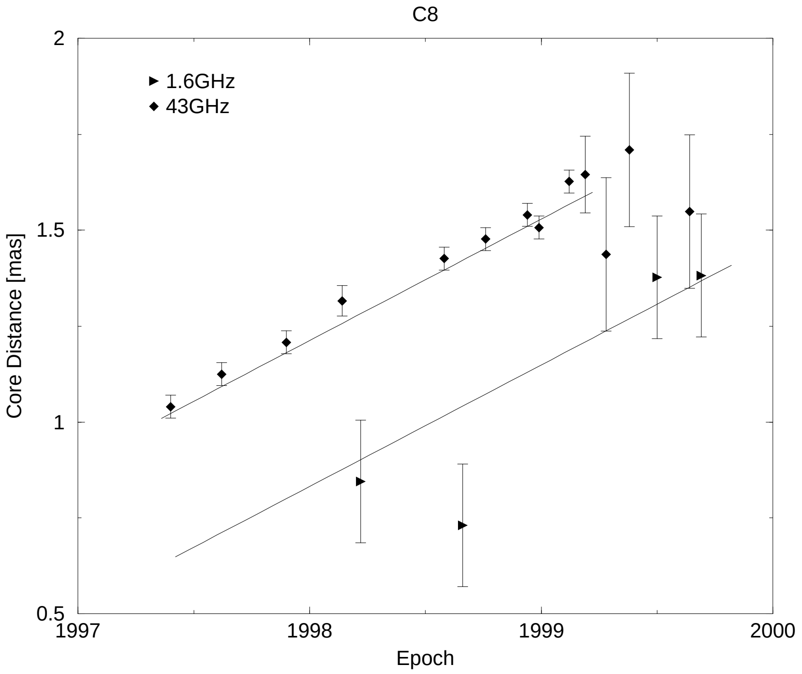

Figure 4.12: Core shift of C8 between 1.6 and 43 GHz. The averaged distance between both frequencies is 0.409 mas.

4.5.2 Trajectory

The ejection epoch has been determined from a linear fit to the positions of C8 measured at the first three epochs. This gives the origin epoch of 1991.43, which

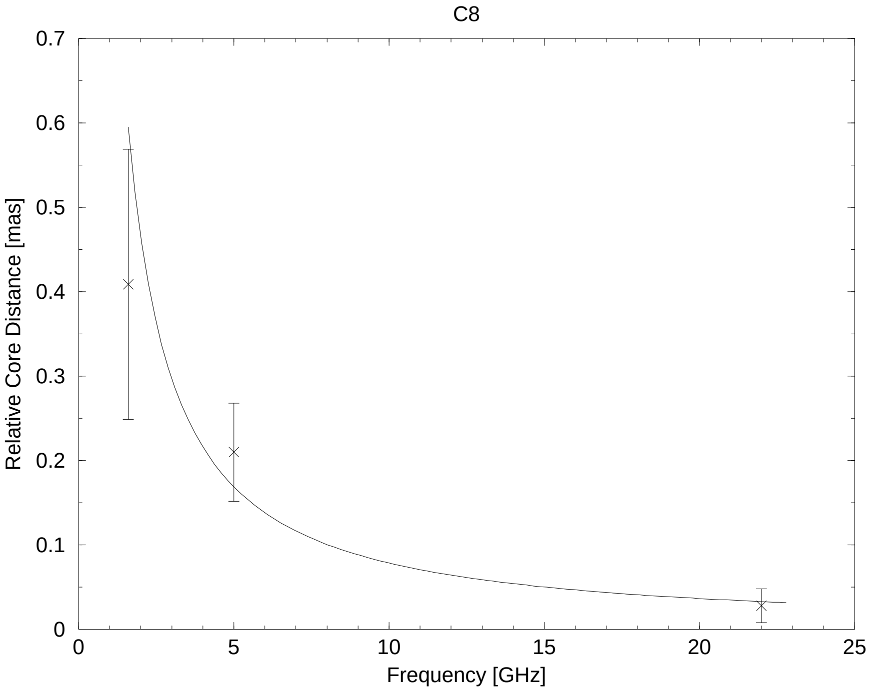

Figure 4.13: Frequency dependent core shift of C8 with the reference frequency of 43 GHz. The fit corresponds to $r \propto \nu^{(-1.10\pm0.14)}$.

perfectly matches the flare observed in middle 1991. This epoch has been used to constrain the $x(t)$ and $y(t)$ fits, which improved the path fit for the first epochs. After applying the core shift corrections, all data at 1.6, 5, 22 and 43 GHz could be combined to get a denser sampling of the data points. The best fit is obtained with a 4 degree polynomial (Figure 4.14). The $y(t)$ curve shows a clear trend to the south until 1997.5, and it turns then back to the north. The reconstructed trajectory (Figure 4.15) shows a curve which makes a bend at $x(t) \approx 1\,\mathrm{mas}$, $y(t) \approx -0.3\,\mathrm{mas}$ and returns back to $y(t) = 0\,\mathrm{mas}$ at $x(t) \approx 1.7\,\mathrm{mas}$. The circles on the trajectory mark time separations of one month and illustrate the acceleration of this component at $x(t) \approx 0.3\,\mathrm{mas}$.

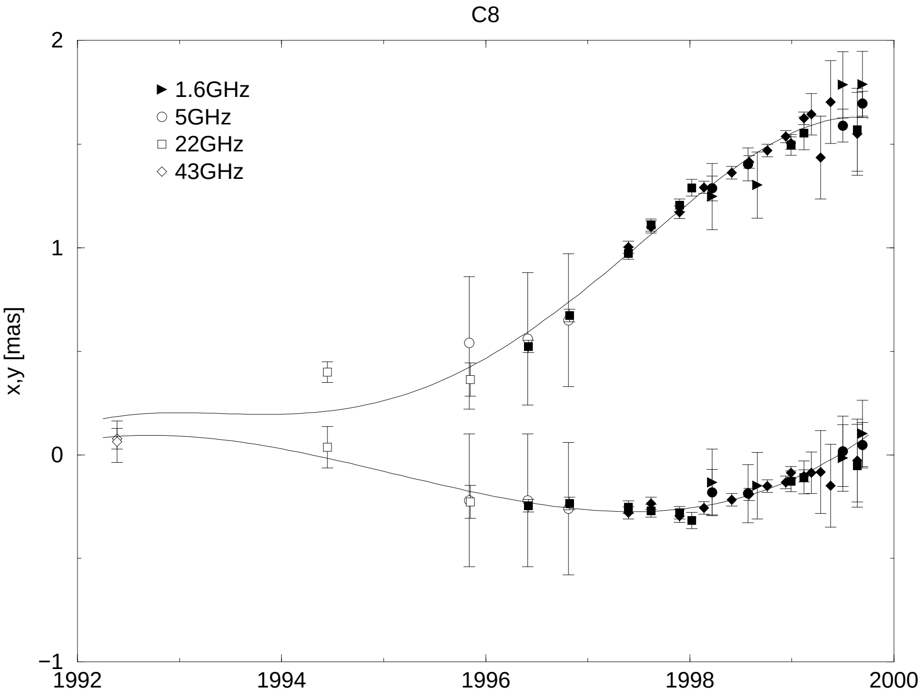

Figure 4.14: Polynomial fits of the $x(t)$ and $y(t)$ position of C8. The determined core shift is applied with 43 GHz as reference frequency. Filled symbols denote data from this thesis.

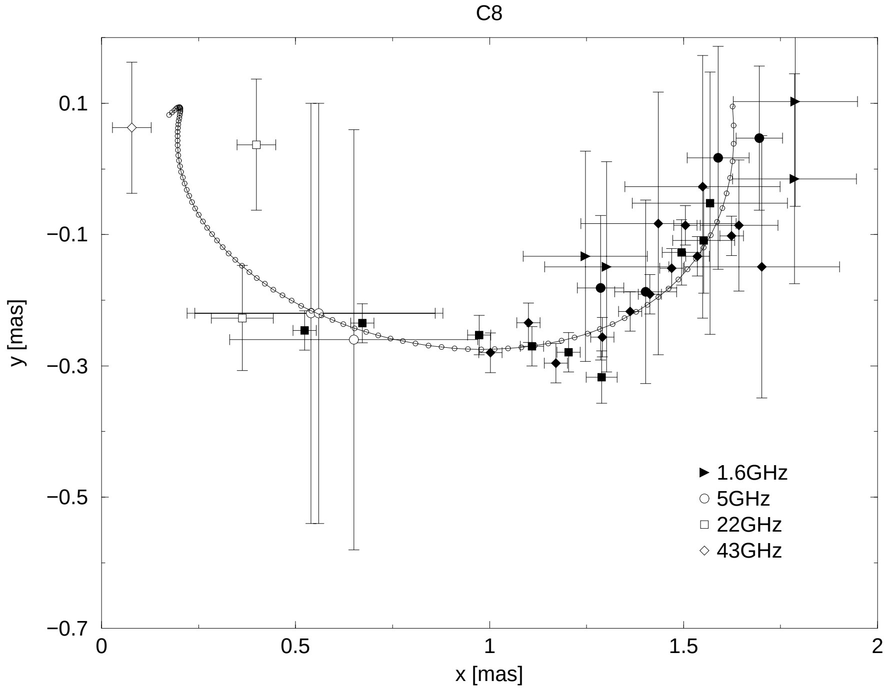

Figure 4.15: Reconstructed trajectory made using the $x(t)$ and $y(t)$ fits. The circles on the trajectory mark times steps of one month. One sees an acceleration of the component after about a quarter of its path.

4.6 Jet Component C9

4.6.1 Core Shift

The component C9 is observed at core distances from 0.1 to 1.1 mas, and it is seen as a compact, unresolved feature at most of the observing epochs. This component could be modeled at 1.6, 5, 22 and 43 GHz. The compactness of C9 and its detection at many epochs at four different frequencies give an excellent opportunity to determine the core shift. The 14 epochs at 43 GHz are the most dense sampling of C9 compared with the other frequencies. At distances below $r = 0.3$ mas only 22 GHz observations exist, and the core shift cannot be determined. The comparison of the 43 GHz data with close 22 GHz epochs shows that the core shift between both frequencies is bigger at distances larger than $r = 0.9$ mas. Thus, the path of C9 has been divided into 2 parts. The first one reflects the inner range between 0.3 and 0.9 mas and the second one covers the distances from 0.9 to about 1.1 mas. A linear fit is used to model the data points (Figure 4.16 and 4.17). The core shift in the inner part is 0.035 mas, whereas the outer part shows a three times larger shift of 0.106 mas. This could be caused by a transition from an optically thick to an optically thin regime at $r \approx 0.9$ mas. At 5 GHz, C9 is detected and fitted at 4 epochs at core distances between 0.3 and 0.9 mas. Using the 43 GHz fit as the reference, a core shift of 0.254 mas is found (Figure 4.18). C9 is detected at 1.6 GHz at two epochs (1999.50 and 1999.69). Within these 69 days, no component motion was detected. Therefore, the core shift is calculated for both epochs with respect to the linear fit at 43 GHz and results in an average value of 0.47 mas. With these results, the frequency-dependent shift of the core at distances up to 0.9 mas is $r_{core} \propto \nu^{(-1.00 \pm 0.11)}$ (Figure 4.19). The core shift at distances larger than 0.9 mas results in $r_{core} \propto \nu^{(-0.76 \pm 0.07)}$ (Figure 4.20).

4.6.2 Trajectory

To determine the ejection epoch of C9, the first two epochs at 22 GHz are used for a linear fit, yielding at 1994.75. This ejection epoch is used as a start point for the fits of $x(t)$ and $y(t)$. Core-shift corrections are applied for 1.6, 5 and 22 GHz with respect to 43 GHz. In Figure 4.21, one sees the polynomial fits that were obtained from the combined data at all frequencies. The reconstructed trajectory shows that the path of C9 went immediately to the south-west until $y(t) = -0.34$ mas at $x(t) = 0.95$ where it turned to the north-west (Figure 4.22). The 1.6 GHz epochs are not plotted because of the big uncertainties in P.A. at small core distances. The white circles mark time steps of one month and illustrate an acceleration of C9 after the first two epochs followed by a constant velocity.

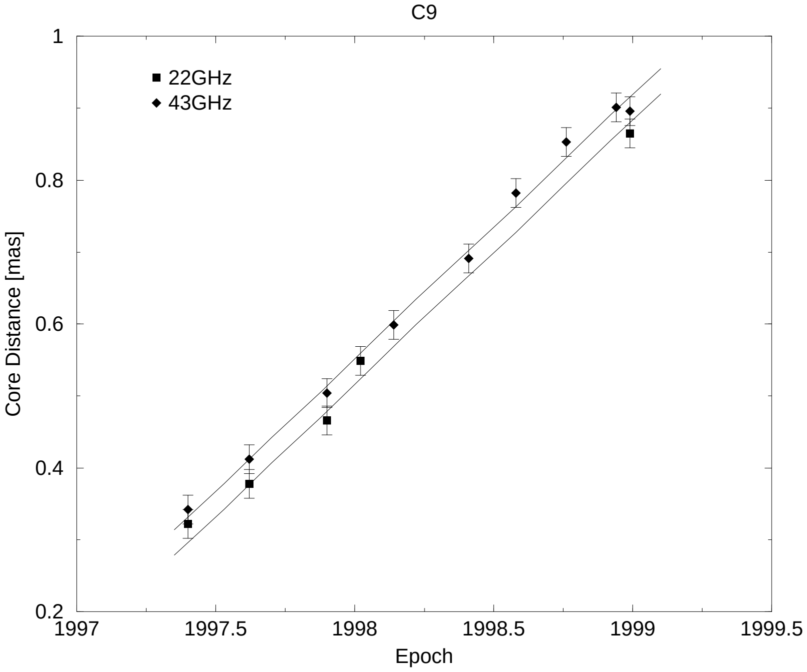

Figure 4.16: Core shift between 22 and 43 GHz measured at core distances between 0.3 and 0.9 mas. The core shift derived is 0.035 mas.

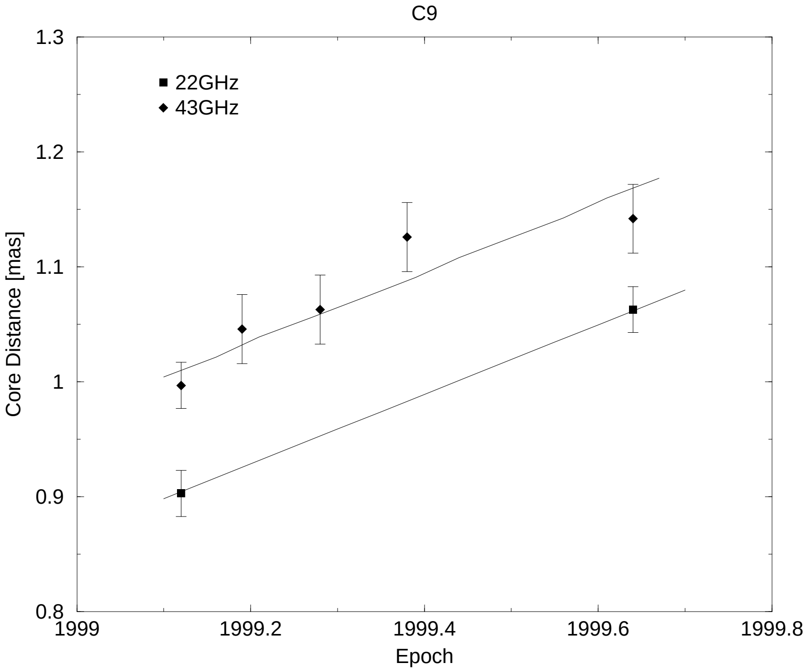

Figure 4.17: Core shift between 22 and 43 GHz measured at core distances between 0.9 and 1.1 mas. The core shift derived is 0.106 mas.

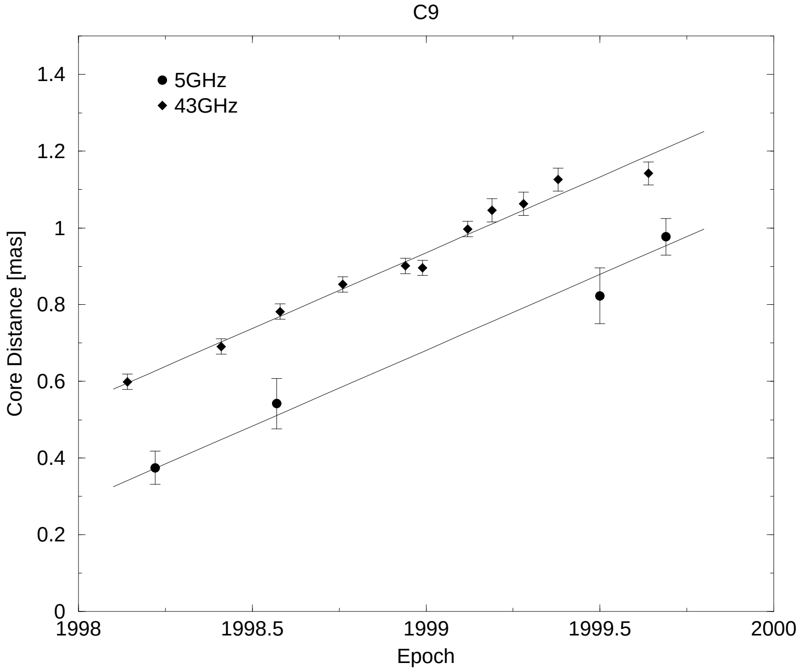

Figure 4.18: Core shift between 5 and 43 GHz. The core shift derived is 0.254 mas.

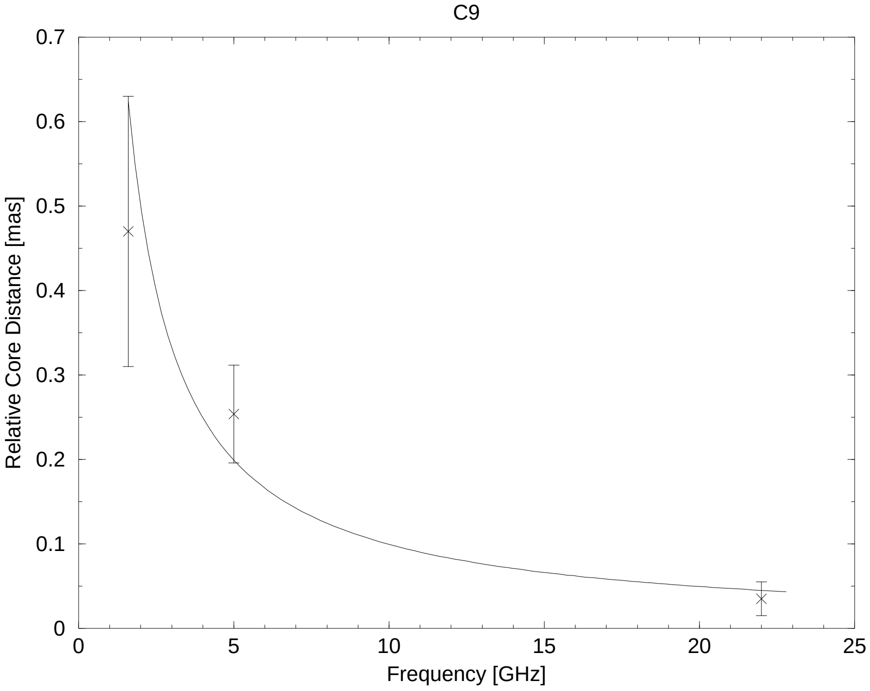

Figure 4.19: Frequency dependent core shift derived with respect to the reference frequency of 43 GHz and for core distances between 0.3 and 0.9 mas. The fit corresponds to $r_{core} \propto \nu^{-1.00\pm0.11}$.

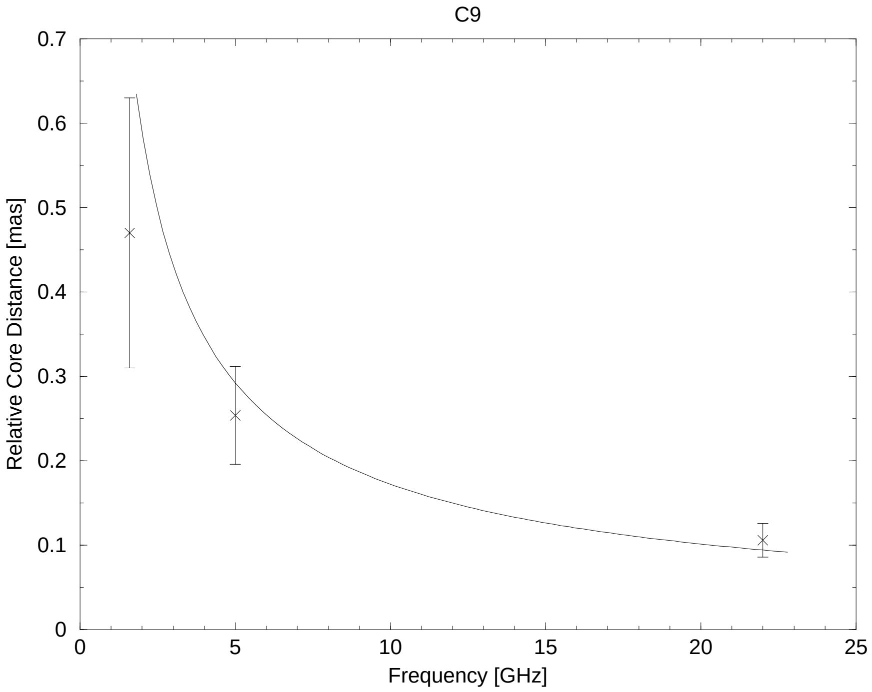

Figure 4.20: Frequency dependent core shift derived with respect to the reference frequency of 43 GHz and for core distances between 0.9 and 1.2 mas. The fit corresponds to $r_{core} \propto \nu^{-0.76\pm0.07}$.

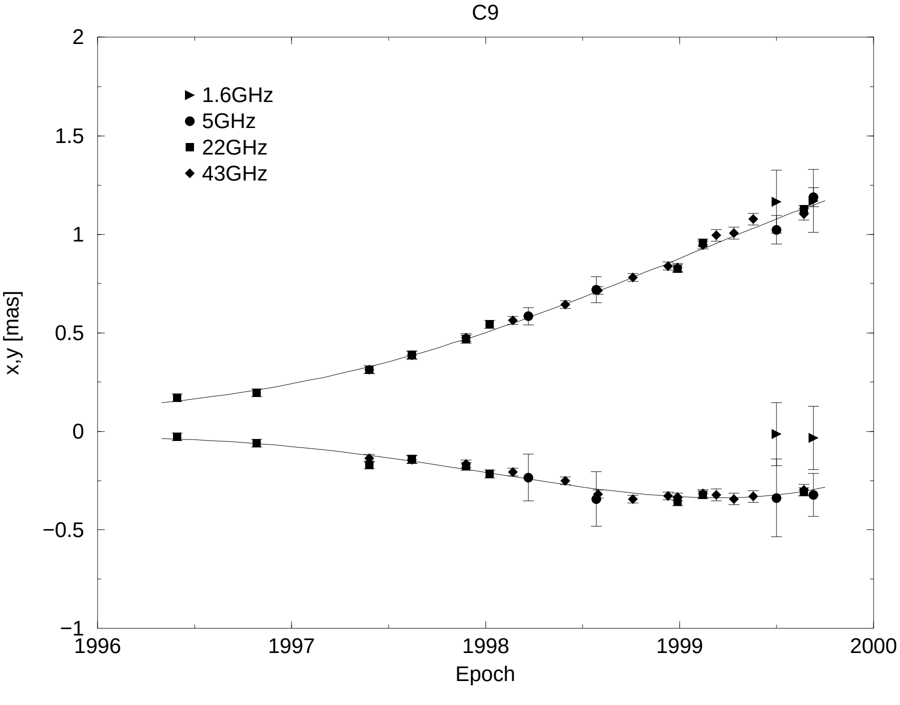

Figure 4.21: Polynomial fits of the relative $x(t)$ and $y(t)$ positions of C9. The determined core shift with respect to the 43 GHz data is applied to the data-points at lower frequencies.

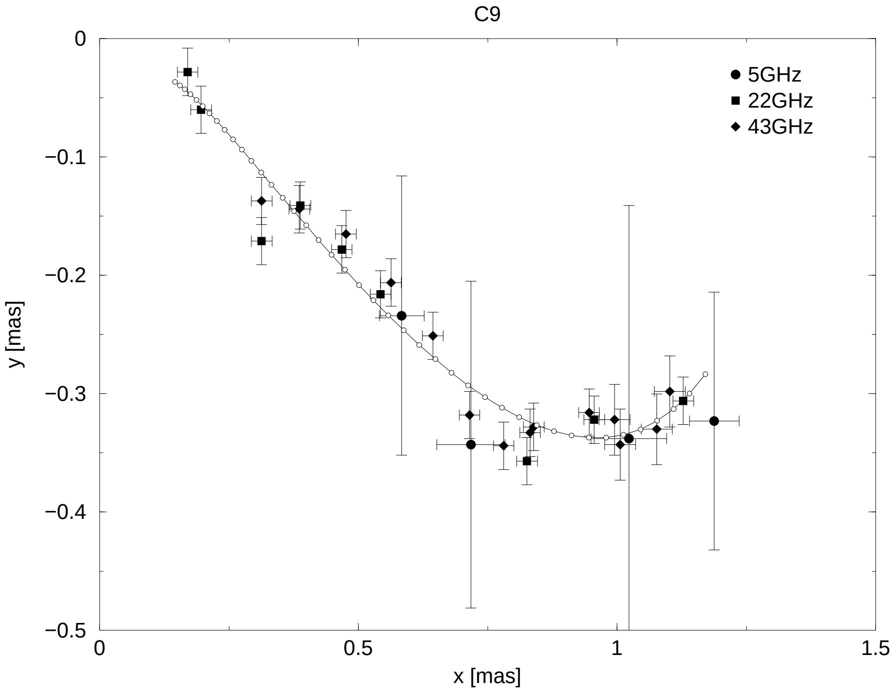

Figure 4.22: Two dimensional trajectory of C9. The line is reconstructed from the polynomial fits for $x(t)$ and $y(t)$. The circles on the trajectory mark time steps of one month and illustrate an acceleration of C9 after the first two epochs followed by a constant velocity.

4.7 Jet Component C10

4.7.1 Core Shift

Within 0.4 mas core distance, no core shift is noticeable between the 22 and 43 GHz measurements (see Figure 4.23). Only the latest data point (1999.64) at around 0.55 mas core distance shows a shift of $\sim$ 0.1 mas between 43 GHz and the lower frequencies. A transition from an optically thick to an optically thin regime occuring at $r \approx 0.4$ mas can cause this behaviour. Because there are as yet no more data at larger distances, one cannot check whether the core shift seen in 1999.66 is real. Thus, the C10 data are not corrected for the effect of the core shift.

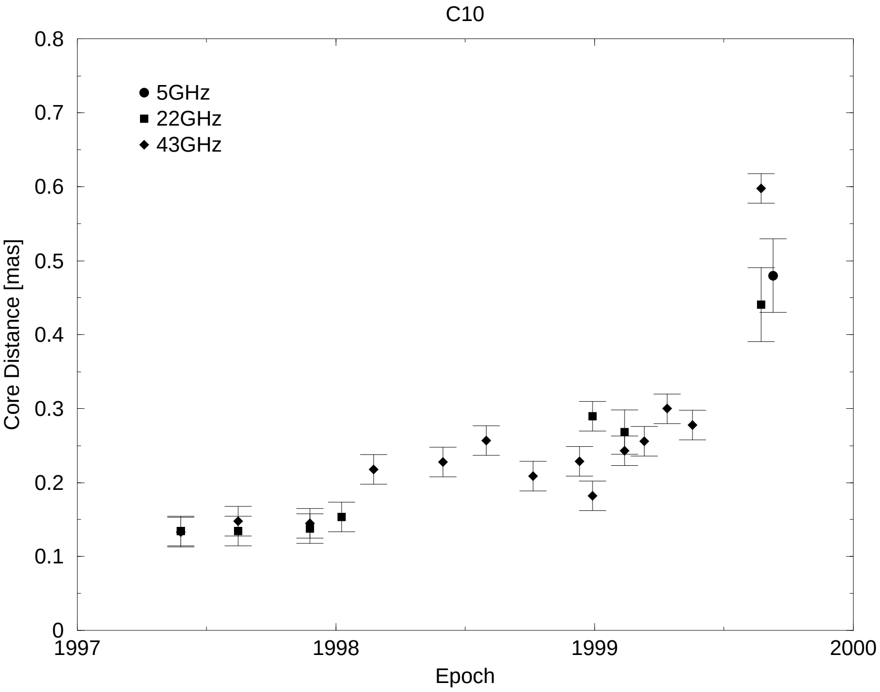

Figure 4.23: Core distance of C10 at 5, 22 and 43 GHz. A core shift below r= 0.4 mas is not noticeable. An optically thick emission regime can cause this behaviour.

4.7.2 Trajectory

From the first epochs, the ejection epoch is extrapolated to 1995.5, which coincides with an observed flare. This presumed ejection epoch is used to constrain the $x(t)$ and $y(t)$ fits. Three artificial data points are introduced between the ejection epoch and the first observed epoch, in order to force the polynomial fit to have a good agreement at the first epoch. These artificial data points are not used in the subsequent investigations. The obtained fits are shown in Figure 4.24, and the reconstructed trajectory is plotted in Figure 4.25. The white circles on the trajectory represent time steps of one month. In both pictures, one sees the long retention period within 0.3 mas followed by a strong acceleration. C10 shows first a small movement to the west followed first by a northward arch and later by a steep motion to south-west.

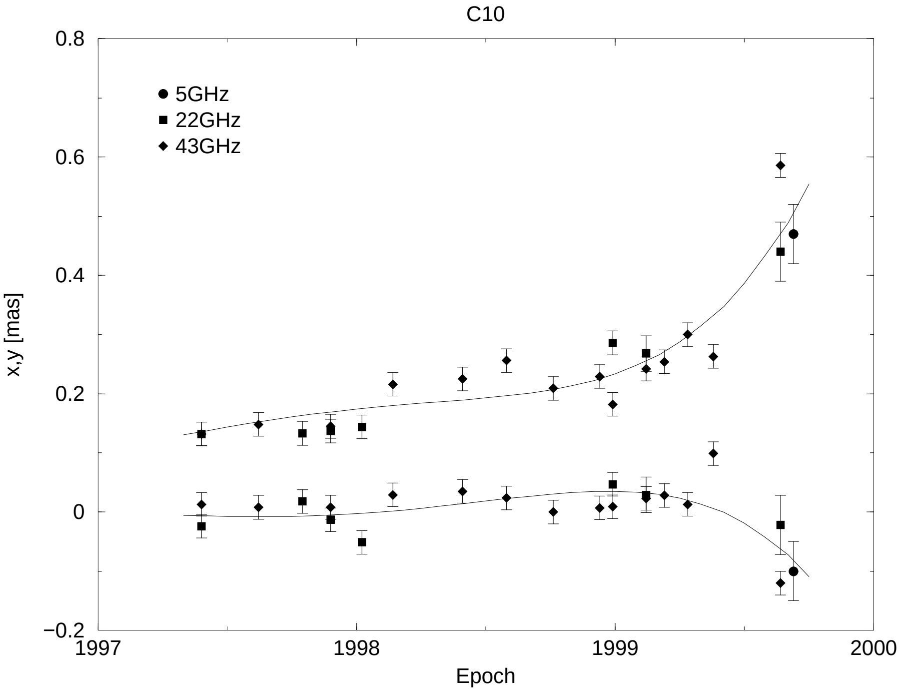

Figure 4.24: Polynomial fits for the relative $x(t)$ and $y(t)$ position of C10. The fits result from the combination of all data points at 5, 22 and 43 GHz. The fits are tied to the ejection epoch 1999.5 but not corrected for the frequency dependent shift of the core.

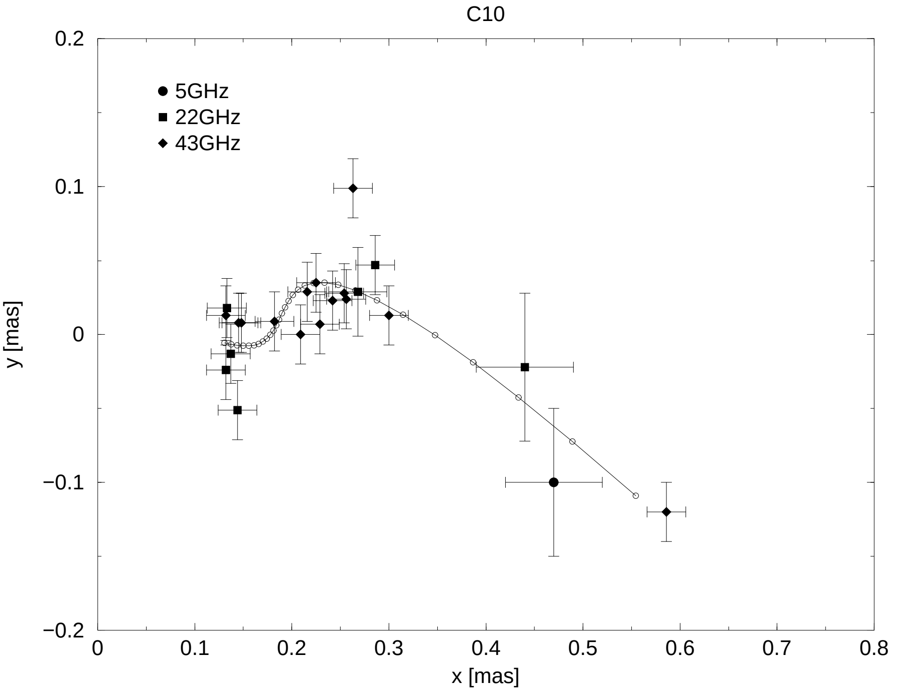

Figure 4.25: Two dimensional trajectory of C10. The path is reconstructed from the polynomial fits for $x(t)$ and $y(t)$. The circles on the trajectory mark time steps of one month.

4.8 Jet Component C11

4.8.1 Trajectory

C11 is the closest jet component detected so far. This feature is only visible in the data sets at 43 GHz. The component is traced within the inner 0.15 mas better than any other jet component in 3C 345. The component motion determined from the first three data points is extrapolated to determine the ejection epoch, yielding at 1996.62. This epoch constrains the polynomials $x(t)$ and $y(t)$ (Figure 4.26). The reconstructed trajectory is shown in Figure 4.27. One sees a slight turn to the north at $x = 0.09$ mas followed by a straight motion to the south-west. The white circles on the trajectory mark time steps of one month. They indicate a strong acceleration at distances larger than 0.1 mas.

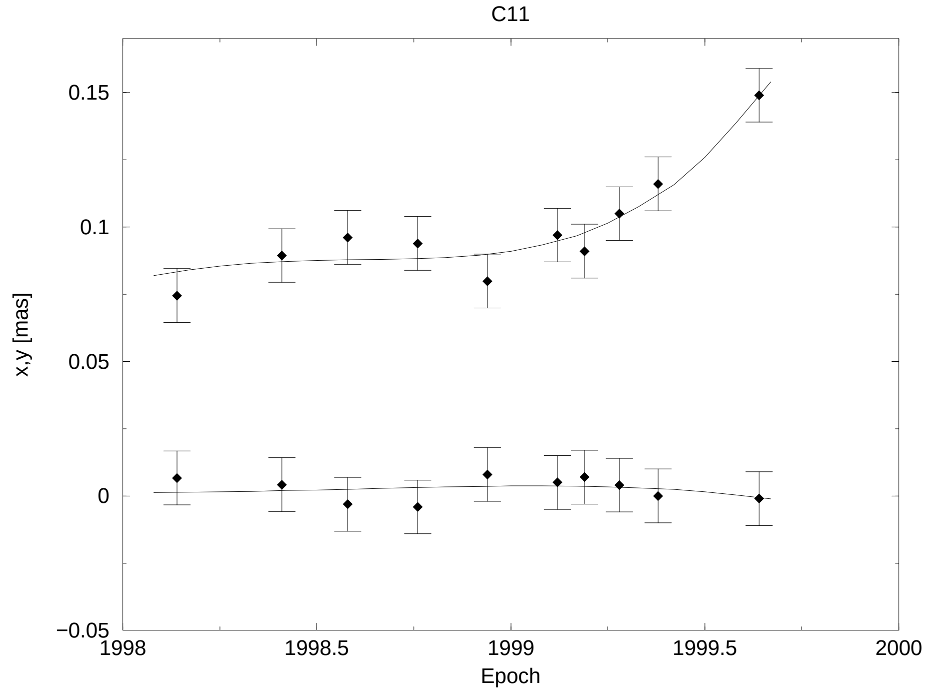

Figure 4.26: Polynomial fits for the $x(t)$ and $y(t)$ position of C11. All data points are measured at 43 GHz.

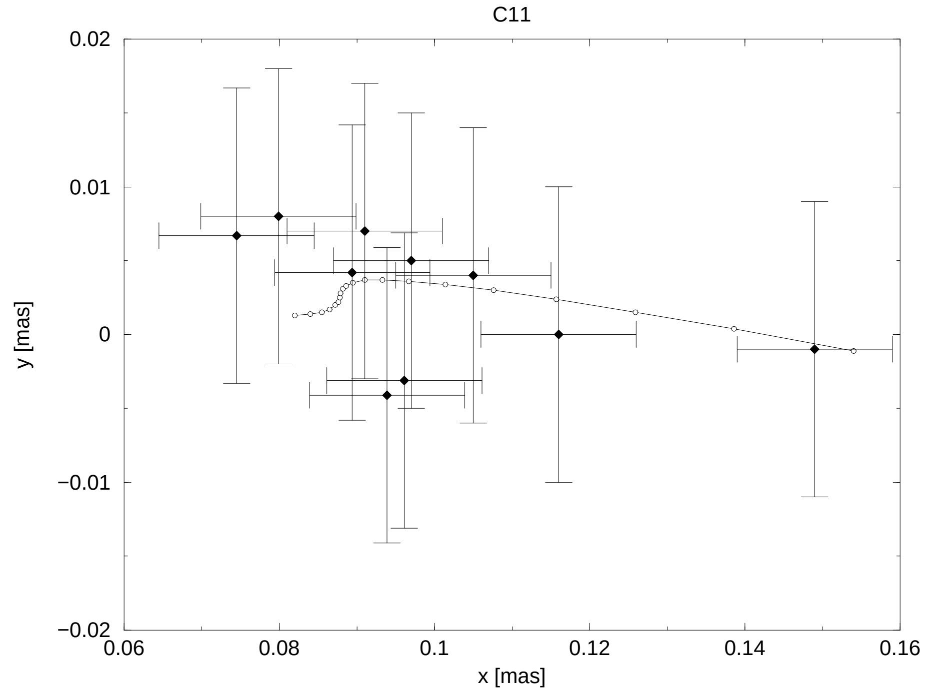

Figure 4.27: Reconstructed trajectory made of the $x(t)$ and $y(t)$ fits. The circles mark time steps of one month.

4.9 Component Trajectories in Comparison

The comparison of the different component trajectories provides an opportunity to search for an underlying mechanism of the curved jet geometry. The two outermost jet features C4 and C5 show completely different tracks at $x(t) \leq 4$, but further out their trajectories become similar. While C4 makes only a small turn to the south, followed by a straight movement to the north-west, C5 goes down to $y(t) \approx -0.5$ mas before it turns back. The feature C7 shows only a motion to the south-west so far, but is expected to turn back during the next few years, in order to comply with the large scale geometry of the jet.

Until this work, C5 was the only component that showed a strong deviation to the south. A comparison between C5 and C8 shows a surprising similarity with the only difference that the trajectory of C8 is tighter and less deep than that of C5 (Figure 4.29). Equivalent points of these trajectories (e.g. turning point, zero-crossing of the y-axis from south to north) are 8–10 years later for C8 than for C5.

The next younger component C9 was ejected close in time to C8 and shows a similar trajectory at distances between $y(t) = -0.08$ mas and $y(t) = -0.23$ mas.

The next younger component, C10, first makes a small turn to the north and follows the previous component C9, with the same slope measured between $x(t) \approx 0.25$–0.5 mas but with a shift to the west. Without the northward turn, C10 would have followed almost exactly the path of C9.

The youngest component C11 is only observed in the immediate vicinity of the core so far. In comparison with C10, the trajectory of C11 looks tiny. Nevertheless, C11 comes from the same direction as C10, which could result from their close ejection epochs and possible relation to the same outburst. Further observations will show whether their trajectories will be similar or evolve differently.

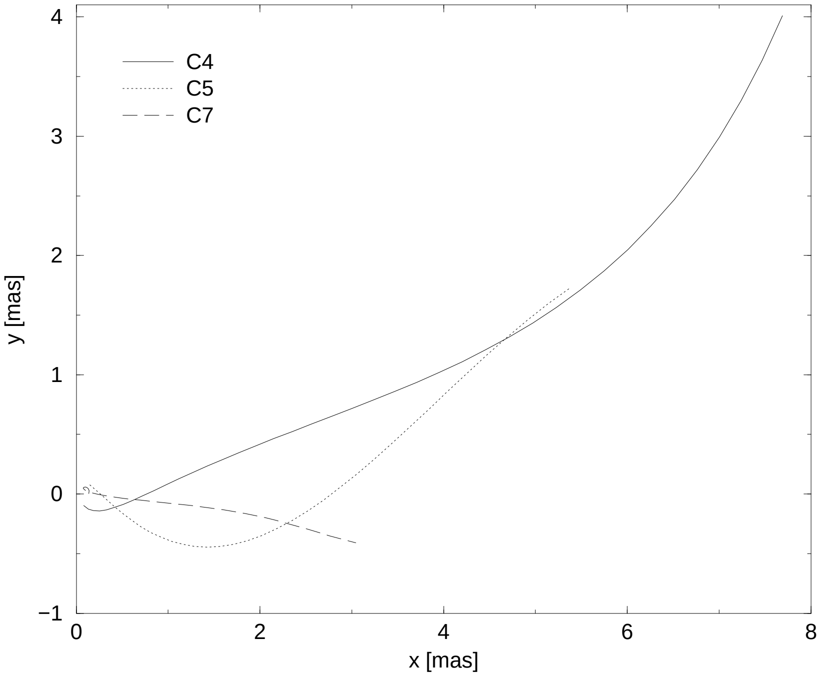

Figure 4.28: Comparison of the trajectories of C4, C5 and C7. The shape of the trajectories is very different.

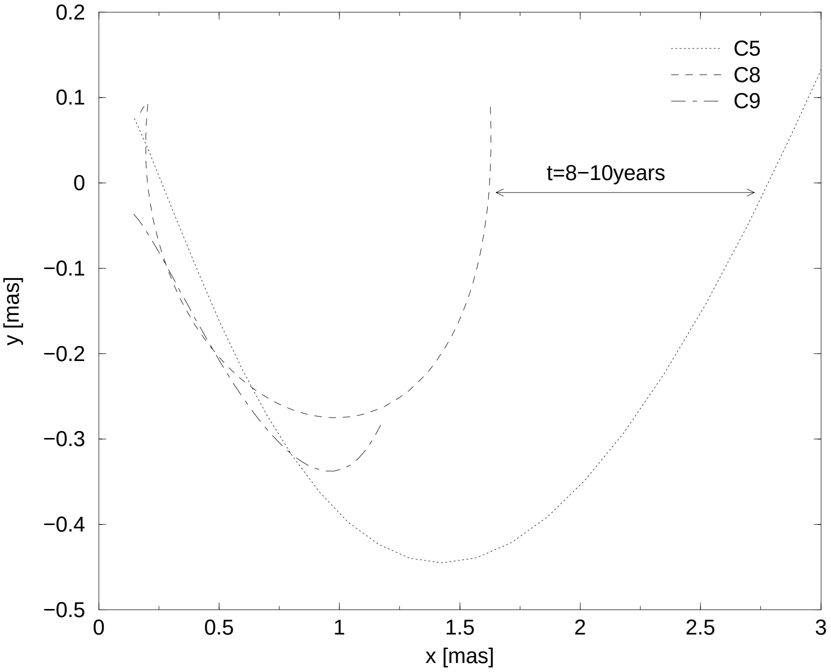

Figure 4.29: Comparison of the trajectories of C5, C8 and C9. Remarkable is the similar shape of the trajectories.

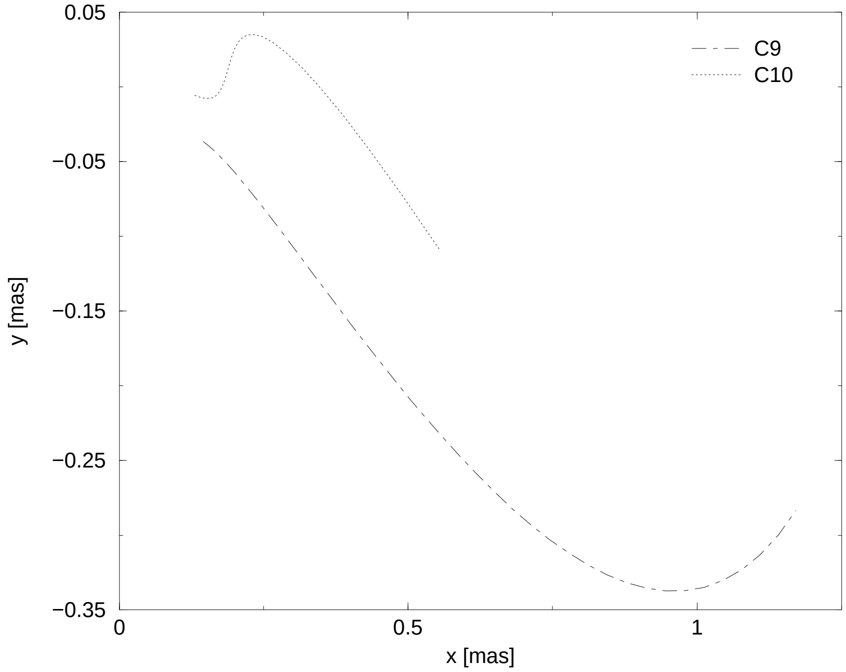

Figure 4.30: Comparison of the trajectories C9 and C10. After C10 makes a turn to the north, the slope of the trajectory becomes the same as for C9.

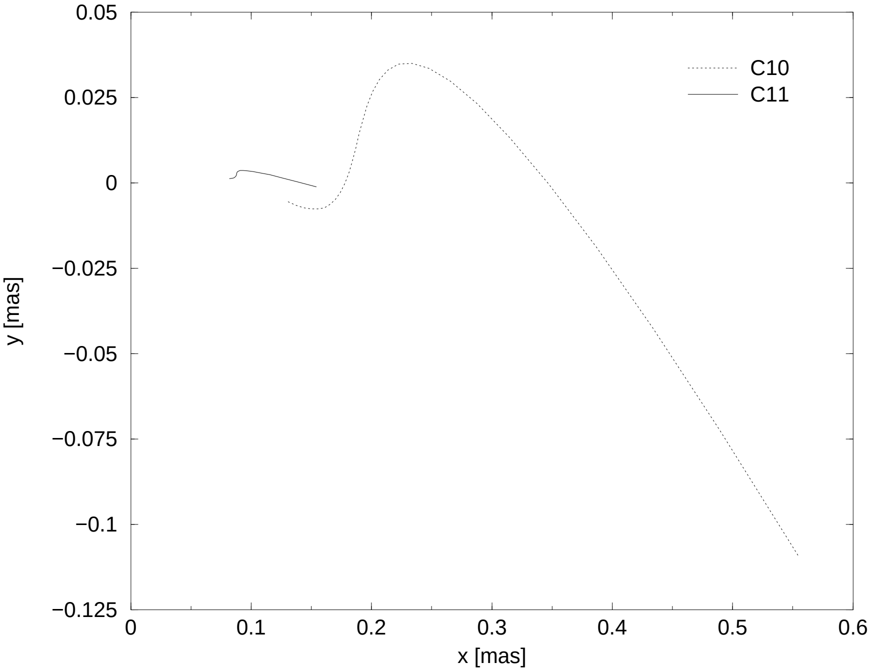

Figure 4.31: Comparison of the trajectories C10 and C11.

4.10 Components Overview

An overview of the separation of the components C4 – C11 relative to the core is shown in Figure 4.32. The polynomials fitted of the data do not take the extrapolated ejection epochs into account and only illustrate the general trend of the moving jet features. After the ejection of C5 there was no new jet component observed for ~ 5 years. After this time, C6 and C7 were ejected very close to each other with estimated ejection epochs less than 1 year apart. While C6 was no longer observable after about 5 1/2 years, C7 stayed a dominant feature of the inner jet. About 3 1/2 years later C8 was observed for the first time and roughly the same time later a group of components (C9, C10 and C11) were ejected within ~ 2 years. Since the groups C6/C7 and C9/C10/C11 are strongly related to each other, C8 lies somewhere in between and approached C9 during its evolution. This illustration shows that the jet features in 3C 345 might be ejected in groups and could be physically related to each other.

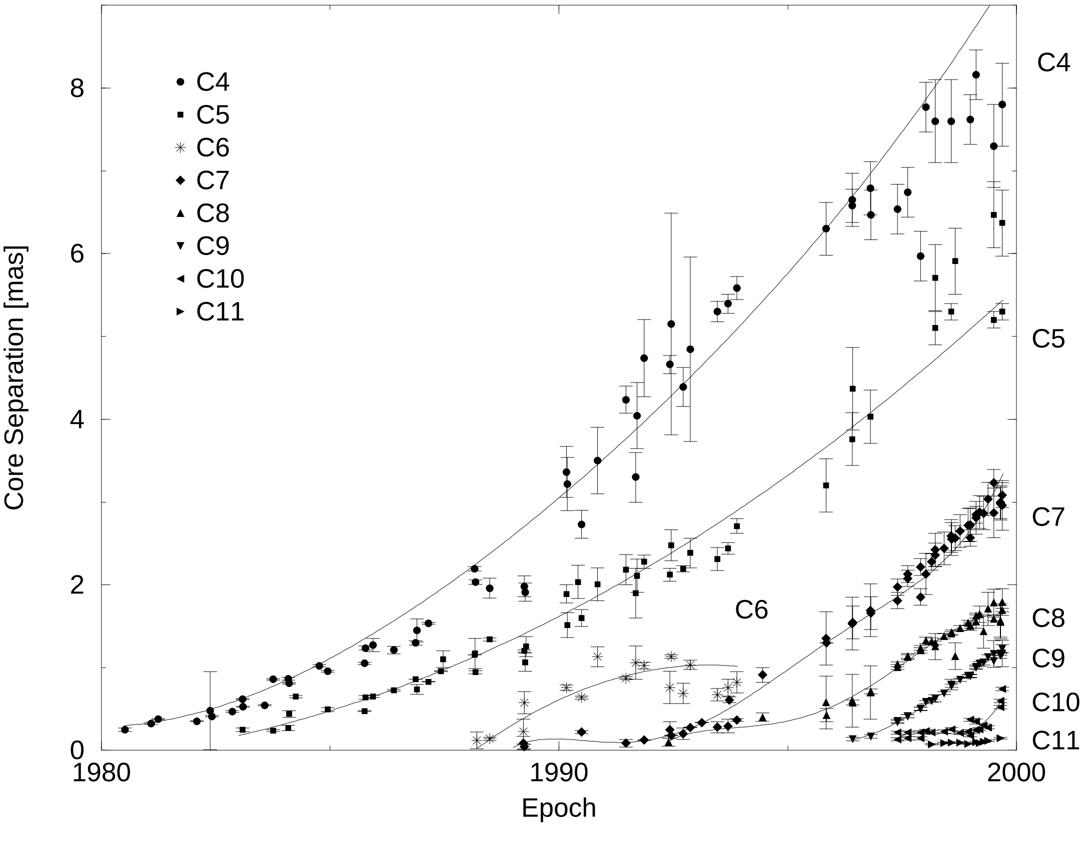

Figure 4.32: Component separation relatively to the core. The jet features were ejected in groups.

4.11 Calculated Kinematic Jet Parameters

Using the polynomials obtained for the different components, one can calculate the evolution of their proper motions:

$$\mu(t) = \left[\left(\frac{dx}{dt} \right)^2 + \left(\frac{dy}{dt} \right)^2 \right]^{1/2} \tag{4.3}$$

The distance traveled along the jet is determined by:

$$\Theta_{app}(T) = \int_{T_0}^{T} \mu(t) dt \tag{4.4}$$

In the standard cosmological model ($\Lambda = 0$), the luminosity distance is given by

$$D_L = \frac{c}{h H_0 q_0^2} \left\{ q_0 z + (q_0 - 1) \left[(1 + 2 q_0 z)^{1/2} - 1 \right] \right\} \tag{4.5}$$

(e.g. Mattig 1958, Weedman 1986). For 3C 345, it results in $D_L = 1.99 h^{-1}$ Gpc (with $H_0 = 100h$ km s^{-1} Mpc^{-1}, $q_0 = 0.5$ and $z = 0.595$) (Hewitt & Burbidge 1993). The angular dimension of 1 mas translates into a linear extension of $3.79\,h^{-1}$pc and a proper motion of 1 mas year^{-1} is equivalent to $19.7\,h^{-1}c$.
The comoving distance is related to the luminosity distance (e.g. Weinberg 1972)

$$D_M = (1 + z)^{-1} D_L \tag{4.6}$$

and the apparent velocity of the jet components is calculated by

$$\beta_{app} = \mu(t) D_M \tag{4.7}$$

and related to β and the angle to the line of sight θ:

$$\beta_{app}(t) = \frac{\beta(t) \sin \theta(t)}{1 - \beta(t) \cos \theta(t)} \tag{4.8}$$

With β=const, one gets two solutions for $\theta(t)$:

$$\cos \theta(t) = \frac{\beta_{app}^2(t) \pm \left[\beta^2 \left(\beta_{app}^2(t) + 1 \right) - \beta_{app}^2(t) \right]^{1/2}}{\beta \left(\beta_{app}^2(t) + 1 \right)} \tag{4.9}$$

The observed superluminal motion and the strong changes of the component trajectories in 3C 345 can be explained as best with the small angle "+" solution (for discussion about both cases see Lobanov 1996). With the determined β and θ, one can now calculate the component Doppler factor

$$\delta = \frac{1}{\gamma (1 - \beta \cos \theta)} \tag{4.10}$$

Taking into account the light aberration correction (e.g.: Rybicki & Lightman 1979) in the rest frame of the jet

$$\cos \theta'(t) = \frac{\cos \theta(t) - \beta(t)}{1 - \beta(t) \cos \theta(t)} \tag{4.11}$$

one can finally calculate the traveled distance in the rest frame of the jet

$$R(T) = (1 + z)^{-1} \int_{T_0}^{T} \frac{\beta(t)}{1 - \beta(t) \cos \theta'(t)} \tag{4.12}$$

4.12 Proper Motion

The equations (4.3) and (4.4) are used to plot the proper motion as a function of the apparent traveled distance. Figure 4.33 shows the inner 3 mas of the jet for components C7 – C11. Figure 4.34 presents the full paths of the features C5 – C11. One sees a strong acceleration of the components within the inner mas followed by an almost linear increase at larger distances. The proper motion of younger features is higher at the same core distances compared with older components. This behaviour was already reported for C1–C7 in Lobanov (1996) and it is present also in the features C8–C11. This is a strong sign that a global change of the jet occurs (e.g. changes of intrinsic physical parameters or a jet precession). There is also a similarity of the slope of close ejected components (C7, C8 and C9). The same behaviour was described by Lobanov (1996) for the features C3, C3a and C4. Also the decrease of proper motion for a short period is observed in most of the components, including C7, C8 and C9. This can be caused by the projection of a helical jet geometry and mark the receding part of a jet component. The youngest components C10 and C11 play a particular role due to their closeness to the core of the jet. To draw a clear picture of their proper motion more observations are needed. Nevertheless, they show the same trend as seen in the earlier components. It will be very interesting to see if new observations confirm the large proper motion of $\mu(t) \approx 0.7\,\mathrm{mas\ year}^{-1}$ within 0.5 mas for C10. A comparable speed was reached by older components (see C5 in Figure 4.34) only at a much longer traveled distance of $r \approx 7\,\mathrm{mas}$.

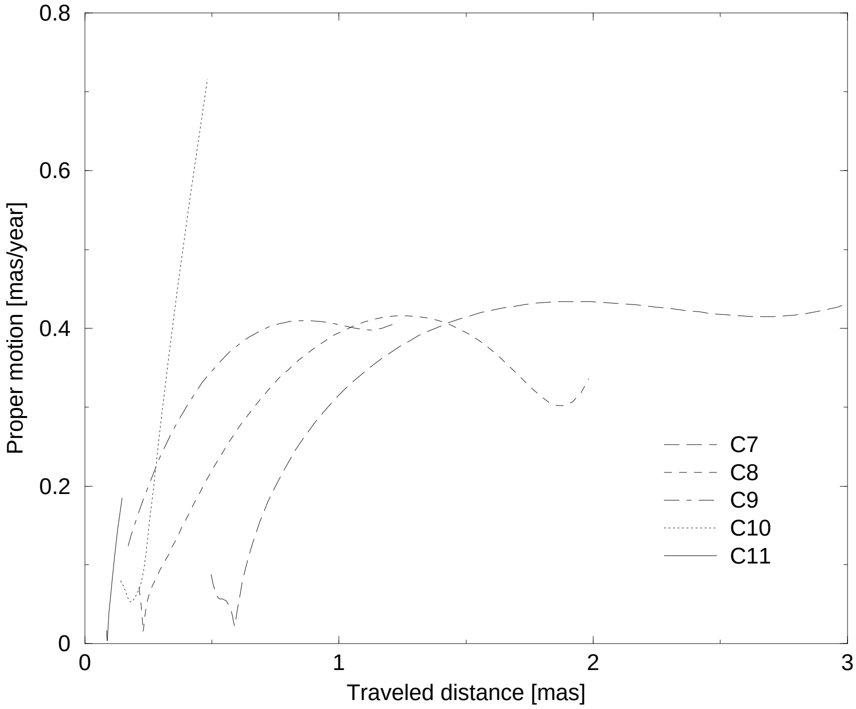

Figure 4.33: Proper motion vs. apparent traveled distance of the inner 3 mas of the jet components C7 to C11.

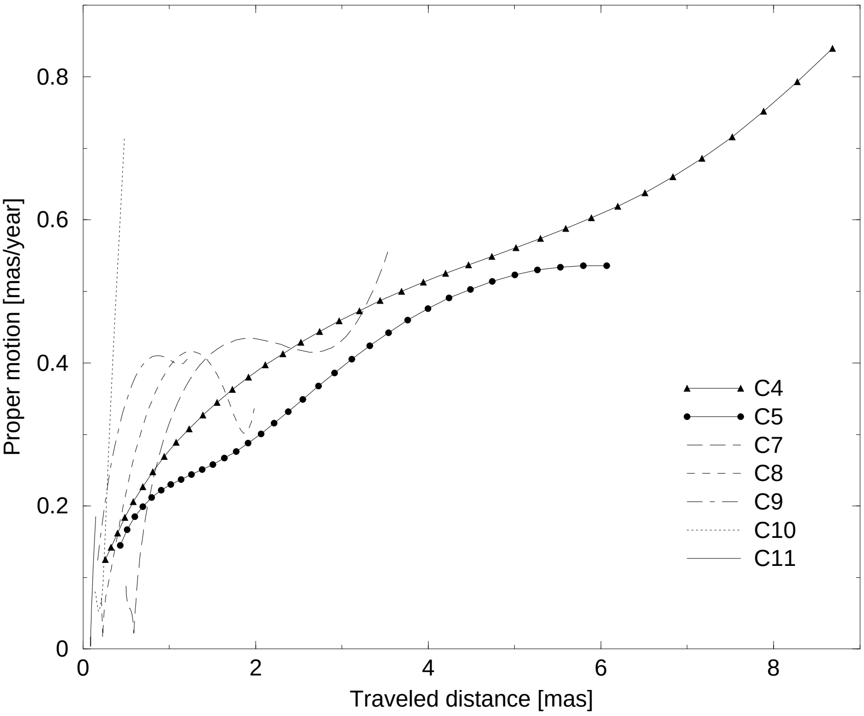

Figure 4.34: Proper motion vs. apparent traveled distance of the jet components C5 to C11.

4.13 Kinematic Jet Parameters

4.13.1 Sensitivity of the Polynomials

The formulae detailed given in section 4.11 are used in the program `jetskin` (Lobanov 1996), to calculate the jet parameters for a given polynomial of a moving component. The shape of the polynomial can be critical for the derived parameters. To illustrate this, the results obtained with `jetskin` are plotted for 8 different polynomials ($\gamma_{jet} = 12$) in Figure 4.35. All polynomials have the same ejection epoch and they all cross at the same point after some time. To provide a physical reference to the jet of 3C 345, the fits are normalized to the apparent distance traveled by C7. All polynomials start at epoch 1988 at $x(t) = 0\,\mathrm{mas}$ and stop after 11 years at $x(t) = 3.25\,\mathrm{mas}$ (epoch 1999). For simplicity, only $x(t)$ varies and $y(t) = 0$. The $x(t)$ polynomials are plotted in the upper left panel. The rest frame traveled distance r, is plotted in the upper right panel, the Doppler factor δ, is in the lower left panel and the angle to the line of sight θ, is in the lower right panel.

Consider first the simplest case of a linear $x(t)$ fit (*solid* line). Then r is also linear and reaches 16.3 pc in 1999 while δ and θ stay constant. A very small change to a second order polynomial $x(t)$ is represented by the *circle* line. The changes in r, δ and θ are also marginal in this case. If one stretches the polynomials $x(t)$ further (as shown with the *square*, *diamond* and *dotted* lines), the component needs progressively longer times in the observers' frame to reach the final distance of $x(t) = 3.25\,\mathrm{mas}$. The apparent velocity is slower in the beginning and increases with time. If one compares the *solid* fit and the *diamond* fit at epoch 1990 then one can see a difference of the apparent distance traveled of only $\Delta x(t) = 0.31\,\mathrm{mas}$, while it corresponds to $\Delta r(t) = 11.4\,\mathrm{pc}$ difference (*solid*: $r(1990) \approx 3\,\mathrm{pc}$ *diamond*: $r(1990) \approx 14.4\,\mathrm{pc}$) in the rest frame of the jet. This means that polynomial fits that differ by only a few tens of 1 mas may in principle have a factor of 5 difference of distances traveled in the rest frame.

The biggest effect is seen in the most extreme case, between the *solid* polynomial fit and the *dotted* one. The difference of $\Delta x = 0.45\,\mathrm{mas}$ at epoch 1990 results in an almost 17 times larger distance traveled in the rest frame of the jet. The component undergoes a huge acceleration during the first years while it slows down substantially later on. The angle to the line of sight changes from 0.26° to 3.5°, and δ decreases from 23.9 to 15.7.

An almost mirrored case with regard to the *dotted* one is the *dashed* one. The component moves very slowly in the rest frame of the jet during the first years and starts to accelerate during the final years. The parameters θ and δ behave in the opposite way compared with the *dotted* case. The total distance traveled in the rest frame after 11 years is almost the same.

To sum up, a steeper polynomial fit causes a slower moving component in the rest frame at a bigger angle to the line of sight and a lower Doppler factor. The *triangle* and the *star* polynomial fits show a combination of changing from flat to steep to flat and vice versa.

Sparsely sampled data can result in artifacts appearing in the polynomial fits between the data points measured, which would yield wrong jet parameters. The dense sampling of this work and the combination of observations at different frequencies warrants a good accuracy of the polynomials and reduces the chance for errors. The most crucial part of the polynomials is the start. The ejection epoch of the jet components can only be extrapolated from the first few observed epochs. To avoid possible artifacts at the beginning of the component trajectories, the extrapolated period between the estimated ejection epoch and the first observation is discarded. Moreover, the rest frame traveled distance is set to 0 for the first observed epoch. The evolution of the components is investigated only in the range where the observations were done.

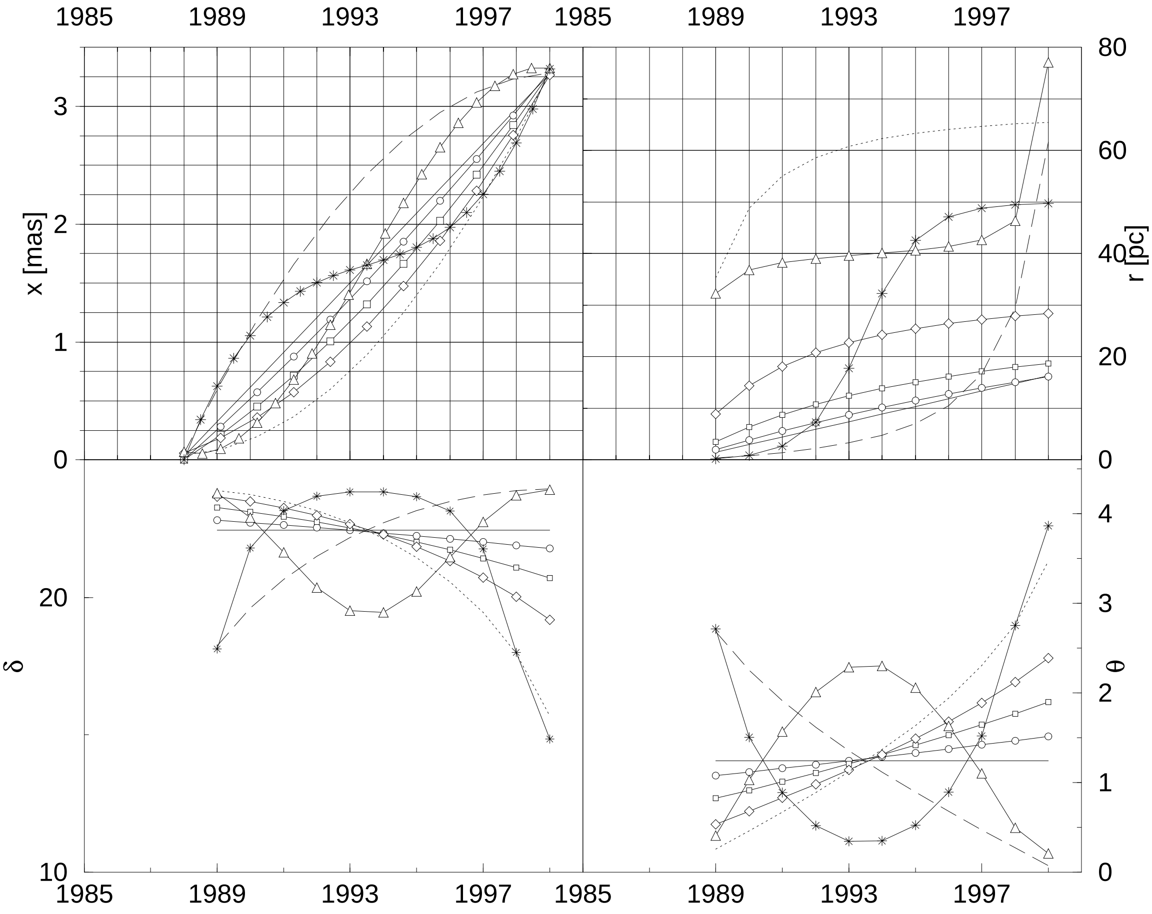

Figure 4.35: Illustration of the effect of slight variations of the polynomials on the calculated jet parameters. In the upper left panel, 8 $x(t)$ polynomials are plotted. The corresponding distance $r(t)$, traveled in the jet rest frame is shown in the upper right panel. The Doppler factor δ and the angle of the line of sight θ are shown in the lower panels. $\gamma = 12$ is used for all calculations. Note the small difference between the solid and dotted lines in the apparent distance plot and the resulting significant discrepancy between these lines in the rest frame distance.

4.13.2 Minimum allowed Lorentz Factor

The value of the Lorentz factor γ_j of the jet is unknown and can be only roughly estimated from the observed X-ray emission (ZCU 1995, Unwin et al. 1997). To get a useful limit of γ_j, a first approach is the lowest possible Lorentz factor, γ_{min}, which describes the least kinetic power for a jet component with the observed apparent velocity $\beta_{app}(t)$:

$$\gamma_{min} = (1 + \beta_{app})^{0.5} \tag{4.13}$$

The obtained minimum allowed Lorentz factors of the innermost jet components (C7–C11) are shown in the upper left panel of Figure 4.36. They vary between $\gamma_{min} = 1.0$ and $\gamma_{min} = 14.2$. The corresponding component distance traveled in the rest frame r, the Doppler factor δ and the angle to the line of sight θ are plotted in the other panels. While r behaves well, one sees substantial changes of θ within a very short time. The components C7, C8 and C10 change their angle from $\theta \approx 60°$ to $\theta \approx 10°$ within 1–2 years. It is very unlikely that the jet could sustain these rapid changes of its direction. This makes the case with the minimum allowed Lorentz factor unlikely.

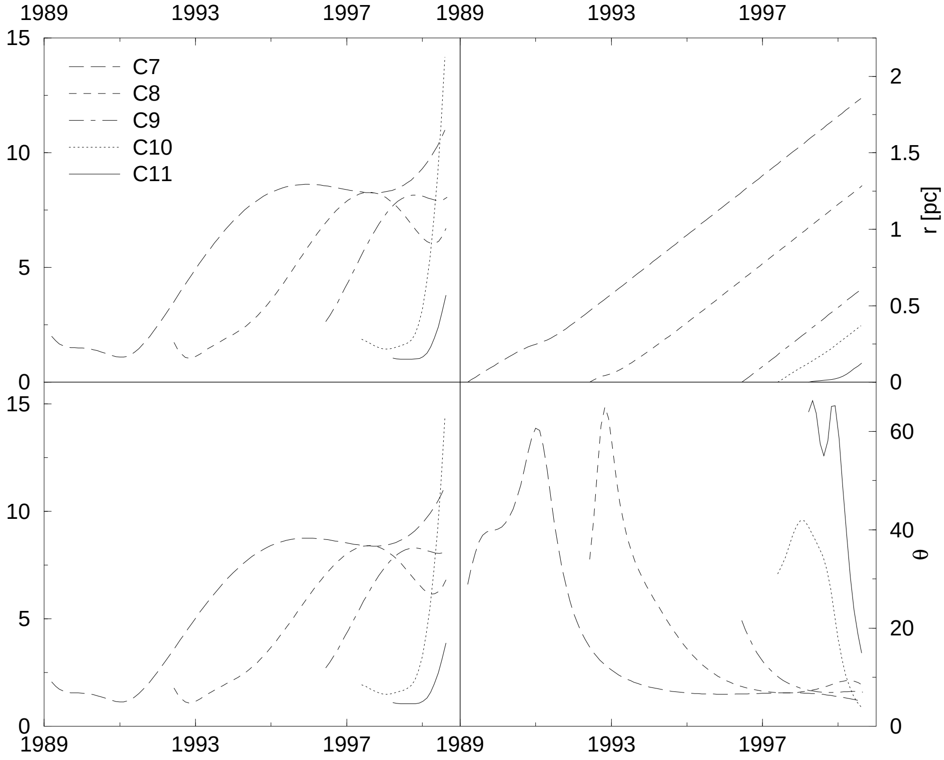

Figure 4.36: Evolution of the component kinematic parameters in the jet. The minimum kinetic power condition $\gamma_{min} = (1 + \beta_{app})^{0.5}$ is used. The variation of the Lorentz factor (upper left), the traveled distance in the rest frame of the jet (upper right), the Doppler factor (lower left) and the angle to the line of sight (lower right) are plotted. While r changes smoothly, θ shows large variations within short time intervals.

4.13.3 Constant Lorentz Factor

The first possibility to introduce a constant Lorentz factor is to assign an individual γ for each component, reflecting the minimum value acceptable for the whole observing period ($\gamma_{C7} = 11.4$, $\gamma_{C8} = 8.3$, $\gamma_{C9} = 8.2$, $\gamma_{C10} = 16.1$, $\gamma_{C11} = 4$). This case is

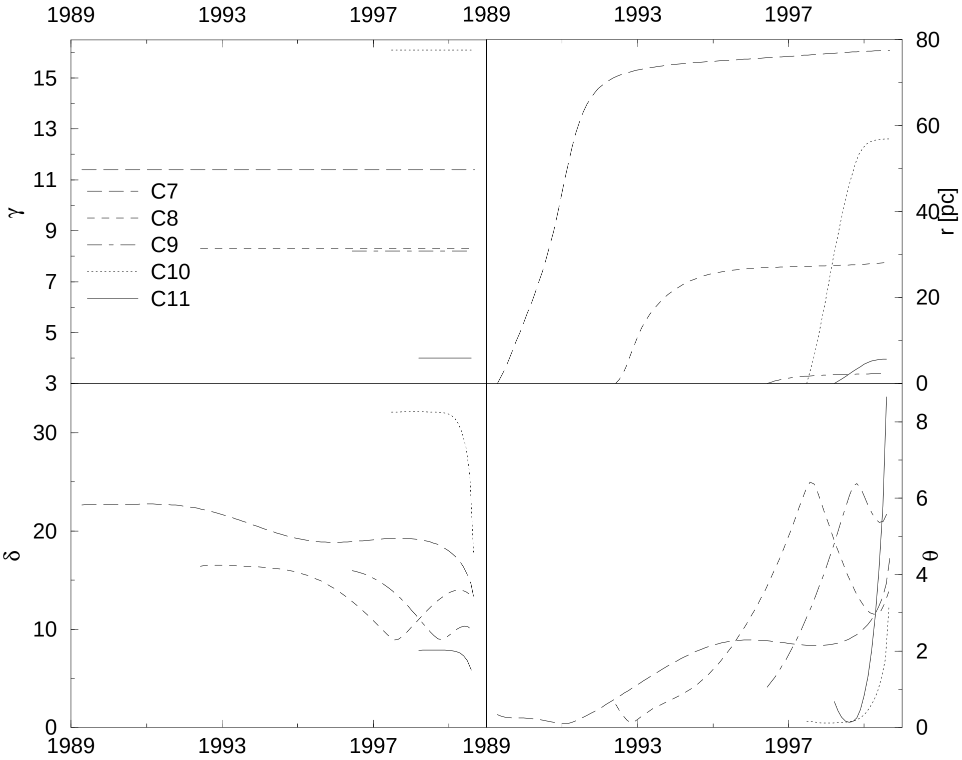

Figure 4.37: Evolution of the component kinematic parameters in the jet. Individual constant Lorentz factors are assumed. The Lorentz factor (upper left), the distance traveled in the rest frame of the jet (upper right), the Doppler factor (lower left) and the angle to the line of sight (lower right) are plotted. θ bends away from the line of sight for all components. The distance traveled in the rest frame of the jet is disordered.

illustrated in Figure 4.37. The viewing angles derived change only slightly, starting at a few tenths of a degree and bending away up to $\theta \approx 8°$ but the distances traveled in the rest frame become chaotic. Jet component C10 overtakes C9 and even C8. Such a disordered motion in the rest frame of the jet can hardly be explained just by an insufficient fit, although the component C10 starts a sharp acceleration only during the last three observed epochs (see Figure 4.24 and 4.25) which has to be confirmed by further observations. The future observations should substantiate the fits, especially for the youngest component C11. This component also shows a strong acceleration only during the last epochs (see Figures 4.26 and 4.27).

A second case for a constant Lorentz factor is described by a single value of γ for all components during their whole evolution within the inner 4 mas. For this constraint, γ has to be at least 15. Since the bulk Lorentz factor is not expected to be higher than $\gamma \approx 20$ (Abramovitz 1992, Henri and Pelletier 1992), this value is within the theoretical limit. If the observed speed belongs to the shock pattern rather than to a bulk motion, the limit is even not so strict. The highest γ derived from polynomials was given by Lobanov (1996) with $\gamma_{C3} = 22.9$. The jet parameters r, δ and θ are shown in Figure 4.38. The viewing angles of all components show a

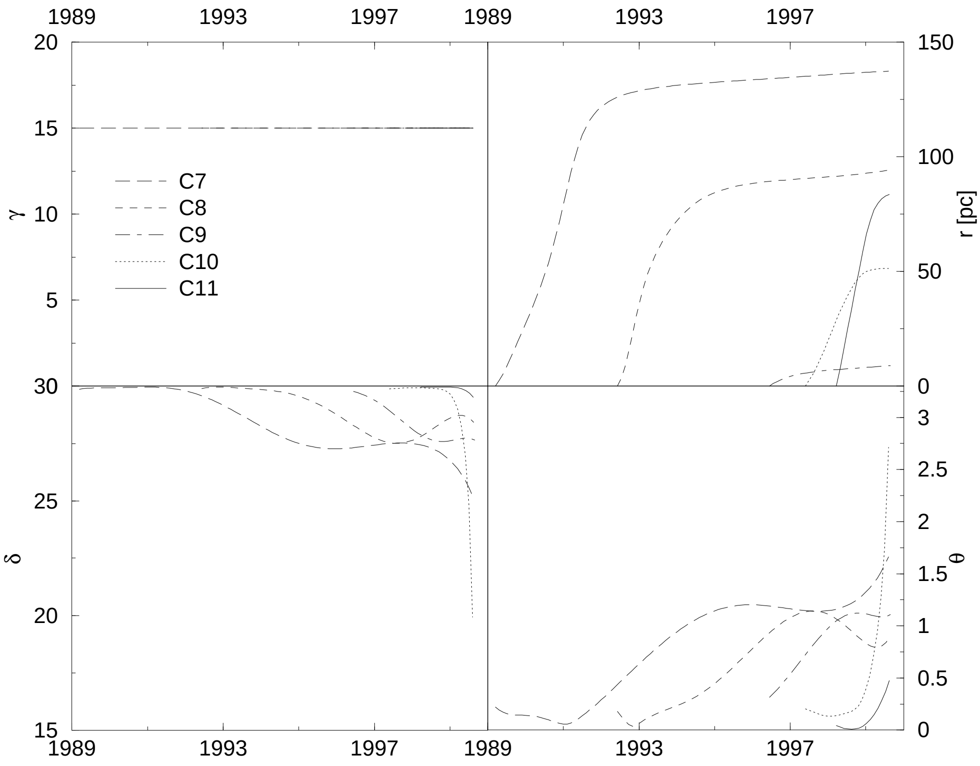

Figure 4.38: Evolution of the component kinematic parameters in the jet. The constant Lorentz factor is assumed to be the same for all components. The Lorentz factor (upper left), the traveled distance in the rest frame of the jet (upper right), the Doppler factor (lower left) and the angle to the line of sight (lower right) are plotted. θ shows for all components a smooth bend away from the line of sight. The traveled distance in the rest frame of the jet is disordered. C11 overtakes C10 and C9. C10 overtakes C9

smooth bend from a few tenths of a degree up to 2.7°. The traveled distance in the jet rest frame shows a similar behaviour as the case with individual constant Lorentz factors. In this case C10 overtakes C9. C11 overtakes C10 and C9. In summary, the case of a constant Lorentz factor, either the same for all components or selected for each component separately, leads to a highly disordered traveled distance in the rest frame of the jet and makes this case unlikely.

4.13.4 Increasing Lorentz Factor

Both the minimum Lorentz factor scenario and the constant γ case are dissatisfying when one considers r and θ together. This suggest a varying Lorentz factor that, in the simplest case, increases with time and reach a maximum at a certain point. A scenario where γ increases steeply with similar slopes for all components and reaches a constant maximum at about 16 is shown in Figure 4.39. For each component, the steepest slope resulting from the 'minimum Lorentz factor' scenario is taken. The viewing angles change rapidly at the beginning, which is caused by the low initial Lorentz factor. As the Lorentz factors increase, the viewing angles closely approach the line of sight and then bend away slowly by a few degrees. The younger components show a similar behaviour, although they start at lower angles due to a higher initial Lorentz factor. The distances traveled in the rest frame of the jet of C11 and C10 still exceed that of C9, but they are much closer together than in the γ=const cases. This indicates a possible deficiency of the simple evolution assumed for the γ factors of the polynomial fits for C10 and C11 at this time range.

However, the arguments above show that only a variable Lorentz factor changing from a minimum value ($\gamma \geq 3$) to a maximum constant value ($\gamma \simeq 16$) can yield a satisfactory description for the component traveled distances in the rest frame of the jet and the corresponding angles to the line of sight.

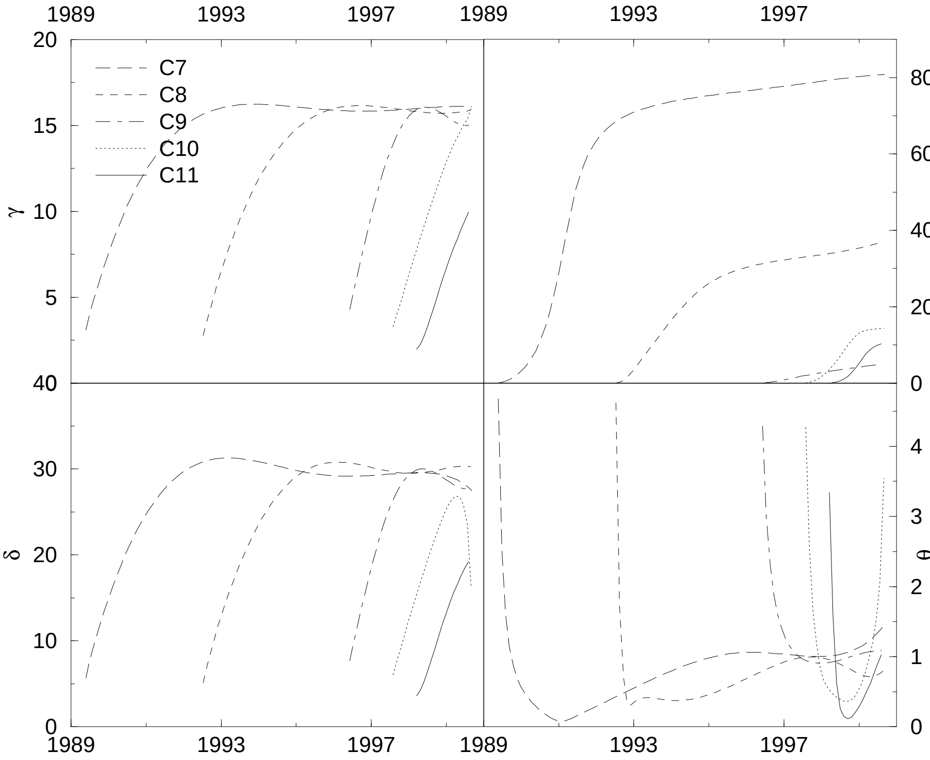

Figure 4.39: Evolution of the component kinematic parameters in the jet. Variable Lorentz factors are assumed, starting at a low value $\gamma \geq 3$ and increasing to a constant value of $\gamma = 16$. The Lorentz factors (upper left), the distance traveled in the rest frame of the jet (upper right), the Doppler factor (lower left) and the angle to the line of sight (lower right) are plotted. The angles to the line of sight are within a few degrees for the most time. The distance traveled in the rest frame of the jet is slightly disordered for C10/C11 and C9.

4.14 Varying Component Ejection Angle

The position angle (P.A) of a jet component at its ejection can reveal an underlying periodic process driven by the central engine. To get an overview of the P.A. evolution of the components within the inner 3 mas, all P.A. of the features C4–C11 at all observed frequencies are plotted in Figure 4.40 as a function of core distance. The error bars are omitted for clearness and are in a range of $0.5° < \Delta$P.A. $< 5°$ from 0.5 to 3 mas. They are larger for shorter ($1.5° < \Delta$P.A. $< 8°$) and longer ($2° < \Delta$P.A. $< 15°$) distances. At small distances ($r < 0.5$ mas) the accuracy of the P.A. determination is influenced by the component closeness to the core. Additionally, the P.A. may vary if the measurements of a component at its first epochs were done at different frequencies. At large distances ($r > 3$ mas) the accuracy of the P.A. determination is influenced by the increased size and the weaker flux density of the components. Polynomial fits to the measured data show the general trend of the P.A. evolution for each component. Since these fits are strongly influenced by the errors mentioned above, they can not be used to simply approximate the ejection P.A. A general trend of all P.A. for the observed components shows that they vary from $-50°$ to $-135°$ within the first 0.5 mas and from only $-80°$ to $-115°$ at core distances from 1 to 3 mas. By comparing several close epochs after the ejection of a new component one can constrain the component ejection angle. The best approach is to use the P.A. of one of the first epochs of a new jet component as its ejection P.A (Figure 4.41).

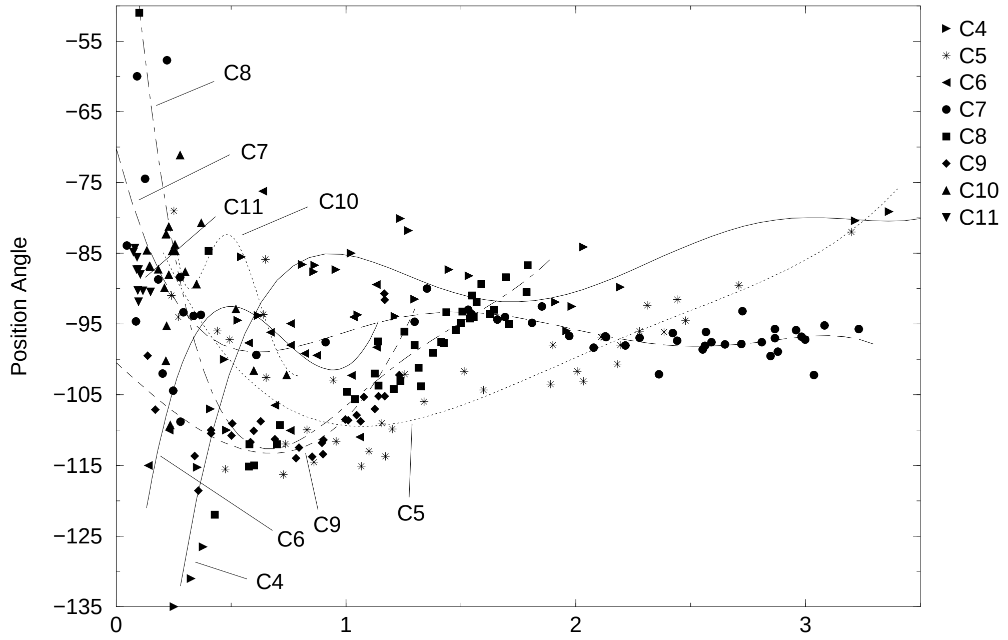

Figure 4.40: Change of the position angle of the inner jet components C4–C11 at all observed frequencies. The lines represent fits to the P.A. for each component. The small numbers in italics mark particular epochs discussed in the text.

The first P.A. values available for C4 show a clear trend of increasing P.A., from which the ejection P.A. can be determined. The P.A. of the first epochs of C5 are within a range of ~ 10° and the P.A. of the first epoch could be used as the ejection P.A. The next component C6, has position angles of P.A.= −110° at 100 GHz and P.A.= −115° at 43 GHz for the first epochs which constrains very well the ejection P.A. C7 is well constraint with a P.A. of −85° at 43 GHz. This makes the P.A. of C7 higher as that for C6. The next feature C8 shows a trend from north to south which makes the P.A. of the first epoch a good estimate of the ejection P.A. This leads to a larger P.A. compared with that of C7. The P.A. of the following three components, C9, C10 and C11 are well determined by the frequent measurements. The P.A of the first observed epochs is used. The very close components C10 and C11 show almost the same initial P.A.

In summary, the starting P.A. of the components shows an oscillation of 8–10 years, illustrated with the dashed line in Figure 4.41. Additionally, an increasing slope ($2.6^\circ \pm 0.3^\circ\,\mathrm{year}^{-1}$) is superimposed to the oscillation which is illustrated by the two dot-dashed lines. This means for instance that the ejection P.A. between C4 and C9 increased by about 36° in 16 years. This periodicity and evolution of the ejection P.A. is a clear hint of an underlying periodic process.

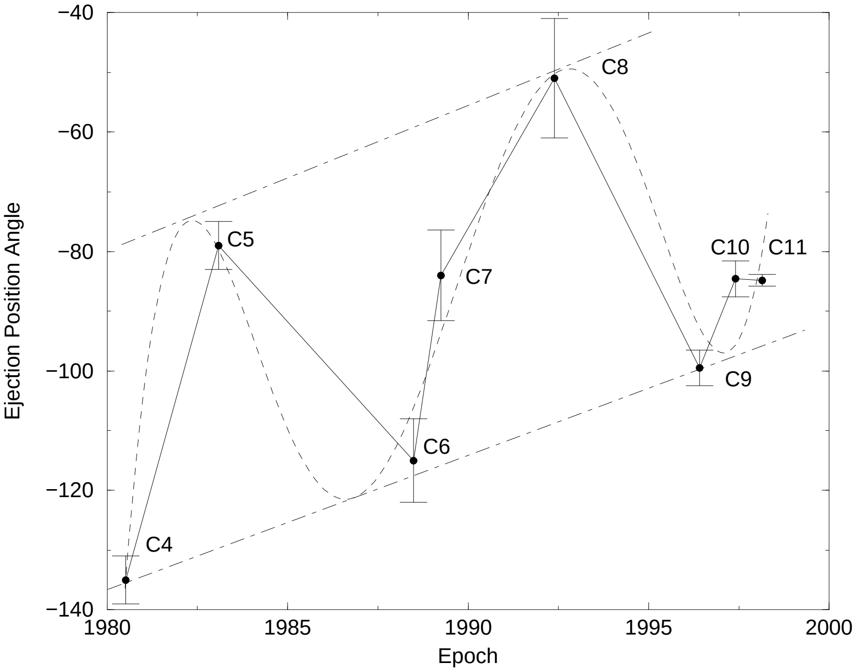

Figure 4.41: Position angles of the jet components at their first observed epochs. The variation of the P.A. indicates a periodicity of 8–10 years. The dashed line represents the best fit and the dot-dashed lines show the general rise ($2.6^\circ \pm 0.3^\circ\,\mathrm{year}^{-1}$) of the initial P.A.

Chapter 5

Flux Density Evolution of the Inner Jet

The flux density evolution of the 5 inner jet components (C7 – C11) and the core (D) of 3C 345 is discussed in this chapter. The observations of the core and each component at all observed frequencies are combined in Figures 5.1 – 5.10. In these Figures open symbols are used for data from the literature and filled symbols denote data from this thesis.

5.1 Jet Component C7

The flux density of component C7 peaks at 22 and 5 GHz between 1991 and 1996 (Figure 5.1). The 5 GHz peak is delayed by 2.4 years with respect to the peak at 22 GHz. Such time delays at different frequencies have been also observed in total flux density monitoring programs (e.g. Lainela *et al.*, 1992). The flux density maximum of the narrow 22 GHz flare can be well approximated with the highest data point resulting in $S_{22peak} = 6.2$ Jy. The broad 5 GHz flare can also be approximated with the highest measured flux density values, resulting in $S_{5peak} = 2.4$ Jy. The strongest increase in flux density is seen at a core distance of about 0.25 mas at 22 GHz (Figure 5.2). This flare correlates quite well with the positional turn to the south-west in the component trajectory (compare Figure 4.9) (for a detailed discussion of these epochs see Lobanov 1996). The fainter and broader flare at 5 GHz at about 1.4 mas core distance correlates with a second turn to the south-west in the component trajectory (compare the 5 GHz epochs in Figure 4.9). Close observations at 1.6, 5, 22 and 43 GHz are available only in the time range 1997–2000 when this jet feature does not show any remarkable flux changes anymore. With the exception of the first epoch at 1.6 GHz, the flux density is higher for lower frequencies in this time range. The small peak at 1.6 GHz might be correlated with the earlier peaks at 5 and 22 GHz to the same physical origin. The time delay of the 1.6 GHz peak is of about 4 years with respect to the 5 GHz peak.

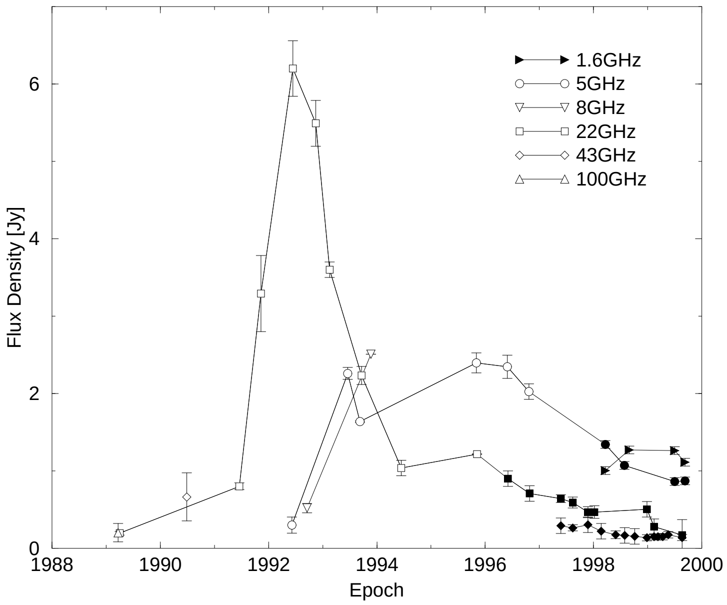

Figure 5.1: Flux density evolution of C7. The big rise in flux density is delayed by 2.4 years at 5 GHz with respect to 22 GHz. The flux density is lower at higher frequencies between 1998 and 2000 (optically thin spectrum). Filled symbols denote data from this thesis.

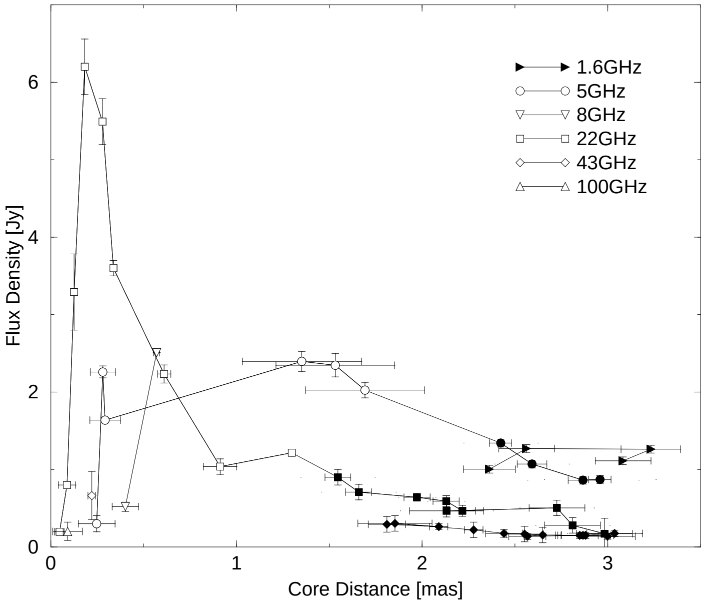

Figure 5.2: Flux density versus core distance of C7. A big rise in flux density is seen at 22 GHz at about 0.25 mas core distance. Filled symbols denote data from this thesis.

5.2 Jet Component C8

Jet component C8 shows a clear rise in flux density at 5 and 22 GHz since 1994 (Figure 5.3). No observations were made at 43 GHz around 1994 when this rise in flux density occurred. The error bars at 1.6 GHz are too large to believe the observed peak. A Gaussian fit to these two peaks yields a time delay of 1.4 years between 22 and 5 GHz. The flux density flare at 5 GHz occurs exactly at the southernmost point of the trajectory at $x \approx 1\,\mathrm{mas}$, $y \approx -0.3\,\mathrm{mas}$ (compare Figures 4.15 and 5.4). The maximum of this flare can be approximated by two linear fits for the rising and decreasing part of the flux density curve and results in $S_{5peak} = 3.69\,\mathrm{Jy}$ ($S(t)_{rise} = 1.365t + 0.419$, $S(t)_{drop} = -1.114t + 6.349$). The best flux density approximation of the 22 GHz flare is the highest flux density measurement with $S_{22peak} = 2.25\,\mathrm{Jy}$. After C8 passes the southernmost point, it grows in size and the flux density drops at all frequencies. While the flux density is higher at 5 GHz than at 1.6 GHz in 1998, it becomes similar for both frequencies in 1999. A similar behaviour is also seen for C7 in 1998–1999. The flux density at 43 GHz is always below the flux densities at the other frequencies and shows just a small peak at $x \approx 1.1\,\mathrm{mas}$ in 1997.

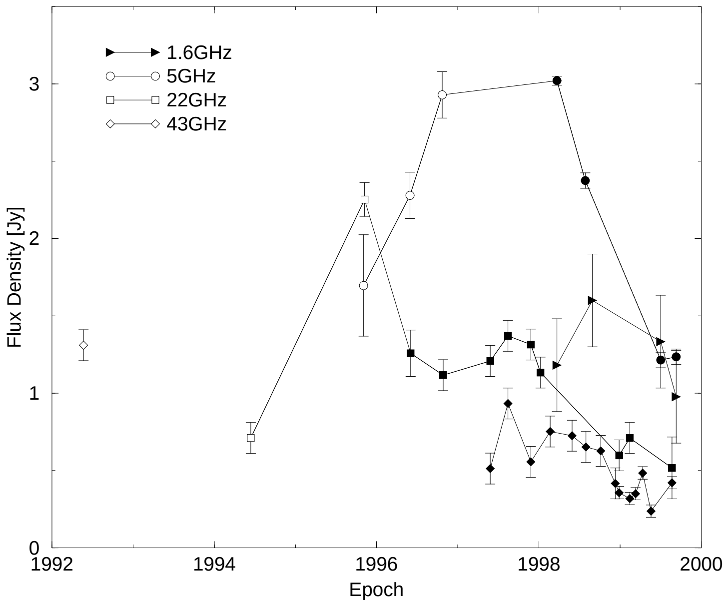

Figure 5.3: Flux density evolution of C8. The big increase in flux density is delayed between 22 and 5 GHz by 1.4 years. Filled symbols denote data from this thesis.

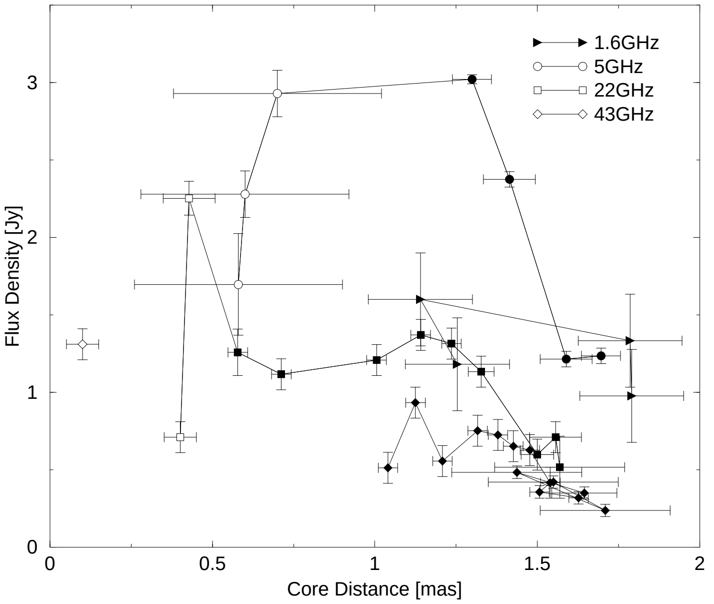

Figure 5.4: Flux density versus core distance of C8. The big increase in flux density at 5 GHz is centered around 1 mas core distance. The flux density at 22 GHz drops at distances larger than $r \approx 1.3$ mas. Filled symbols denote data from this thesis.

5.3 Jet Component C9

Unlike for C7 and C8, an increase in flux density by more than a factor of 2 is not seen for C9 at any frequency (Figure 5.5). The flux density variations are rather smooth, in contrast to C7 and C8, and have values close to 0.5 Jy at 43 GHz, 1 Jy at 22 GHz, 2 Jy at 1.6 GHz and 2.5 Jy at 5 GHz. Only a small increase in flux density between 0.5 and 1.2 mas at 43 GHz is measured (Figure 5.6). Since no significant peak in flux density is observed, it is not possible to see a correlation with the turning point of the trajectory at $x(t) \approx 1$ mas (Figure 4.22). This behaviour is quite different from that of C7 and C8. One should note that these observations end at the turn of the trajectory and later observations will show if the flux density drops immediately with the direction change of C9. In this context, it is also remarkable that the uniform flux density at 5 GHz has about the same value as the peaks of C7 and C8 at the same frequency. It might be that a possible geometric effect is overlayed with an intrinsic effect of the component itself. Another possibility could be small flares around 1998.5 at 22 GHz and around 1999.0 at 5 GHz when no observations were done. Support for this assumption is that the highest flux density at 5 and 22 GHz is measured at the penultimate epoch. It may also be that the high flux density plateau at 5 GHz is simply the peak of a long duration flare because it spans about the same time range ($\Delta t = 1.5$ years) as the highest flux density points of C8 at the same frequency.

The feature C9 is also seen at two epochs at 1.6 GHz. The flux lies below the flux density at 5 GHz and above the 22 GHz value which is also seen for the first epoch of C7 and for epochs 1–3 of C8.

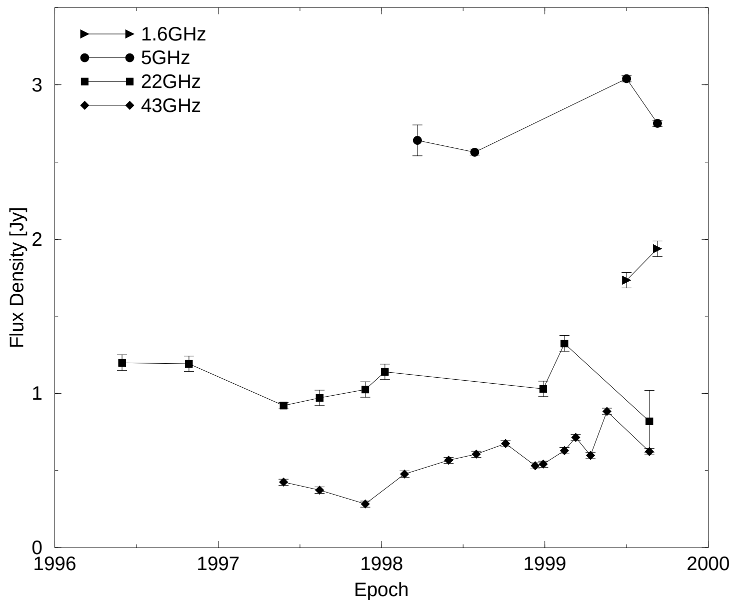

Figure 5.5: The flux density evolution of C9 is rather smooth. The flux density at 1.6 GHz is lower than at 5 GHz.

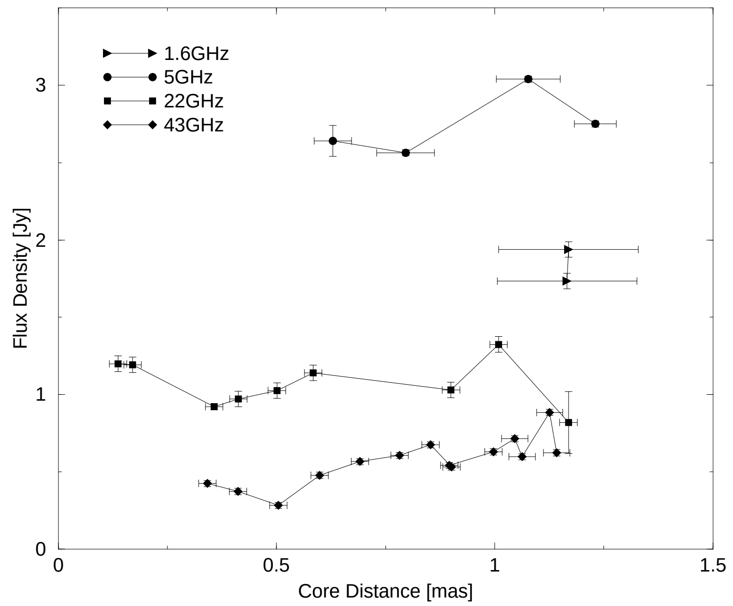

Figure 5.6: Flux density versus core distance of C9. A small increase in flux density is seen at about 1 mas core distance at 5, 22 and 43 GHz. The flux density at 1.6 GHz is lower than at 5 GHz.

5.4 Jet Component C10

The component C10 shows two peaks at 43 GHz and one at 22 GHz. The time between the first peak at 43 GHz and the highest value at 22 GHz is 0.5 years, while 1.5 years elapsed between the two 43 GHz peaks. At 22 GHz there are only two observations in 1998. Thus one cannot determine whether there is only one narrow peak or two narrow peaks as at 43 GHz or even only one broad peak, covering the time span between both 43 GHz peaks. Anyhow, the fitted time delay between both frequencies is at least a lower limit. A possible second peak at 22 GHz could still have occured before mid 2000.

The trajectory of C10 (Figure 4.25) shows two strong turns (one to the north-west and one to the south-west). The two flux density peaks at 43 GHz occur exactly when the component approaches these turns at $x = 0.15$ mas and at $x = 0.22$ mas. Thus it is likely that there were also two peaks at 22 GHz correlating with the 43 GHz peaks and the turns of the trajectory.

The flux density maxima of the first 43 GHz peak ($S_{43peak1} = 0.95$ Jy) and of the 22 GHz peak ($S_{22peak} = 1.60$ Jy) can be approximated by taking the highest flux density values. The 0.96 Jy flux density data point during the second 43 GHz flare in 1998.99 is too high because the accuracy of this flux density determination is strongly affected by the low image resolution resulting from the short observation time of only 10 minutes. In this image the closest component C11 is blended with the core. The lower flux density data point at the close epoch 1998.94 is more reliable since it comes from an 8 hour long observation and C11 can be identified properly in that image. The flux densities of these core-jet regions (D/C11/C10 at 1998.94 and D/C10 at 1998.99) differ only by 0.17 Jy. Thus the flux density which is represented by C11 at epoch 1998.94 is distributed between C10 and the core at epoch 1998.99. This makes the flux densities of C10 and the core too high at this epoch. If one omits this data point, the shape of the second flux density flare at 43 GHz shows a steep increase and a smooth drop. Thus, a good approximation of the flux density maximum of the second 43 GHz peak is the highest flux density value ($S_{43peak2} = 0.78$ Jy) at epoch 1998.76.

At 5 GHz, C10 is only detected at one epoch and shows a flux density of 1.1 Jy, which is above the values at 22 and 43 GHz. This higher flux density at 5 GHz compared with the other frequencies is also seen for the features C7–C9.

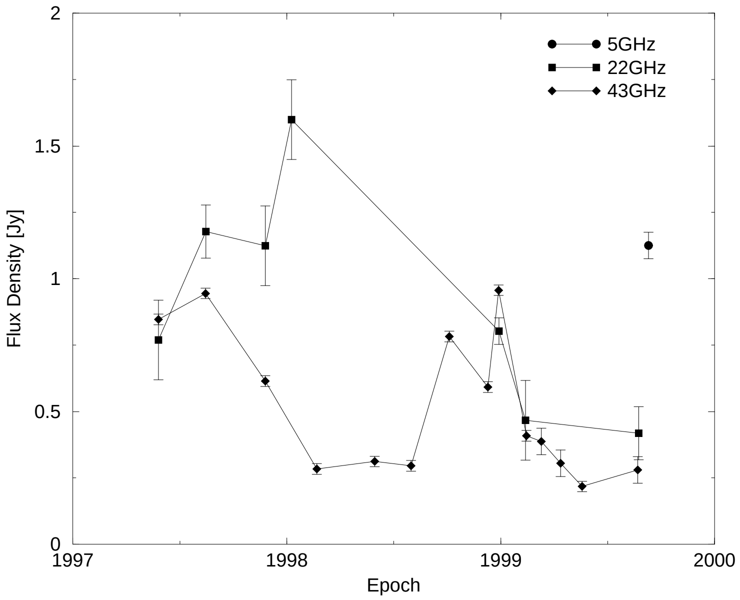

Figure 5.7: Flux density evolution of C10. There are two peaks at 43 GHz separated by 1.5 years. The flux rise at 22 GHz is delayed by 0.5 years with respect to the first 43 GHz peak. C10 has been detected at 5 GHz at only one epoch so far, with a flux density of 1.1 Jy.

5.5 Jet Component C11

The youngest component C11 (Figure 5.8) has only been observable at 43 GHz so far, and shows a behaviour similar to that of C10, with two peaks at the same frequency but at a much smaller core distance. The time separation between these two peaks is about 0.9 years. The first flux density peak occurs soon after the ejection of this component. A relation between this peak and a particular part of the trajectory is not visible. The second peak can be identified with a component acceleration and a turn to the south-west (compare the component trajectory in Figures 4.26 and 4.27).

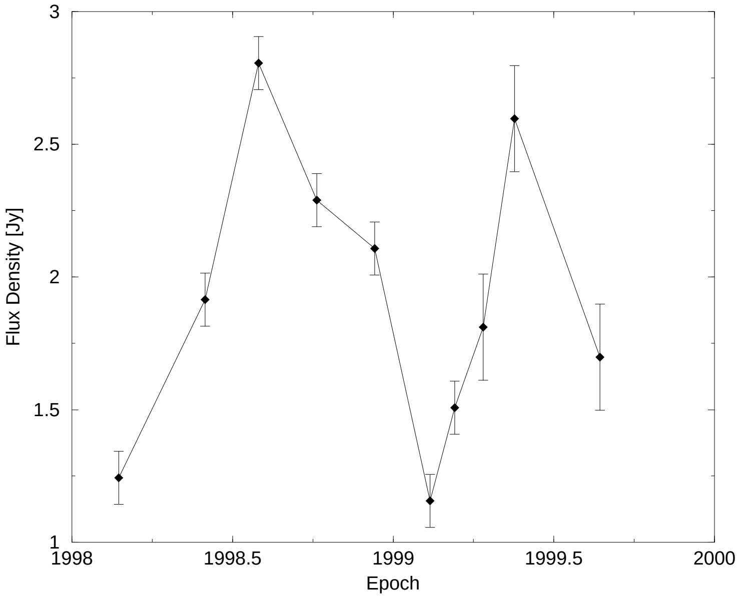

Figure 5.8: Flux density evolution of C11 at 43 GHz. The two peaks are separated by a 0.9 year gap.

5.6 The Core

The flux density evolution of the core is shown in Figure 5.9 for the time range when the components C7–C11 were ejected. An enlargement for the time range when observations for this thesis were made is shown in Figure 5.10. The epochs of first detection for the jet components are marked in these Figures (these are not the extrapolated ejection epochs!).

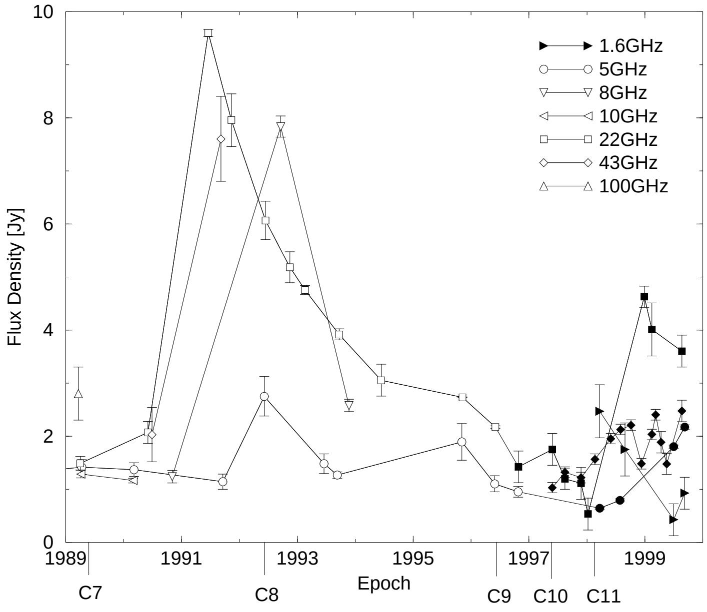

Figure 5.9: Flux density evolution of the core. The jet components C7–C11 were ejected in this time range. The epochs of first detection for these components are marked. Filled symbols denote data from this thesis.

Only two measurements are available at 43 GHz before 1997, indicating a rise in flux density in 1991. An increase in flux density is also exhibited by the 8 GHz observations between 1991 and 1993. The dense 22 GHz observations show a clear flare in the same time range. The time delay between the increased flux density at 22 GHz and a 5 GHz peak in 1992 is about 1 year. This rise in flux density at four different frequencies is correlated with the ejection of the components C6, C7 and C8. No peak at 22 GHz and only a small increase in flux density at 5 GHz is seen at the time of ejection of C9. No observations are available at 43 GHz when C9 was detected for the first time.

The D/C11 region is only resolved at 43 GHz and cannot be separated at lower frequencies so far. This means that this region is identified as the core at frequencies below 43 GHz. For a better comparison, the sum of the flux densities of the core and C11 at 43 GHz is plotted in the bottom graph in Figure 5.10. The result is a flux density peak at 43 GHz around 1998.6. The epoch 1998.99 at this frequency is omitted because the flux density measurement is unreliable. (see the discussion in the 3rd paragraph of section 5.4).

A big increase in flux density is also seen at 22 GHz. A clear determination of the maximum of this peak is not possible, because no observations were done at this frequency in 1998. One can set only an upper limit to a time delay with respect to the 43 GHz peak of about 0.5 years. There is also a flux density increase at 5 GHz, which has not reached its maximum yet. One can only estimate that the flux density peak at 5 GHz is at least delayed by about 1.5 years with respect to the peak at 43 GHz. The core flux density for the first 2 epochs at 1.6 GHz also includes the unresolved jet feature C9 (see section 3.3.1) and shows therefore too high a value in comparison with the other frequencies.

In summary, the core-region (D+C11) increases in flux density at 5, 22 and 43 GHz after the ejection of the jet components C10 and C11. This is similar to the rise in flux density at four different frequencies after the ejection of the jet components C6–C8. This means that a core flux density increase is coupled with the ejection of a new group of jet components. In both cases the increase in flux density of the core is observed after the ejection of the jet components.

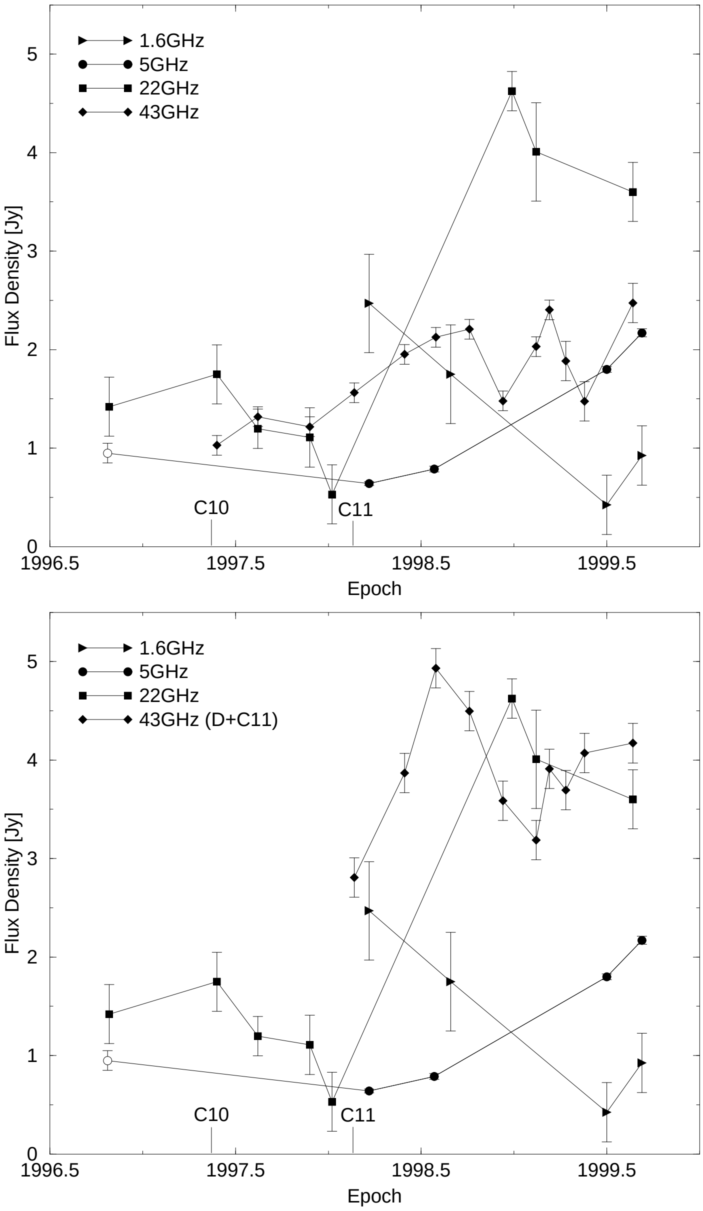

Figure 5.10: Top: Flux density evolution of the core in the time range of the observations presented in this thesis. Bottom: Same as 'top', but using the sum of the flux densities of the core and C11 at 43 GHz. This region is identified as the core at lower frequencies. The first observed epochs of C10 and C11 are marked.

5.7 Periodicity of Component Flux Density Maxima

In the shock-in-jet model, one can decompose the flux density variations into contributions from the underlying jet and the shocks. To first order the flux density of the underlying jet (the base or quiescent flux) remains constant. The growth and decay of shocks contribute the additional flux density. The flux density of the underlying jet obviously has to be below the lowest flux density of the jet components, which gives an upper limit of $S \approx 100$ mJy within the inner 3 mas of 3C 345. Furthermore, the lowest flux density levels between the jet components in 3C 345 are mostly much smaller than $S \approx 30$ mJy. Since the peak of a component flare is usually much larger than $S \approx 1$ Jy, one can use the fitted component flux density peaks versus time for a study of the long term evolution of the jet.

The accuracy of determine a component flux density peak is strongly dependent on the spacing between the epochs. In an ideal case one has close observations around the peak epoch and can constrain it quite well. In most cases, one can only fit the peak from the measured rise and decay of the flux density curve. Depending on the available data points and the broadness of the flux density flare, the peak can be approximated by two exponential fits, two linear fits, one Gaussian fit or simply with the highest measured flux density value. The corresponding error bars can be asymmetric due to the density of data points at the rising and decreasing part of the flux density flare.

A plot of the peaks of the component flares versus the peak epochs (Figure 5.11) reveals a quasi periodicity of 11.3 years at 5 GHz ($t_0 = 1983.57$) and 9.0 years at 22 GHz ($t_0 = 1982.42$) and can be fitted with:

$$S_{Cmax5GHz}(t) = -1.18159 \sin(0.558177t + 3.02596) + 3.724 - 0.101426t \qquad (5.1)$$

$$S_{Cmax22GHz}(t) = 3.16398 \sin(0.703741t + 0.42418) + 3.98932 - 0.0220894t \qquad (5.2)$$

These periods are in the same range as the time period ($t = 8$–10 years) deduced from the similarity of the component trajectories of C5 and C8 (section 4.9) and the time period ($t = 8$–10 years) deduced from the component ejection position angles (section 4.14). The continuation of the fits with a dot-dashed line in Figure 5.11 shows the predicted trend. The sparse 43 GHz observations are not plotted here because the precise determination of the peaks for the older components C4, C6 and C7 could not be done.

The observed difference between the periods at 5 and the 22 GHz is within the errors because in both cases only 1.5 periods are covered by 6 and 7 data points respectively. Observations in the near future will give a better constraint on the period.

Moreover, there is no reason why a component should not have more than one flux density peak. Actually this has been observed for the youngest components C10 and C11 which are traced very precisely after their ejection. Observation gaps exist especially for the older components and it could be that only one out of more flux density peaks was observed for a given component. This means that one might

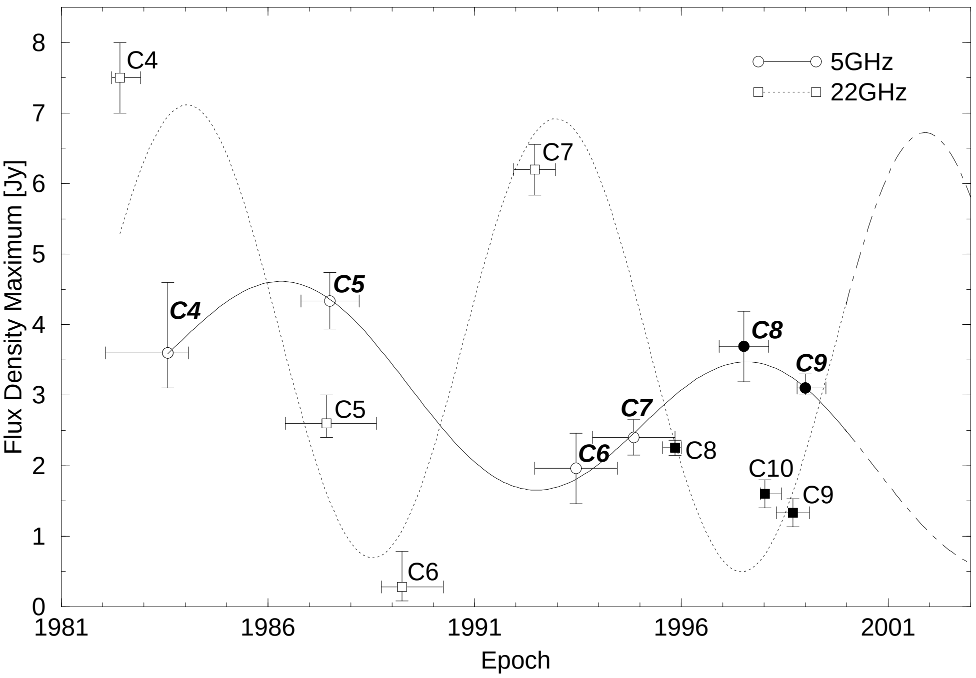

Figure 5.11: The component flares versus time reveal a quasi periodicity with a period of 9.0 years.

compare a first flux density peak of component A with a second flux density peak of component B which would obviously change the fitted period.

Another reason why there is a shift between the 5 and 22 GHz fit comes from the opacity. The components peak later at 5 GHz than at 22 GHz which is caused by the different optical thickness at different frequencies. This means one looks deeper into the jet at higher frequencies and sees the component earlier.

Also the amplitudes of the 5 and 22 GHz fits are quite different. The strength of the component peaks varies between 0.5 and 7.5 Jy at 22 GHz but only between 2 and 4.5 Jy at 5 GHz. As a result, components with a low flux density peak at 22 GHz (e.g. C6 and C8) can have a higher flux density peak at 5 GHz. In contrast to this, components with a high flux density peak at 22 GHz (e.g. C4 and C7) can have a lower flux density peak at 5 GHz. This gives an additional shift between the curves. For instance, the flux density peak of C8 marks a maximum at 5 GHz but is close to a minimum at 22 GHz. In contrast to this, C7 marks a maximum at 22 GHz but is quite close to a minimum at 5 GHz. This behaviour is likely be caused by the different optical thickness of the components.

In summary, the shift between the 5 GHz and 22 GHz fits can be explained by a combination of the uncertainty of the period, a mixing of different flux density peaks, an opacity shift and the different range of the flux density strength. This means one has to consider the quasi-periodicity at different frequencies independently from each other. Follow-up observations might complete these results and better constrain the main cause of this period shift at different frequencies.

In our data the observations at 22 GHz give the best coverage and can be compared with other results at the same frequency presented in Lobanov & Zensus

(1999). They described a quasi-periodicity of the core flux density at 22 GHz which correlates with the total flux density at the same frequency. It is remarkable that the core flux density evolution correlates also with the strength of the component peaks. This means for instance that the high flux density peaks of the jet components C4 and C7 correlate with core flux density maxima and with total flux density maxima. In contrast to this, C6 has the lowest flux density peak which correlates with a low core flux density and a low total flux density. Lobanov & Zensus (1999) applied a flare model to the data of the total and the core flux density. This model describes a core flux density flare in October 2001 (Lobanov priv. comm.). Also the fit of the component flux density peaks has a maximum in October 2001 (dot-dashed line at 22 GHz in Figure 5.11) which is comparable with those of C4 and C7. The analysis of observations made around this epoch will show if the observations match with this fit. One has to note that a new jet component must not necessarily be ejected in 2001. But if a new jet component was ejected in 2000/2001 and it flared in October 2001 and the component flux density maxima have the described quasi-periodicity, then the flux density peak of this assumed new jet component should be comparable with those of C4 and C7. This would show the strong correlation of the component flux density strength with the amplitude of the nuclear flares. Furthermore, the total flux density at 22 GHz increased from 1997 to spring 2001 and dropped at the end of 2001 until January 2003 (Harri Teräsranta, priv. comm.).

In summary, this work has shown that the evolution of the component flux density peaks in the jet of 3C 345 behave very likely quasi-periodicly. Because of the long period of about 8–11 years and the time range of available epochs of only about 20 years, there is of course an uncertainty in the period. Moreover, it might also be that the jet undergoes a slow global change such that, for instance, the time between successive high flux density flares changes with time and/or the general flux density strength of individual components changes.

5.8 Dependence of the Flux Density on Component Trajectories

The correlation of the component flux density changes with the component trajectories reveals that a flux density maximum occurs typically when a component trajectory makes a turn either from south-west to north-west or from north-west to south-west (Figure 5.12). The components C8, C10 and C11 have their flux density maxima at the first part of the turns. This means that the flux density decreases after the turning point. Due to the relatively sparse time sampling of C7 after its ejection, it is only possible to say that the flux density rise occurs during the turn, but not whether it correlates with the beginning or the end of the turn. C9 is a special case and shows only slight flux density variations compared to the other components. The slight increase of the flux density of C9 at the second to last epoch at all frequencies is correlated with its turn from south to north at about 1 mas. A possible increase in flux density due to this geometric condition might be compounded by intrinsic evolution of C9. This assumption is in agreement with the relatively high and constant flux density of C9 at 5 GHz, which has value similar to the peaks of C7 and C8 at the same frequency. The flux density of the core region increases after the ejection of the jet component groups C6/C7/C8 and C9/C10/C11.

In summary, a flux density rise is mainly correlated with the approach of a component at its turning points of the trajectory. Hence the flux density peaks of the components have their main origin in the geometric path of the components, caused by Doppler boosting. This is in good agreement with the bend of the viewing angles to the line of sight derived from the increasing Lorentz factor (Section 4.13.4). If one assumes a helical path of the trajectories (e.g. Steffen *et al.* 1995) and a jet component revolves a straight jet two times then the flux density is Doppler boosted also two times. If additionally the intrinsic flux density evolution remains nearly constant, two flux density peaks will be observed. Thus, it is likely that the two observed flux density peaks of C10 are caused by a helical path. The flux density peaks of the jet components C4–C10 at 22 GHz versus the core distances at which the respective maxima occurred are shown in Figure 5.13. The component C11 is plotted at 43 GHz. The sequence of the jet components is illustrated by the dashed arrows. If one follows this sequence from C4 to C11 one can imagine a spiral-like path (solid hand-drawn curve). This means that besides intrinsic changes of the component flux density the trajectory of a component determines the observed flux density evolution.

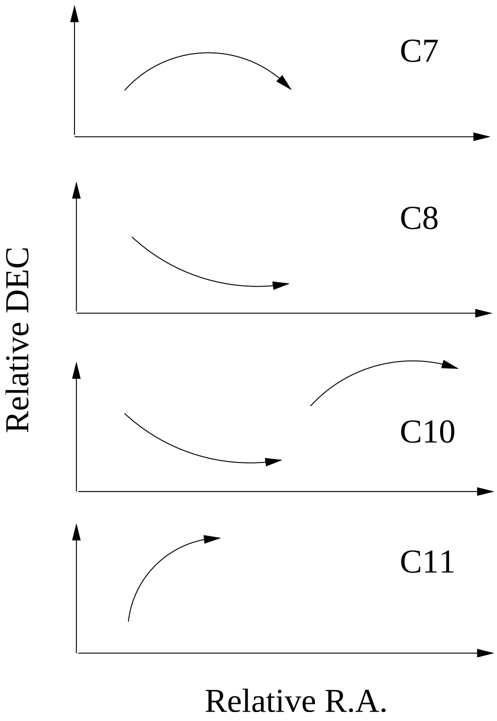

Figure 5.12: Illustration of the sections of the component trajectories where the flux densities show a peak. When a component changes its path from north-west to south-west or vice versa, the flux density shows a peak.

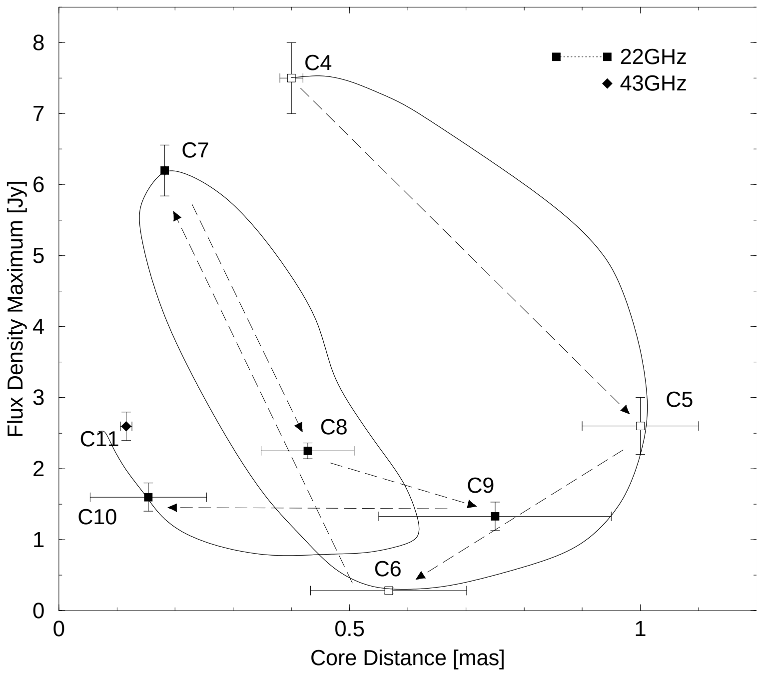

Figure 5.13: Flux density maxima of the jet components C4–C10 versus core distance of the observed flux density peak.

5.9 Dependence of the Flux Density on Frequencies

The time delays between the flux density peak epochs at different frequencies with respect to 43 GHz are shown in Figure 5.14. The best pronounced and determined flux density peaks of the components C7–C10 are used. It is obvious that a flux density peak occurs first at the highest frequency and subsequently at lower frequencies. One can define $\Delta t = \text{epoch}_{43GHz} - \text{epoch}_{\nu[GHz]}$. The approximation of this frequency dependent delay results in $\Delta t = 4.22488 \exp(-0.10343\nu)$ (Δt in years and ν in GHz). The epochs of the frequency dependent flux density peaks of the jet components and the time delays to each other are summarized in Table 5.1.

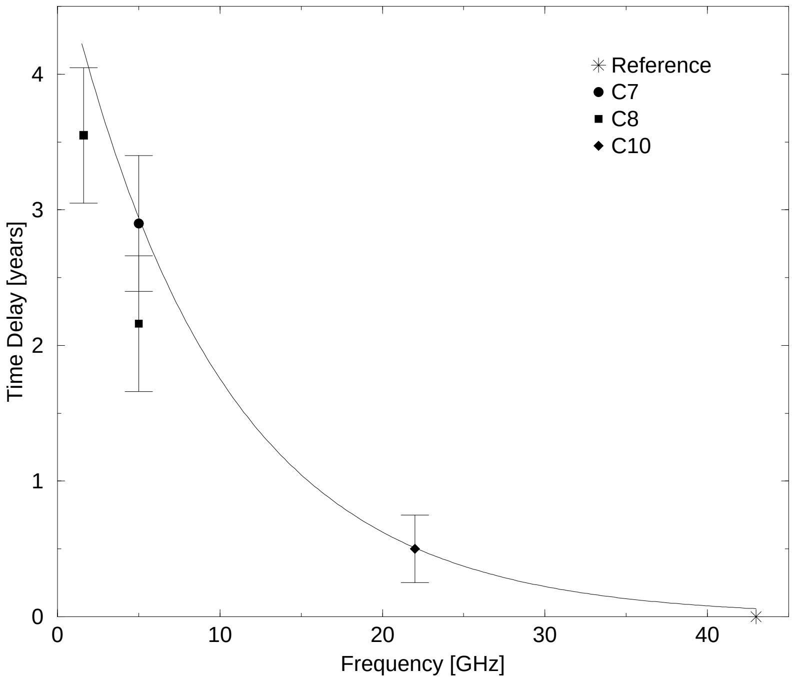

Figure 5.14: Time delay of the flux density peaks with respect to 43 GHz. The delay is higher at lower frequencies and can be approximated with $\Delta t = 4.22488 \exp(-0.10343\nu)$ (Δt in years and ν in GHz).

Component	τ_0	τ_{obs}	t_{43}	$t_2{}^2$	t_5	$t_{1.6}$	$\Delta t_{(2-43)}$	$\Delta t_{(5-22)}$	$\Delta t_{(1.6-5)}$
C4	1979.00	1980.52	-	1982.42	1883.57	-	-	1.15	-
C5	1980.00	1983.09	-	1987.42	1987.50	-	-	0.08	-
C6	1987.50	1988.49	-	1989.24	1993.45	-	-	4.21	-
C7	1988.00	1989.20	-	1992.45	1994.85	199.1*	-	2.4	4.25
C8	1991.43	1992.39	-	1995.85	1997.51	1998.9	-	1.66	1.39
C9	1994.75	1996.41	$\sim$ 199.4$^\bullet$	$\sim$ 1998.7$^\bullet$	$\sim$ 199.0$^\bullet$	-	-	0.3	-
C10	1995.50	1997.40	1997.62	1998.02	-	-	0.5	-	-
C11	1996.62	1998.15	1999.38	-	-	-	-	-	-
D	-	-	1998.7	199.1	2000	-	0.4	0.9	-

Table 5.1: Summary of the peak flux density delays. τ_0 - extrapolated ejection epoch, τ_{obs} - first observed epoch, t_{43} - epoch of maximum flux density at 43 GHz, $t_2{}^2$ - epoch of maximum flux density at 22 GHz, t_5 - epoch of maximum flux density at 5 GHz, $t_{1.6}$ - epoch of maximum flux density at 1.6 GHz, $\Delta t_{(2-43)}$ - time delay between 43 and 22 GHz in years, $\Delta t_{(5-22)}$ - time delay between 22 and 5 GHz in years, $\Delta t_{(1.6-5)}$ - time delay between 5 and 1.6 GHz in years, $*$ - not clear if the 1.6 GHz peak belongs to the peaks at the other frequencies, $\bullet$ - no pronounced peak visible

Chapter 6

Spectral Index Maps

Spectral index maps made from the images presented in chapter 3 are discussed in this chapter. A short introduction about the special requirements for producing these spectral index maps is given in section 6.1. A detailed description of the results is presented in sections 6.2 – 6.4. An overall discussion about the spectral properties of the jet in 3C 345 is given in section 6.5.

6.1 Introduction

The relativistic plasma of a radio jet produces synchrotron radiation. The spectrum can be described by power laws

$$S(\nu) \propto \nu^{\alpha}. \tag{6.1}$$

The spectrum is characterized by a maximum, the turnover point (S_m, ν_m) and two spectral indices, $\alpha_{thick} > 0$ ($\nu \ll \nu_m$) and $\alpha_{thin} < 0$ ($\nu \gg \nu_m$). The radio spectrum of the jet provides essential information about its physical conditions and helps distinguish between different jet models. Observations at different frequencies made sufficiently close in time can be used to determine the spectrum along the jet. The so-called *spectral index maps* are produced by combining two VLBI images at different frequencies. The spectral index is calculated for each pixel and is given by:

$$\alpha = a_1 \frac{\ln(S_1/S_2)}{\ln(\nu_1/\nu_2)} + a_2 \tag{6.2}$$

The scaling factors $a_{1,2}$ are usually omitted. A valid spectral index map has to fulfill some requirements:

- The observed epochs have to be close in time, otherwise the source structure might have changed and could produce artifacts in the spectral index map.
- Since the VLBI technique does not provide a fixed reference point, the registration of the images has to be done using selected, distinct regions in the images as reference.
- The VLBI technique produces different spatial frequency samplings at different frequencies and with different arrays which results in different synthesized beams. This can cause spurious features and confusion in the spectral index maps.

In order to produce spectral index maps from the 3C 345 images presented in this thesis, special conditions were required. First of all, only those epochs at different frequencies which are close enough in time were selected. For instance, with a maximum proper motion of the inner jet components of $\mu(t) \approx 0.4\,\mathrm{mas\ year}^{-1}$ and a pixel size of 0.04 mas, the images can be made up to one months apart from each other. To provide matching uv-ranges (not uv-coverages!), the smaller uv-range of the lower frequency image was also adopted for the higher frequency image. The task `uvrange` in DIFMAP was used for this. A circular restoring beam was used, with a diameter of 60 – 70% of the major axis of the beam of the lower frequency. This led to a good compromise between keeping the resolution of the spectral index maps, and reducing the number of spurious features and the confusion level. The core could not be used as a reference point for the alignment of the maps because it is located in an optically thick environment and its position depends on the observing frequency (see chapter 4). A combination of the calculated core-shift and the identification of optically thin regions in the jet were used to align the images. The decrease in sensitivity at higher frequencies of multi-frequency observations leads to artifacts in the low emission regions of the spectral index maps. A clipping level was used, with a SNR and flux density cut-off threshold, to avoid these artifacts. A detailed discussion on producing spectral index maps is given in Lobanov (1998b).

The epochs and frequencies of the spectral index maps are summarized in Table 6.1. Figures 6.1 – 6.12 show at the left-hand side the original uv-tapered images convolved with a circular beam. The corresponding spectral index maps obtained from these images are shown on the upper right-hand side. A slice along the jet axis (shown in the lower right) illustrates the spectral evolution in the jet. The angle of the slice is chosen so that the center of the core and the jet components are present in the profile. In some cases a second slice is used when some jet features are obviously not aligned with the jet axis and are not represented in the first slice.

ν_{low} [GHz]	$epoch_{\nu_{low}}$	ν_{high} [GHz]	$epoch_{\nu_{high}}$	Figure
1.6	1998.22	5	1998.22	6.1
1.6	1998.66	5	1998.57	6.2
1.6	1999.50	5	1999.50	6.3
1.6	1999.69	5	1999.69	6.4
5	1999.69	22	1999.64	6.6
22	1997.40	43	1997.40	6.7
22	1997.62	43	1997.62	6.8
22	1997.90	43	1997.90	6.9
22	1998.99	43	1998.99	6.10
22	1999.12	43	1999.12	6.11
22	1999.64	43	1999.64	6.12

Table 6.1: Summary of the spectral index maps presented in this chapter.

6.2 Spectral Index between 1.6 and 5 GHz

Four spectral index maps are presented in this section, covering a time range of one year and six months. The registration of the images was done with respect to the optically thin component C4. The spectral index maps obtained are shown in Figures 6.1 – 6.4. The spectral evolution of the jet is presented in Figure 6.5. The spectral index of the core is about zero within the errors. A slight decrease is seen for the last epoch (1999.69) with $\alpha = -0.3$. The spectral index of the jet feature C7 is steeper than of C4 and the core at the epochs 1998.22, 1998.57 and 1999.50. Its spectral index ranges between -0.8 and -1.3. The last epoch is likely to be influenced by a sidelobe in the 1.6 GHz image which appears as a positive peak in the spectral index map and is not seen at the other epochs. This results in a spectral index of 0.2 for C7. As seen in this spectral index map, a value around -1 is reached between the core and the peak. Thus, the true α of C7 is probably similar to those at the other epochs. The spectral index of the more extended component C4 shows a decrease from -0.4 to -0.8 between the first and the last epoch.

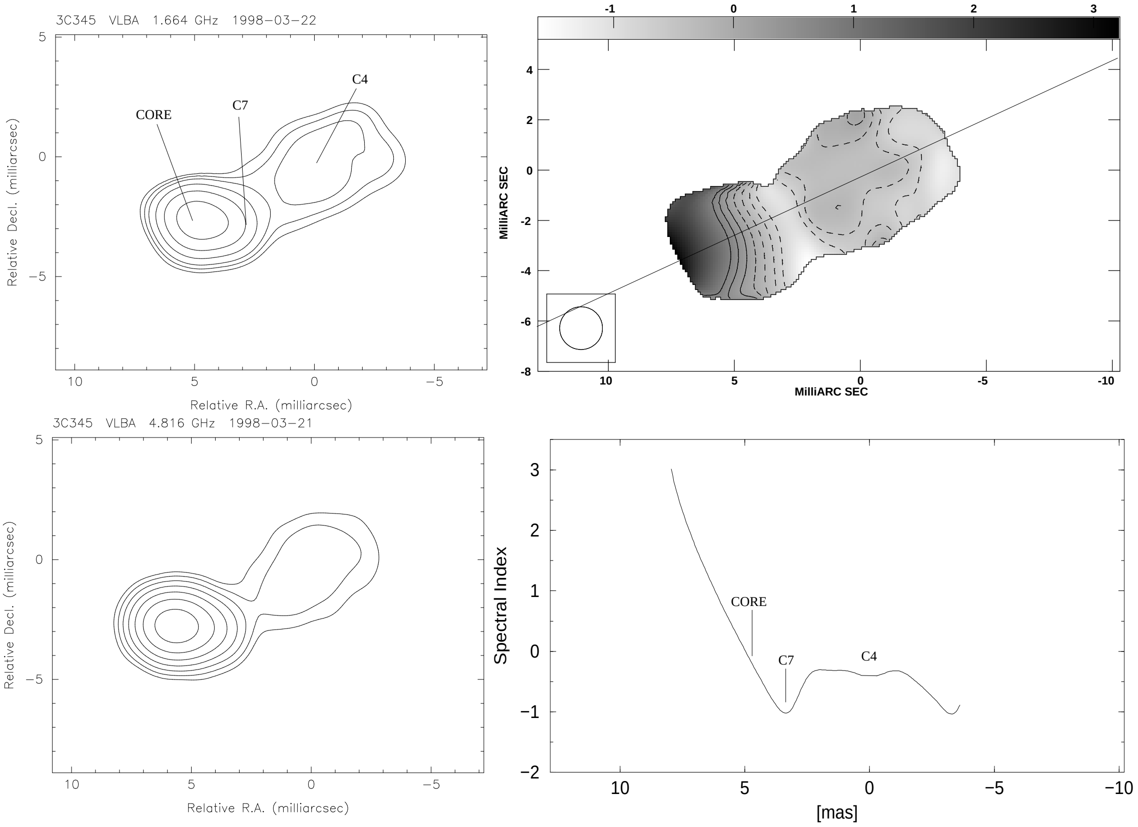

Figure 6.1: Left: Images at 1.6 and 5 GHz (epoch 1998.22), convolved with the same circular beam and produced with the same *uv*-range. Upper right: Spectral index map of 3C 345 from these images. The images are registered at the peaks of the optically thin jet feature C4. The profile of the slice in the jet direction is shown in the lower right. The spectral index of the core is zero whereas $\alpha = -0.9$ for C7 and $\alpha = -0.4$ for C4.

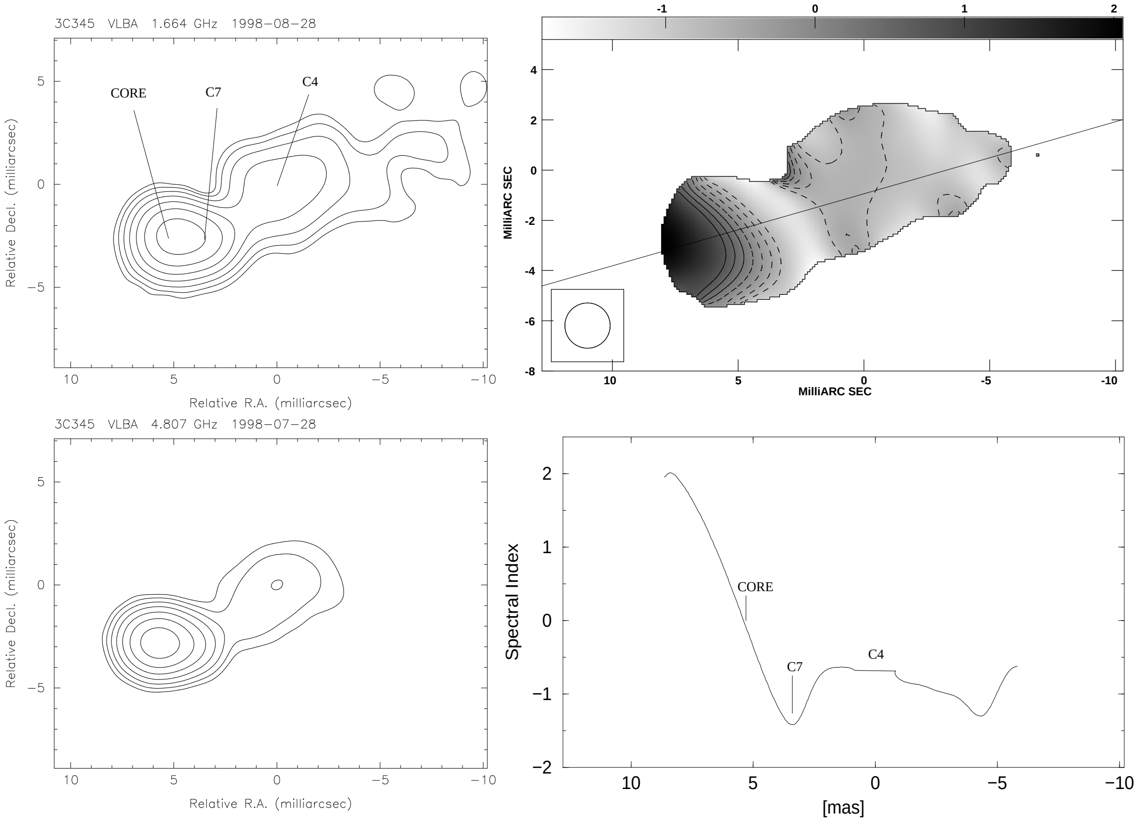

Figure 6.2: Left: Images at 1.6 (1998.66) and 5 GHz (1998.57), convolved with the same circular beam and produced with the same *uv*-range. Upper right: Spectral index map of 3C 345 from these images, about five months later as in Figure 6.1. The images are registered at the peaks of the optically thin jet feature C4. The profile of the slice in the jet direction is shown in the lower right. The spectral index for the core is −0.1. The jet features C7 and C4 have a spectral index of −1.3 and −0.7 respectively.

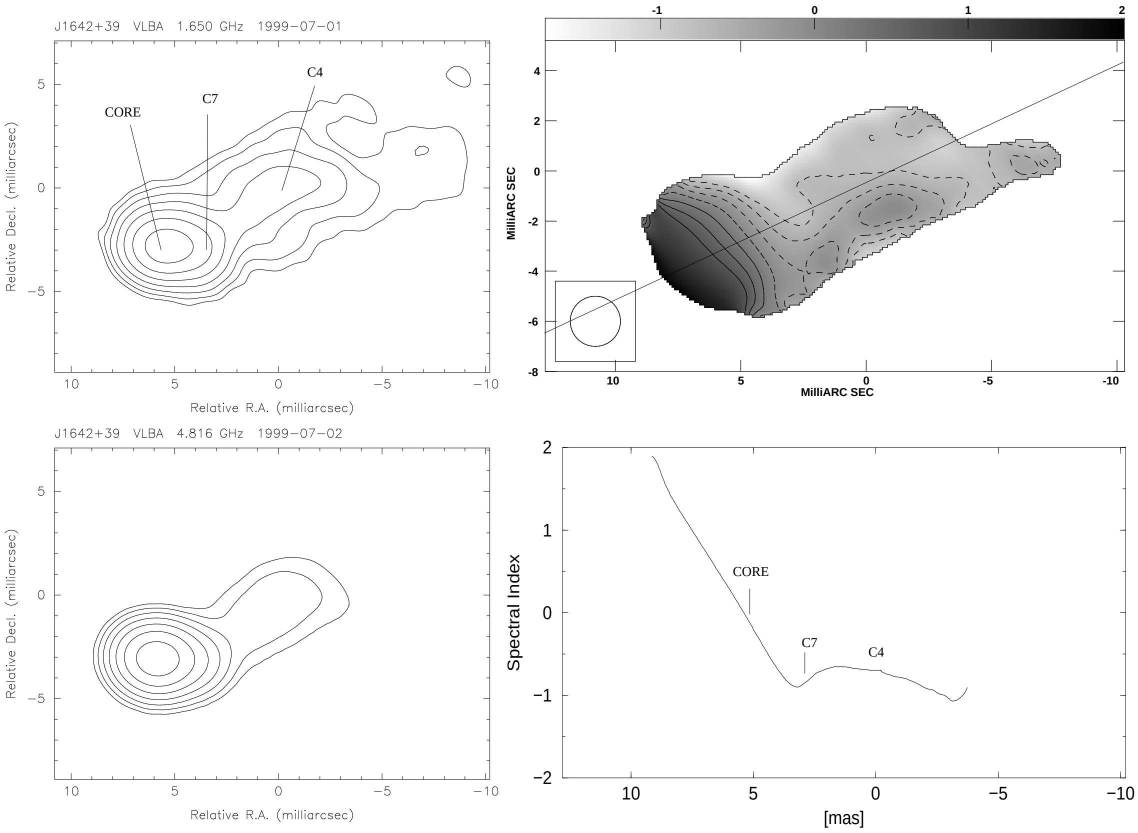

Figure 6.3: Left: Images at 1.6 and 5 GHz (epoch 1999.50), convolved with the same circular beam and produced with the same *uv*-range. Upper right: Spectral index map of 3C 345 from these images, about ten months later as in Figure 6.2. The images are registered at the peaks of the optically thin jet feature C4. The profile of the slice in the jet direction is shown in the lower right. The spectral index for the core is −0.1. The jet features C7 and C4 have a spectral index of −0.8 and −0.7 respectively.

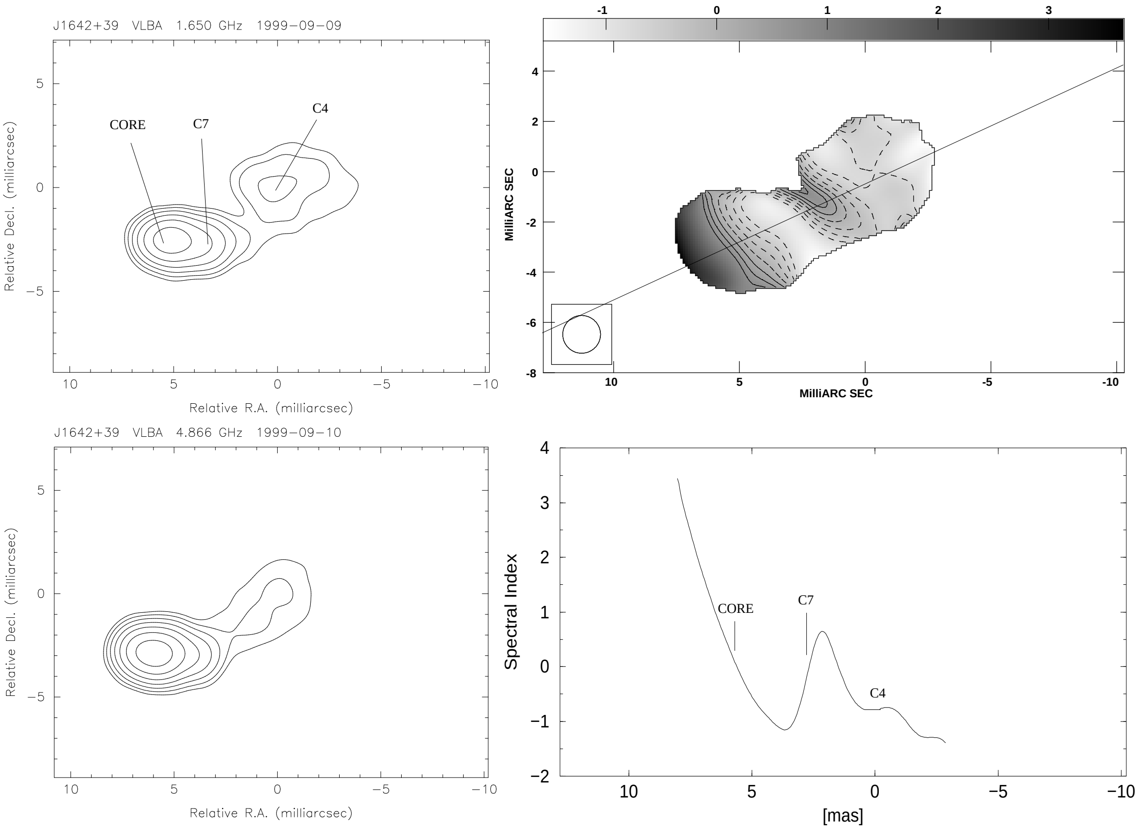

Figure 6.4: Left: Images at 1.6 and 5 GHz (epoch 1999.69), convolved with the same circular beam and produced with the same *uv*-range. Upper right: Spectral index map of 3C 345 from these images, about two months later as in Figure 6.3. The images are registered at the peaks of the optically thin jet feature C4. The profile of the slice in the jet direction is shown in the lower right. The spectral index of the core is -0.3. The jet features C7 and C4 have a spectral index of 0.2 and -0.8 respectively. The spectral index of C7 is likely influenced by the peak caused by a sidelobe in the 1.6 GHz image. At a slightly closer position towards the core, $\alpha \approx -1$ lies in the same range as for C7 at the other epochs.

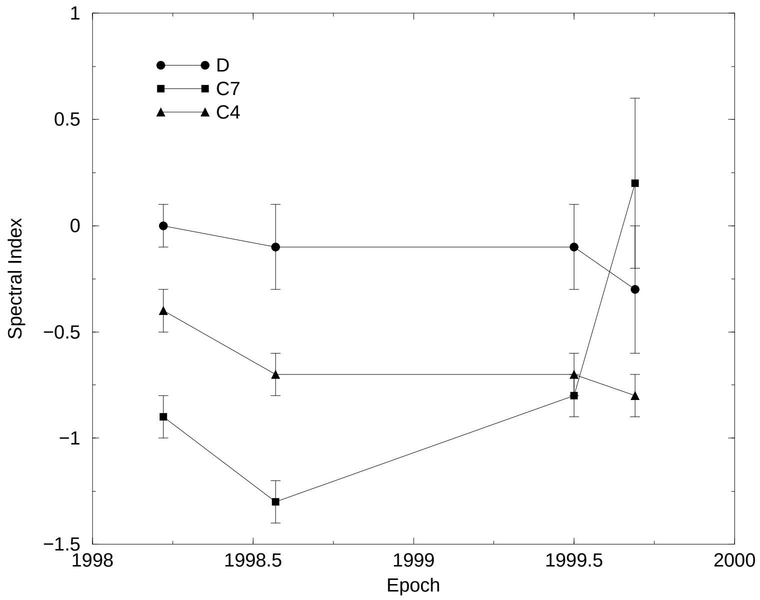

Figure 6.5: Evolution of the spectral index between 1.6 and 5 GHz (1998.22 – 1999.69), derived from the spectral index maps. The spectral index of the core (D) is nearly zero, with a slight decrease to −0.3 for the last epoch. The innermost jet feature C7 has a spectral index of −1 for the first 3 epochs. The fourth epoch of C7 is probably influenced by an artefact caused by the 1.6 GHz image. The true value should be in the same range as for the earlier epochs. The extended jet component C4 has a spectral index between −0.4 and −0.8. The error-bars of the spectral indices of the jet components are dependent on the position errors of the components.

6.3 Spectral Index between 5 and 22 GHz

One pair of observations at 5 and 22 GHz were close enough in time to be combined for producing a spectral index map (Figure 6.6). The calculated core shift between these frequencies (sections 4.4.1, 4.5.1 and 4.6.1) was used to align both images with each other. The core has a positive spectral index of $\alpha \approx 0.4$. The spectral indices of C10, C9 and C8 are almost the same within a range of -0.4 to -0.6. The outermost component C7 has the steepest spectral index with $\alpha = -1.0$. The jet plasma in between the components has a different spectral index from the components themselves.

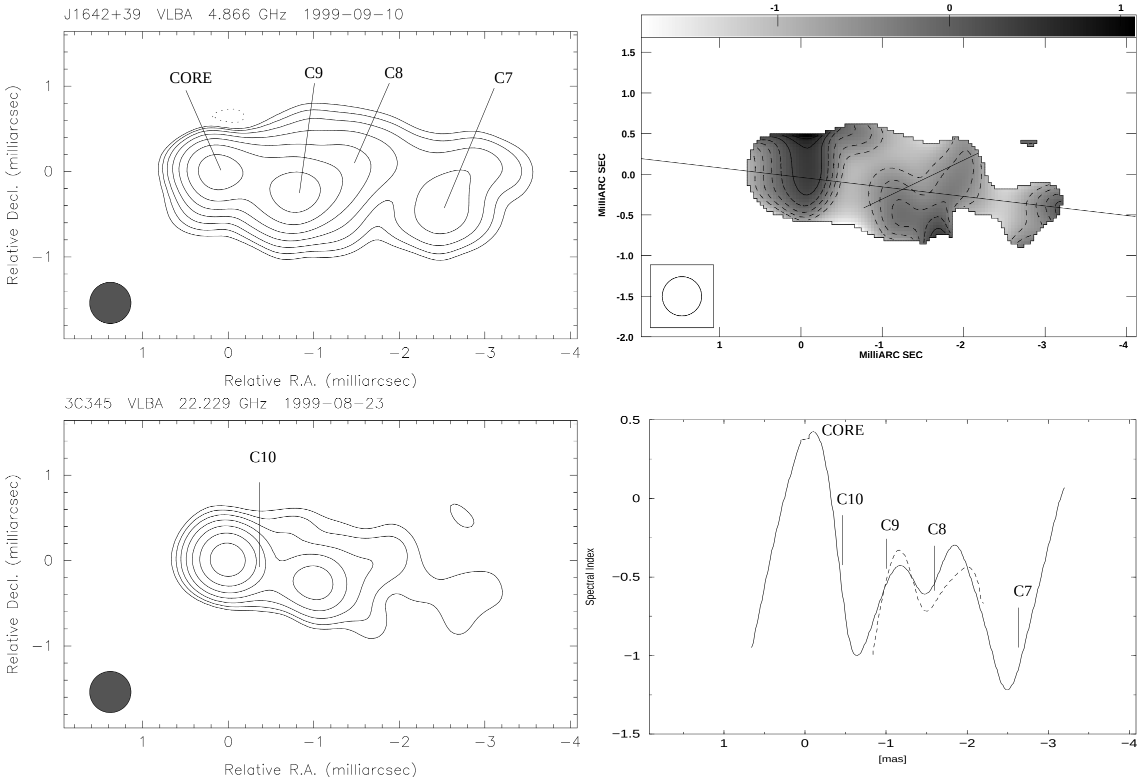

Figure 6.6: Spectral index map (top right) obtained by combining the 5 GHz VSOP image at epoch 1999.69 (top left) and the 22 GHz VLBA image at epoch 1999.64 (bottom left). The long slice made in the jet direction shows the distribution of the spectral index along the jet (bottom right). The short slice (dashed in the profile) passes through C8 and C9. Both slices show a similar spectral shape for C9 and C8. The optically thick core has a spectral index of about 0.4. A steep spectrum of $\alpha \approx -0.5$ is seen at the location of the youngest component C10. After a minimum with $\alpha \approx -1$, the jet features C9 ($\alpha \approx -0.5$) and C8 ($\alpha \approx -0.6$) appear at the rising edge of small peaks. The spectral index of the outermost component C7 is $\alpha \approx -1$.

6.4 Spectral Index between 22 and 43 GHz

Six sets of observations were made close enough in time to allow making spectral index maps between 22 and 43 GHz (Figures 6.7 – 6.12). The core shift correction was used to align these images. The time evolution of the spectral indices of the jet components and the core is shown in Figure 6.13. A chronological order of all slices is presented in Figure 6.14. At some epochs, a combination of two different slices is used in order to show all jet components. These slices in the jet direction (and through the components) show shocked regions. The core region varies between optically thin and flat which implies that its turnover frequency cannot be higher than 22 GHz for the most epochs. The closest jet component C10 changes from optically flat to thick (Figure 6.14). The spectral index of C9 is always about -1 (except for the last epoch), but the spectral index of the surrounding medium to the east and to the west of this component increases. C8 is related to a broad region with a higher spectral index than the surrounding medium at a core distance of $r \approx 1$ mas in 1997. One year later C8 lies on the descending and C9 on the ascending edge of this region. This means, a component position is not necessarily related to a higher spectral index (a peak in these slices) at core distances of about 1.5 mas anymore. In this case, the former "C8-peak" appears as an optically thick region between the jet features C9 and C8 in 1998.99 and 1999.64. The spectral indices of the components drop in the descending order of C10/C8/C9/C7 for the 3 epochs in 1997 while this order varies for epochs in 1998 and 1999.

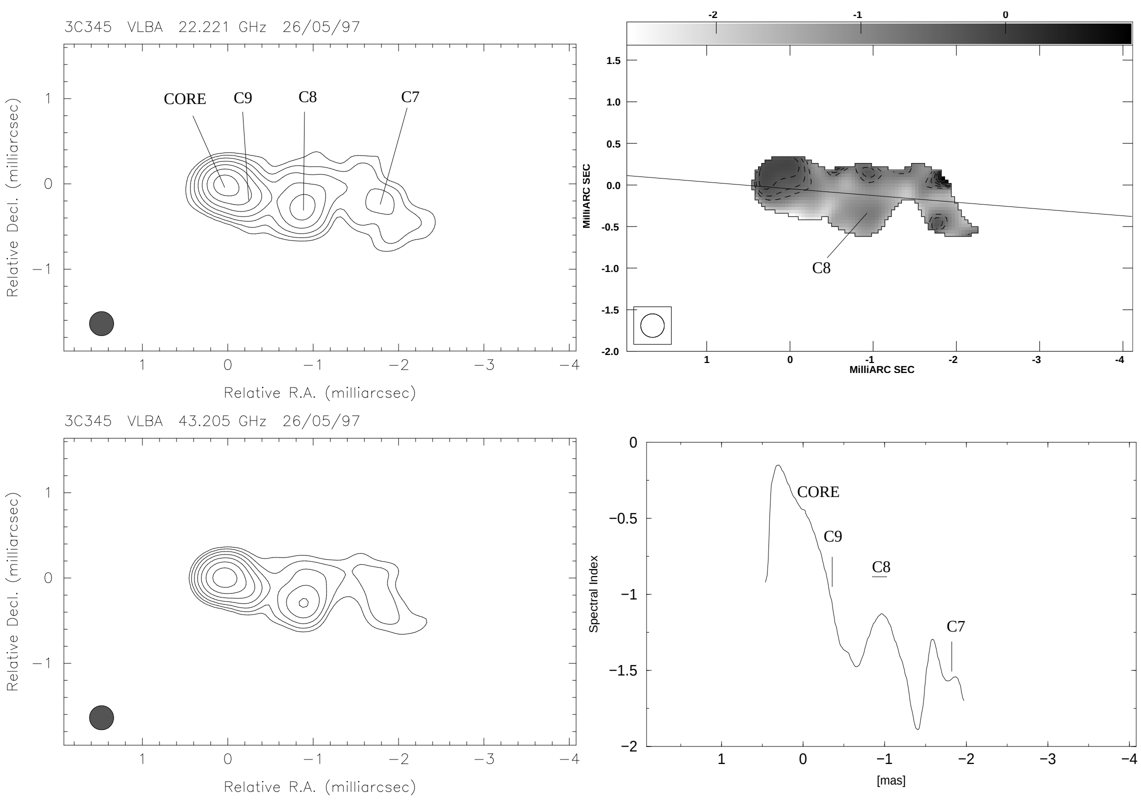

Figure 6.7: Spectral index map (top right) obtained by combining the VLBA images at 22 GHz (top left) and 43 GHz (bottom left), both at epoch 1997.40. The slice made along the jet direction illustrates the distribution of the spectral index (bottom right). Since the slice does not go through the center of C8, its correct value is given as the short horizontal dash above the profile. The jet plasma between the jet components C9 and C8 and between C8 and C7 has a lower spectral index. The core has a spectral index of -0.5. For the jet features C9, C8 and C7, the spectral indices results in -1, -0.7 and -1.5 respectively.

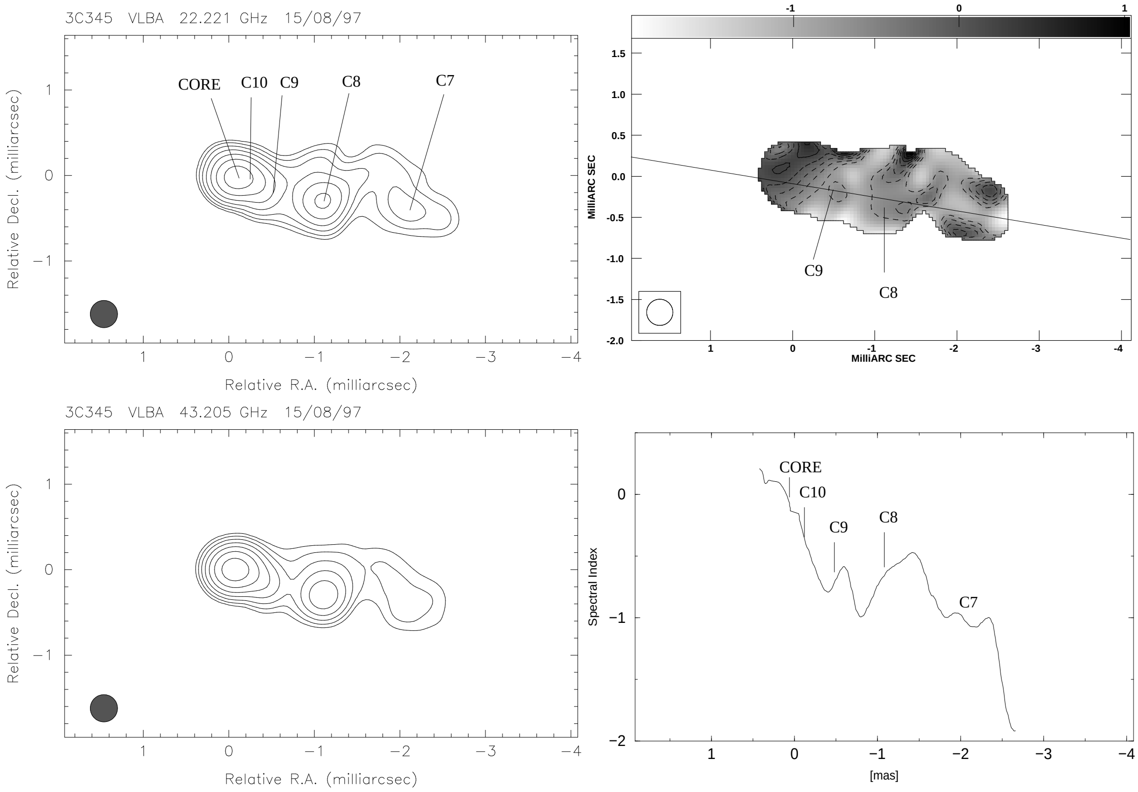

Figure 6.8: Spectral index map (top right) obtained by combining the VLBA images at 22 GHz (top left) and 43 GHz (bottom left), both at epoch 1997.62. The slice made along the jet direction illustrates the distribution of the spectral index (bottom right). With the appearance of C10, the spectral index of the core increases to −0.1 ($\alpha \approx -0.5$ at 1997.40). The components C10, C9, C8 and C7 have spectral indices of about −0.4, −0.7, −0.5 and −1.5. C9 and C8 have higher spectral indices than the ambient jet medium.

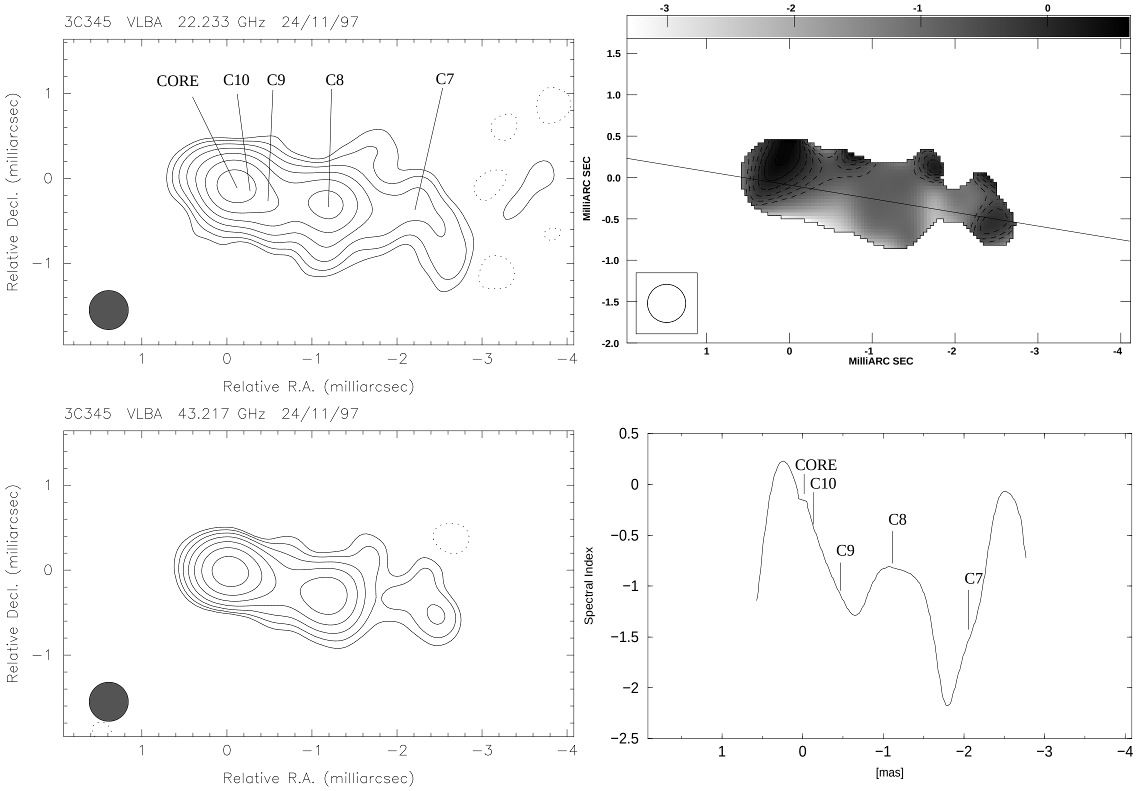

Figure 6.9: Spectral index map (top right) obtained by combining the VLBA images at 22 GHz (top left) and 43 GHz (bottom left), both at epoch 1997.90. The slice made along the jet direction illustrates the distribution of the spectral index (bottom right). From the core to C9, the spectral index decreases from −0.2 to −1.1. The spectral index distribution of C8 shows a plateau (similar as in the previous epoch) with $\alpha \approx -0.8$. The jet feature C7 has the lowest spectral index of $\alpha \approx -1.5$.

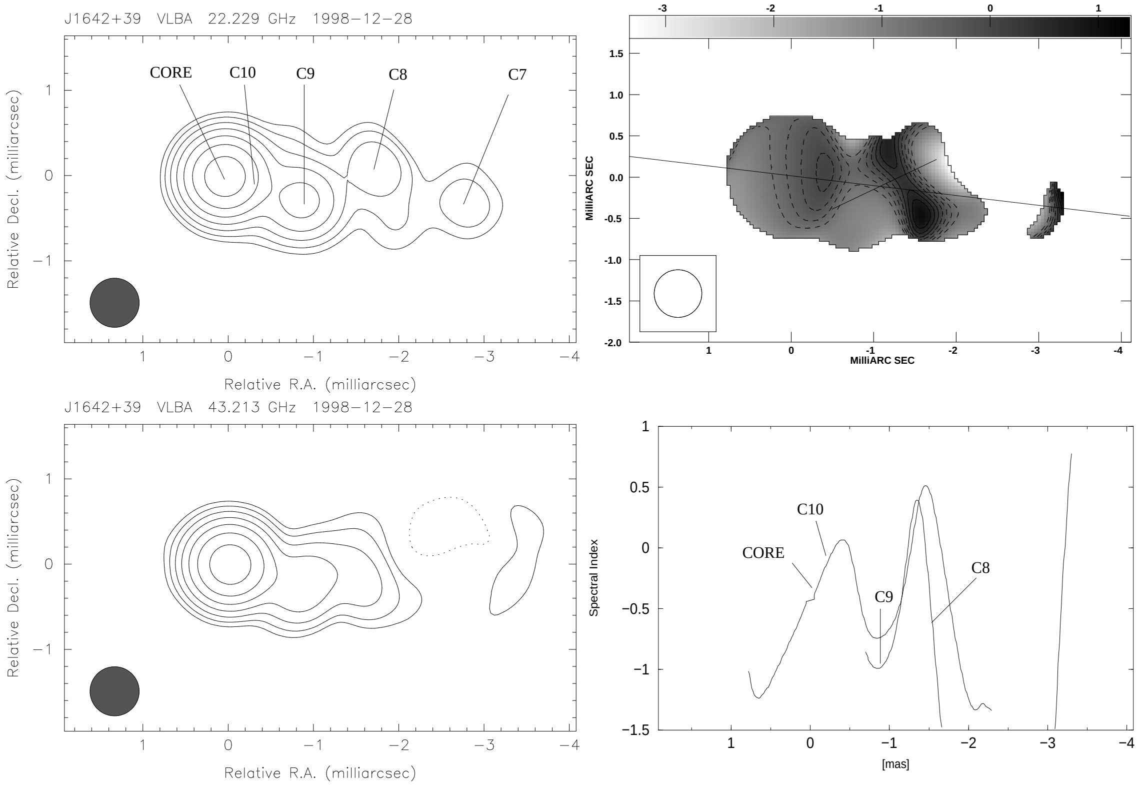

Figure 6.10: Spectral index map (top right) obtained by combining the VLBA images at 22 GHz (top left) and 43 GHz (bottom left), both at epoch 1998.99. The slice made along the jet direction illustrates the distribution of the spectral index (bottom right). The core and C10 have the highest spectral index with $\alpha \approx -0.4$ and $\alpha \approx -0.1$ respectively. A second slice is introduced to give a better fit of C9 and C8 which results in $\alpha \approx -1$ and $\alpha \approx -0.5$ respectively. An optically thick region lies between C9 and C8. The spectral index of the feature C7 can not be determined.

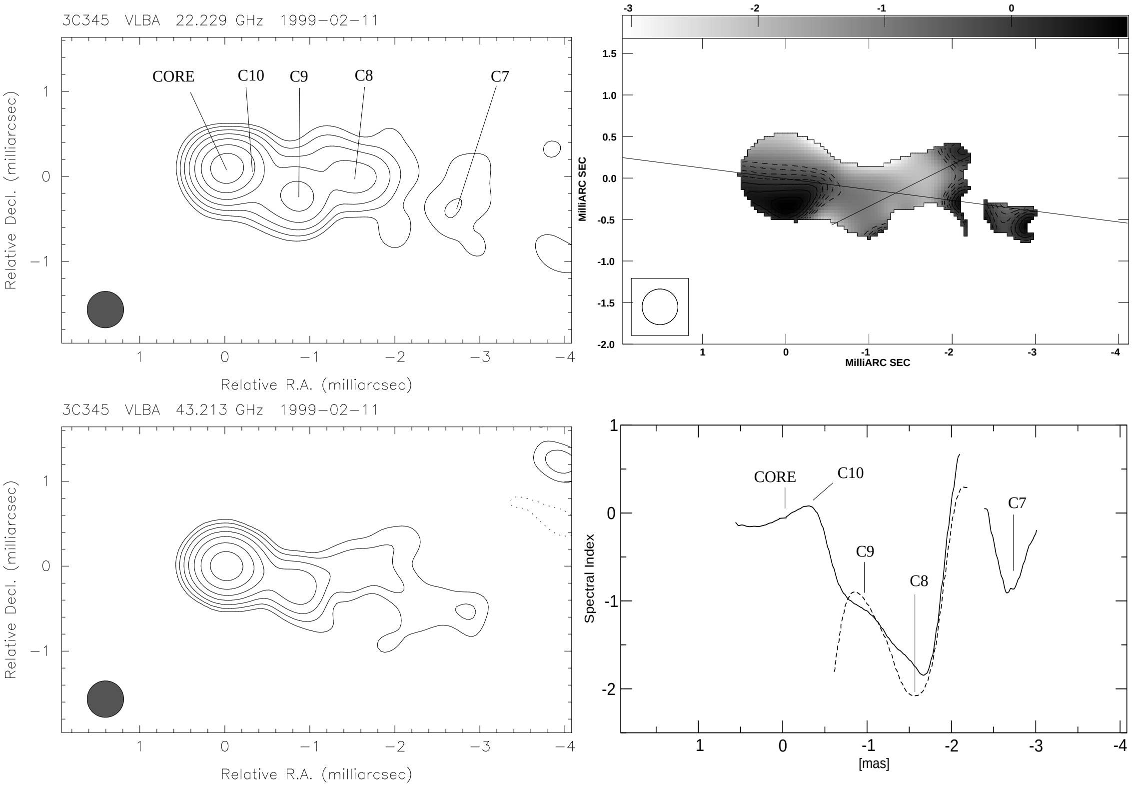

Figure 6.11: Spectral index map (top right) obtained by combining the VLBA images at 22 GHz (top left) and 43 GHz (bottom left), both at epoch 1999.12. The slice made along the jet direction illustrates the distribution of the spectral index (bottom right). A second slice (dashed in the profile) is introduced to show the values for C9 and C8. Their spectral indices are $\alpha \approx -1.0$ for C9 and $\alpha \approx -2.0$ for C8. As well the core as C10 have a spectral index of about zero. The uncertainty of the position of the expanded jet feature C7 led to a likely value of $\alpha \approx -0.9$.

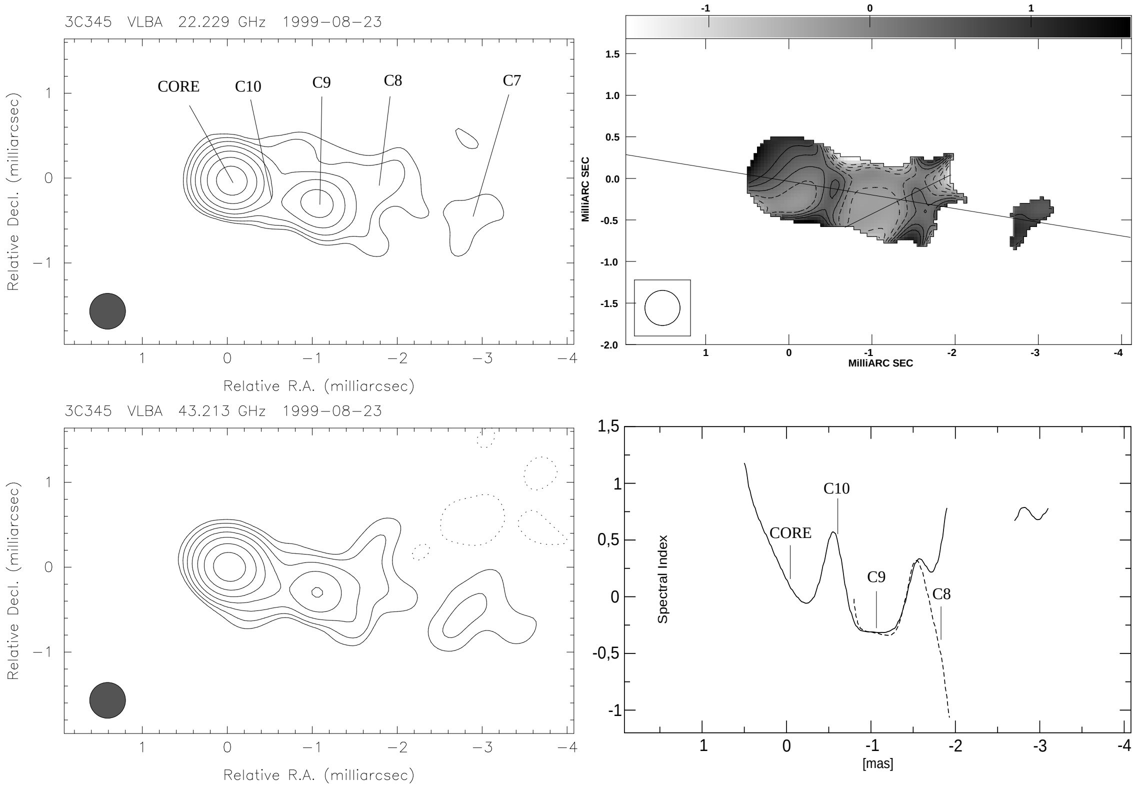

Figure 6.12: Spectral index map (top right) obtained by combining the VLBA images at 22 GHz (top left) and 43 GHz (bottom left), both at epoch 1999.64. The slice made along the jet direction illustrates the distribution of the spectral index (bottom right). A second slice (dashed in the profile) is introduced to show the values for C9 and C8. Between C9 ($\alpha \approx -0.3$) and C8 ($\alpha \approx -0.5$) an optically thick region of $\alpha \approx 0.3$ is visible. At a core distance of $r \approx 0.5$ mas the feature C10 ($\alpha \approx 0.5$) has a higher spectral index than the core ($\alpha \approx 0.1$). C7 is already too much resolved for a correct determination of its spectral index from the map.

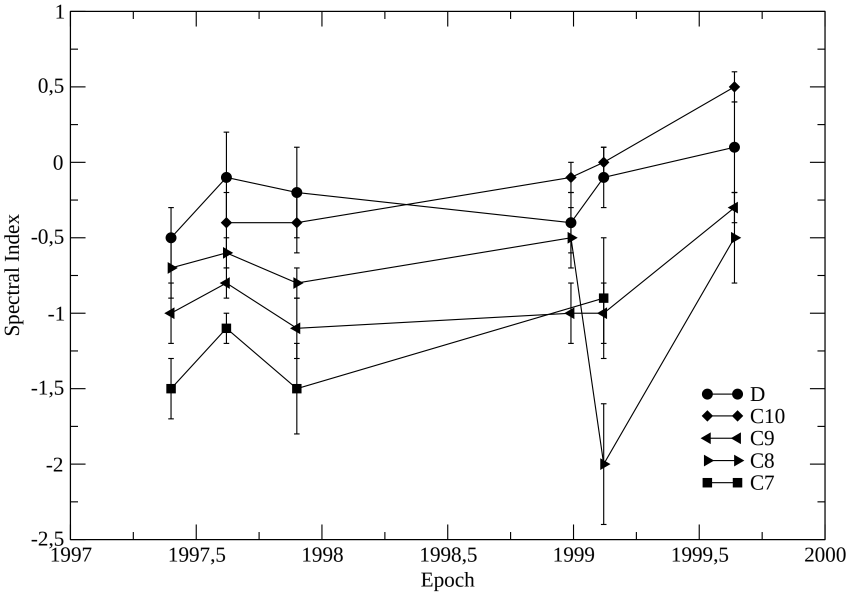

Figure 6.13: Evolution of the spectral index between 22 and 43 GHz from 1997.40 to 1999.64. The core (D) varies between optically thin and flat. The spectral index of the closest component C10 increases from optically thin to thick. Within 1997, α dropped in the descending order from C8 to C9 to C7 within a range of $\alpha \approx -0.7$ to $\alpha \approx -1.5$. The spectral indices of the outermost and partially resolved components C8 and C7 were difficult to determine in 1999. The error-bars of the spectral indices of the jet components are dependent on the position errors of the components.

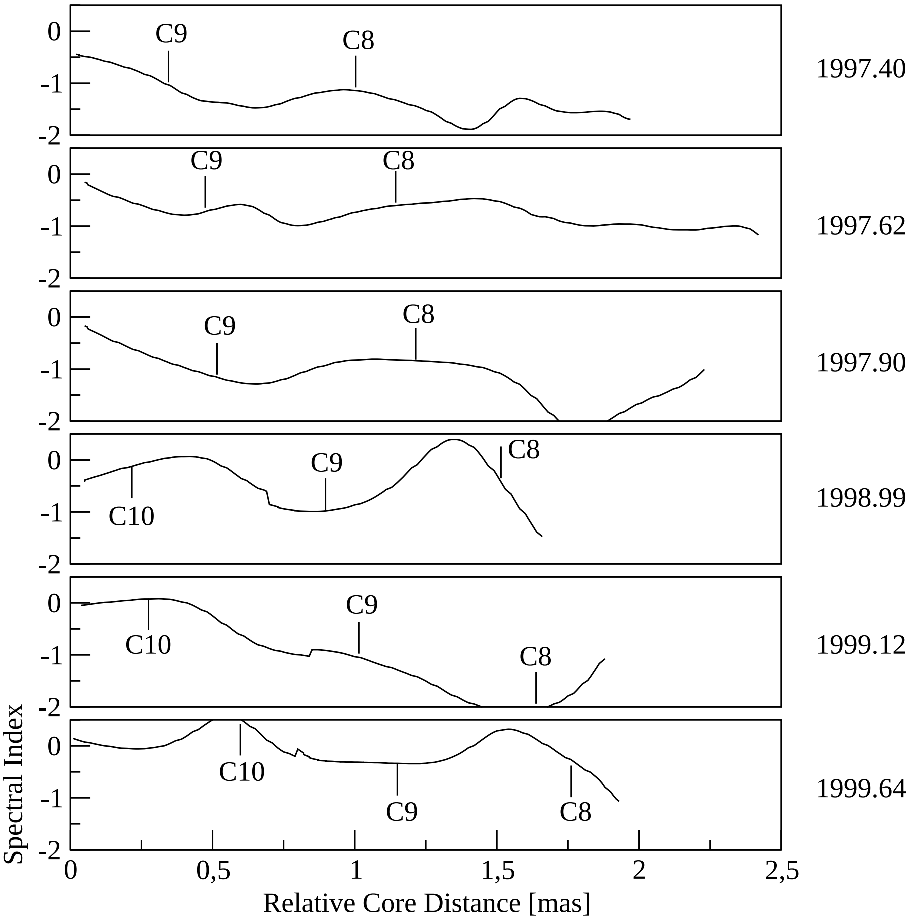

Figure 6.14: All slices which go through the core and the components C10, C9 and C8 are presented in chronological order. The x- and y axes are plotted with the same range for a better comparison. Small jumps in the profiles as seen for the last 3 epochs occur when two slices were combined with each other. A new component is located on a peak within $r \approx 1.2$ mas core distance (C8: 1997.40, 1997.62, 1997.90, C9: 1997.62, C10: 1999.64). This indicates that the surrounding medium of a component is at this distances optically thinner than the component medium itself. Further out, an optically thick region is seen between C8 and C9 in 1998.99 and 1999.64.

6.5 Summary

At low frequencies, the spectral index $\alpha_{5\mathrm{GHz}}^{1.6\mathrm{GHz}}$ is nearly flat at the central position of the core (Figures 6.1 – 6.4) which confirms earlier observations made at low frequencies by Lobanov & Zensus (1994). The spectral index rises up to $\alpha_{5\mathrm{GHz}}^{1.6\mathrm{GHz}} = 2$–3 in the direction of the eastern edge of the core. At higher frequencies $\alpha_{22\mathrm{GHz}}^{5\mathrm{GHz}} \approx 0.3$ around the central position of the core and increases up to $\alpha_{22\mathrm{GHz}}^{5\mathrm{GHz}} \approx 1$ at the eastern edge of the core region (Figure 6.6). This shows that the eastern edge of the core is optically thick at frequencies below 22 GHz. However, the spectral index between 5 and 22 GHz could be falsified because the turnover frequency at the core region is reported to be about 15 GHz (Lobanov 1998b), but could have also changed due to a change of physical jet parameters (Lobanov & Zensus 1999). The spectral index maps at the highest frequencies (Figures 6.7 – 6.12) show an optically thin to flat region around the central core position ($\alpha_{43\mathrm{GHz}}^{22\mathrm{GHz}} =$ -0.5 – 0) which confirms that the turnover frequency has to be below 22 GHz for the most epochs.

The resolution of the spectral index maps for the jet region is strongly dependent on the VSOP and VLBA images used. For the spectral index maps made out of the 1.6 and 5 GHz VSOP images (Figures 6.1 – 6.4), two different jet regions can be identified. The inner one with C7 ($1.7 < r < 2.7$ mas) and the outer one with C4 ($7 < r < 8$ mas). Both regions are optically thin, but the inner jet region has a steeper spectral index ($\alpha \approx -1$) than the outer one ($\alpha \approx -0.5$). The outer jet component C4 shows a continuous decrease of its spectral index during about 1.5 years. Ros et al. (1999) showed that C7 was still in an optically thick region at a core distance of $r < 1.5$ mas. This strong decrease of the spectral index of C7 from optically thick to thin indicates a transition zone in the jet at a core distance of about 1.5 mas. This transition zone is also described for other observational aspects, e.g. kinematic and polarization properties and flux density behavior (e.g. Lobanov 1996, Lobanov & Zensus 1999). It could be that at this distance, strong shocks have already been dissipated and the jet emission is mainly dominated by interactions between the jet and the ambient medium.

A clear identification of the inner jet components C8, C9 and partly C10 is possible in the spectral index maps, made out of images at 5, 22 and 43 GHz (Figures 6.6 – 6.12). The spectral evolution of C10 could be followed in the immediate vicinity of the core. C10 shows a change from optically thin at $r \approx 0.2$ mas to optically thick ($0.2 < r < 0.6$ mas) in 1999. Thus, between the observed component ejection and the aforementioned transition zone from optically thick to thin around 1.5 mas, the component can undergo an increase in the optical depth. The spectra of C9 and C8 show a remarkable change when these components approach and pass the assumed transition zone around 1.5 mas. Especially for $\alpha_{43\mathrm{GHz}}^{22\mathrm{GHz}}$ one can identify propagating optically thick peaks for the inner jet components in the spectra for $r \leq 1$ mas (Figure 6.14). These peaks correlate quite well with the position of jet components and are consistent with a shock evolution. At a core distance of about 1.5 mas, one optically thick peak occur in between the components C9 and C8. The components itself become optically thin (see epochs 1998.99 and 1999.64 in Figure 6.14). This illustrates again a change of physical jet parameters at a core distance of about 1.5 mas.

A north-south gradient with an optically thinner region at the north edge of the jet as reported by Ros et al. (1999) can not be confirmed for all except one spectral index map presented in this chapter. Only for one epoch at the lowest frequencies (Figure 6.3), does one see a gradient with an optically thinner region at the north edge of the jet. Due to the higher resolution of the spectral index maps of the inner jet presented in this thesis compared with the maps of Ros et al. (2000), it can be that the different spectral regions in the inner jet described above blend together at a lower resolution.

In summary, one can conclude that the spectra of the jet components and the jet spectra between these components change in a systematic way while the features travel along the jet. Based on this systematics one can draw a rough general picture which divides the jet in 4 regions. A newly born jet feature can become optically thick shortly after its ejection ($0.2 \leq r \leq 0.6\,\mathrm{mas}$) as seen for C10 (Region A). Up to a core distance of about 1.5 mas the components become optically thin but the ambient jet medium is optically thinner (Region B). This situation changes in the jet at about $1.5 \leq r \leq 3\,\mathrm{mas}$ (Region C). The ambient jet medium to the west and to the east of the components has a higher spectral index and can even become optically thick. Further out at a core distance of $3 < r < 8\,\mathrm{mas}$ (Region D) the spectral index of a jet feature can be higher than for jet features in region C as seen for C4 at low frequencies. Relativistic, time-dependent, hydrodynamical simulations of jets confirm the hypothesis that optically thick regions can occur between jet components during their evolution (M. Aloy, priv. comm.). This shows that the jet properties of 3C 345 obtained from high resolution spectral index maps are consistent with general theoretical jet simulations.

Chapter 7

Summary

7.1 The Results

The observations of 3C 345 made for this thesis cover a time range from 1997.40 to 1999.69. They consist of 4 VSOP observations at 1.6 GHz, 4 VSOP observations at 5 GHz, 7 VLBA observations at 22 GHz and 9 VLBA observations at 43 GHz (chapter 3). The use of space-VLBI (section 2.5) enabled a high resolution study of 3C 345 to be made at lower frequencies also. Additionally, 2 VLBA observations at 22 GHz of Ros *et al.* (2000) and 5 VLBA observations at 43 GHz of Marscher have been re-modelled for consistency. Together with earlier data from the literature, the evolution of 11 jet components of 3C 345 has been studied in detail. The youngest jet components C9–C11 have been modelled for the first time. C11 was traced from the shortest core distance of 0.075 mas up to 0.149 mas which is the most precise measurement of a jet component at this small core distance ever made for 3C 345.

The 4 observing frequencies used in this thesis allowed a determination of the core shift for the inner jet components to be made (section 4.1). This provided a common reference frame for epochs at all frequencies, and enabled an accurate determination of trajectories of the jet components to be made. In general, the component trajectories in 3C 345 differ from each other, but this work has also shown that the trajectories of the jet components C5 and C8 are similar in shape (section 4.9). The jet component C8 passed through similar stages in its trajectory (e.g. the turning point) 8–10 years later than C5. The study of the component ejection angles shows a quasi-periodicity of 8–10 years (section 4.14) which emphasizes the similar trajectories of C5 and C8. Additionally, an increase of $2.6° \pm 0.3°\text{year}^{-1}$ of the component ejection angles is superimposed to the oscillation.

Younger jet components have a higher proper motion at a given core distance than older components (section 4.12). This can be an evidence of a global change of intrinsic jet parameter. An increasing Lorentz factor from $\gamma \approx 3$ to $\gamma \approx 16$ for the jet components is necessary to explain the observed kinematics (section 4.13). The angle to the line of sight of the moving jet components varies from $\Theta \approx 0.2°$ to $\Theta \approx 3.5°$ and the corresponding Doppler factor changes from from $\delta \approx 3$ to $\delta \approx 30$.

Flux density flares of the components have been observed within the inner 1.2 mas (section 5). The magnitude of individual component flares changes with a time period of $t \approx 9$ years (section 5.7). Together with the observed quasi-periodicity of the component ejection angles and the similarity of the C5/C8 trajectories, this indicates that the jet in 3C 345 is driven by a quasi-periodic process. Furthermore, the peaks of the component flares occur mostly when a jet component change its direction from south-west to north-west or vice versa. This correlation can be explained by Doppler boosting which enhances the component emission when the component makes a turn, traveling along a 3D helical path. This is in good agreement with the bend of the viewing angles to the line of sight derived from the increasing Lorentz factor.

The study of the spectral evolution of 3C 345 shows optically thick regions which are related to the jet components within $0.2 \leq r \leq 0.6$ mas (section 6). Up to a core distance of about 1.2–1.5 mas the components become optically thin and have a steep spectral index. The spectral index of the ambient jet medium is steeper. This situation changes at core distances between about 1.5 and 3 mas. In this region, the spectral index of the jet components is steeper and the ambient jet medium can even become optically thick. This observed behaviour is also reproduced in recent theoretical jet simulations (M. Aloy, priv. comm). Further out at a core distance of $3 < r < 8$ mas the spectral index of a jet feature can be higher than for jet features at core distances between 1.5 and 3 mas.

7.2 The Model of 3C 345

The Two-Fluid Model

The perturbation of the jet itself can be explained by the two fluid model (Sol *et al.* 1989). They describe the jet with an ultra-relativistic ($v_b \simeq c$) electron-positron ($e^{\pm}$) plasma (the beam) and a surrounding slow electron-proton (e^-p) plasma with a speed of $v_j \simeq 0.4c$. The beam is already ejected with a relativistic speed at the nucleus and has a bulk Lorentz factor of $3 \leq \gamma_b \leq 20$. This is in the same range as the Lorentz factor $3 \leq \gamma_b \leq 16$ derived for 3C 345 in this thesis. Most of the mass and kinetic energy is carried by the e^-p-jet which is coming from the outer part of the accretion disc (AD). This plasma is responsible for the extended structure on kpc-scales, the formation of hot spots and extended lobes. The ultra-relativistic jet moves through a channel in the e^-p-jet and is responsible for the VLBI parsec-scale jet, the observed superluminal components and the γ-ray emission (Roland *et al.* 1994). The relativistic beam can propagate when the magnetic field B is strong enough and when it is parallel to the flow in the beam and the mixing layer (Pelletier *et al.* 1988). The magnetic field in the e^-p-jet becomes toroidal (Pelletier & Roland 1990). The two fluid model has the advantage that only a small fraction of the electrons and positrons have to reach the bulk Lorentz factor to explain the superluminal motion. It also solves the discrepancy between the high relativistic jet at parsec scales and the classical jet speed expected for the large scale structures. Also the observed discrepancy between the position angles of the parsec scale jet and the extended structure can be explained by the two fluids because the emitting region need not necessarily be the same. Thus the beam and the e^-p-jet can be ejected at a different angle. The beam confinement is stabilized by a relaxation zone in the strong magnetic field zone which can also reinforce the collimation of the jet.

The Binary Black Hole Model

Since this work has shown that the jet of 3C 345 is driven by a quasi-periodic process with a time period between 8 to 10 years, one has to think about the origin of this period. It is widely accepted that the engines of AGNs are Supermassive-Black-Holes (SBH) in the center of galaxies. Furthermore, the merging of galaxies is a very common phenomenon in the universe. Since AGNs are observed in elliptical galaxies it is very likely that these ellipticals are products of merged galaxies. If two galaxies merge and both contain a SBH then they can form a Binary-Black-Hole (BBH) system (Figure 7.1). Theoretical studies of such BBH systems have been done, for instance, by Begelman *et al.* (1980) and Yu (2002).

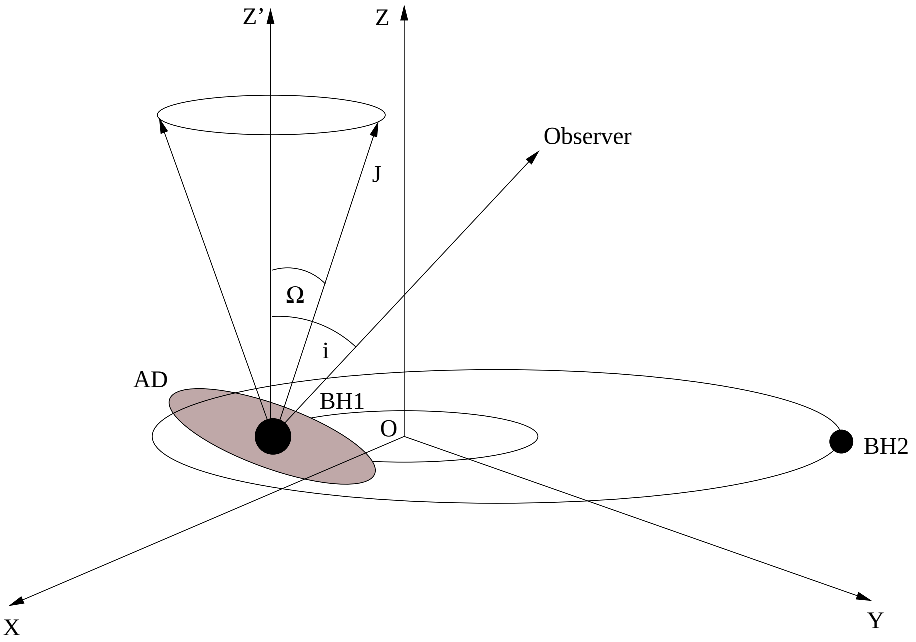

Figure 7.1: Supermassive binary black hole system. The coordinate system is centered on the centre of mass of the system. The super-massive black holes BH1 and BH2 have masses M1 and M2. The precession of the AD is denoted by the angle Ω and the vector **J**. The line of sight is inclined to the precession axis Z' by the angle i.

In the BBH models, one assume that at least one of the two SBHs has an AD. The observed variability in the optical and radio regime is created by dynamic processes of the AD together with the binary system. These include precession of the SBHs, precession of the AD, orbital motion of the secondary SBH and its passage through the AD.

BBH models have already been applied to some AGNs (e.g. 3C 345, Lobanov & Roland (2002); PKS 0420-014, Britzen *et al.* (2001); 1928+738, Roos *et al.* (1993)). Lobanov & Roland (2002) used the BBH model together with the two fluid model (Sol *et al.* 1989) to describe the kinematic-, optical- and flux density evolution of the jet component C7 in 3C 345. The optical and radio flux density evolution and the component trajectory of C7 can be well described by their BBH model. The model parameters derived result in SBH masses of $M_1 = 1.5 \cdot 10^9 M_\odot$ and $M_2 = 1.0 \cdot 10^9 M_\odot$

(Lobanov & Roland 2002). The orbital major axis is 0.64 pc (0.13 mas), the orbital period is given by T_{orb} =170years (8.5 years) and the precession period is given by T_{prec} =2500 years (125 years). The numbers in brackets are the values in the observer's frame. One sees immediately that the derived orbital period perfectly matches the quasi-periodicity obtained in this thesis. The $t \approx 9$ year period of the component peak flux changes (section 5.7) fits well with the orbital period derived from the BBH model. Also the period of the component ejection angle of 8–10 years (section 4.14) can be explained by the dynamic process caused by the second SBH. Moreover, the component ejection angle variation requires a linear term for the observed long period (section 4.14) which can be ascribed to the derived precession period of 125 years in the observers frame. The long term change of the observed component ejection angle of $2.6° \pm 0.3°\,\mathrm{year}^{-1}$ match perfectly with the predicted change of $2.9°\,\mathrm{year}^{-1}$ from the BBH model.

One would also expect similar trajectories for jet components which are ejected at a time interval which is comparable with the orbital period. This has been confirmed by the observed similarity of the trajectories of C5 and C8 (section 4.9). But one has also to note that the precession period of 125 years, together with other effects, makes it unlikely that the trajectories of two components, which are ejected about 9 years apart, look exactly equal. Thus, the shapes of the C5 and C8 trajectories are similar, but the sizes are different. In summary, the quasi-periodicity in the parsec-scale jet of 3C 345 shown in this thesis can be well explained by the BBH model derived from Lobanov & Roland (2002).

7.3 Outlook

In future work, we will continue the VLBI monitoring of 3C 345 to pursue our intensive study of this quasar. It is important to trace the future evolution of the jet components in 3C 345, in order to verify and to improve the picture which we have obtained of this archetypical quasar. We have made several new observations at 86 GHz during recent years. These observations will supplement our extensive study at core distances smaller than 0.1 mas. The BBH model of Lobanov & Roland (2002) will be applied to the jet components C8 and C9 when their trajectories have been sampled sufficiently. A possible motion of the core could influence the observed component trajectories. To avoid this influence, we started a phase-referencing program at the VLBA at 43 and 86 GHz in 2002. This provides the highest precision achievable today and allows us to verify the assumed stationarity of the core. In summary, the detailed study of this archetypical quasar will be continued to enhance our knowledge of these most powerful objects in the universe.

Chapter 8

References

Abramovicz, M. A., 1992, Page 206 of: Roland, J., Sol, H., Pelletier, G. (eds), *Extragalactic Radio Sources; From Beams to Jets.* Cambridge: Cambridge University Press.

Baade, W., Minkowski, R., 1954, *Astrophys. J.*, **119**, 206.

Babadzhanyants, M.K., Belokon, E.T., 1984, *Astrophysics*, **20**, 461.

Babadzhanyants, M.K., Belokon, E.T., 1984, *Astrophysics*, **21**, 148.

Babadzhanyants, M.K., Belokon, E.T., Gramm, N.G., 1995, *Astron. Zhurnal*, **72**, 447B.

Bartel, N., Herring, T. A., Ratner, M. I., Shapiro, I. I., Corey, B. E., 1986, *Nature*, **319**, 733B.

Bate, R.R., Mueller, D. D., White, J. E., 1971, *Fundamentals of Astrodynamics*, p.59

Begelman, M.C., Blandford, R.D., Rees, M.J., 1980, *Nature*, **287**, 307

Begelman, M.C., Blandford, R.D., Rees, M.J., 1984, *Rev. Mod. Phys.*, **56**, 255.

Bevington, P.R., Robinson, D.K., 1992, *Data Reduction and Error Analysis for the Physical Science.* New York, USA: McGraw-Hill, 2nd edition.

Biretta, J.A., Moore, R.L., Cohen, M.H., 1986, *Astrophys. J.*, **308**, 93.

Blandford, R.D., Königl, A., 1979, *Astrophys. J*, **232**, 34.

Blandford, R.D., Rees, M.J., 1974, *Monthly Notices of the Royal Astronomical Society*, **169**, 395.

Britzen, S., Roland, J., Laskar, J., Kokkotas, K., Campbell, R.M., Witzel, A., 2002, *Astron. Astrophys.*, **374**, 784.

Boden, D. R., 1992, Chapter 6 of: W.J., Larson, J.R., Wertz (eds), *Space Mission Analysis and Design.* 2nd edition, Torrance, CA, USA: Microcosm, Inc.

Bolton, J., Stanley, G., Slee, O., 1949, *Nature*, **164**, 101.

Clark, B.G., Kellermann, K.I., Bare, C.C., Cohen, M.H., Jauncey., D.L., 1968a, *Astrophys. J., Letters*, **153**, L67.

Clark, B.G., Kellermann, K.I., Bare, C.C., Cohen, M.H., Jauncey., D.L., 1968b, *Astrophys. J.*, **153**, 705.

Clark, B.G., 1980, *Astron. Astrophys.*, **89**, 377.

Cohen, M.H., Cannon, W., Purcell, G.H., Shaffer, D.B., Broderick, J.J., Kellermann, K.I., Jauncey, D.L., 1971, *Astrophys. J.*, **170**, 207.

Cornwell, T.J., Braun, R., 1989, Page 167 of: Perley, R.A., Schwab, F.R., Bridle, A.H. (eds), *Synthesis imaging in radio astronomy*, San Francisco, USA.

Cornwell, T.J., 1995, Page 217 of: Zensus, J.A., Diamond, P.D., Napier, J.P. (eds), *Very Long Baseline Interferometry and the VLBA.* Cambridge, UK: Cambridge University Press.

Cornwell, T.J., Fomalont, E.B., 1999, Page 187 of: Taylor, G.B., Carilli, C.L., Perley, R.A. (eds), *Synthesis Imaging in Radio Astronomy II*, NRAO/NMIMT, ASP Conference Series, **180**, San Francisco, CA, USA.

Cotton, W.D., 1979, *Astrophys. J.*, **84**, 1122.

Cotton, W.D., 1995, Page 179 of: Zensus, J.A., Diamond, P.D., Napier, P.J. (eds), *Very Long Baseline Interferometry and the VLBA.* Cambridge, UK: Cambridge University Press.

Doeleman, S., Krichbaum, T.P., 1999, Page 73 of: Greve, A., Krichbaum, T.P., d'Heres, St. Martin (eds), *2nd millimeter-VLBI science workshop*, Institut de Radio Astronomie Milliétrique, France.

Ferrari, A., 1998, *Astron. Astrophys.*, **36**, 539.

Gómez, J.L., Alberdi, A., Marcaide, J.M., 1994, *Astron. Astrophys.*, **284**, 51.

Guirado, J.C., Ros, E., Jones, D.L., Lestrade, J.-F., Marcaide, J.M., Pérez-Torres, M.A., Preston, R.A., 2001, *Astron. Astrophys.*, **371**, 766.

Hardee, P.E., 1987, *Astrophys. J.*, **318**, 78.

Henri, G., Pelletier, G., 1992, Page 221 of: Roland, J. Sol, H., Pelletier, G. (eds), *Extragalactic Radio Sources: From Beams to Jets.* Cambridge, UK: Cambridge University Press.

Hewitt, A., Burbidge, G., 1993, *Astrophys. J.*, **87**, 451.

Hirabayashi, H., 1989, *The Impact of VLBA on Astrophysics and Geophysics.*, IAU Symp. 129, 441.

Hirabayashi, H., 2000a, Page 3 of: Hirabayashi, H., Edwards, P.G., Murphy, D.W. (eds), *Astrophysical Phenomena Revealed by Space VLBI*, Sagamihara, Japan: ISAS.

Hirabayashi, H. 2000b, Page 277 of: Hirabayashi, H., Edwards, P.G., Murphy, D.W. (eds), *Astrophysical Phenomena Revealed by Space VLBI*, Sagamihara, Japan: ISAS.

Hirotani, K., Iguchi, S., Kimura, M., Wajima, K., 2000, *Astrophys. J.*, **545**, 100.

Högbom, J. 1974, *Astrophys. J. Suppl.*, **15**, 417.

Hughes, P.A., Aller, H.D., Aller, M.F., 1991, *Page 142 of*: Valtaoja, E., Valtonen, M. (eds), *Variability of Blazars*, Cambridge, UK: Cambridge University Press.

Jennison, R.C., 1958, *Monthly Notices of the Royal Astronomical Society*, **118**, 276.

Kardashev, N.S., 1997, *Experimental Astronomy*, **7**, 329.

Kidger, M.R., 1990, *Astron. Astrophys.*, **226**, 9.

Kobayashi, H., 2000, Page 109 of: Hirabayashi, H., Edwards, P.G., Murphy, D.W. (eds), *Astrophysical Phenomena Revealed by Space VLBI*, Sagamihara, Japan: ISAS.

Königl, A., 1981, *Astrophys. J.*, **243**, 700.

Krichbaum, T.P., Witzel, A., Zensus, J.A., 1999, Page 5 of: Greve, A., Krichbaum, T.P., d'Heres, St. Martin (eds), *2nd millimeter-VLBI science workshop*, Institut de Radio Astronomie Milliétrique, France.

Lainela, M., Valtaoja, E., Teräsranta, H., 1992, *American Astronomical Society*, 180th AAS Meeting, **24**, 731.

Leppänen, K.J., 1995., Ph.D. thesis, Helsinki University of Technology, Helsinki, Finnland.

Levy, G.S., Linfield, R.P., Edwards, C.D., Ulvestad, J.S., Jordan, J.F. Jr., Dinardo, S.J., Christensen, C.S., Preston, R.A., Skjerve, L.J., Stavert, L.R., Burke, B.F., Whitney, A.R., Cappallo, R.J., Rogers, A.E.E., Blaney, K.B., Maher, M.J., Ottenhoff, C.H., Jauncey, D.L., Peters, W.L., Reynolds, J., Nishimura, T., Hayashi, T., Takano, T., Yamada, T., Hirabayashi, H., Morimoto, M., Inoue, M., Shiomi, T., Kawaguchi, N., Kunimori, H., Tokumaru, M., Takahashi, F., 1989, *Astrophys J.*, **336**, 1098.

Levy, G.S., Linfield, R.P., Ulvestad, J.S., Edwards, C.D., Jordan, J.F. Jr., di Nardo, J., Christensen, C.S., Preston, R.A., Skjerve, L.J., Blaney, K.B., 1986, *Science*, **234**, 187.

Linfield, R.P., 1990, *Astrophys J.*, **358**, 350.

Lobanov, A.P., Zensus, J.A., 1994, Page 157 of Zensus, J.A., Kellermann, K.I. (eds), *Compact Extragalactic Radio Sources*, Socorro, New Mexico, USA.

Lobanov, A.P., 1996, Ph.D. thesis *Physics of the Parsec-Scale Structures in the Quasar 3c 345*, New Mexico Institute of Mining & Technology, Socorro, New Mexico, USA.

Lobanov, A.P., 1998b, *Astron. Astrophys. Suppl.*, **132**, 261.

Lobanov, A.P., Zensus J.A., 1999, *Astrophys. J.*, **521**, 509.

Lobanov, A.P., Krichbaum, T.P., Graham, D.A., Witzel, A., Kraus, A., Zensus, J.A., Britzen, S., Greve, A., Grewing, M., 2000, *Astron. Astrophys.*, **364**, 391.

Lobanov, A.P., Roland, J., 2002, Page 121 of: Ros, E., Porcas, R.W., Lobanov, A.P., Zensus, J.A., *New Developments in VLBI Science and Technology*, 6th European VLBI Network Symposium, Bonn, Germany

Marscher, A.P., Gear, W.K., 1985, *Astrophys. J.*, **298**, 114.

Mattig, W., 1958, *Astronomische Nachrichten*, **284**, 109.

Mirua, K., 1986, *Concept of Tension Activated Cable Lattice Antenna*, 37th Congress of Int. Astronautical Federation, IAF-86-206, Innsbruck, Austria.

Moran, J.M., Dhawan, V., 1995, Page 151 of: Zensus, J.A., Diamond, P.D., Napier, J.P. (eds), *Very Long Baseline Interferometry and the VLBA*, Cambridge, UK: Cambridge University Press.

Moffet, A.T., Gubbay, J., Robertson, D.S., Legg, J.A., 1971, Page 228 of: Evans, D.S. (eds), *External Galaxies and Quasi-Stellar Objects*, IAU Symposium, **44**, Dordrecht, The Netherlands: Reidel.

Narayan, R., Nityananda, R., 1986, *Ann. Rev. Astron. Astrophys.*, **24**, 127.

Pearson, T.J., 1999, Page 341 of: Taylor, G.B., Carilli, C.L., Perley, R.A. (eds), *Synthesis Imaging in Radio Astronomy II*, NRAO/NMIMT, ASP Conference Series, **180**.

Pearson, T.J., Shepherd, M.C., Taylor, G.B., Myers, S.T., 1994, *Bulletin of the American Astronomical Society*, **26**, 1318.

Pelletier, G., Sol, H., Asseo, E., 1988, *Phys. Rev. A.*, **38**, 2552.

Pelletier, G., Roland, J., 1990, Page 323 of: Zensus, A., Pearson, T.J. (eds), *Parsec-Scale Jets*, Cambridge, UK: Cambridge University Press.

Porcas, R.W., Rioja, M.J., Machalski, J., Hirabayashi, H., 2000, Page 245 of: Hirabayashi, H., Edwards, P.G., Murphy, D.W. (eds), *Astrophysical Phenomena Revealed by Space VLBI*, Sagamihara, Japan: ISAS

Press, W.H., Teukolsky, S.A., Vetterling, W.T., Flannery, B.P., 1992, *Numerical Recipes 2nd edition*, chapter 15, Cambridge, UK: Cambridge University Press

Priorities in Space Research, 1971-1980, 86 National Academy of Science-National Council, Washington DC.

Qian, S.J., Krichbaum, T.P., Quirrenbach, A., Hummel, C.A., Zensus, J.A., 1992, *Chin. Astron. Astrophys.*, **16/2**, 137.

Qian, S.J., Krichbaum, T.P., Zensus, J.A., Steffen, W., Witzel, A., 1996, *Astron. Astrophys.*, **308**, 395.

Rantakyrö, F.T., Baath, L.B., Matveenko, L., 1995, *Astron. Astrophys.*, **293**, 44.

Readhead, A.C.S., Walker, R.C., Pearson, T.J., Cohen, M.H., 1980, *Nature*, **285**, 137.

Readhead, A.C.S., Wilkinson, P.N., 1978, *Astrophys. J.*, **223**, 25.

Rees, M.J., 1966, *Nature*, **211**, 468.

Rees, M.J., 1984, *Astron. Astrophys, Ann. Rev.*, **22**, 571.

Rohlfs, K., Wilson, T.L., 1996, *Tools of Radio Astronomy*, Berlin: Springer.

Roland, J., Teyssier, R., Roos, N., 1994, *Astron. Astrophys*, **231**, 327.

Ros, E., Zensus, J.A., Lobanov, A.P., 2000, *Astron. Astrophys*, **354**, 55.

Roos, N., Kaastra, J.S., Hummel, C.A., 1993, *Astrophys J.*, **409**, 130.

Rybicki, G.B., Lightman, A.P., 1979, *Radiative processes in astrophysics*, p110.

Ryle, M., 1957, *Nature*, **180**, 110.

Ryle, M., Neville A.C., 1962, *Monthly Notices of the Royal Astronomical Society*, **125**, 39.

Sade, R.S., Deerkoski, L., 1981, *Proc. AIAA/NASA Symposium on Space Tracking and Data Systems*, 77.

Schilizzi, R.T., 1988, *The Impact of VLBI on Astrophysics and Geophysics*, **129 IAU Symp.**, 469: Dordrecht, The Netherlands: Kluwer.

Schmidt, M., 1963, *Nature*, **197**, 1040.

Schwab, F.R., 1980, *Proc. S.P.I.E.*, **231**, 18.

Schwab, F.R., Cotton, W.D., 1983, *Astron. J.*, **88**, 688.

Scott, P.E., Ryle, M., Hewish, A., 1961, *Monthly Notices of the Royal Astronomical Society*, **122**, 18.

Smith, F.G., 1951, *Nature*, **168**, 192.

Sol, H., Pelletier, G., Asséo, E., 1989, *Monthly Notices of the Royal Astronomical Society*, **237**, 411.

Steffen, W., Zensus, J.A., Krichbaum, T.P., Witzel, A., Qian, S.J., 1995, *Astron. Astrophys.*, **302**, 335.

Stevens, J.A., Litchfield, S.J., Robson, E.I., Hughes, D.H., Gear, W.K., Teräsranta, H., Valtaoja, E., Tornikoski, M., 1994, *Astrophys J.*, **437**, 91.

Taylor, G.B., Carilli, C.L., Perley, R.A. (eds), 1999, *Synthesis Imaging in Radio Astronomy II*, NRAO/NMIMT, ASP Conference Series, **180**, San Francisco, CA, USA.

Teräsranta, H., Tornikoski, M., Valtaoja, E., Urpo, S., Nesterov, N., Lainela, M., Kotilainen, J., Wiren, S., Laine, S., Nilsson, K., Valtonen, L., 1992, *Astron. Astrophys Suppl.*, **94,1**, 121.

Thompson, A.R., Moran, J.M., Swenson, G.W. Jr., 1998, *Interferometry and Synthesis in Radio Astronomy*, Malabar, Florida, USA: Krieger Publishing Company.

Ulvestad, J.S., Linfield, R.P., 1998, Page 397 of: Zensus, J.A., Taylor, G.B., Wrobel, J.M. (eds), *Radio Emission from Galactic and Extragalactic Compact Sources*, ASP Conference Series, Volume 144, IAU Colloquium 164.

Ulvestad, J.S., 1999, Page 513 of: Taylor, G.B., Carilli, C.L., Perley, R.A. (eds), *Synthesis Imaging in Radio Astronomy II*, NRAO/NMIMT, ASP Conference Series, **180**, San Francisco, CA, USA.

Unwin, S.C., Wherle, A.E., Lobanov, A.P., Zensus, J.A., Madejski, G.M., Aller, M. F., Aller, H.D., 1997, *Astrophy. J.*, **480**, 596.

VSOG (VSOP Science Operations Group), 2000, *AO5 Proposer's Guide VSOP*, Sagamahira, JAPAN: ISAS.

Walker, R.C., 1989a, Page 141 of: Feli, M., Spencer, R. (eds), *Very Long Baseline Interferometry*, NATO ASI Series C, **283**, Dordrecht, The Netherlands: Kluwer.

Walker, R.C., 1989b, Page 355 of: Perley, R.A., Schwab, F.R., Bridle, A.H. (eds), *Synthesis Imaging in Radio Astronomy*, San Francisco: Astronomical Society of the Pacific.

Walker, R.C., 1999, Page 437 of: Taylor, G.B., Carilli, C.L. Perley, R.A. (eds), *Synthesis Imaging in Radio Astronomy II*, NRAO/NMIMT, ASP Conference Series, **180**, San Francisco, CA, USA.

Weedman, D.W., 1986, *Quasar Astronomy*, 60, Cambridge Univiversity Press.

Whitney, A.R., Shapiro, I.I., Rogers, A.E.E., Robertson, D.S., Knight, C.A., Clark, T.A., Goldstein, R.M., Marandino, G.E., Vandenburg, N.R., 1971, *Science*, **173**, 225.

Wilkinson, P.N., 1989, Page 183 of: Felli, M., Spencer, R. (eds), *Very Long Baseline Interferometry*, NATO ASI Series. Dordrecht, The Netherlands: Kluwer.

Weinberg, S. 1972, *Gravitation and Cosmology*, New York, USA: Wiley and Sons.

Yu, Qingjuan, 2002, *Monthly Notices of the Royal Astronomical Society*, **331**, 935

Zensus, J.A., Pearson, T.J., (eds), 1987, *Superluminal Radio Sources*, Cambridge: Cambridge University Press.

Zensus, J.A., Cohen, M.H., Unwin, S.C., 1995, *Astrophys J.*, **35**, 433.

Zhang, X., Xie, G.Z., Bai, J.M., Zhao, G., 2000, *Astrophys. & Space Science*, **271**, 1

Danksagung

An dieser Stelle möchte ich all denjenigen mein Dank aussprechen, die mir bei der Anfertigung meiner Doktorarbeit mit Rat und Hilfe zur Seite gestanden, und mir den Weg dorthin ermöglicht haben.

An erster Stelle möchte ich mich bei dem geschäftsführenden Direktor des MPIfR, Dr. J.A. Zensus und den Direktoren Prof. Dr. K. M. Menten, Prof. Dr. G. Weigelt und Prof. Dr. R. Wielebinski bedanken, daß sie mir die Möglichkeit gegeben haben, meine Doktorarbeit am Max-Planck-Institut für Radioastronomie anzufertigen und meine wissenschaftlichen Ergebnisse auf internationalen Konferenzen zu präsentieren. Mein ganz besonderer Dank gilt dabei Herren Dr. J.A. Zensus der mir die Bearbeitung dieses interessanten Themas ermöglichte, und der mich immer bei dem Fortgang meiner Arbeit unterstützt hat.

Bedanken möchte ich mich für die offizielle Betreuung meiner Doktorarbeit bei meinen Referenten Prof. Dr. U. Klein und Priv.-Doz. Dr. W. K. Huchtmeier.

Weiterhin danke ich all meinen akademischen Lehrern, die mir auf meinem Weg in die Wissenschaft entscheidende Impulse gegeben haben.

Ganz besonders hervorheben möchte ich unseren Forschungsgruppenleiter Herrn Dr. Arno Witzel, der für mich immer als Ansprechpartner in allen Lebenslagen da war und der immer eine Lösung für Probleme jeglicher Art fand. Seine überaus freundliche Art, sein starkes persönliches Engagement beim Fortgang meiner Arbeit und das hervorragende Arbeitsklima haben mich während meiner gesamten Doktorarbeit begleitet und diese Arbeit erst möglich gemacht.

In alphabetischer Reihenfolge möchte mich mich ganz besonders bei den drei Wissenschaftlern bedanken, mit denen ich während meiner Doktorarbeit am engsten zusammengearbeitet habe: Dr. Thomas P. Krichbaum, Dr. Andrej P. Lobanov und Dr. Eduardo Ros. Ich bedanke mich bei ihnen für die unzähligen fruchtbaren Diskussionen, die zahlreichen gute Ideen, die vielen konstruktiven Vorschläge beim Zusammenschreiben meiner Arbeit und nicht zuletzt für die überaus freundliche Arbeitsatmosphäre.

Für fachlichen Rat, die viele hilfreiche Diskussionen und nicht zuletzt die zahlreichen konstruktiven Anmerkungen zu meiner Doktorarbeit (besonders auch für den englischen Feinschliff) möchte ich mich bei den Doktoren Richard W. Porcas und Dave Graham bedanken.

Herrn Dr. Alex Kraus danke ich für seine fachliche Hilfe während meiner Einarbeitungszeit in die Radioastronomie und sein starkes persönliches Engagement bei der erfolgreichen Durchführung unserer Beobachtungen am 100 m Radioteleskop in Effelsberg.

Herrn Dr. Walter Alef danke ich besonders für seine kompetente Hilfe bei Korrelator- und Computer Fragen.

Dank gilt auch allen Operateuren des 100m Radioteleskopes, die mir bei meinen zahlreichen Beobachtungen unterstützend zur Seite gestanden haben.

Bedanken möchte ich mich bei all meinen Zimmerkollegen für das erstklassige Arbeitsklima. Hervorheben möchte ich Dipl. Phys. Lars Fuhrman, besonders auch für die vielen Themen übergreifenden Diskussionen bzgl. der schönen Dinge im Leben. Auch den Doktoranden Giuseppe Cimò und Alessio Medici möchte ich für die Hilfe bei der Lösung der kleinen Probleme im Alltag eines Doktoranden danken.

Natürlich richtet sich mein Dank auch an alle hier namentlich nicht erwähnten Mitarbeiter des MPIfR und besonders an die Mitglieder der VLBI-Gruppe für viele hilfreiche Diskussionen und das gute Arbeitsklima.

Herrn Prof. A. Marscher danke ich für die Überlassung von VLBA-Daten, welche ich zur Ergänzung unserer eigenen Beobachtungen verwenden durfte.

Ganz besonderer Dank gilt auch den Personen meines engsten Familienkreises, die mir während meiner Doktorarbeit unterstützend zur Seite gestanden haben. Das wären zum einen meine Eltern Monika und Günter und zum anderen meine Verwandten Dipl. Ing. Siegfried Buchert, Lissi Buchert und Jürgen Gedert.

Bedanken möchte ich mich auch bei Dr. Tatiana Egorova, Dr. Sabrina Casanova und all meinen Freundinnen und Freunden für ihre moralische Unterstützung beim Fortgang meiner Arbeit.

Dank gilt auch meinem ehemaligem Lehrer Wolfgang Finis, der meinen Weg in die Wissenschaft entscheidend mitgeprägt hat.